Models for prebiotically-relevant self-reproducing systems

Andrew J. Bissette

A dissertation presented in partial fulfilment of the requirements

for the award of the degree of

Doctor of Philosophy

of the

University of Oxford

Exeter College

Trinity Term

July 2015

Declaration

This thesis describes work carried out in the Chemistry Research Laboratory, Oxford, between July 2011 and May 2015 under the supervision of Dr Stephen Fletcher and Dr Mark Wallace. The thesis is a result of my own work, except when stated otherwise, and has not been submitted for any other degree at this or any other university.

Andrew J. Bissette

Abstract: Models for prebiotically-relevant self-reproducing systems.

Andrew J. Bissette, Exeter College, Trinity 2015.

Autocatalysis is central to the propagation of living systems and is widely agreed to have played a central role in the emergence of life on earth. Chemical systems which self-reproduce like living cells can offer insight into the transition from chemistry to biology. Self-reproducing micelles and vesicles, or physical autocatalysts, are an important class of autocatalytic chemical systems that have used to model the first living systems for several decades.

The study of physical autocatalysis has been restricted to a limited set of reactions, and hindered by experimental difficulties precluding full characterisation. Together these limitations pose both conceptual and technical barriers to a deeper understanding of this important class of prebiotic system. This thesis addresses both limitations in turn.

Chapter 1 introduces the concept of physical autocatalysis and argues for its importance in the field of prebiotic chemistry. A survey of chemical models of physical autocatalysis is presented and the present work is placed into context.

Chapter 2 describes the development of the first examples of physical autocatalysis driven by irreversible bond-forming reactions. Steps towards the development of asymmetric variations and systems of self-reproducing vesicles are discussed.

Chapter 3 describes the application of interferometric scattering microscopy to physical autocatalysis, allowing for the first time the observation of micellar self-reproduction on the single particle level.

Chapter 4 discusses the limitations of this work and argues that the results described in Chapters 2 and 3 respectively address major conceptual and technical barriers to the study of physical autocatalysis, with recommendations for future work.

Acknowledgements

I am utterly indebted to Stephen Fletcher for providing patient and thoughtful supervision during the execution of this work. The past four years I have felt like a partner in a conversation rather than a student in a classroom. I thank Steve for engaging me as an intellectual equal and consistently challenging me, guiding me, and providing me the opportunity and encouragement to identify and develop my talents.

This work would not have been as exciting or challenging without the enthusiasm and unique interests of Philipp Kukura and Jaime Oretga-Arroyo. Both have invited me into new and unexpected places and I am the richer for it. In particular, Jaime’s boundless energy and love for his work is infectious and made those 2am iSCAT sessions a real pleasure to participate in. Both have been patient and proactive in teaching me the black magic of super-resolution microscopy.

I would further like to thank Mark Wallace for providing support and guidance as my co-supervisor. Thanks to Barbara Odell for training me in the use of DOSY NMR, to Omer Markovitch for stimulating discussions about the lipid world, and to Alistair Holdsworth for proof-reading portions of this thesis.

Thanks to all the members of the Fletcher group past and present for being utterly ridiculous and making labs S5 and G3 a happy place to be. Since I started the list of Fletcherites has grown considerably; fortunately, I can take all the space I like to enumerate them! Thanks to Becky, Phil ‘M. Cuir-moustache’ Roth, and Tina for welcoming me back in 2011 and being friends ever since; to Mireia, Manu ‘anger’ Anger, the champagne-swilling Emeline, Hengzhi, Elle, and Florian; to Elise, Philipp, Laura, Ina, Nod, Zhenbo, night-time Nisha, and mon grand Palacin. And of course the many part ii students who have come and gone over the years, Nancy and Ed, Simon and Nessa, and most recently Sarah, who finally brought Les Mis to the lab.

Most importantly, thanks to the members of the Fletcher lab whom I had the pleasure of working with directly: Nessa Carson, Alexandra Bogdanova, and Sarah Morrow. All have had a taste of the glorious interdisciplinary mess that is prebiotic chemistry and emerged unscathed and, I hope, with their enthusiasm intact. Alexandra and Sarah carried out experiments which contributed directly to this thesis, and did so with flair. Thanks.

Beyond the hallowed doors of lab G3 I found friendship among former members of the Ed Anderson group, particularly Craig, Steven, Bryony, and Ross. Craig in particular is a bottomless well of trivia, chemical and otherwise, and was a kind mentor during my first year in the lab. Similarly, Philipp Kukura's students are a delightful bunch who made me feel very welcome as I played with their expensive and finely-calibrated instruments; I would especially like to thank MJ, Boozy and Dan for helping me over the past year.

Bhaskar Bhushan has been like a brother to me over the past five years, in that he has consistently attempted to wind me up at every turn, but I love him anyway. I'd like to thank him specifically for providing me with ligand A in Chapter 2, for proof-reading that chapter, and for not repeating his diffusion coefficient joke when doing so. Any typographical errors in that chapter are his fault alone.

Finally, I'd like to thank my parents for accepting the disappearing act I've pulled over the past five years. And last but never least, my wonderful partner Courtney: no brief witticism could ever express sufficient love and gratitude.

"If you chase two rabbits, you will lose them both."

Andrew J. Bissette

Abbreviations

Å Ångstrom(s)

Ac acetyl

aq. aqueous

Ar aryl

br. broad (spectral)

i-Bu isobutyl

n-Bu normal (primary) butyl

t-Bu tertiary butyl

Bz benzoyl

°C degrees Celsius

CAC critical aggregation concentration

cat. catalytic

Cbz benzyloxycarbonyl

cm^{-1} wavenumber

CMC critical micelle concentration

δ chemical shift

d doublet (spectral)

DCE 1,2-dichloroethane

dd doublet of doublets (spectral)

ddd doublet of doublet of doublets (spectral)

ddt doublet of doublet of triplets (spectral)

DMAP 4-dimethylaminopyridine

dq doublet of quartets (spectral)

dt doublet of triplets (spectral)

dtd doublet of triplet of doublets (spectral)

ee enantiomeric excess

EI electron ionisation

eq equivalents

ESI electrospray ionisation

Et ethyl

FI flame ionisation
g gram(s)
GARD gradied autocatalysis replication domain
gCOSY gradient Correlation Spectroscopy
gHSQC gradient Heteronuclear Single Quantum Coherence
^{1}H proton
h hour(s)
HPLC High Performance Liquid Chromatography
HRMS High Resolution Mass Spectrometry
Hz hertz
IR (Fourier transform) infra-red
iSCAT interferometric scattering microscopy/microscope
IUPAC International Union of Pure and Applied Chemistry
J coupling constant
L litre(s)
µL microlitre(s)
µm micrometre(s)
M molar (moles per litre)
m multiplet (spectral)
mbar millibar(s)
Me methyl
mg milligram(s)
MHz megahertz
min minute(s)
mL millilitre(s)
mmol millimole(s)
mol mole(s)
M.p. melting point
m/z mass to charge ratio
nm nanometre(s)
NMR nuclear magnetic resonance
Nu nucleophile

PG protecting group

Ph phenyl

ppm parts per million

i-Pr isopropyl

PTFE polytetrafluoroethylene

q quartet (spectral)

quant quantitative

quin quintet (spectral)

R generic organic group

rt room temperature

s singlet (spectral)

sat. saturated

sxt sextet (spectral)

t triplet (spectral)

t-BuOMe *tert*-butyl methyl ether

td triplet of doublets (spectral)

tdd triplet of doublet of doublets (spectral)

TFA trifluoroacetic acid

TLC thin layer chromatography

TBDMS *t*-butyldimethylsilyl

Ts *para*-toluenesulfonyl

THF tetrahydrofuran

UV ultraviolet

Table of Contents

Chapter 1

Introduction

1. Introduction

1.1. General introduction

The origin of life on Earth is largely a mystery despite the efforts of generations of researchers. In the last century significant advances have been made towards a convincing and well-supported model accounting for the emergence of the first living systems from non-living matter, but nonetheless this goal remains out of reach. This is not simply the result of unresolved technical challenges: our understanding of prebiotic chemistry lacks the basic conceptual framework that must underlie any such model.

It is widely agreed that any account of the origins of life will involve the concept of autocatalysis.[1,2] Autocatalysis and self-replication more generally are central to the propagation of life and intrinsic to many other biological processes. Studies of autocatalysis offer valuable insight into the behaviour of proto-living systems, contribute to our conceptual understanding of the principles driving abiogenesis, and bear directly on the deeper questions at hand: what is life, and might it exist elsewhere?

This thesis describes the development and characterisation of novel chemical models of prebiotic behaviour, and their study by single-particle microscopy. The research discussed within contributes to our understanding of the fundamental principles of autocatalysis, models the behaviour of prebiotically-plausible self-replicating systems, and demonstrates the potential for simple chemical systems to generate molecular and supramolecular complexity relevant to the origins of life.

This chapter outlines the place of autocatalysis in the field of prebiotic chemistry and argues for the relevance of the work contained herein. The historical and conceptual underpinnings of the work are briefly discussed, and systems analogous to those described in subsequent chapters are reviewed. Parts of this chapter have previously been published in *Angewandte Chemie*[3] and *Origins of Life and Evolution of Biospheres*.[4]

1.2. Definitions

An autocatalytic reaction is one in which the product acts as the catalyst for its own formation (Scheme 1.1):

$$A + B \xrightarrow{C} C$$

Scheme 1.1. General autocatalytic reaction. Compound C catalyses a chemical reaction in which a second molecule of C is formed.

Autocatalysis is usually demonstrated in two ways (Figure 1.1): by the presence of a sigmoidal product/time curve, and by a positive correlation between initial product concentration and reaction rate. Both effects arise because the rate of reaction is proportional to the concentration of product. Often, efficiency is limited and fully exponential growth is not realized, but rather parabolic growth is seen. Only very inefficient systems are expected to show linear growth.

Throughout, the term ‘exponential’ refers to very efficient systems, and ‘parabolic’ refers to those with limited efficiency. Ambiguous cases are described as ‘sigmoidal’. This is a qualitative term, as both exponential and parabolic plots share an S-shaped profile.

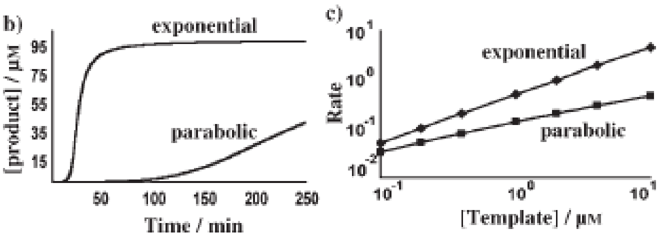

Figure 1.1. Kinetic signatures of autocatalysis. Left: exponential vs. parabolic growth. Right: the rate of reaction is proportional to initial concentration of product. From [5] with permission.

It is essential to note that sigmoidal kinetic profiles and product-induced rate acceleration can arise from processes other than autocatalysis.[6] For example, the slow activation of a catalyst may induce a lag period, or the side-reaction of a starting material may yield a catalyst for the major reaction pathway, in both cases giving rise to sigmoidal kinetics. Similarly, the product of the reaction may interact with a catalyst and increase its activity, a process called *autoinduction*.

Blackmond has distinguished between true autocatalysis and autoinduction, which she defines as a process in which a reaction product *"accelerates the rate of a kinetically meaningful step of a reaction sequence without directly producing more of itself"*[1] (Scheme 1.2). Blackmond argues convincingly that only a truly autocatalytic cycle can persist independently of secondary reaction cycles and their catalysts. This argument, if successful, undermines proposed prebiotic scenarios in which autoinductive reaction cycles are invoked as a means of prebiotic self-replication. Nonetheless, as discussed in section 1.5, the study of autoinductive reactions remains a valuable endeavour.

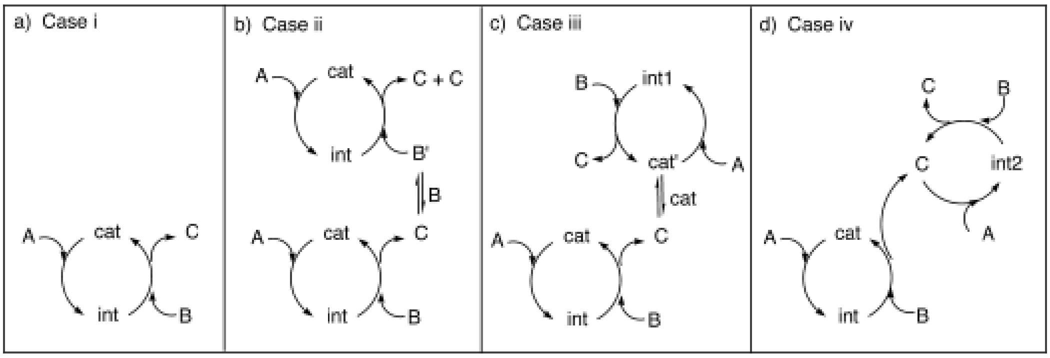

Scheme 1.2. Classification of catalytic and autocatalytic reactions by Blackmond. (a) Simple catalytic cycle; **(b)** Simple catalytic cycle plus product-enhanced cycle; **(c)** Simple catalytic cycle plus ligand-accelerated cycle; **(d)** Simple catalytic cycle plus autocatalytic cycle From [1] with permission.

Other catalytic relationships are intimately related to discussions of autocatalysis (Scheme 1.3). Cross-catalysis involves multiple species which catalyse each other's formation. This is often a symmetrical relationship, called mutual catalysis, with two species cross-catalysing the formation of each other. However, it is not necessarily symmetrical: one species may catalyse a competitor's formation without its own formation being mutually catalysed by the competitor. A species which catalyses only its own formation, and not that of a closely-related competitor, is termed a *selfish* autocatalyst.

Two autocatalysts which are mutually catalytic form a hypercycle. Eigen and Schuster proposed that hypercycles had a key role to play in the origins of life and that vestiges of hypercyclic structure exist in modern biology.[7] The stability of hypercycles under prebiotic conditions has been disputed;[8] indeed, King argued that hypercycles are intrinsically less stable than selfish autocatalysts.[9] As the work described in this thesis concerns directly autocatalytic reactions, rather than hypercycles or other autocatalytic sets, this debate will not be discussed further.

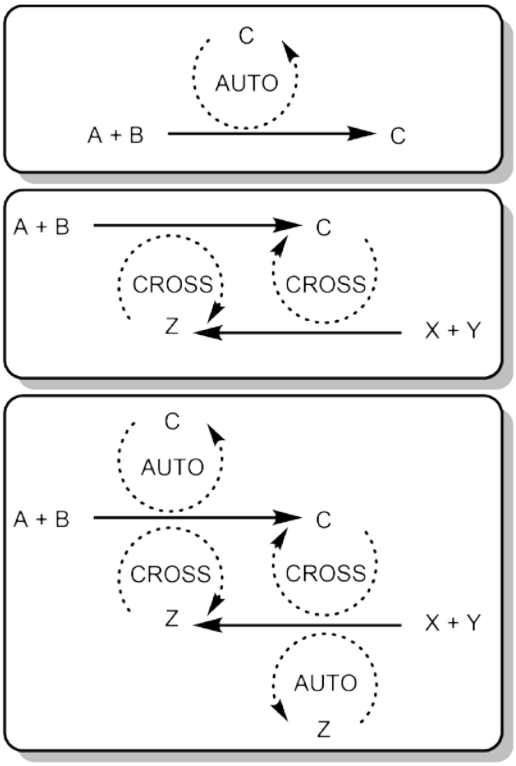

Scheme 1.3. Auto- and cross-catalysis, and a hypercycle. Top: autocatalytic cycle; Middle: mutually cross-catalytic cycle; Bottom: hypercycle. Dashed lines indicate catalytic relationships, while solid lines indicate synthetic reactions.

1.3. Autocatalysis and the origins of life

Autocatalytic chemical processes have repeatedly been implicated in the emergence of life on Earth.[1,10] From the prebiotic synthesis of molecular building blocks to the self-reproduction of the first life-like systems, roles for autocatalysis have been proposed at several stages in the transition from inanimate matter to the first life-like systems. Autocatalysis in one form or another has become an essential part of any origins of life scenario.[2]

The RNA world hypothesis is the archetypal example of an origins of life scenario which gives a central role to autocatalysis.[11] While there are several formulations of the RNA world hypothesis, broadly speaking this ‘replicators-first’ scenario posits that prebiotic chemical processes generated autocatalytic oligomers of RNA. A population of closely-related oligomers would then arise through imperfect replication, allowing primitive selection processes to act upon the population. This is argued to lead to evolution[12] and then presumably to life as we know it.

Autocatalysis has been proposed to be the cause of biological homochirality, most notably in the model proposed by Frank.[13] If an enantioselective autocatalytic reaction displays a strong positive non-linear effect arising from the formation of inert heterochiral dimers of the product, then very small enantiomeric excesses can be amplified to enantiomeric purity. Small ees may arise stochastically or from a variety of prebiotically-plausible physical sources.[14] The Frank model has been experimentally realized by Soai and co-workers,[15,16] but it remains to be demonstrated that this mechanism can operate on prebiotically plausible substrates.

These examples highlight one reason for the widespread association of autocatalysis with the origins of life: its potential to drive chemical systems away from equilibrium, and to maintain them there. As life operates far from equilibrium, any process capable of sustainably driving chemical systems away from equilibrium has a strong intuitive appeal for the prebiotic chemist.

Despite the many potentially important prebiotic roles for equilibrium processes,[17] it seems clear that kinetically stable states maintained by autocatalytic processes are profoundly interesting and that the study of autocatalysis is of fundamental importance to understanding the origins of life.

1.4. Physical autocatalysis

Numerous chemical models have been developed in order to better understand autocatalytic behaviour.[3,18–20] Since King's observation in 1978 that *"autocatalysis is viewed as a peripheral kinetic problem of little interest"*[21] and that *"few simple autocatalysts in solution are known"*, interest in autocatalysis as a fundamental class of chemical reaction has grown considerably, and chemists are now spoiled for choice when it comes to small, autocatalytic molecules.[3,15,18,22–25]

The mechanisms driving autocatalysis are diverse, ranging from template-based replicators that act as models for genetic replication[18,26,27] to systems exploiting the phase behaviour of solids in solution.[28,29] Importantly, the lessons derived from these model studies have been applied to prebiotically-relevant systems of much greater complexity, such as the chemical self-replication of RNA oligomers.[30]

A number of systems are known in which the autocatalyst is not an individual molecule or well-defined oligomer thereof, but rather a dynamic supramolecular aggregate such as a micelle or vesicle.[3,19] Here, autocatalysis occurs in the reaction between molecules occupying physically separate phases, such as organic and aqueous phases, and arises because the product of the reaction enables the reaction components to interact more efficiently (Scheme 1.4). These systems are of great interest as models of prebiotic behaviour and components of synthetic protocells, and their behaviour is described here as *physical autocatalysis* (see section 1.4.1 for a justification of this term).

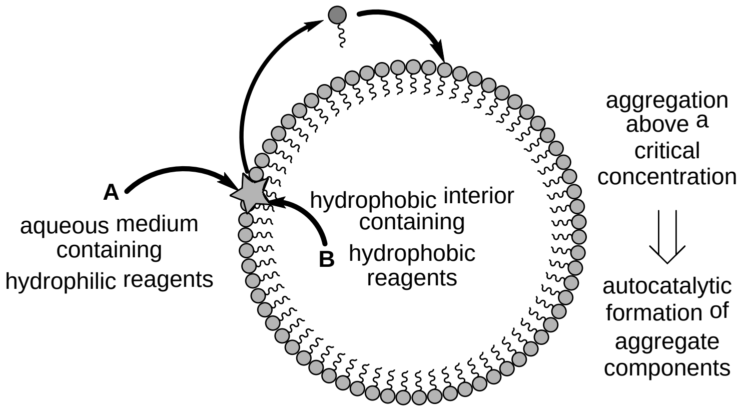

Scheme 1.4. Concept of physical autocatalysis illustrated by a self-reproducing micelle.

In the case of micelles and vesicles, the most widely studied and prebiotically significant physical autocatalysts, the product is an amphiphilic molecule which aggregates above a critical concentration. This is either called a critical micelle concentration (CMC) or a critical aggregation concentration (CAC), and is typically a narrow range of concentrations rather than a single well-defined point. The micelles or vesicles incorporate some of the hydrophobic reagent into their hydrophobic regions (the core of a micelle, or the bilayer of a vesicle), effectively transporting it into the aqueous phase for reaction. The exact mechanisms of this process are not necessarily this simple and are debated[19,31] (section 1.5.1).

There are also cases of autocatalysis in which the product does not form supramolecular aggregates but is instead a phase-transfer catalyst, hydrotrope, or cosolvent.[3] These are arguably operating on the same principle as self-reproduction of micelles or vesicles: a biphasic reaction generates a product which enables more efficient interaction of the reagents. From this perspective physical autocatalysis can be considered a general phenomenon. As pointed out by Buhse *et al.*[31], tentative evidence of autocatalysis in phase-transfer reactions was reported over 40 years ago[32] and unambiguously autocatalytic phase transfer reactions have been reported since at least 2000.[33] Reports continue to appear, and many more examples certainly lurk undetected in the literature. However as the prebiotic relevance of these processes is unclear, they are not discussed further here.

1.4.1. Autopoiesis & physical autocatalysis

The self-reproduction of micelles and vesicles has traditionally been connected to and indeed called *autopoiesis*, because early research into these systems by Luisi and co-workers was motivated by an interest in the philosophical concept of the same name.[34,35] Varela and Maturana[36] proposed autopoiesis as an operational definition of life forty years ago, and it has been controversial ever since.[35,37]

Autopoiesis has been formulated in different ways by various authors.[35–38] Recently Razeto-Barry defined autopoiesis as *"a network of processes which produces all the components whose internal production is necessary to maintain the network operating as a unit".*[37] Citing Varela, Luisi[35] offered a more concrete set of criteria for identifying an autopoietic entity: *"verifying (1) whether the system has a semipermeable boundary that (2) is produced from within the system and (3) that encompasses reactions that regenerate the components of the system"*.

It is important to note that Luisi's criteria are not a definition of autopoiesis, but rather a set of epistemic guidelines for the identification of autopoietic entities in the laboratory. This distinction has consequences, but has occasionally been overlooked by experimentalists.[39] Following Luisi's lead, chemists have consistently emphasised the importance of a semi-permeable boundary in not only identifying autopoietic systems, but in defining autopoiesis. Theorists are more divided on this subject. Several authors, including Varela, agree that a self-produced boundary is part of the definition of autopoiesis, but others do not consider this to be a general requirement but rather a practical matter.[37] Razeto-Barry offers a concrete illustration of a more general alternative, in which an autopoietic system is held together by surface tension and other cohesive forces rather than a distinct membrane.

While these questions are somewhat abstract, their implications are far-reaching and controversial. On a practical level, if a self-produced boundary is not necessary for autopoiesis then a broader range of structures, such as simple oil-in-water droplets,[40] may meet the criteria for autopoiesis under the right conditions. More provocatively, if one accepts that autopoiesis is sufficient for life, and that a self-reproducing vesicle is indeed an autopoietic entity, then the conclusion that these simple chemical systems are living inevitably follows. A proponent of this position is committed to the claim that life has already been created de novo in the laboratory.

Understandably this controversial view is not widely-held, and is not endorsed here. The foremost proponent of autopoiesis in the scientific community, Luisi, concluded that autopoiesis is necessary but insufficient for life, and thus that self-reproducing vesicles may be autopoietic but non-living.[35] Further, it is debated whether a simple self-reproducing vesicle is indeed autopoietic; it is not clear whether the mechanisms of micelle or vesicle self-reproduction actually meet the requirements of autopoiesis,[31,35] although a more elaborate protocell of the kind envisaged by Szostak, Bartel and Luisi[41] may well do so.

Given the controversies associated with autopoiesis and its ambiguous relationship to self-reproducing micelles and vesicles, we have instead adopted the term physical autocatalysis to describe these systems. We adapted this term from Stano & Luisi[19] who used the term "physical catalysis" to emphasise that physical autocatalysts may not perform catalysis according to some definitions, i.e. they may not increase the rate constant/decrease the activation energy of the reaction, and do not typically catalyse the reverse reaction.[42]

In these systems the autocatalyst is a poorly-defined dynamic aggregate rather than a well-defined single molecule or oligomers(s) thereof. This lack of molecular identity between the catalyst and the product leads to the common (but disputed) distinction between self-replication and self-reproduction.[26,43,44] However, as the behaviour of these systems is empirically and conceptually autocatalytic, in our view at the very least the use of the term autocatalysis in a somewhat looser sense is justified.

It should be noted that despite these qualifications, these processes are not autoinductive: the active catalyst is an aggregate of product molecules only and does not require a secondary catalyst. In this sense, these systems are no different to the catalytically-active oligomers involved in the Soai reaction,[15] an archetypal example of 'true autocatalysis'.[1,6]

Use of the term physical autocatalysis thus offers several advantages: it avoids the additional complexities associated with autopoiesis, distinguishes these systems from classically autocatalytic systems, and emphasises the intrinsically interesting chemistry at play in these reactions.

1.4.2. Prebiotic roles for lipid aggregates

Several prebiotic roles for micelles and vesicles have been proposed. These include catalysis, compartmentalisation, and, naturally, self-replication and the transmission of compositional information.[45–48] Walde has thoroughly reviewed the potential roles for lipid aggregates in the prebiotic world.[46,49] The prebiotic plausibility of lipid aggregates is well-established:[47,50–53] numerous simple surfactants are widely agreed to have been available on the early Earth, including fatty acids[54] and alkyl phosphonic acids.[55]

Self-assembly of lipids in water is spontaneous, which is naturally appealing to the prebiotic chemist. While micelles typically represent thermodynamic minima, the formation of vesicles of defined lamellarity or size typically requires the input of energy, for instance through sonication, and well-defined vesicles of this kind are typically metastable species.[49] Nonetheless, once formed, vesicles can persist for long periods of time.[46] Beyond self-assembly, prebiotically-plausible mixtures similar to those found in carbonaceous meteorites can demonstrate surprisingly complex catalytic properties driven by the incorporation of hydrophobic materials into the vesicle membrane.[56]

Both micelles and vesicles are capable of compartmentalising and concentrating reagents which otherwise would be unstable or too dilute to interact. For example, hydrophobic reagents partition into the hydrophobic interior of micelles or of vesicle membranes, which can stabilise them towards hydrolysis and promote reactivity with other hydrophobic species[48] or reagents in the aqueous phase; indeed, this is the mechanistic basis for physical autocatalysis. A wide variety of reactions can be promoted by the membrane surface,[49] and the altered physical environment within the aqueous interior can alter reactivity. For example, the notoriously unselective formose reaction can be tamed to a significant extent by encapsulating it within a phospholipid vesicle.[57] Hydrophilic reagents can be encapsulated within the aqueous interior of vesicles, depending on the composition of the membrane and hence how easily they can cross it or 'leak'. Polymers are readily encapsulated even within rather leaky fatty acid vesicles.[58]

During division encapsulated or membrane-bound reagents can be retained by the newly-formed vesicles.[59,60] By encapsulating reagents in this way, vesicles offer the first semi-living systems a semblance of identity and the ability to persist long enough to reproduce. Given these properties and their obvious analogy to modern cells, vesicles are generally of more interest to prebiotic chemists than are micelles.[61]

The use of lipid aggregates to compartmentalise prebiotic systems is also conceptually appealing as it offers a degree of continuity with modern biology. If lipid membranes were present in the very earliest living systems, we have only to explain the transition to more complex compositions. Interestingly, there are reports that the inclusion of small quantities of phospholipids, monoacyl glycerols, or other components into fatty acid vesicles can impart a number of favourable properties.[54,62,63] Even simply including multiple fatty acids of varying chain lengths, the typical products of prebiotic fatty acid synthesis, can improve vesicle stability.[64] These observations may suggest a selective pressure towards more complex membrane compositions.[54]

By contrast, alternative scenarios in which the first living systems were compartmentalised by inorganic structures[65,66] must eventually account for the transition to lipid-based biochemistry.[61] This is not a fatal flaw of such scenarios and certainly does not diminish the importance of studying inorganic systems, which have achieved a remarkable degree of sophistication[67,68] and are even capable of self-reproduction.[69]

As well as having numerous proposed roles on the early Earth, lipid aggregates are a central component of many synthetic protocells.[47] Protocells are widely studied in order to understand the minimal criteria for life and to model the behaviour of prebiotic systems. Szostak, Bartel, and Luisi influentially proposed a synthetic protocell composed of a simplified self-replicating genome encapsulated by, and coupled to, a self-reproducing vesicle.[41] This coupling of vesicle reproduction to the replication of functional molecules within the vesicle, often called core-and-shell reproduction,[70] is crucial to the viability of protocells of this kind. Without this, the concentrations of essential molecules cannot be maintained at the appropriate range, presumably leading to death by dilution or over-concentration.

More profoundly, Szostak *et al.* suggest such a protocell may be capable of evolving. By coupling the fates of the genetic and membrane components, the system as a whole may be subject to selection. For example, a genetic system capable of synthesizing fresh membrane components would presumably result in a protocell which reproduces more efficiently as a unit, and therefore be selected for over less prolific competitors. If this is the case, such as system might be considered living or semi-living; certainly such a system would instantiate *"the skeleton of Darwinian dynamics"*.[71] Among others, Sugawara and co-workers have made significant progress towards realising this vision,[60] and Szostak and co-workers continue to improve the efficiency of non-enzymatic RNA replication.[72] It seems that this ambitious proposal may be realised in the near future.

1.4.3. Physical autocatalysis in the lipid world

The self-reproduction of micelles and vesicles forms a cornerstone of the lipid world scenario.[45] This postulates that life arose from a population of auto- and mutually-catalytic lipid aggregates. These are proposed to be subject to a form of natural selection based on the relationship between composition and function, which is here termed *compositional inheritance*.

Compositional inheritance, put briefly, suggests that the composition of a lipid aggregate determines its functions, that composition is inherited during aggregate fission, and that populations of these species can respond to natural selection. The most obviously relevant functions of an aggregate are its autocatalytic efficiency, that is the rate at which it can produce new lipids, and its selectivity, the fidelity with which it maintains its composition over time. Cross-catalytic function is also relevant: aggregates which also promote the growth of competing species may be out-competed, or form relationships analogous to hypercycles.[73] The nuances and plausibility of compositional inheritance of this kind are the subject of much discussion, simulation, and theoretical analysis.[73–76] At present, it is unclear that any kind of natural selection can act on non-living chemical networks,[10,74] although forceful arguments to the contrary have been presented.[77,78]

The development of experimental demonstrations of compositional inheritance has proven challenging,[79] and novel approaches to the topic would contribute significantly to the debate. Chemical selectivity appears on the face of it to be critical to the viability of compositional inheritance: intuitively, it seems that for an aggregate to maintain its composition over time it must be able to synthesise or incorporate lipid molecules at the correct rate. Too fast, and a particular species will come to dominate the aggregate; too slow, and the species will be diluted by the uptake of other species. These complex relationships lend themselves naturally to mathematical analysis.

Simulations of compositional inheritance in lipid systems typically use the graded autocatalysis replication domain (GARD) model.[78,80,81] This model describes the non-equilibrium behaviour of mixtures of up to thousands of lipid species that form catalytically-active aggregates of heterogeneous composition. The model has several parameters which determine the kinetic and thermodynamic behaviour of the system, and from which the population-level dynamics emerge. Where possible, these parameters are guided by experimental data.[81,82] Typical GARD simulations follow one aggregate over many generations rather than many aggregates in parallel. The key equation is shown in equation 1.1.

$$\frac{dn_i}{dt} = (k_f p_i N - k_b n_i)(1 + \sum_{j=1}^{N_G} \beta_{ij} \frac{n_j}{N} \qquad 1.1$$

Firstly, for each lipid i there are parameters describing the rates of aggregation k_f and disaggregation k_b, and by extension the equilibrium distribution of the lipid between monomeric and aggregated states. There are N_G lipid species in the system.

Secondly, the quantity of each lipid i in bulk solution p_i and in the aggregate n_i at any given time is tracked, as is the size N of the aggregate at any given time.

Thirdly, there are catalytic parameters describing the influence of each lipid species on every other lipid species. This matrix of parameters allows each molecule of one lipid species present in the aggregate to influence, however slightly, the association/dissociation rate parameters of every other lipid species in the system. The influence of lipid i on the rates of lipid j is denoted β_{ij}. Each molecule of a lipid species present in a given aggregate may catalyse or inhibit either or both the association and dissociation of any lipid species, including itself, to the aggregate.

Finally, rules for the system are given, such as whether the system is open or closed and hence whether the pool of monomers is finite or not. Importantly, it is assumed that above a certain size N_{max}, the aggregate destabilises and divides into two new aggregates of size $N_{max}/2$ with randomly-determined compositions that are closely related to that of the original aggregate. In typical simulations only one of these aggregates is retained and simulated in subsequent generations, thereby simplifying the calculation.

The behaviour that emerges from this basis is complex: aggregates form and their compositions and catalytic functions change over time. In closed multispecies systems, the distribution of aggregate compositions passes through a kinetic peak before eventually decaying to the equilibrium concentration, as determined solely by the relative forward and backward rates of aggregation for each lipid (Figure 1.2).[79]

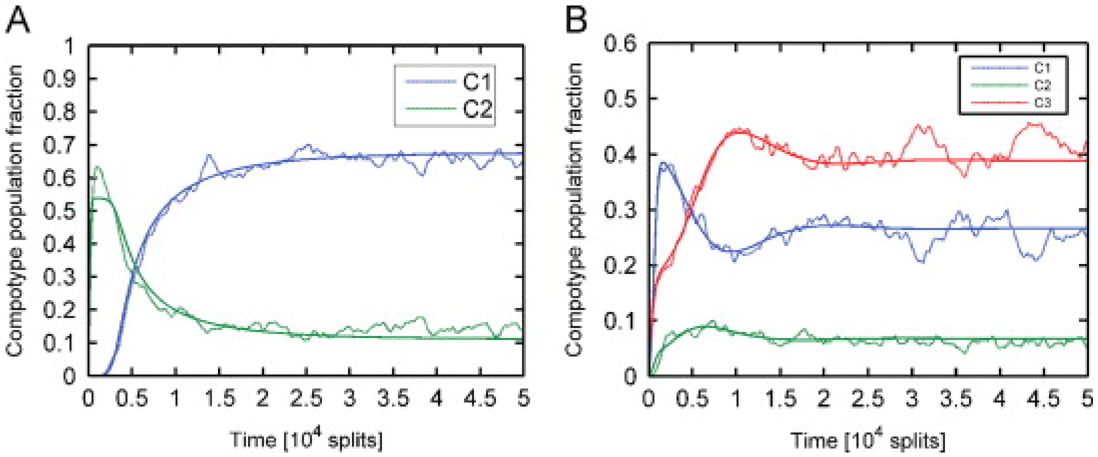

Figure 1.2. Population dynamics in the GARD model. The distribution of aggregate compositions in systems containing **(A)** two and **(B)** three major compotypes varies over time before decaying to the equilibrium composition. Reproduced from [79] with permission.

Selectivity in this model is given by the matrix of catalytic parameters.[81] Each lipid species has a catalytic effect on the association behaviour of every other lipid species, including itself. This effect is dependent on the number of molecules of the lipid in each aggregate. The system tends to be dominated by populations of aggregates which can maintain their composition over time, called compotypes, through autocatalytic or mutually catalytic processes. These have been shown to be analogous to the quasi-species found in models of template-based self-replicating systems.[76]

It is important to emphasise that an individual lipid species does not need to selectively catalyse its own formation or aggregation in this model: rather, a given compotype needs to, overall, promote its own propagation or the propagation of a mutually catalytic aggregate of a different composition. Indeed, it has been argued that the latter process tends to produce more diverse sets of compositions that are stable over multiple generations and is required for evolution to occur in the lipid world.[73]

Overall, the model describes a pool of lipid monomers which may or may not be replenished over time, which form heterogeneous aggregates. The kinetic behaviour of the aggregates is influenced by the composition of the aggregates, and the system is transiently dominated by aggregates with compositions that can, one way or another, maintain and propagate their own composition.

This treatment may well capture the behaviour of proposed scenarios in which lipids are synthesised geochemically rather than through physical autocatalysis, and the surrounding solution becomes populated with lipid aggregates that propagate by exchanging monomers with the environment. This resembles common experimental conditions rather closely (see section 1.5.3). Nonetheless, it contains questionable assumptions even for this scenario. Most obviously, under many conditions vesicles do not simply divide upon reaching a critical size (see section 1.5.2); indeed, single-lipid vesicles of differing hydrodynamic radii can coexist,[83] and vesicles can coexist with micelles of the same compound.[84] While there are conditions under which spontaneous division occurs,[85–87] in other studies of self-reproducing vesicles division must be induced manually, for example through extrusion[88] or shear force.[89]

Further, there are multiple pathways by which vesicles may reproduce:[19] some mechanisms do not involve the division of a single vesicle into two vesicles with closely-related compositions, but rather the external growth of fresh vesicles from lipid micelles either in solution[85,86,90] or on the surface of a vesicle.[91] Under these conditions, it is not clear that the new vesicles would inherit the composition of the original.

In cases of physical autocatalysis these assumptions are further stretched. Here, factors other than the affinity of an aggregate for fresh monomers may be relevant: the capacity to solubilise hydrophobic reagents and promote their interaction with reagents in the aqueous phase; whether the autocatalytic reaction occurs within a vesicle, in a bilayer or micelle, or in bulk solution; and the relative rates of division vs. release of freshly-synthesised lipids into solution. This is without considering further heterogeneities in the system, such as the role of mineral surfaces to organise vesicles and provide reaction sites. Given these additional factors, the GARD model may not accurately capture the selectivity of physical autocatalysts.

These limitations are necessary evils: any simulation can only approximate experimental conditions and indicate what is possible, just as any experiment can only ever model the prebiotic world. Thus, this criticism is not intended to impugn the value or quality of this body of work, but rather to emphasise the need for caution in extrapolating from these simulations to prebiotic scenarios, and the need for experimental validation of its predictions.

Unfortunately, and in contrast to template-based self-replicating systems,[3,18] the chemical fidelity of physical autocatalysts has not been studied experimentally in any detail. As such the relationship between aggregate composition and autocatalytic function is unclear. To date there have been no direct competition experiments between different physical autocatalysts, although as alluded to above there are examples of differences in stability between vesicles of varying composition.

The most common experimental approach to this topic has been to examine the influence of additives to the stability of fatty acid or phospholipid vesicles. A number of factors have been used to select for different populations of vesicles. Membrane heterogeneity can improve the stability and propensity for growth of fatty acid vesicles relative to homogeneous vesicles.[54,83,92] The influence of encapsulated materials is also significant. Encapsulated ribonucleotides can induce osmotic swelling, which in turn increases the affinity of fatty acid vesicles for monomers to the point where swollen vesicles leech monomers from neighbouring empty vesicles.[58] Similarly, the production of hydrophobic dipeptides by an encapsulated catalyst can induce the growth of fatty acid vesicles. In this scenario, selectivity between vesicles containing catalysts of differing efficiencies was even detected.[93] There is also a report of selection on the basis of enantiomeric composition: below 10 °C, vesicles of racemic 2-methyldodecanoic acid are unstable and undergo phase separation, while enantiopure vesicles remain intact and capable of autocatalytic growth (albeit without enantioselectivity).[94] Selection on the basis of higher levels of organisation may also be possible: Luisi and co-workers have shown that 'colonies' of multiple giant vesicles display increased stability and permeability to nucleotides.[95]

It remains to be seen whether the assumptions of the GARD model can be applied to physical autocatalysts, and whether compositionally diverse physical autocatalysts can maintain their composition over time. It has also yet to be shown experimentally that physical autocatalysts can form higher-order networks such as hypercycles, or whether this is limited in practice to intrinsically selective autocatalysts such as template-based self-replicators. Whether compositional inheritance is a powerful force of evolution,[73] or is merely a *"poor man's natural selection"*[74] leading to only a limited elaboration of prebiotic chemical networks, self-reproducing systems of this kind are prebiotically relevant and worthy of study.

1.5. Chemical models of physical autocatalysis

Numerous chemical models of physical autocatalysis have been developed and are reviewed here. These studies illustrate the mechanistic basis for physical autocatalysis, the conditions under which it can occur, and the limits of the current literature. Physical autocatalysis not involving lipid aggregates is not discussed as the prebiotic significance, and the relevance to this work, is not obvious (section 1.4).

Here systems are divided into those involving micelles and those involving vesicles. In general, the focus is on systems driven by chemical reactions, rather than enzyme-catalysed reactions or simple physical forces. However, a number of illuminating studies not involving chemical reactions are reviewed in section 1.5.3.

As will become apparent, while sophisticated examples of physical autocatalysis have been developed, the topic remains relatively poorly understood and there are opportunities for the development of novel examples of physical autocatalysis driven by chemical reactions.

1.5.1. Self-reproducing micelles

The first examples of autocatalytic reverse micelles[96,97] and micelles[98,99] were reported by Luisi and co-workers in the early 1990s. Aggregates composed of octanoate anions were found to catalyse the formation of additional octanoate (Figure 1.3).

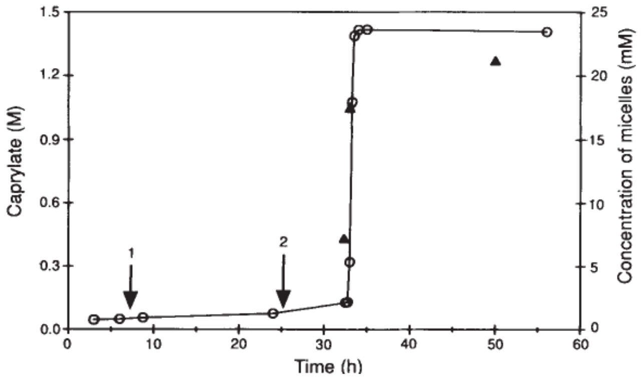

Figure 1.3. Kinetics in Luisi's self-reproducing micelles. The exponential phase could be promoted earlier by either rapidly stirring the reaction to increase the surface area (1) or seeding the reaction with product (2). From [99] with permission.

Octanoate was produced by ester hydrolysis, either under strongly basic conditions[96,99] or through enzyme catalysis[98] by lipases. The oxidation of 1-octanol to octanoate by permanganate[98] was also shown to be autocatalytic (Scheme 1.5). Similar behaviour was observed by Kust and Rathman in the oxidation of amines to *N*-oxides by hydrogen peroxide.[100] All of these reactions are autocatalytic with respect to the amphiphilic product, and Luisi interpreted this behaviour as arising from the autopoietic mechanism described above (Scheme 1.4).

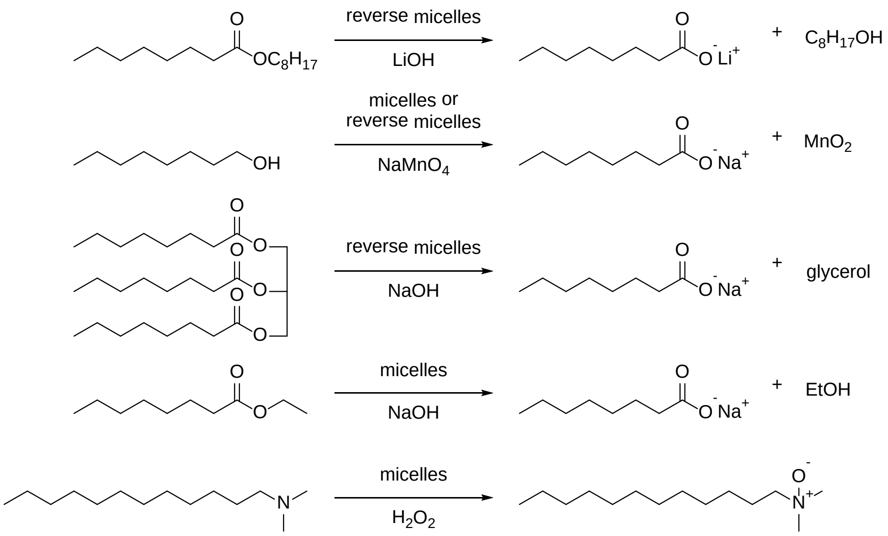

Scheme 1.5. Autocatalytic micellar systems reported by Luisi (1-4) and Kust and Rathman (5). Co-surfactants, stoichiometry, and side-reactions are omitted for clarity.

Luisi's ester hydrolysis reactions have been modelled by several groups. Mavelli[101] and Coveney[102,103] treated the reaction as classical micelle catalysis, while Buhse *et al.*[31,104] modelled the reaction as phase transfer catalysis (Scheme 1.6). In the case of long-chain (including C_8) alkanoates, Buhse's work confirms the broad strokes of Luisi's proposal: mixed micelles composed of product and ester form during the reaction and solubilize the ester in the aqueous phase, thus catalysing the reaction. However, there is a crucial mechanistic distinction: the hydrolysis reaction itself does not occur at or in the micelles, but rather in bulk solution. The micelles act as a phase-transfer catalyst.

The authors also emphasise that the active species is a mixed micelle of the product and hydrophobic reagent, rather than pure product; empty micelles must be recycled and take up more of the hydrophobic reagent in order to turn over as catalysts.

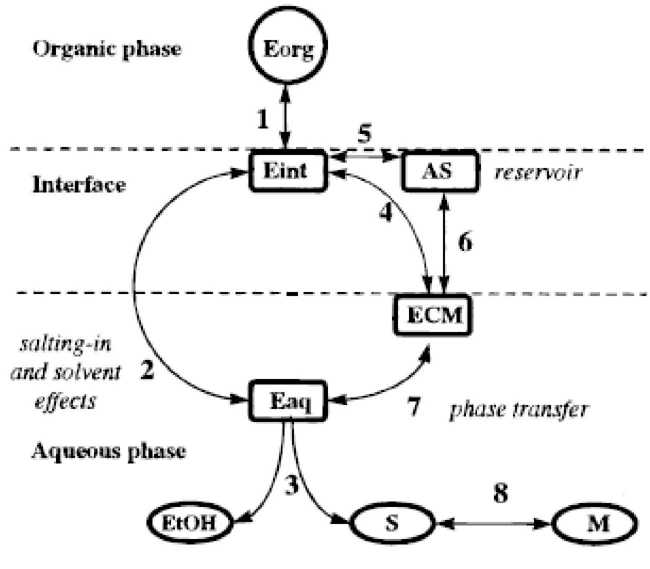

Scheme 1.6. Phase-transfer kinetic model for self-reproducing micelles. From [104] with permission.

This model accounts for the experimental data well, and explains some unusual behaviour. The ethanol by-product acts as a cosolvent, increasing the solubility of the ester and allowing the reaction to proceed faster. This leads to autocatalysis even when the alkanoate is too short (C_4) to form micelles (Scheme 1.7).

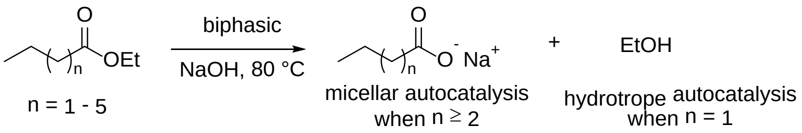

Scheme 1.7. Hydrotropic autocatalysis in ester hydrolysis.

More recently, Nguyen *et al.*[39] described a dynamic combinatorial library comprising a hydrophobic aldehyde and eight hydrophilic amines which reversibly condense into eight imine surfactants (Scheme 1.8). Micelles of these imines exhibited varying degrees of autocatalytic efficiency and thermodynamic stability. While competition experiments between multiple autocatalysts were described, the equilibrium product distribution reflected only the thermodynamic stabilities of the products rather than any differences their autocatalytic or other kinetic properties. As such, these experiments have little to contribute to the discussion of selection and competition in section 1.4.3.

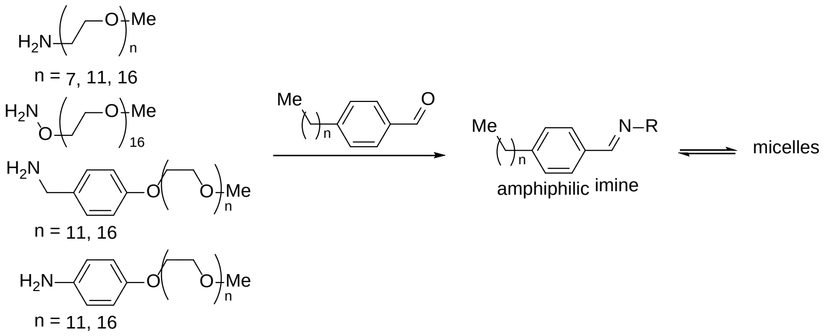

Scheme 1.8. Giuseppone's self-reproducing micelles. The micelles demonstrate autocatalysis with different efficiencies.

While a full kinetic model of this system has not been reported, some evidence was provided that it operates by micellar catalysis rather than by the phase transfer mechanism proposed for Luisi's systems. A diffusion-ordered NMR spectroscopy (DOSY) study (Figure 1.4) of one imine at equilibrium indicated that the hydrophobic aldehyde was fully associated with the micelles, and the hydrophilic amine was free in solution. If the micelles do act as phase transfer catalysts, the quantity of free aldehyde in the aqueous phase is below the detection limit in this experiment.

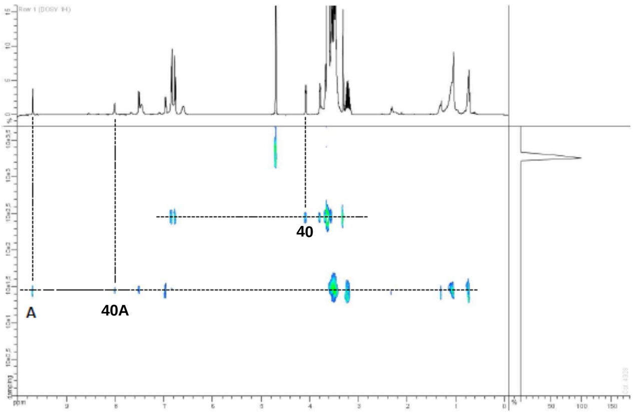

Figure 1.4. DOSY spectrum of self-reproducing imine 40A. Aldehyde **A** is associated with the imine micelles, while hydrophilic amine **40** is free in solution. These compound numbers do not correspond to the numbering in this thesis and are solely for reference within this figure. From [39] with permission.

1.5.2. Self-reproducing vesicles

Vesicles are generally held to have greater prebiotic relevance than micelles, in part because of their ability to compartmentalize and retain polar solutes and polymers (see section 1.4.2), and in part because of their obvious analogy to modern cells.[49,61] The self-reproduction of vesicles is therefore an important topic for the prebiotic chemist, and the coupled 'core-and-shell' reproduction of a vesicle and an encapsulated genetic molecule is a long-standing research goal.[19]

The mechanisms by which vesicles self-reproduce have been the focus of many experimental and theoretical studies. Vesicles have been shown to divide, fuse together, or undergo other phase behaviour that may be relevant to primitive prebiotically relevant processes.[19,105–107] The route(s) by which vesicles divide varies depending upon the source of new amphiphiles (e.g. reactions vs. pre-formed micelles), the size and composition of the vesicles, and other factors.[19,71]

As with self-reproducing micelles, in these vesicle-based systems sigmoidal growth is observed and the presence of pre-formed vesicles reduces the induction phase. A number of kinetic models have been developed and have highlighted several important variables governing the division of vesicles.[71] These include the structure and diversity of membrane components, the size and shape of the vesicle, and the rates of chemical processes occurring at the membrane. A general point of these studies has been that, in many vesicle-based systems, changes beyond simple growth are required in order for division to occur. For example, the stability of a vesicle may be reduced by changes in shape or localized deformations in the membrane arising from compositional imbalances between the inner and outer membrane leaflets.

Early efforts by Luisi and co-workers to develop self-reproducing vesicles using enzyme catalysis to drive the autocatalytic hydrolysis of either octanoic or oleic anhydrides proved troublesome.[108,109] These reactions proceeded slowly and vesicle division was not unambiguously demonstrated. In these experiments, the enzymes were encapsulated within the vesicles rather than bound to the membrane.

Non-enzymatic methods proved more successful: alkaline hydrolysis of fatty acid anhydrides allowed efficient self-reproduction,[110,111] as did later systems driven by base-catalysed cleavage of phosphate esters[112,113] (Scheme 1.9). Anhydride-based systems were successfully combined with enzymatic reactions contained within the vesicles,[70,114,115] including enzymatic RNA replication. The latter experiments are a step towards ‘core-and-shell’ reproduction, a simple model of a cell. However, replication of the ‘genetic’ component and reproduction of the vesicle are not coupled in a controlled manner in these systems.

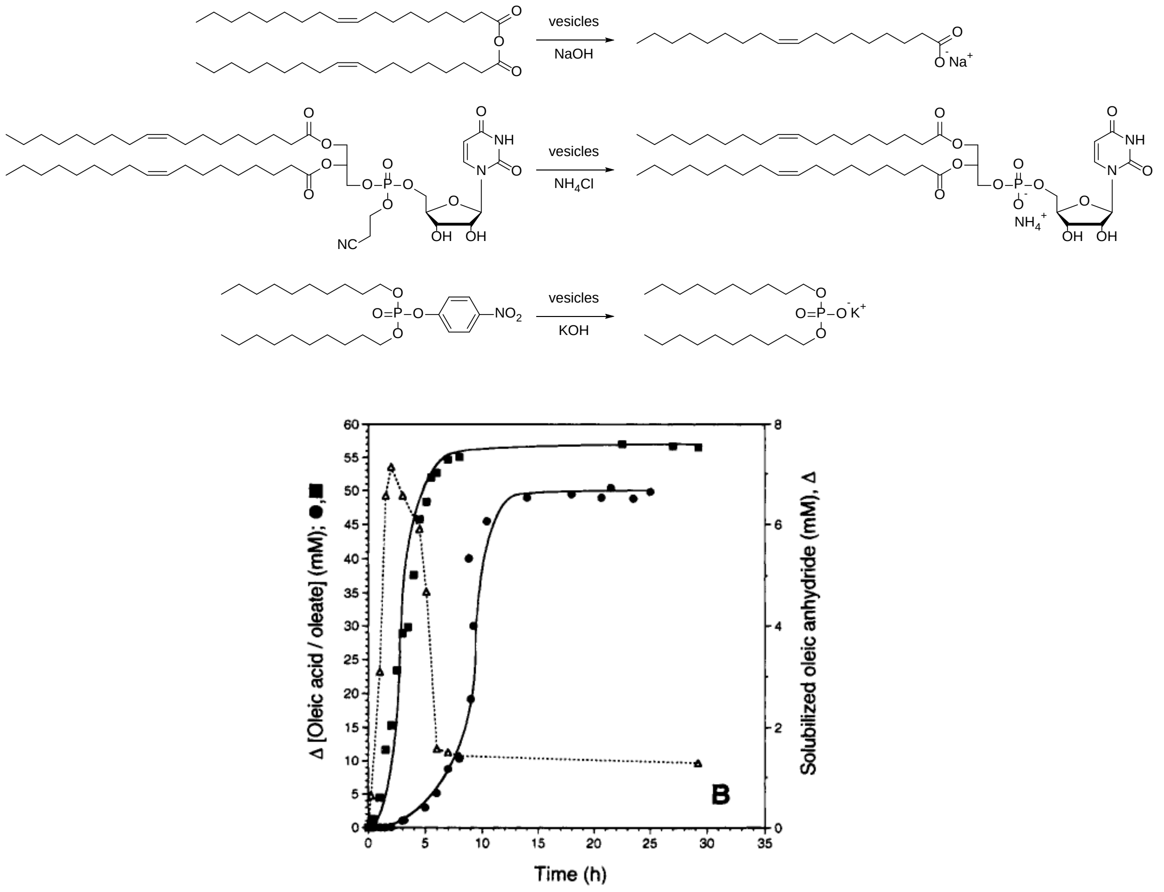

Scheme 1.9. Self-reproducing vesicles reported by Luisi demonstrate efficient growth. Bottom panel reproduced from [110] with permission.

The hydrolysis of chiral fatty acid anhydrides showed no evidence of stereoselectivity, a prerequisite for asymmetric physical autocatalysis.[94] Interestingly, vesicles of enantiopure fatty acids were shown to be more stable than their corresponding racemates. Below 10 °C, vesicles of racemic 2-methyldodecanoic acid are unstable and undergo phase separation, while enantiopure vesicles remain intact and capable of (racemic) autocatalytic growth.

Later research by Monnard and co-workers has shown that photocatalytic ester hydrolysis can drive physical autocatalysis (Figure 1.5).[59,116,117] These systems depend on a secondary catalytic cycle, which is not reproduced, and can thus be thought of as autoinductive rather than truly autocatalytic[*] (Scheme 1.2). In both cases, decanoate esters are hydrolysed through a photocatalytic system involving a ruthenium complex, an electron donor (either a modified nucleobase or ascorbate), and a hydrogen donor (either an amino acid or ascorbate). The catalytic complex and electron donor are both bound to the membrane rather than encapsulated in the aqueous interior, providing significant rate enhancements comparable to covalently linking the two species together. By immobilizing vesicles on glass beads, cycles of growth and division could be demonstrated, with newly-formed vesicles inheriting the photocatalytic complex during division. While sigmoidal kinetics were not described, vesicle division driven by a membrane-catalysed reaction was clearly demonstrated.

---

[*] Despite the emphasis by some researchers on the primacy of 'true' autocatalysis[1] over autoinductive processes, the study of more complex catalytic networks in which autocatalysis on the supramolecular level is coupled with autoinduction on the molecular level is interesting and ambitious, and has led to remarkable advances (see below).

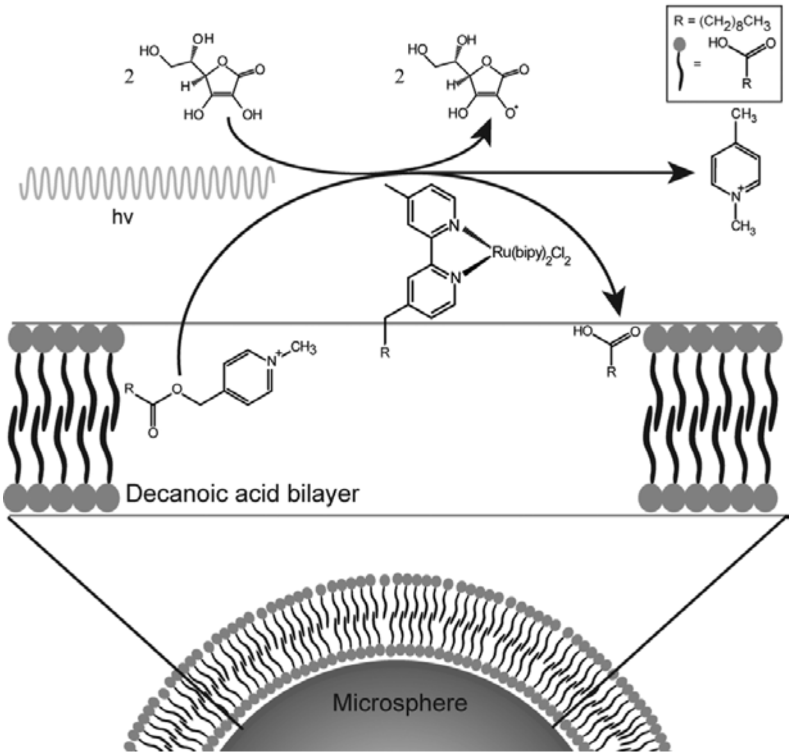

Figure 1.5. Autoinductive photocatalytic ester hydrolysis with inheritance of the secondary catalyst. From [59] with permission.

A single example of autopoietic homeostasis has been reported, in which the synthesis and destruction of vesicle components are balanced to give a steady state of vesicles as monomers are constantly turned over.[118] Vesicles of oleate are produced autocatalytically by alkaline hydrolysis of oleic anhydride. Simultaneously, oleate is oxidized to a compound which does not form vesicles. A point of interest is that the OsO_4 oxidant was artificially bound to the vesicle membrane, to ensure that the destruction reaction took place at the vesicle surface rather than in bulk solution. The two processes could be balanced to give growth, death, or homeostatic stages.

This system has been modelled theoretically[119] (Scheme 1.10). Notably, simulations of populations of self-reproducing vesicles including both production and destruction of vesicle components were shown to be subject to primitive selection, based on their stability to stochastic fluctuations.[120]

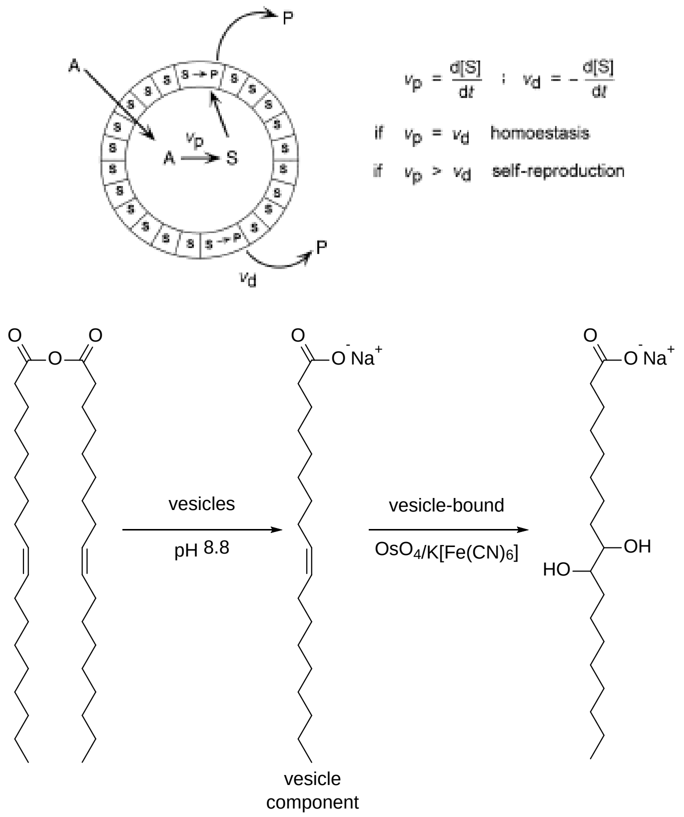

Scheme 1.10. Homeostatic vesicles based on the balance between synthetic and destructive reactions. From [118] with permission.

More recently, Sugawara and co-workers have used novel bolaamphiphiles to develop several generations of self-reproducing GVs.[91,121,122] These systems demonstrate innovative methods of controlling the location of the reaction within the vesicle using autoinductive reactions, and culminated in a striking example of core-and-shell reproduction.

An early system used a membrane-bound catalyst to deprotect an aldehyde, ensuring that condensation with an amine to produce the surfactant occurred inside the vesicle[121] (Scheme 1.11). This is a rare example of self-reproduction driven by a bond-forming reaction, similar to that described by Nguyen *et al.*[39] (section 1.5.1).

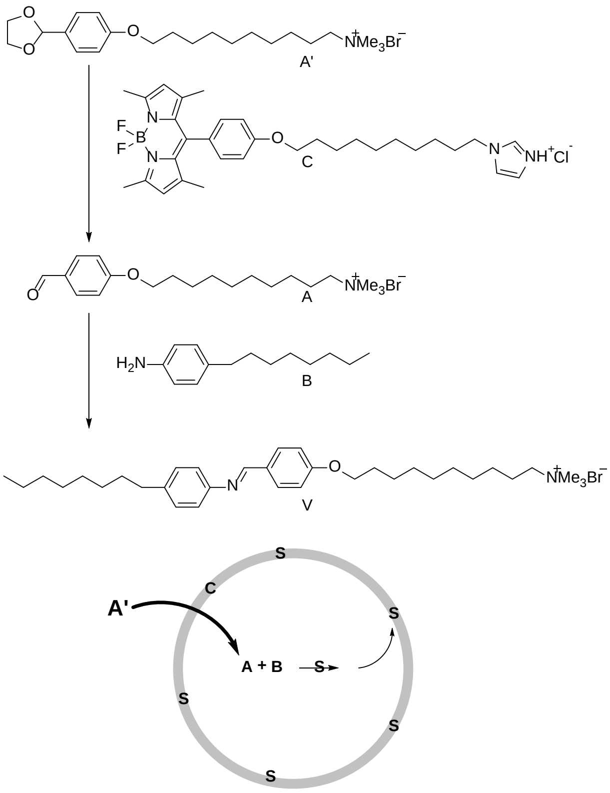

Scheme 1.11. Imine formation drives vesicle self-reproduction. Adapted from [19].

Several systems based on imine hydrolysis were used to study the factors influencing growth and division[122–124] (Scheme 1.12). The interaction of non-amphiphilic organic ions with the charged membrane was shown to induce division. By including a phosphate moiety in the surfactant precursor, the reaction was localized to the membrane. As a consequence, new vesicles formed at the membrane, a process described as 'peeling'.

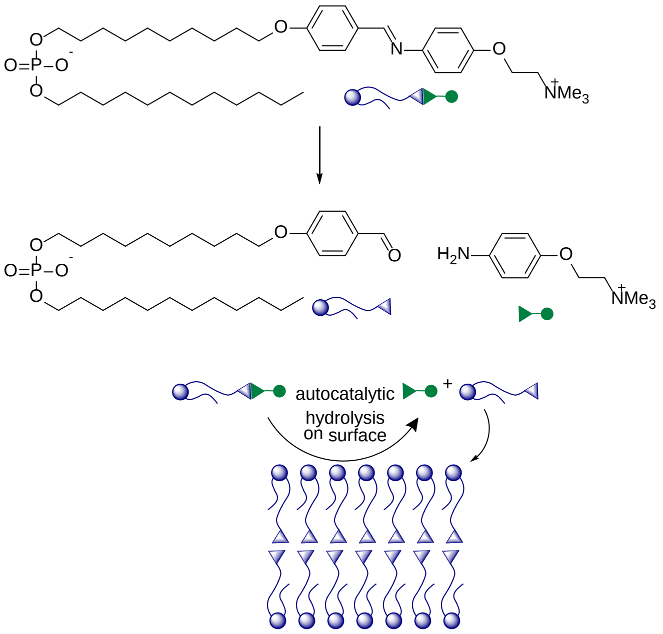

Scheme 1.12. 'Peeling' driven by surfactant structure. Adapted from [91].

The system was modified to tolerate the conditions necessary for the polymerase chain reaction,[60,122] allowing the development of an ambitious protocell (Scheme 1.13). Here, imine hydrolysis was mediated by a membrane-bound catalyst, and thus the system is autoinductive rather than autocatalytic.

Importantly, newly-formed DNA synthesized by PCR inside vesicles associates with the charged membrane. This interaction promotes division of the vesicles, just as simpler organic ions were shown to do previously. Consequently, vesicles containing larger amounts of DNA divided faster. The increased rate of division of vesicles here is not simply a function of DNA destabilising vesicles and inducing division, as the rate of the autocatalytic imine hydrolysis is increased by the presence of DNA. This creates a one-way coupling between DNA replication and vesicle reproduction: only after DNA replication reaches a critical threshold do the vesicles divide. The study represents an important step towards full 'core-and-shell' self-replication, and thus a model of a minimal cell. As the catalyst for surfactant formation and the PCR enzymes are not replicated, this ground-breaking model stops just short of that ideal. The significant implications of this system for synthetic biology have been discussed elsewhere.[125]

Moreover, this demonstrates a simple form of selection between otherwise identical physical autocatalysts on the basis of composition: DNA-containing membranes exhibit enhanced autocatalytic efficiency. As discussed in section 1.4.3, any demonstration of selectivity between competing physical autocatalysts offers sorely-needed experimental support for 'lipid world' models.

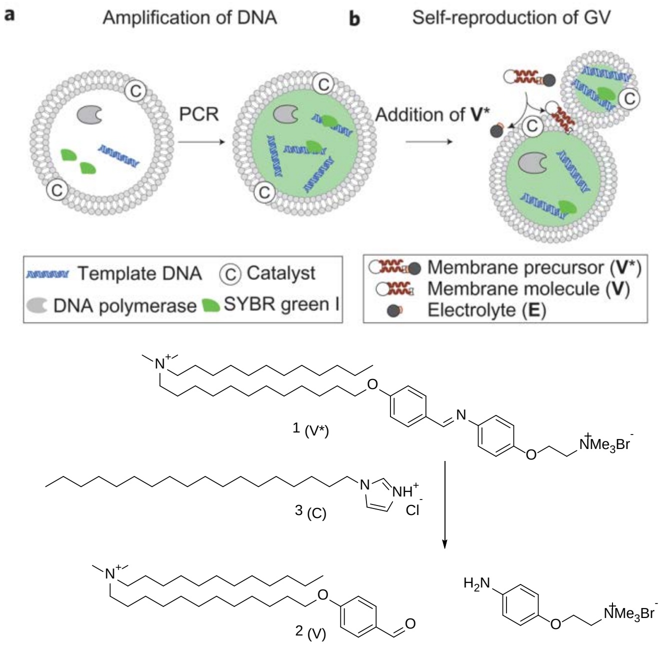

Scheme 1.13. DNA replication in a replicating vesicle. From [60] with permission.

1.5.3. Autocatalytic micelle-to-vesicle transitions

Given the complexities associated with studying biphasic reactions, it has been popular to study vesicle self-reproduction driven by the direct addition of vesicle components to the system rather than by generating them in situ.[2,19] This is justified by the observation that freshly-synthesised product molecules aggregate into micelles before rearranging into vesicles. Further, the rearrangement of micelles into vesicles is itself vesicle-catalysed, and exhibits autocatalytic kinetics. Thus the addition of product micelles to product vesicles gives rise to an autocatalytic micelle-to-vesicle transition. As well as autocatalytic effects, the rearrangement from micelles to vesicles has been shown to be catalysed by a variety of mineral surfaces.[88]

The value of this approach has been proven repeatedly through studies which shed light upon the complex and varied routes through which prebiotic vesicles may have undergone growth and division. While the division of large and giant vesicles has been observed visually,[60,93] direct observation of the division of nanometre-scale vesicles remains elusive.[2,126] Nonetheless, elegant studies using indirect methods have revealed multiple division pathways in nanometre-scale vesicles.

These studies have revealed a phenomenon termed the ‘matrix effect’, which may represent a form of compositional inheritance. Specifically, the size distribution of extruded vesicles can be inherited by subsequent generations of vesicles formed upon the addition of micelles to the vesicle solution. As size is one factor influencing the behaviour of vesicles, a convincing mechanism for its prebiotic inheritance would be an exciting finding indeed. This body of work has been thoroughly reviewed by Stano and Luisi, and only an overview is given here.[19] The focus here is on how these studies inform the study of chemically-driven physical autocatalysis and questions of compositional inheritance, rather than giving a comprehensive discussion of vesicle dynamics.

Most studies of the matrix effect and autocatalytic micelle-to-vesicle transitions more generally have used fatty acids, often in combination with small quantities of phospholipids. Oleic acid is particularly popular, as it aggregates in convenient temperature and concentration ranges. The popularity of fatty acid models is in part because fatty acids are considered prebiotically-relevant, and are well-known to be capable of physical autocatalysis (section 1.5.2). Most importantly, their aggregation behaviour responds significantly to changes in pH.

At high pH, typically around pH 10-11, fatty acids are fully deprotonated and form anionic micelles. However, at pH values close to the pK_a of the acid, vesicles form.[127] This is because in this pH range there are roughly equal amounts of the acid and conjugate base present, dimers of which can form stable bilayers, in contrast to either component in isolation. Incorporation of the acid into a bilayer also alters the apparent pK_a of the acid, typically from $pK_a = 3\text{-}4$ to $pK_a = 7\text{-}8$. As a result of these properties, when micelles of a fatty acid are transferred into a solution of lower pH, they undergo an autocatalytic micelle-to-vesicle transition. This pH response greatly facilitates studies of this process.

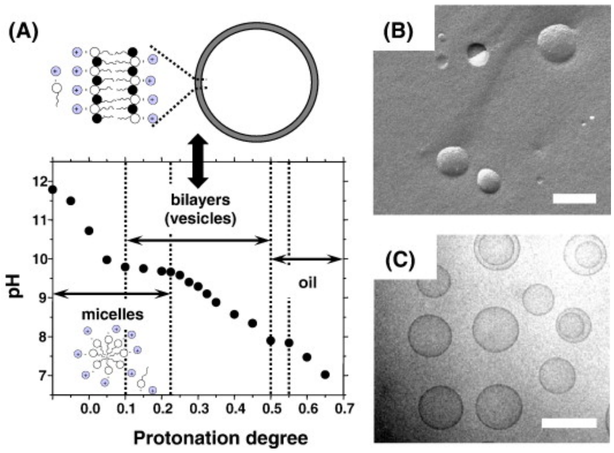

Figure 1.6. Aggregation of fatty acids as a function of pH. Scale bars = 100 nm. **(A)** titration curve of 80 mM sodium oleate/oleic acid; **(B)** ffEM image of small vesicles of racemic 2-methyldodecanoic acid; **(C)** Cryo-TEM image of decanoate vesicles. Reproduced with permission from [127].

The matrix effect was first observed by Blöchliger *et al.*[105] in 1998 in freeze-fracture electron microscopy (ffEM) studies of oleate vesicles. When oleate micelles are injected into a pH 8.8 buffer solution they rearrange to give vesicles with a broad size distribution ranging from 50 nm to >1 µm. However, in the presence of pre-formed vesicles of defined size distributions (centred around 50 nm or 100 nm) the newly-formed vesicles inherit the existing size distribution. This effect occurred whether the new oleate was added as aqueous micelles, monomers in methanol, or synthesised in situ through autocatalytic hydrolysis of oleic anhydride.

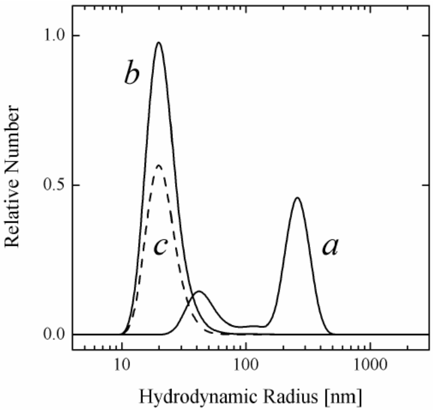

Figure 1.7. Number-weighted size distribution of oleate vesicles. (A) Vesicles formed by addition of sodium oleate micelles to buffer; **(B)** Vesicles formed by addition of sodium oleate micelles to a solution of preformed 50 nm oleate vesicles; **(C)** Size distribution of preformed 50 nm oleate vesicles. Reproduced from [87] with permission.

Subsequent studies have hinted at a degree of generality for the matrix effect: mixed fatty acid/phospholipid systems[105] and cationic surfactants mixed with phospholipids[128] both exhibit matrix effects. Further, size distributions inherited in this way can persist through multiple rounds of oleate addition and self-reproduction.[87]

Extensive efforts to unravel the mechanism or mechanisms of the matrix effect have been made. Early studies used ferritin-labelled vesicles to probe the distribution of the interior contents of vesicles following self-reproduction.[85,86] These studies strongly supported a process in which the new vesicles are formed by division of existing vesicles. Further study of unlabelled oleate vesicles by ffEM confirmed this.[126] By examining aliquots taken within the first few minutes following addition of oleate micelles by ffEM, direct evidence of dimeric intermediate states was obtained. Several observations support the intermediacy of these species. They are common, accounting for around 20% of the observed vesicles, and no clusters of three or more vesicles were observed, suggesting a specific preference for dimers rather than simple aggregation. Further, these species are only observed in the early stages of the process and not towards the end, when the concentration of vesicles is higher. If these were simply formed by concentration-driven aggregation of two vesicles, towards the end of the reaction they might be expected to be more common or to form higher oligomers. To date, these images remain the most direct evidence for vesicle division processes on the nanometre scale.

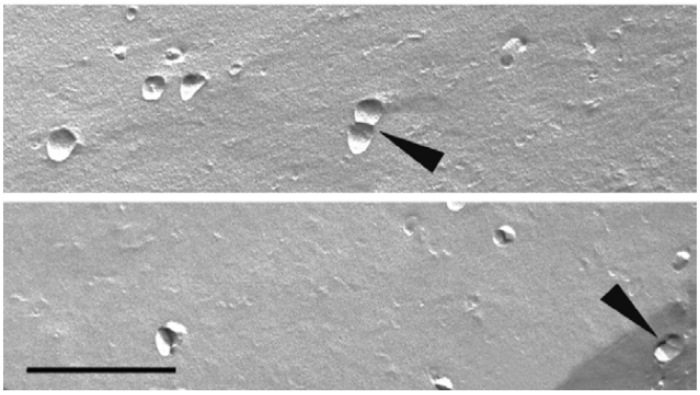

Figure 1.8. ffEM images of intermediate 'twinned' vesicles observed during vesicle self-reproduction. Scale bar = 500 nm. Reproduced from [126] with permission.

However, under other conditions no division is observed. The relative importance of the growth of existing vesicles, division of existing vesicles, and de novo aggregation of new vesicles depends upon the experimental conditions and substrates, and can be quantified.[129]

The source and mechanism of the matrix effect is still unclear and disputed. Chen and Szostak[90] used a FRET assay to monitor the growth and division of preformed oleate vesicles following addition of oleate micelles in real time. These data pointed to a two-step mechanism of growth involving a metastable intermediate species. Upon addition to preformed vesicles, oleate micelles are proposed to rapidly coat the vesicles. Excess micelles instead convert to the hypothesised intermediate. There is then a rapid growth phase as the micelles coating the vesicles are absorbed, increasing the size of the vesicles. Subsequently, the slow conversion of the intermediate to more vesicles leads to a lag phase followed by a second rapid growth phase.

Markvoort *et al.*[130] examined the mechanism of the matrix effect in oleate and mixed oleate/phospholipid systems in detail. Varying the rate of addition of oleate micelles or monomers altered the behaviour of the system: slowing the rate of addition lead to preferential growth of vesicles rather than division. Supported by both experimental and computational approaches, the authors concluded that the rate of movement of monomers across the membrane is critical. When the rate of transmembrane movement is slow relative to the rate of monomer addition, an imbalance in the amount of material in the inner and outer leaflets of the membrane is generated. This alters the stability of the membrane, leading to division. By slowing the rate of addition of fresh oleate considerably, this effect could be neutralised; under these conditions, growth is favoured over division.

Meaningful comparison of the experimental conditions of different studies is difficult, and as the studies by Chen and Szostak and by Markvoort *et al.* demonstrate, even similar observations under comparable conditions may be interpreted in different ways. Clearly, a full understanding of the matrix effect remains elusive. The variables determining whether growth or division dominate under given conditions remain to be fully elucidated.

Aside from these direct questions, studies of the matrix effect have also provided more general insight into the properties of fatty acids. For example, study of oleate solutions by ESR revealed the coexistence of monomeric, micellar, and vesicular oleate in the pH 8.5-10 range.[131] This has been independently confirmed using fluorescence spectroscopy.[132]

More generally, this body of work emphasises the dynamic, complex nature of prebiotically-relevant physical autocatalysts. These systems operate far from equilibrium and thus their behaviour depends crucially on environmental and kinetic factors, such as the rate of addition of monomers. This poses significant barriers to the development of models of prebiotic behaviour, but also offers exciting opportunities for the study of emergent, systems-level properties relevant to the origins of life.

1.6. Hypothesis & thesis outline

As the examples reviewed here illustrate, physical autocatalysis offers a method for the generation of complex supramolecular behaviour from simple precursors. The origins of life can be thought of as a process by which mixtures of simple molecules self-assembled into more complex supramolecular structures with emergent properties. The aggregation of lipids into catalytically-active structures capable of self-reproduction, orthogonal catalysis, and potentially compositional evolution is surely a striking illustration of this principle. Studying systems which generate increased complexity is profoundly important and contributes fundamentally to our understanding of the origins of life.

The study of reactions which produce increasingly complex and functional molecules has long been central to our understanding of the origins of life.[133–135] These absolutely require bond-forming chemical reactions to covalently assemble molecules of interest. The combination of bond-forming chemistry with self-assembly into functional supramolecular species would represent the coupled generation of both molecular and supramolecular complexity from simple precursors, using principles readily applicable to the prebiotic world. This has been demonstrated in template-based autocatalysts previously.[3] For example, several groups have described self-replicating peptides which assemble into β-sheets, leading to the autocatalytic growth of supramolecular fibres.[136–140] These studies have offered insight into the behaviour of far-from-equilibrium systems generally, and served to model biological processes such as selection and inheritance.

To our knowledge, the only examples of physical autocatalysis driven by bond-forming reactions published at the outset of this work both involve reversible imine condensation[39,121] (section 1.5). The first of these examples is the dynamic combinatorial library of self-reproducing micelles described by Nguyen *et al.*[39] (Scheme 1.8), and the second is the system of self-reproducing vesicles described by Takakura *et al.*[121] (Scheme 1.11). While related systems involving irreversible bond-formation are known, none of these have had their kinetics measured and shown to be unambiguously autocatalytic.[141,142] To our knowledge, therefore, no examples of physical autocatalysis driven by irreversible bond-forming reactions had been reported prior to the work described in this thesis.

Irreversibility in such reactions allows the study of systems far from equilibrium, where the stability of molecules or higher-order species is a kinetic rather than thermodynamic property. Additionally, the development of physical autocatalysis driven by irreversible bond-forming reactions would enable experiments that complement existing work concerning vesicle growth and division, and enable tests of competition and selection between physical autocatalysts (see Chapter 4).[4]

With these considerations in mind, this work was undertaken to develop and characterise novel examples of physical autocatalysis driven by irreversible bond-forming reactions. Chapter 2 discusses the development of self-reproducing micelles and efforts towards self-reproducing vesicles and related asymmetric processes. Chapter 3 concerns the application of single-particle microscopy to physical autocatalysis with the goal of discovering complex behaviours, in collaboration with Jaime Ortega-Arroyo and Prof. Philipp Kukura. Chapter 4 discusses the limitations of this work and promising future experimental approaches to physical autocatalysis.

1.7. References

1 D. G. Blackmond, *Angew. Chemie Int. Ed.*, 2009, **48**, 386–390.
2 K. Ruiz-Mirazo, C. Briones and A. de la Escosura, *Chem. Rev.*, 2014, **114**, 285–366.
3 A. J. Bissette and S. P. Fletcher, *Angew. Chem. Int. Ed.*, 2013, **52**, 12800–12826.
4 A. J. Bissette and S. P. Fletcher, *Orig. Life Evol. Biosph.*, 2015, **45**, 21–30.
5 Z. Dadon, N. Wagner and G. Ashkenasy, *Angew. Chem. Int. Ed.*, 2008, **47**, 6128–6136.
6 M. P. Mower and D. G. Blackmond, *J. Am. Chem. Soc.*, 2015.
7 M. Eigen and P. Schuster, *Naturwissenschaften*, 1977, **64**, 541–565.
8 P. V Coveney, J. B. Swadling, J. A. D. Wattis and H. C. Greenwell, *Chem. Soc. Rev.*, 2012, **41**, 5430–5446.
9 G. A. M. King, *BioSystems*, 1981, **13**, 225–234.
10 L. E. Orgel, *PLOS Biol.*, 2008, **6**, e18.

11 M. P. Robertson and G. F. Joyce, *Cold Spring Harb. Perspect. Biol.*, 2012, **4**.

12 A. Pross and R. Pascal, *Open Biol.*, 2013, **3**, 120190.

13 F. C. Frank, *Biochim. Biophys. Acta*, 1953, **11**, 459–463.

14 B. L. Feringa and R. A. van Delden, *Angew. Chem. Int. Ed.*, 1999, **38**, 3418–3438.

15 T. Gehring, M. Busch, M. Schlageter and D. Weingand, *Chirality*, 2010, **22**, E173–E182.

16 D. A. Singleton and L. K. Vo, *Org. Lett.*, 2003, **5**, 4337–4339.

17 D. G. Blackmond, *Cold Spring Harb. Perspect. Biol.*, 2010, **2**, a002147.

18 A. Vidonne and D. Philp, *Eur. J. Org. Chem.*, 2009, 593–610.

19 P. Stano and P. L. Luisi, *Chem. Commun.*, 2010, **46**, 3639–3653.

20 I. Weissbuch and M. Lahav, *Chem. Rev.*, 2011, **111**, 3236–3267.

21 G. A. M. King, *Chem. Soc. Rev.*, 1978, **7**, 297.

22 B. G. Bag and G. von Kiedrowski, *Pure Appl. Chem.*, 1996, **68**, 2145–2152.

23 A. W. Schwartz, *Heterocycles*, 2010, **82**, 11–14.

24 E. A. Wintner and J. Rebek, *Acta Chem. Scand.*, 1996, **50**, 469–485.

25 R. F. Ludlow and S. Otto, *Chem. Soc. Rev.*, 2008, **37**, 101–108.

26 E. A. Wintner, M. M. Conn and J. Rebek, *Acc. Chem. Res.*, 1994, **27**, 198–203.

27 V. Patzke and G. von Kiedrowski, *Arkivoc*, 2007, **v**, 293–310.

28 C. Viedma, *Phys. Rev. Lett.*, 2005, **94**, 065504.

29 D. K. Kondepudi, R. J. Kaufman and N. Singh, *Science (80-.).*, 1990, **250**, 975–6.

30 A. E. Engelhart, M. W. Powner and J. W. Szostak, *Nat. Chem.*, 2013, **5**, 390–4.

31 T. Buhse, R. Nagarajan, D. Lavabre and J. C. Micheau, *J. Phys. Chem. A*, 1997, **101**, 3910–3917.

32 C. M. Starks and R. M. Owens, *J. Am. Chem. Soc.*, 1973, **95**, 3613–3617.

33 H. J. Glatzer and L. K. Doraiswamy, *Chem. Eng. Sci.*, 2000, **55**, 5149–5160.

34 P. L. Luisi and F. J. Varela, *Orig. Life Evol. B.*, 1989, **19**, 633–643.

35 P. L. Luisi, *Naturwissenschaften*, 2003, **90**, 49–59.

36 F. G. Varela, H. R. Maturana and R. Uribe, *BioSystems*, 1974, **5**, 187–196.

37 P. Razeto-Barry, *Orig. Life Evol. B.*, 2012, **42**, 543–567.

38 G. R. Fleischaker, *BioSystems*, 1988, **22**, 37–49.

39 R. Nguyen, L. Allouche, E. Buhler and N. Giuseppone, *Angew. Chem. Int. Ed.*, 2009, **48**, 1093–1096.

40 J. M. P. Gutierrez, T. Hinkley, J. W. Taylor, K. Yanev and L. Cronin, *Nat. Commun.*, 2014, **5**, 5571.

41 J. W. Szostak, D. P. Bartel and P. L. Luisi, *Nature*, 2001, **409**, 387–390.

42 P. D. I. Fletcher and B. H. Robinson, *J. Chem. Soc. Faraday Trans. 1*, 1984, **80**, 2417.

43 F. Dyson, *Origins of Life*, Cambridge University Press, Cambridge, 1985.

44 P. L. Luisi, *Emergence of Life: From Chemical Origins to Synthetic Biology*, Cambridge University Press, Cambridge, 2006.

45 D. Segré, D. Ben-Eli, D. W. Deamer and D. Lancet, *Orig. Life Evol. B.*, 2001, **31**, 119–145.

46 P. Walde, *Orig. Life Evol. B.*, 2006, **36**, 109–150.

47 A. J. Dzieciol and S. Mann, *Chem. Soc. Rev.*, 2012, **41**, 79–85.

48 P. L. Luisi, P. Walde and T. Oberholzer, *Curr. Opin. Colloid Interface Sci.*, 1999, **4**, 33–39.

49 P. Walde, H. Umakoshi, P. Stano and F. Mavelli, *Chem. Commun.*, 2014, **50**, 10177–97.

50 I. A. Chen and P. Walde, *Cold Spring Harb. Perspect. Biol.*, 2010, **2**.

51 L. B. Mullen and J. D. Sutherland, *Angew. Chem. Int. Ed.*, 2007, **46**, 4166–8.

52 A. N. Albertsen, C. D. Duffy, J. D. Sutherland and P.-A. Monnard, *Astrobiology*, 2014, **14**, 462–72.

53 R. M. Hazen and D. W. Deamer, *Orig. Life Evol. B.*, 2007, **37**, 143–52.

54 I. Budin and J. W. Szostak, *Proc. Natl. Acad. Sci. U.S.A.*, 2011, **108**, 5249–54.

55 R. M. de Graaf, J. Visscher and A. W. Schwartz, *Nature*, 1995, **378**, 474–7.

56 J. L. Cape, P.-A. Monnard and J. M. Boncella, *Chem. Sci.*, 2011, **2**, 661.

57 P. M. Gardner, K. Winzer and B. G. Davis, *Nat. Chem.*, 2009, **1**, 377–383.

58 I. A. Chen, R. W. Roberts and J. W. Szostak, *Science (80-.).*, 2004, **305**, 1474–1476.

59 A. N. Albertsen, S. E. Maurer, K. A. Nielsen and P.-A. Monnard, *Chem. Commun.*, 2014, **50**, 8989–92.

60 K. Kurihara, M. Tamura, K. Shohda, T. Toyota, K. Suzuki and T. Sugawara, *Nat. Chem.*, 2011, **3**, 775–781.

61 J. Lombard, P. López-García and D. Moreira, *Nat. Rev. Microbiol.*, 2012, **10**, 507–15.

62 S. E. Maurer, D. W. Deamer, J. M. Boncella and P. A. Monnard, *Astrobiology*, 2009, **9**, 979–987.

63 A. Rendón, D. G. Carton, J. Sot, M. García-Pacios, L.-R. Montes, M. Valle, J.-L. R. Arrondo, F. M. Goñi and K. Ruiz-Mirazo, *Biophys. J.*, 2012, **102**, 278–86.

64 I. Budin, N. Prwyes, N. Zhang and J. W. Szostak, *Biophys. J.*, 2014, **107**, 1582–90.

65 R. E. Mielke, K. J. Robinson, L. M. White, S. E. McGlynn, K. McEachern, R. Bhartia, I. Kanik and M. J. Russell, *Astrobiology*, 2011, **11**, 933–50.

66 L. M. Barge, S. S. S. Cardoso, J. H. E. Cartwright, G. J. T. Cooper, L. Cronin, A. De Wit, I. J. Doloboff, B. Escribano, R. E. Goldstein, F. Haudin, D. E. H. Jones, A. L. Mackay, J. Maselko, J. J. Pagano, J. Pantaleone, M. J. Russell, C. I. Sainz-Díaz, O. Steinbock, D. A. Stone, Y. Tanimoto and N. L. Thomas, *Chem. Rev.*, 2015, **115**, 8652–8703.

67 M. Li, R. L. Harbron, J. V. M. Weaver, B. P. Binks and S. Mann, *Nat. Chem.*, 2013, **5**, 529–36.

68 G. J. T. Cooper, P. J. Kitson, R. Winter, M. Zagnoni, D.-L. Long and L. Cronin, *Angew. Chem. Int. Ed.*, 2011, **50**, 10373–6.

69 M. Li, X. Huang and S. Mann, *Small*, 2014, **10**, 3291–8.

70 P. L. Luisi, P. Walde and T. Oberholzer, *Ber. Bunsen-Ges. Phys. Chem*, 1994, **98**, 1160–1165.

71 R. V Sole, *Int. J. Biochem. Cell B.*, 2009, **41**, 274–284.

72 J. W. Szostak, *J. Syst. Chem.*, 2012, **3**, 2.

73 O. Markovitch and D. Lancet, *Artif. Life*, 2012, **18**, 243–266.

74 V. Vasas, C. Fernando, M. Santos, S. Kauffman and E. Szathmáry, *Biol. Direct*, 2012, **7**, 1.

75 F. Al Anet, *Curr. Opin. Chem. Biol.*, 2004, **8**, 654–659.

76 R. Gross, I. Fouxon, D. Lancet and O. Markovitch, *BMC Evol. Biol.*, 2014, **14**, 2623.

77 A. Pross, *J. Syst. Chem.*, 2011, **2**, 1.

78 D. Segré, B. Shenhav, R. Kafri and D. Lancet, *J. Theor. Biol.*, 2001, **213**, 481–91.

79 O. Markovitch and D. Lancet, *J. Theor. Biol.*, 2014, **357**, 26–34.

80 D. Segré, D. Lancet, O. Kedem and Y. Pilpel, *Orig. Life Evol. B.*, 1998, **28**, 501–514.

81 D. Segre, D. Ben-Eli and D. Lancet, *Proc. Natl. Acad. Sci. U.S.A.*, 2000, **97**, 4112–4117.

82 D. L. Armstrong, O. Markovitch, R. Zidovetzki and D. Lancet, *Phys. Biol.*, 2011, **8**, 066001.

83 Z. L. Cheng and P. L. Luisi, *J. Phys. Chem. B*, 2003, **107**, 10940–10945.

84 B. Dejanović, K. Mirosavljević, V. Noethig-Laslo, S. Pecar, M. Sentjurc and P. Walde, *Chem. Phys. Lipids*, 2008, **156**, 17–25.

85 N. Berclaz, M. Muller, P. Walde and P. L. Luisi, *J. Phys. Chem. B*, 2001, **105**, 1056–1064.

86 N. Berclaz, E. Blochliger, M. Muller and P. L. Luisi, *J. Phys. Chem. B*, 2001, **105**, 1065–1071.

87 P. L. Luisi, P. S. S. Rasi and F. Mavelli, *Artif. Life*, 2004, **10**, 297–308.

88 M. M. Hanczyc, S. M. Fujikawa and J. W. Szostak, *Science (80-.).*, 2003, **302**, 618–22.

89 T. F. Zhu and J. W. Szostak, *J. Am. Chem. Soc.*, 2009, **131**, 5705–5713.

90 I. A. Chen and J. W. Szostak, *Biophys. J.*, 2004, **87**, 988–998.

91 H. Takahashi, Y. Kageyama, K. Kurihara, K. Takakura, S. Murata and T. Sugawara, *Chem. Commun.*, 2010, **46**, 8791–8793.

92 C. F. Thomas and P. L. Luisi, *J. Phys. Chem. B*, 2005, **109**, 14544–50.

93 K. Adamala and J. W. Szostak, *Nat. Chem.*, 2013, **5**, 495–501.

94 K. Morigaki, S. Dallavalle, P. Walde, S. Colonna and P. L. Luisi, *J. Am. Chem. Soc.*, 1997, **119**, 292–301.

95 P. Carrara, P. Stano and P. L. Luisi, *Chembiochem*, 2012, **13**, 1497–502.

96 P. A. Bachmann, P. Walde, P. L. Luisi and J. Lang, *J. Am. Chem. Soc.*, 1990, **112**, 8201–8203.

97 P. A. Bachmann, P. L. Luisi and J. Lang, *Chimia (Aarau).*, 1991, **45**, 266–268.

98 P. A. Bachmann, P. Walde, P. L. Luisi and J. Lang, *J. Am. Chem. Soc.*, 1991, **113**, 8204–8209.

99 P. A. Bachmann, P. L. Luisi and J. Lang, *Nature*, 1992, **357**, 57–59.

100 P. R. Kust and J. F. Rathman, *Langmuir*, 1995, **11**, 3007–3012.

101 Y. A. Chizmadzhew, M. Maestro and F. Mavelli, *Chem. Phys. Lett.*, 1994, **226**, 56–62.

102 J. Billingham and P. V Coveney, *J. Chem. Soc. Faraday Trans.*, 1994, **90**, 1953–1959.

103 P. V Coveney and J. A. D. Wattis, *P. Roy. Soc. Lond. A Mat.*, 1996, **452**, 2079–2102.

104 T. Buhse, D. Lavabre, R. Nagarajan and J. C. Micheau, *J. Phys. Chem. A*, 1998, **102**, 10552–10559.

105 E. Blochliger, M. Blocher, P. Walde and P. L. Luisi, *J. Phys. Chem. B*, 1998, **102**, 10383–10390.

106 S. Lonchin, P. L. Luisi, P. Walde and B. H. Robinson, *J. Phys. Chem. B*, 1999, **103**, 10910–19016.

107 F. Mavelli and P. L. Luisi, *J. Phys. Chem.*, 1996, **100**, 16600–16607.

108 P. K. Schmidli, P. Schurtenberger and P. L. Luisi, *J. Am. Chem. Soc.*, 1991, **113**, 8127–8130.

109 P. A. Vonmont-Bachmann, P. Walde and P. L. Luisi, *J. Liposome Res.*, 1994, **4**, 1135–1158.

110 P. Walde, R. Wick, M. Fresta, A. Mangone and P. L. Luisi, *J. Am. Chem. Soc.*, 1994, **116**, 11649–11654.

111 R. Wick, P. Walde and P. L. Luisi, *J. Am. Chem. Soc.*, 1995, **117**, 1435–1436.

112 A. Veronese and P. L. Luisi, *J. Am. Chem. Soc.*, 1998, **120**, 2662–2663.

113 P. Walde, M. Wessicken, U. Rädler, N. Berclaz, K. Conde-Frieboes and P. L. Luisi, *J. Phys. Chem. B*, 1997, **101**, 7390–7397.

114 P. Walde, A. Goto, P. A. Monnard, M. Wessicken and P. L. Luisi, *J. Am. Chem. Soc.*, 1994, **116**, 7541–7547.

115 T. Oberholzer, R. Wick, P. L. Luisi and C. K. Biebricher, *Biochem. Biophys. Res. Commun.*, 1995, **207**, 250–257.

116 M. S. DeClue, P.-A. A. Monnard, J. A. Bailey, S. E. Maurer, G. E. Collis, H.-J. J. Ziock, S. Rasmussen and J. M. Boncella, *J. Am. Chem. Soc.*, 2009, **131**, 931–933.

117 S. E. Maurer, M. S. DeClue, A. N. Albertsen, M. Dörr, D. S. Kuiper, H. Ziock, S. Rasmussen, J. M. Boncella and P.-A. Monnard, *ChemPhysChem*, 2011, **12**, 828–35.

118 H. H. Zepik, E. Blochliger and P. L. Luisi, *Angew. Chem. Int. Ed.*, 2001, **40**, 205–208.

119 F. Mavelli and K. Ruiz-Mirazo, *Phil. T. Roy. Soc. B*, 2007, **362**, 1789–1802.

120 F. Mavelli and P. Stano, *Phys. Biol.*, 2010, **7**, 16010.

121 K. Takakura, T. Toyota and T. Sugawara, *J. Am. Chem. Soc.*, 2003, **125**, 8134–8140.

122 K. Kurihara, K. Takakura, K. Suzuki, T. Toyota and T. Sugawara, *Soft Matter*, 2010, **6**, 1888–1891.

123 K. Takakura and T. Sugawara, *Langmuir*, 2004, **20**, 3832–3834.

124 T. Toyota, K. Takakura, Y. Kageyama, K. Kurihara, N. Maru, K. Ohnuma, K. Kaneko and T. Sugawara, *Langmuir*, 2008, **24**, 3037–3044.

125 P. L. Luisi and P. Stano, *Nat. Chem.*, 2011, **3**, 755–756.

126 P. Stano, E. Wehrli and P. L. Luisi, *J. Phys-Condens. Mat.*, 2006, **18**, S2231.

127 K. Morigaki and P. Walde, *Curr. Opin. Colloid Interface Sci.*, 2007, **12**, 75–80.

128 C. F. Thomas and P. L. Luisi, *J. Phys. Chem. B*, 2004, **108**, 11285–11290.

129 S. Rasi, F. Mavelli and P. L. Luisi, *Orig. Life Evol. B.*, 2004, **34**, 215–224.

130 A. J. Markvoort, N. Pfleger, R. Staffhorst, P. A. J. Hilbers, R. A. van Santen, J. A. Killian

and B. de Kruijff, *Biophys. J.*, 2010, **99**, 1520–1528.

131 H. Fukuda, A. Goto, H. Yoshioka, R. Goto, K. Morigaki and P. Walde, *Langmuir*, 2001, **17**, 4223–4231.

132 I. Budin, A. Debnath and J. W. Szostak, *J. Am. Chem. Soc.*, 2012, **134**, 20812–20819.

133 S. Miller, *Science (80-.).*, 1953, **117**, 528–529.

134 A. Eschenmoser, *Tetrahedron*, 2007, **63**, 12821–12844.

135 M. W. Powner, B. Gerland and J. D. Sutherland, *Nature*, 2009, **459**, 239–242.

136 J. M. A. Carnall, C. A. Waudby, A. M. Belenguer, M. C. A. Stuart, J. J.-P. Peyralans and S. Otto, *Science (80-.).*, 2010, **327**, 1502–1506.

137 S. Matsumura, T. Takahashi, A. Ueno and H. Mihara, *Chem. Eur. J.*, 2003, **9**, 4829–4837.

138 Y. Takahashi and H. Mihara, *Bioorg. Med. Chem.*, 2004, **12**, 693–699.

139 B. Rubinov, N. Wagner, H. Rapaport and G. Ashkenasy, *Angew. Chem. Int. Ed.*, 2009, **48**, 6683–6686.

140 B. Rubinov, N. Wagner, M. Matmor, O. Regev, N. Ashkenasy and G. Ashkenasy, *ACS Nano*, 2012, **6**, 7893–7901.

141 I. Budin and N. K. Devaraj, *J. Am. Chem. Soc.*, 2012, **134**, 751–753.

142 R. J. Brea, C. M. Cole and N. K. Devaraj, *Angew. Chemie Int. Ed.*, 2014, **53**, 14102–14105.

Chapter 2

Self-reproducing systems

2. Self-reproducing systems.

2.1. Overview

This chapter describes the development of self-reproducing systems driven by bond-forming reactions. Two generations of autocatalytic thiol-ene reactions are described and characterised by ^{1}H and DOSY NMR spectroscopy in order to demonstrate autocatalysis and explore the mechanism of operation. Steps towards the development of autoinductive reactions, self-reproducing vesicles, and asymmetric autocatalytic systems are described.

Parts of this chapter have been published in *Nature Communications.*[1] All experiments in this chapter were designed and performed by Andrew Bissette with the exception of those reported in Table 2.7, which were performed by Alexandra Bogdanova.

2.2. Introduction

Our efforts to develop new examples of physical autocatalysis driven by bond-forming reactions focused on self-reproducing micelles. Beginning this work with the study of micelles, rather than vesicles, offered a number of advantages both practically and in the development of more ambitious future experiments.

Single-tailed surfactants typically aggregate spontaneously in water to give thermodynamically stable populations of micelles. In contrast to the simplicity of micelles, the size and lamellarity of vesicles depends upon how they are prepared, and may require the input of energy through sonication or other techniques. Vesicles are not necessarily thermodynamically stable structures and have lifetimes varying from hours to months.[2] As a result micelles are considerably simpler to study than are vesicles.

The growth and division of micelles is likewise simpler than that of vesicles. Typically, micelles grow and divide spontaneously upon the addition or autocatalytic synthesis of surfactant monomers,[3] even if they undergo changes in shape or size first.[4] The division of vesicles is more complicated. Under some conditions vesicles will grow and divide spontaneously as one might naively expect,[5] but in many cases must be prompted to divide through, for example, the application of shear forces.[6] New vesicles may be formed by other mechanisms beyond the fission of existing vesicles: new vesicles may grow on the surface of existing vesicles,[7] or form within the aqueous interior and then translocate to the external solution.[8]

The structural requirements for micelle formation are also simpler. While single-tailed surfactants can form vesicles,[9] they more commonly form micelles. Vesicle formation typically requires two-tailed surfactants, the synthesis of which is more challenging. The formation of a single-tailed surfactant by the autocatalytic coupling of one hydrophobic and one hydrophilic reagent is simple to design and characterise compared to the synthesis of two-tailed surfactants.

Studying micelles rather than vesicles is also advantageous when considering demonstrations of competition and selection. As discussed in Chapter 1, the lipid world model requires selectivity between competing and cooperating physical autocatalysts.[10] In the GARD model the catalytic properties of each aggregate are determined by its composition.[11] Each individual molecule in an aggregate exerts a small influence over the overall affinity of the aggregate for different surfactant species. Thus this model predicts that in an aggregate made of a smaller number of molecules, i.e. one with a low aggregation number, each individual molecule will influence the overall affinity of the aggregate to a greater extent than in an aggregate with a larger aggregation number. Aggregation numbers vary considerably with surfactant structure, but as a generalisation, the aggregation number of vesicles is typically higher than that of micelles. From this perspective, the study of competition between self-reproducing micelles is more likely to reveal selection based on composition than is the study of vesicles.

Together, these factors made the study of self-reproducing micelles an ideal starting point for this project. Micelles are simpler to make and characterise than are vesicles, and the development of this chemistry will be valuable for future studies of competition processes. These studies focused on racemic reactions rather than asymmetric variations for simplicity.

2.3. First-generation autocatalytic thiol-ene reactions

2.3.1. Initial development and kinetic studies

As a starting point we opted to study the 1,4-conjugate addition of thiols to α,β-unsaturated carbonyls, also called the thiol-ene reaction.[12] The thiol-ene reaction can be promoted by bases, nucleophilic catalysts such as phosphines, or photochemically. The base-mediated thiol-ene reaction is well suited to studies of physical autocatalysis as it proceeds in water, has broad functional group tolerance, and its components are synthetically accessible.

A candidate substrate was identified based a library of micelle-forming phospholipids described by Matsuno *et al.*[13] The authors synthesised these compounds by coupling hydrophobic alkyl thiols to highly polar phosphatidylcholine-derived Michael acceptors, to give stable amphiphilic products. The CMCs of these products were reported. By simply performing the reaction in alkaline water rather than ethanol, this system offered a simple test reaction to explore physical autocatalysis (Scheme 2.1). Conveniently, the required Michael acceptor **1** was commercially available.

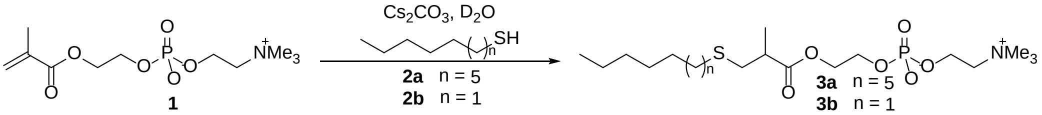

Scheme 2.1. First-generation thiol-ene reaction.

Preliminary investigation by TLC revealed that the reaction between 1-decanethiol **2a** and 2-methacryloyloxyethyl phosphorylcholine **1** (170 mM) proceeds efficiently in water when rapidly stirred and can be promoted by a variety of bases. This test reaction was chosen as product **3a** has a CMC of 0.4 mM,[13] meaning that product micelles would form at very low conversions, minimising any lag period before the onset of autocatalysis and hence maximising the efficiency of the reaction.

The use of catalytic amines to promote the reaction gave variable results (Table 2.1). Acyclic secondary amines and benzylamine gave very slow conversion, with product only appearing after several days, while triethylamine gave product after overnight reaction. Cyclic secondary amines were the most efficient, giving product within hours. This is in contrast to the reaction in ethanol, where acyclic primary and secondary amines are highly efficient catalysts.[13] Using inorganic bases consistently gave significant conversion within two hours and had the advantage of being invisible to ^1H NMR spectroscopy.

Base	**Quantity**	**Result**
Triethylamine	cat.	16 h
Piperidine	cat.	4 h
Pyrrolidine	cat.	4 h
N,N-Dimethylethylene diamine	cat.	4 d
Diisobutylamine	cat.	4 d
Dicyclohexylamine	cat.	-
Diisopropylamine	cat.	-
Benzylamine	cat.	4 d
LiOH	0.1 M	2 h
NaOH	0.1 M	2 h
KOH	0.1 M	2 h
Cs_2CO_3	0.1 M	2 h
LiOH	0.2 M	2 h
NaOH	0.2 M	2 h
KOH	0.2 M	2 h
Cs_2CO_3	0.2 M	2 h

Table 2.1. Screen of bases for the reaction of 1 (170 mM) and 2a (5 eq). A total aqueous volume of 2 mL was rapidly stirred and the appearance of **3a** monitored by TLC.

With these promising reaction conditions in hand we attempted to quantify the reaction kinetics. We opted to use ^{1}H NMR of aliquots to monitor the reaction. While the signals of product and starting material overlapped considerably, the peaks corresponding to the alkene protons in **1** were well-resolved, allowing the consumption of starting material to be monitored.

Whereas before we had stirred the reactions vigorously, here we imitated the reaction conditions used by Bachmann *et al.* in their classic paper establishing physical autocatalysis in micelles:[3] two clearly separated phases, stirred gently at 150 rpm, and monitored by removal of aliquots. To quench aliquots we simply diluted them with D_2O in an NMR tube: under these conditions, the reaction does not proceed even after

24 hours. Other authors studying physical autocatalysis have opted to rapidly mix the two phases in order to reduce the reaction time;[14] our choice was motivated by the desire to sample the aqueous phase directly and thereby minimise the amount of thiol present in the NMR tube in order to improve spectral quality.

Preliminary experimentation was required to achieve reproducible kinetic behaviour. Without rapid stirring the reaction was much slower, taking over 24 hours to reach completion. By increasing the concentration of **1** to 680 mM and increasing the number of equivalents of thiol from 5 to 10, a more tolerable reaction time was achieved. Nonetheless, with thiol **2a** the reaction time was still inconveniently long. Using 1-hexanethiol **2b**, to give product **3b** (CMC = 25 mM), gave a total reaction time of less than 10 hours. The increased rate of reaction with shorter thiols is consistent with their higher solubility in water, which presumably increases the rate of the background reaction and promotes micelle formation after a shorter lag period.

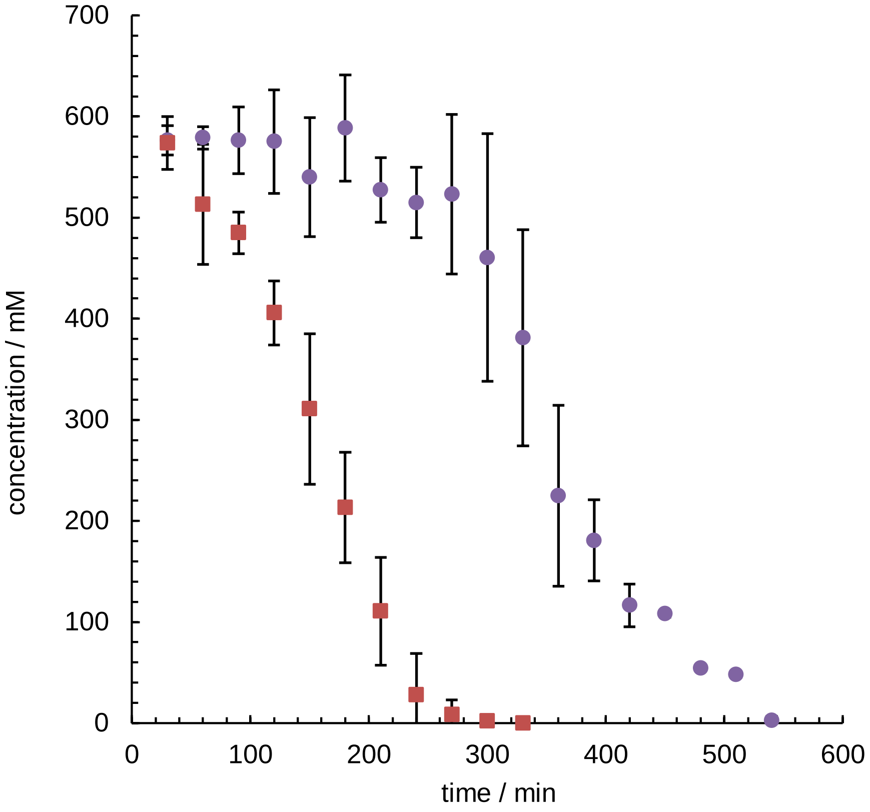

Figure 2.1. Evidence of autocatalysis in the reaction of 1 and 2b. The reaction is monitored by disappearance of **1** by ^{1}H NMR spectroscopy. Data points are the mean of three experiments and error bars show the s.d. ● Control reaction: when **1** and **2b** are stirred gently, a lag period followed by a faster reaction period is observed. ■ Seeded reaction: when the reaction is seeded with **3b** at t = 0, the lag period is eliminated and the reaction proceeds in a more linear fashion. Representative stacked spectra and detailed reaction conditions are provided in Chapter 5.

The kinetic data showed two characteristics of autocatalytic processes (Figure 2.1).[15,16] The first of these was an increase in rate of the reaction following a lag period. Secondly, the reaction rate increased when 20 mol% (130 mM, CMC = 25 mM[13]) of the product **3b** was added at the start of the reaction. Both of these observations were consistently reproducible, although the length of the lag period was somewhat variable.

Consistent with kinetic studies of Luisi's autocatalytic hydrolysis reactions,[14] the kinetics of this reaction were sensitive to various physical factors including the size and orientation of the stirrer bar and the shape of the reaction flask. As shown in Figure

2.2, performing the reaction in a 250 mL round-bottomed flask rather than a vial led to a shorter lag period despite slower stirring at 80 rpm. This may be explained by the larger interfacial surface area to volume ratio in the round-bottomed flask compared to the vial, which allowed more thiol to be in contact with the aqueous phase and promoted more efficient mixing of the reagents.

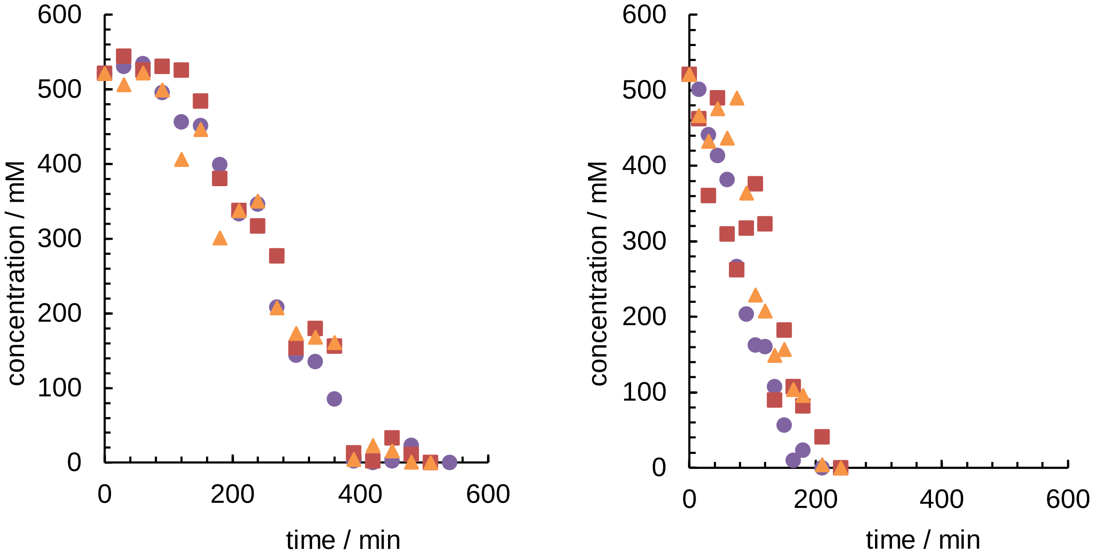

Figure 2.2. Kinetics in an alternative reaction vessel. When the reaction between **1** and **2b** is performed on 3 mL scale in a 250 mL round-bottomed flask and stirred at 80 rpm the following data are obtained (left: control; right: +20 mol% **3b**; each graph shows three independent experiments denoted by ●■▲). The catalytic effect of added product is clearly seen here. Changing the shape and size of the reaction vessel or the rate of stirring alters the shape of the plot, but the overall trends remain.

A side-reaction was observed, namely the hydrolysis of the ester in starting material **1**. This hydrolysis occurred over the first hour following the combination of **1** with Cs_2CO_3, and was not affected by the presence or absence of thiol (Figure 2.3). The hydrolysis was ultimately self-limiting owing to the formation of methacrylate **4** and resultant neutralisation of excess base, and at this point both **1** and product **3b** were stable in solution. Similarly, after the autocatalytic reaction reached completion the concentration of product **3b** was stable for days in solution. We therefore did not take steps to mitigate this side-reaction, as it did not disrupt the reaction of interest.

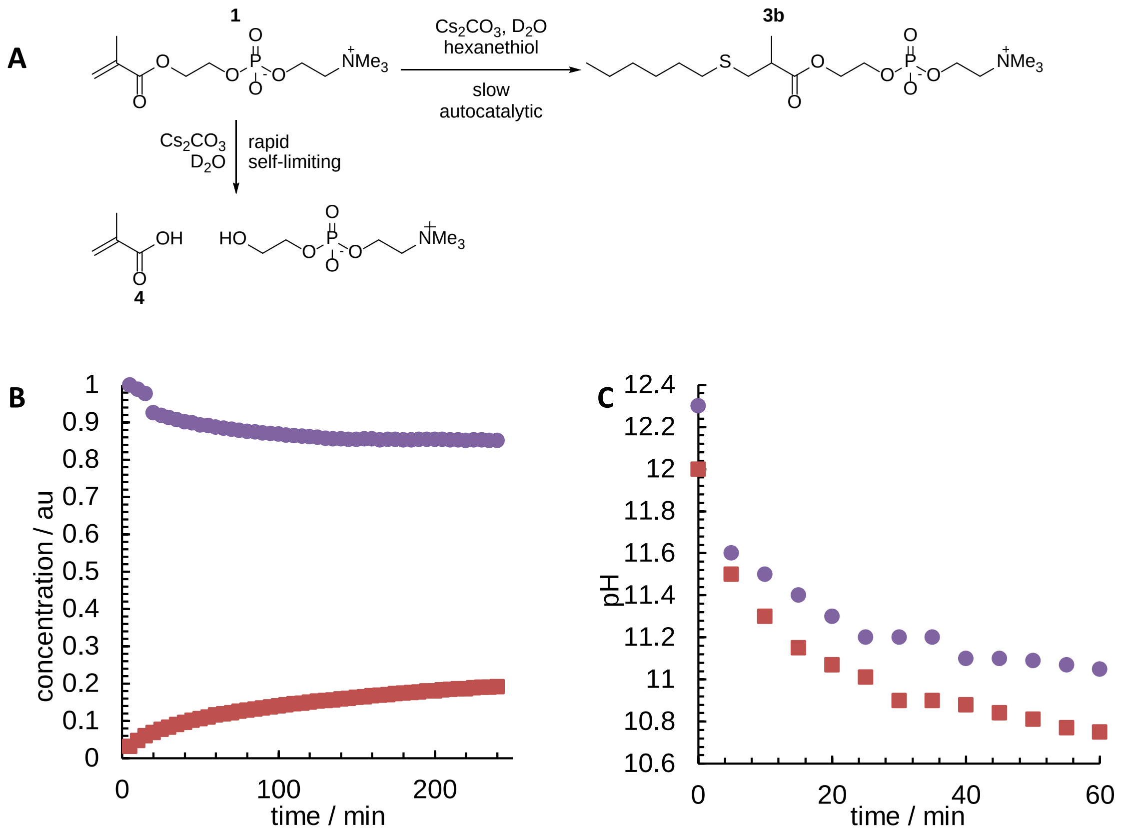

Figure 2.3. Hydrolysis side-reaction. (A) At high pH **1** undergoes rapid, self-limiting hydrolysis to give unreactive by-products. **(B)** Consumption of **1** (●) and formation of **4** (■) over time when **1** (680 mM) and Cs_2CO_3 (200 mM) are combined in D_2O and monitored in situ by ^{1}H NMR. **(C)** Change in pH following addition of **1** (final concentration 680 mM) to either ● a solution of Cs_2CO_3 (200 mM, 2 mL) or ■ a rapidly-stirred biphasic mixture of aqueous Cs_2CO_3 (200 mM, 2 mL) and **2b** (2 mL).

Comparison of an authentic sample of dihexyl disulfide with reaction aliquots indicated that any disulfide formed during the reaction remained in the organic phase and was insoluble in the aqueous phase. No disulfide was detected during the DOSY experiments described below, even in the presence of micelles of **3b**.

2.3.2. Mechanistic study by DOSY NMR

With the autocatalytic reaction established, we turned our attention to mechanistic study. Distinguishing between autocatalysis and other processes which lead to sigmoidal kinetics can be challenging,[17] and it is important to obtain independent evidence for the proposed mechanism. Unfortunately, as seen in Figure 2.1, our kinetic data were too noisy for detailed kinetic studies which might distinguish between different mechanistic scenarios.

As an alternative to kinetic studies we opted to study the behaviour of the reaction components at equilibrium. If the proposed autocatalytic mechanism was in operation, an association between micelles of product **3b** and hydrophobic thiol **2b** ought to be detectable. Diffusion-ordered NMR spectroscopy (DOSY) is a simple, information-rich method that allows the association of molecules in solution to be probed. This technique has been used to study the formation of micelles and uptake of solutes into micelles for several decades, and provides insight into aggregation phenomena by measuring the self-diffusion coefficient of molecules, which is strongly correlated with the average size and shape of a species or an aggregate.[18,19] The diffusion coefficient is obtained as a time and population average of all molecules contributing to a given NMR signal.

Nguyen *et al*. have previously used DOSY to study the association of hydrophobic precursors and autocatalytic reaction products.[4] However, their study was limited by the reversibility of their reaction: in aqueous solution, their imine surfactants disassociated into a hydrophobic aldehyde and a hydrophilic amine. This precluded the possibility of studying the diffusion behaviour of isolated product micelles rather than mixed aldehyde-imine micelles. As compound **3b** was stable in solution we had the advantage of being able to combine the reaction components freely to probe their association in a controlled manner.

As discussed in Chapter 1, the mechanism by which physical autocatalysis proceeds has been debated. Early work on self-reproducing micelles assumed that these reactions proceed through micellar catalysis, roughly meaning that the reaction occurs at or in association with the micelle. This was convincingly disputed by Buhse *et al*.[14,20] who developed kinetic models and concluded that physical autocatalysis can be thought of as a form of phase transfer catalysis. Essentially, the difference between the two models is in the location of the key reaction: Luisi *et al.*[3,21] assumed the reaction occurred at the micelle, while Buhse *et al.* provide compelling evidence that product micelles effectively solubilise the hydrophobic reagent in the aqueous phase, and thus the reaction likely occurs in bulk solution. Nguyen *et al.* did not entertain a phase-transfer model and assumed that the reaction proceeds as Luisi proposed, couching their interpretation in terms of autopoiesis.

The distinction between a micellar or autopoietic mechanism, wherein the reaction occurs at the micelle, and a phase-transfer mechanism, where the reaction occurs in bulk solution, is valuable. It is an important distinction for proponents of autopoiesis, as autopoiesis arguably requires the reaction to be contained within the micelle (see Chapter 1). For our purposes it is less crucial: in either scenario the reaction is autocatalytic. Detecting the formation of mixed micelles of **2b** and **3b** by DOSY NMR provides evidence for an autocatalytic mechanism in either case.

Our first step was to confirm the CMC of **3b** by DOSY. Matsuno *et al.* reported a value of 25 mM as determined by surface tension measurements;[13] by DOSY we measured a CMC of 26.5 mM, in close agreement (Figure 2.4). Beyond the obvious value of reproducing the literature measurement, this served to validate the application of DOSY to these compounds. The CMC in the presence of thiol **2b** (100 mM) was slightly lower at 23.4 mM, consistent with the thermodynamically favourable formation of mixed micelles of **3** and **2**.[14]

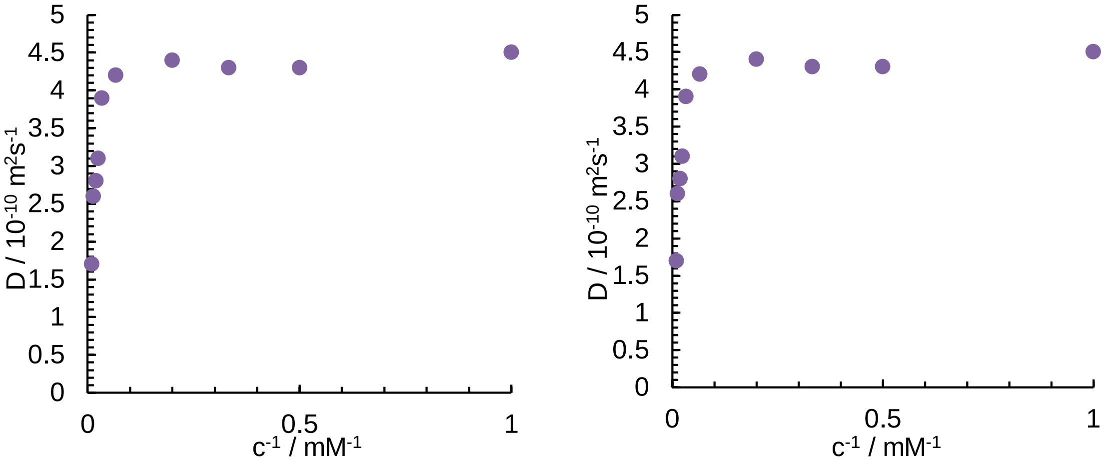

Figure 2.4. Critical micelle concentration of 3b. Left: CMC of **3b** measured by DOSY NMR. Right: CMC of **3b** in the presence of excess thiol **2b** measured by DOSY NMR.

Using the Stokes-Einstein equation (equation (2.1)) it is possible to estimate the hydrodynamic radius or Stokes radius, R_H, of micelles from the experimentally-obtained diffusion coefficient.[18] By this method we estimated the R_H of **3b** at 100 mM to be 1.0 nm. While the diffusion coefficient and by extension the R_H of **3b** was highly sensitive to changes in concentration above 25 mM (Figure 2.4), this estimate at least provided an order-of-magnitude estimate of the size of these aggregates during the course of the reaction.

$$D = \frac{k_b T}{6\pi\eta R_H} \tag{2.1}$$

We next probed the association behaviour of thiol **2b** with lipid **3b**. This required the following measurements: the diffusion coefficients of isolated **2b** and isolated **3b** both above and below its CMC, and the diffusion coefficients of mixtures of **2b** and **3b** above and below the CMC of **3b**. The formation of mixed micelles of **2b** and **3b** would then be indicated by the decrease of the diffusion coefficient of **2b** to a value close to that of micelles of **3b**.

Analysis of the data used to calculate the CMC of **3b** in the presence and absence of thiol **2b** revealed that, in the presence of 100 mM **3b** the thiol was significantly bound to micellar species. This observation supported our hypothesis that an autocatalytic mechanism was in operation, whether via phase-transfer or micellar pathways.

Unexpectedly, **2b** appeared to move more slowly than the micelles of **3b**. This observation is readily accounted for by considering the equilibria between the various components of the system. Molecules incorporated into micelles typically exchange with monomers in solution rapidly on the NMR timescale, and thus the NMR signal of a given species reflects the average of the micellar and solution environments. The diffusion coefficients obtained by DOSY are therefore weighted averages of the diffusion coefficients of monomeric and micelle-bound molecules.

This accounts for the lower diffusion coefficient of **2b** compared to micelles of **3b**. Thiol **2b** is close to insoluble in water, and thus the diffusion coefficient observed by DOSY reflects almost exclusively the micellar environment. Conversely, lipid **3b** is water-soluble, and millimolar quantities of monomeric **3b** coexisted with micelle-bound molecules. Its diffusion coefficient therefore has a non-negligible contribution from fast-moving monomeric **3b** and is higher than the diffusion coefficient of pure micelles would hypothetically be.

To overcome this limitation we used a method reported by Stilbs[22] which uses tetramethylsilane (TMS) as a reporter molecule for the micellar diffusion coefficient.

This method assumes that TMS is completely insoluble and therefore its diffusion coefficient is equal to that of the micelles. The required diffusion coefficients are those of the free thiol (D_{free}), the micelle-bound TMS ($D_{micellar}$, assumed to be equal to the true diffusion coefficient of the micelle), and the micelle-bound thiol (D_{obs}). We repeated the appropriate experiments with the addition of TMS (Figure 2.5), and using equation (2.2) calculated the degree of solubilisation of **2b** into micelles of **3b** ([**3b**] = 100 mM) as $p > 99\%$.

$$p = \frac{D_{free} - D_{obs}}{D_{free} - D_{micellar}} \tag{2.2}$$

As noted above this observation supports either a micellar or phase-transfer autocatalytic pathway. Tentatively, the significant solubilisation of **2b** into **3b** would seem to support a micellar pathway. The phase-transfer pathway would require that the very low concentration of monomeric thiol have very high activity and be the dominant reactive species. This is, however, a real possibility that cannot be ruled out.

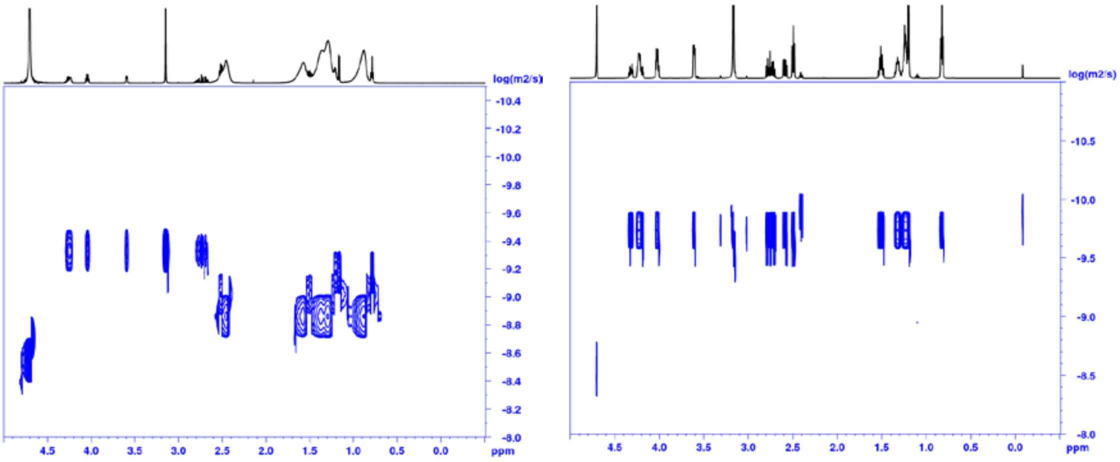

Figure 2.5. Evidence for the association of 2b and 3b. Left: 2D DOSY spectrum shows the difference in D for **2** and **3**. Peaks between 2.5–0.5 ppm correspond to protons of **2b** and the alkyl chain of **3b**, with an isolated triplet at 2.42 ppm providing D for **2b**. Left: Experiment performed on a mixture of **3b** (1mM) and **2b** (saturated); Right: 2D DOSY spectrum shows the coincidence of diffusion coefficients for **2b**, **3b** and TMS. Experiment performed on a mixture of **3b** (100 mM), **2b** (saturated) and TMS (saturated). Full data are provided in Chapter 5.

Unfortunately the applicability of these results to our reaction conditions was not clear. These NMR experiments were performed at neutral pD; the reaction was performed at high pD, meaning that significant quantities of thiolate ion were present. These would be expected to be more soluble in water than the thiol and hence the degree of solubilisation into the micelle may have been lower than indicated by these experiments. Further, the higher ionic strength due to the presence of Cs_2CO_3 may well have affected the aggregation properties of **3b**. We opted not to repeat the DOSY experiments at high pD as any hydrolysis of **3b** would affect the obtained diffusion coefficients, and the higher ionic strength of the solution gave poor spectral resolution in preliminary measurements, leading to overlap of peaks of **2b** and **3b**.

Species present	**D (lipid 3)**	**D (thiol 2)**	**D (TMS)**
2b (saturated)	-	16	-
3b (5 mM)	4.4	-	-
3b (100 mM)	1.7	-	-
2b (saturated) **3b** (5 mM)	4.4	9.6	-
2b (saturated) **3b** (100 mM) TMS (saturated)	1.5	1.0	0.95

Table 2.2. Uptake of 2 into micelles of 3. The diffusion coefficient (D) of **2** decreases significantly in the presence of **3** when [**3**] > 25 mM, indicating the formation of mixed micelles of **2** and **3**. D values reported in 10^{-10} m^2 s^{-1}.

This first-generation system provided valuable experience in the study of physical autocatalysis, and demonstrated that the self-reproduction of micelles can be driven by irreversible bond-forming reactions. The system suffered from several limitations, however, most obviously the need for harsh conditions: high concentrations of the starting materials and high pH leading to partial hydrolysis of the starting material, incompatibility with DOSY NMR conditions, and considerable noise in the resulting kinetic data.

2.4. Second-generation autocatalytic thiol-ene reactions

2.4.1. Design, synthesis, and kinetic studies

With these issues in mind we decided to design a second generation system. We predicted that a more reactive alkene would allow the reaction to proceed at lower pH and at lower concentrations, and possibly allow the use of longer thiols, which react more slowly. The use of a longer thiol has two advantages: firstly it lowers the CMC of the product, meaning that the autocatalytic pathway can operate early in the reaction even at lower reagent concentrations. Secondly, longer thiols are less soluble, hopefully disfavouring background pathways and potentially the autocatalytic phase-transfer pathway. Additionally, a reaction carried out at close to neutral pH would allow our DOSY study to be directly applicable to the reaction conditions and lower the concentration of thiolate in solution, again potentially disfavouring background and phase-transfer pathways.

Maleimides are highly electrophilic alkenes which readily react with thiols at close to neutral pH. These are several times more reactive than the methacrylates used above[13] and are widely used in bioconjugation reactions,[23] offering a promising substrate for a second-generation system. While thiol-maleimide adducts are known to undergo retro-Michael reactions back to the starting materials, at physiological pH and in the absence of confounding structural factors, these adducts are typically stable with a typical equilibrium constant estimated as 10^9 M^{-1}.[24] As such they are suitable for our studies of irreversible bond-forming reactions.

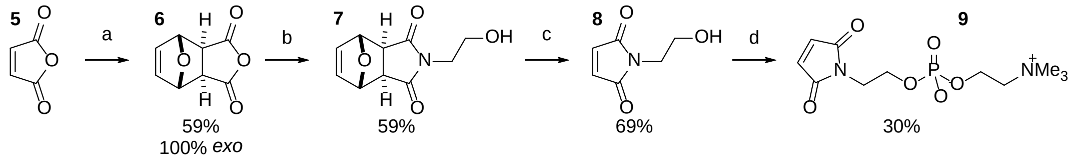

Scheme 2.2 Synthesis of 9. (a) Furan, benzene, rt, 18 h; (b) ethanolamine, MeOH, reflux, 18 h; (c) toluene, reflux, 18 h; (d) i. 2-chloro 1,3,2-dioxaphospholane 2-oxide, Et_3N, THF, 0 °C to rt; ii. trimethylamine, MeCN, heated in sealed vessel, 18 h.

A maleimide-containing analogue of compound **1** was synthesised from the known alcohol **8**, which is readily prepared on the gram scale in three steps from maleic anhydride.[25] The reaction of alcohol **8** with 2-chloro-1,3,2-dichlorophospholane 2-oxide followed by ring-opening with freshly-distilled trimethylamine[26] gave **9** in acceptable yield and purity. Compound **9** was highly polar and did not crystallise, requiring purification by chromatography eluting with 30% H_2O in acetonitrile.

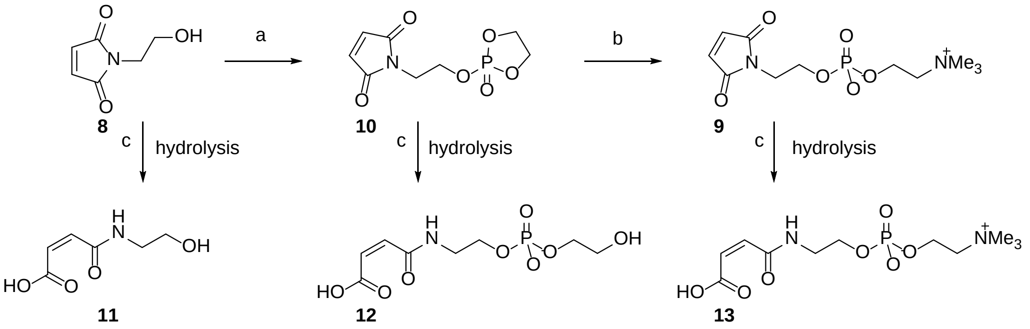

Scheme 2.3. Yield-limiting hydrolysis reactions. (a) 2-chloro 1,3,2-dioxaphospholane 2-oxide, Et_3N, THF, 0 °C to rt; (b) trimethylamine, MeCN, heated in sealed vessel, 18 h; (c) hydrolysis by trace H_2O during step b.

The yield of the final step was limited by the instability of both the intermediate phospholane and the maleimide moieties in both **8** and **9** towards hydrolysis under basic conditions (Scheme 2.3). It was difficult to rigorously exclude water and air during the distillation and transfer of trimethylamine into the reaction vessel. Consequently, upon heating the intermediate phospholane and trimethylamine in acetonitrile, a deep red precipitate developed which was characteristic of hydrolysis of the maleimide ring in these compounds. This material was presumably a mixture of the ring-opened species **12**, **13**, and potentially **11**, as suggested by the presence of alkene peaks in the crude NMR spectrum. However this methanol-soluble material was immobile on TLC plates even under very polar conditions, so could not be purified and characterised. Attempts to close the maleimide ring by refluxing the crude precipitate in acetic acid[27] failed.

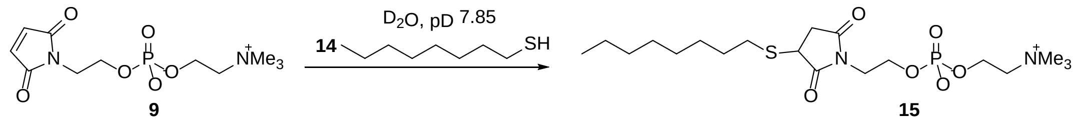

Scheme 2.4. Second-generation thiol-ene reaction.

The development of appropriate reaction conditions was considerably simpler than before. Here octanethiol **14** was chosen for the reasons outlined above: to keep the CMC of the product low enough to allow it to form early in the reaction and to disfavour reaction pathways relying on dissolution of the thiol. Compound **15**, the adduct of **9** and octanethiol **14**, was prepared and its CMC was measured by DOSY NMR as 4.8 mM (Figure 2.6). A starting concentration of 100 mM in **9** was chosen and the reaction with 10 eq thiol **14** in Tris buffer in the pH 7-8 range was followed by TLC. Pleasingly, these reactions proceeded to completion within 12 hours.

The reaction required careful control of pH: below pH 7, the reaction hardly proceeded, and at pH 8 hydrolysis of the maleimide in **9** (~5%) was observed. Around pH 7.4, adducts of thiols and *N*-alkyl maleimides typically hydrolyse slowly, with a half-life of months.[24] However the electron-withdrawing phosphate group in **9** and **15** may be expected to accelerate hydrolysis via an inductive effect.[28] At the intermediate value of pH = 7.85 we observed no hydrolysis of either species, and the reaction proceeded efficiently.

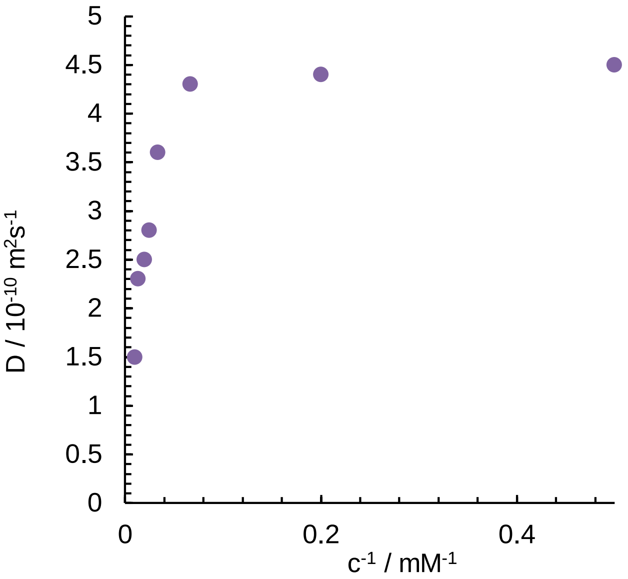

Figure 2.6. Critical micelle concentration of 15 as measured by DOSY NMR.

Kinetics were recorded by ^{1}H NMR in 21 mM Tris buffer, pD = 7.85, and autocatalytic behaviour was again observed (Figure 2.7). As before, autocatalysis was suggested by an increase in the rate of reaction following a lag period, and by the elimination of this lag period by the addition of lipid **15** at the start of the reaction.

The reaction of **9** and **14** exhibited a longer lag period than did the first-generation system. This is likely a result of the lower solubility of octanethiol in neutral D_2O compared to hexanethiol in alkaline D_2O. However, upon the formation of quantities of **15** in excess of its CMC, the reaction proceeded at a similar rate to the first generation system, reflecting the higher reactivity of the maleimide. The large standard deviation of peaks in the linear reaction phase are an artefact of the fact that each reaction reached this phase at a slightly different time; the raw data are plotted in Chapter 5.

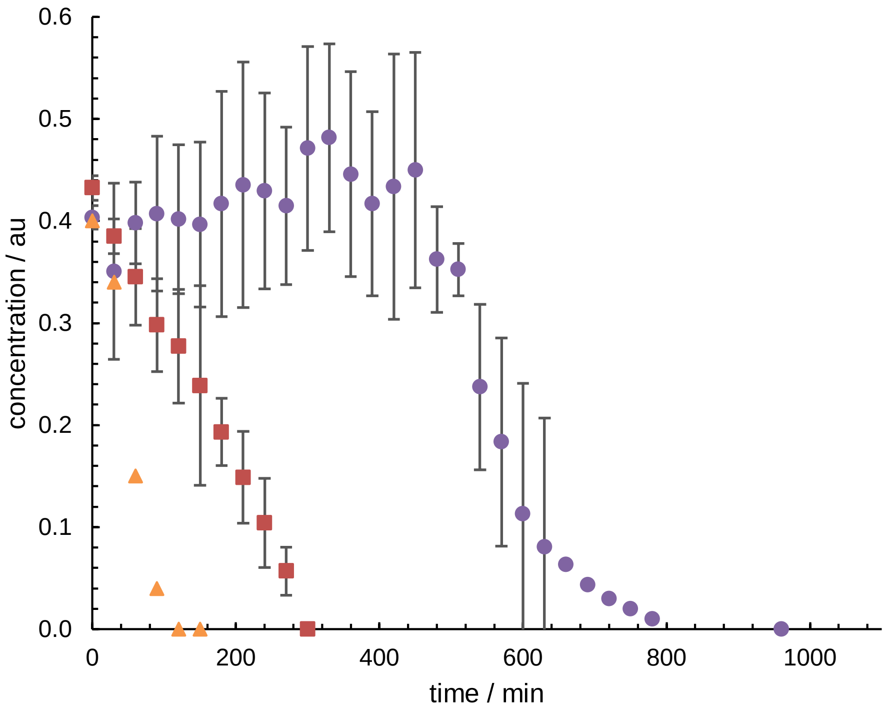

Figure 2.7. Evidence of autocatalysis in the reaction of 9 and 14. The reaction is monitored by disappearance of **9** by ^{1}H NMR spectroscopy. Data points are the mean of three experiments and error bars show the s.d. ● Control reaction: when **9** and **14** are stirred gently, a lag period followed by a faster reaction period is observed. ■ Seeded reaction: when the reaction is seeded with 20 mol% **15** at t = 0, the lag period is eliminated and the reaction proceeds linearly. ▲ Seeded reaction (single experiment): addition of 70 mol% of **15** at t = 0 further increases the rate of reaction. Representative stacked spectra are shown in Chapter 5.

2.4.2. Mechanistic study by DOSY NMR

Following the experimental design described in section 2.3.2 we studied the maleimide-based system by DOSY NMR. At 50 mM lipid **15** was estimated to form micelles with R_H = 1.5 nm. Experiments performed on mixtures of the thiol and lipid clearly showed that **14** was entirely bound within micelles of **15** when **15** was present in a large excess of its CMC (Figure 2.8). Here we studied the aggregation behaviour at a greater range of concentrations, and confirmed that the maleimide starting material **9** neither aggregated nor was taken into the micelles of **15** (Table 2.3, rows I-K).

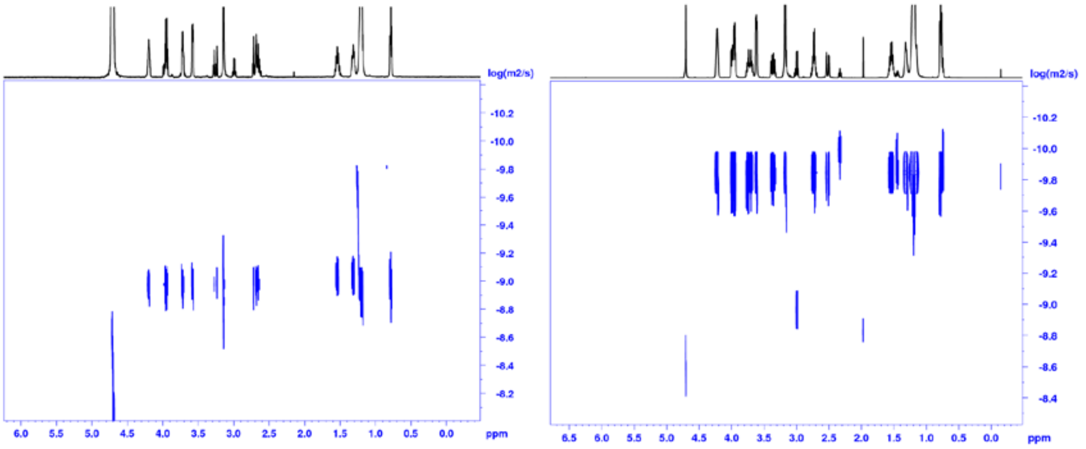

Figure 2.8. Evidence for the association of 14 and 15. Left: 2D DOSY spectrum shows rapid diffusion of **15**. Thiol **14** was not directly observed in this experiment despite the solution being saturated before measurement. Experiment corresponds to Table 2 row D; Right: 2D DOSY spectrum shows the coincidence of diffusion coefficients for **14**, **15** and TMS. Experiment performed corresponds to Table 2 row H. Full data are provided in Chapter 5.

In the presence of sub-CMC concentrations of **15**, thiol **14** was not reliably detectible by ^{1}H NMR (Figure 2.8, left; Table 2.3, row D). Trace quantities were seen in the 2D DOSY spectrum but a diffusion coefficient could not be obtained from these data.

In the presence of 50 mM **15** (~10 times the CMC; Table 2.3, row H) thiol **14** was completely bound to slow-diffusing aggregates. Unexpectedly, under these conditions we found that thiol **14** had a lower diffusion coefficient than did TMS. The method we previously used to calculate the quantity of bound thiol assumed TMS is fully bound to micelles.[22] This diffusion coefficient was taken as an approximation the ideal diffusion of micelles, as the observed diffusion coefficient of lipids is an average of the free and aggregated lipid. Finding that lipid **14** has a lower diffusion coefficient than TMS suggested the assumption that TMS was completely contained within the micelles does not hold. While this precluded quantification of the degree of binding of thiol **14** to micelles of **15**, it did strongly suggest that **14** was completely bound to micelles of **15**, i.e., all **14** was either in a bulk thiol layer or contained within micelles.

Entry	Species present	D (lipid 15)	D (thiol 14)	D (TMS)	D (alkene 9)
A	**14** (saturated)	-	9.6	-	-
B	**15** (2 mM)	4.0	-	-	-
C	**15** (50 mM)	1.2	-	-	-
D	**14** (saturated) **15** (2 mM)	3.8	Not detected	-	-
E	**14** (saturated) **15** (5 mM) TMS (saturated)	3.3	12	3.5	-
F	**14** (saturated) **15** (10 mM) TMS (saturated)	2.8	1.2	2.3	-
G	**14** (saturated) **15** (20 mM) TMS (saturated)	1.9	0.77	2.1	-
H	**14** (saturated) **15** (50 mM) TMS (saturated)	1.1	0.64	1.06	-
I	**9** (100 mM)	-	-	-	5.0
J	**9** (100 mM) **15** (3 mM)	3.8	-	-	4.6
K	**9** (100 mM) **15** (50 mM)	1.3	-	-	4.6

Table 2.3. Uptake of 5 into micelles of 6. The diffusion coefficient (D) of **5** decreases significantly in the presence of **15** when **15** is above its CMC (4.8 mM), indicating the formation of mixed micelles of **14** and **15**. TMS is seen to have a higher D than **15**, suggesting slight solubility of TMS in water and quantitative binding of **14** to **15**. D values reported in 10^{-10} m^2 s^{-1}. No interaction between polar maleimide **9** and micelles of **15** is observed. 2D spectra for all experiments are available in Chapter 5.

Despite this limitation, we studied the uptake of thiol at intermediate concentrations at and above the CMC (Table 2.3, rows E-G). As can be seen from Table 2.3, close to the CMC (5-10 mM) the diffusion coefficient of **15** changed rapidly with concentration. This is consistent with either the formation of increasingly large micelles with lower diffusion coefficients, or with the formation of larger numbers of micelles that shift the observed diffusion coefficient towards the micellar diffusion coefficient. Nonetheless, even at concentrations barely in excess of the CMC, the thiol appeared to bind entirely to the small concentration of micelles that were present.

We therefore conclude that this reaction is unlikely to proceed via a phase transfer mechanism as described by Buhse *et al.*[14] Thiol **14** is negligibly soluble in aqueous solution and as the concentration of lipid **15** increased beyond the CMC, the diffusion coefficient of **14** continued to decrease as it bound tightly to growing micelles of **15**. We interpret this as suggesting that the reaction occurred in association with the micelles, in agreement the mechanism proposed by Luisi.[3]

As noted above it is possible that a micromolar concentration of thiol, invisible to these NMR experiments, was present in the aqueous layer and that its reactivity constituted the major reaction pathway. The Curtin-Hammett principle indicates that the equilibrium distribution of species between the micellar and solution phases does not necessarily reflect the kinetically significant species; it may be that the reaction primarily proceeded via this proposed solvated thiol. Conversely, the lack of association between **9** and micelles of **15** does not preclude the possibility of small quantities of **9** overcoming the barrier to association, becoming incorporated into the micelle and reacting with micelle-bound **14**. Further mechanistic study may be able to disentangle these different pathways.

2.5. Towards autocatalytic azide-alkyne cycloaddition reactions

We next designed a system which used the copper-catalysed 1,3-dipolar cycloaddition of azides and terminal alkynes (CuAAC)[29] as the key reaction. Like the thiol-ene reaction, this ‘click’ reaction has valuable features which seem ideal for the development of bond-forming physical autocatalysis. The starting materials, azides and alkynes, are readily accessible and stable in the presence of water and air. The reaction proceeds in water under conditions that are broadly compatible with common functional groups, tolerating considerable structural diversity in the two coupling partners. Like the thiol-ene reaction, CuAAC is widely used in bioconjugation reactions to couple remarkably complex molecules together.[30] The products are formed selectively and irreversibly, giving exclusively the 1,4-substituted triazole, and are stable.

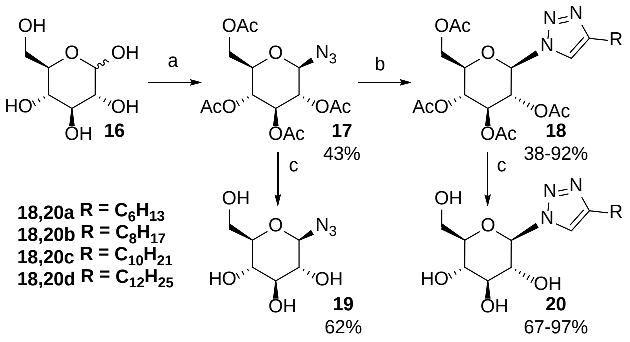

Scheme 2.5. Synthesis of glucose-derived reaction components. (a) i) Ac_2O, I_2; ii) AcOH/HBr, 0 °C then rt; iii) NaN_3, TBAI, $CHCl_3$, aq. $NaHCO_3$; (b) alkyne, CuI, AcOH, DIPEA, CH_2Cl_2; (c) NaOMe, MeOH.

Whereas before we used phospholipid analogues, here we opted to use sugar-derived surfactants. This decision was taken with future development in mind. These sugar derivatives are easily synthesised (Scheme 2.5), can be varied simply by using different sugar head groups, and importantly the potential for sugar derivatives to catalyse prebiotically-relevant reactions is relatively unexplored. Anomerically pure glycosyl azides are easily synthesised on gram scales,[31] and terminal linear alkynes of varying chain lengths are commercially available. The coupling of these components by CuAAC gives products which we predicted to be surfactants based on literature reports of closely-related compounds.[32,33]

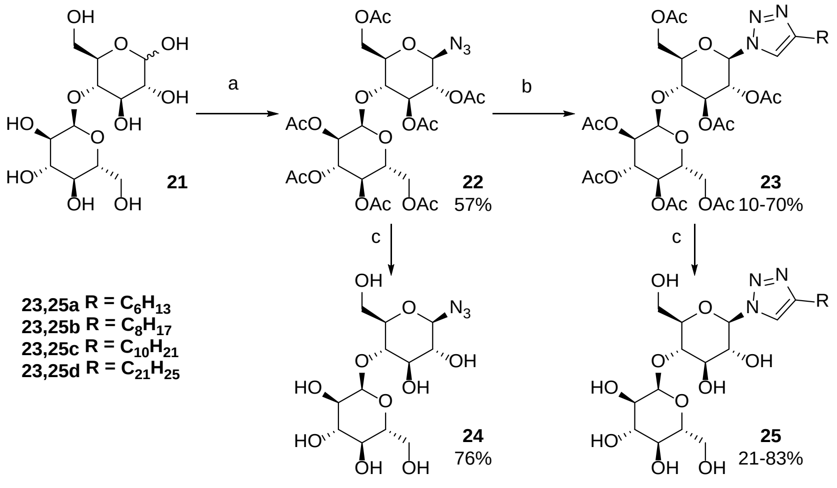

Scheme 2.6. Synthesis of maltose-derived reaction components. (a) i) Ac_2O, I_2; ii) AcOH/HBr, CH_2Cl_2 0 °C then rt; iii) NaN_3, TBAI, $CHCl_3$, aq. $NaHCO_3$; (b) alkyne, CuI, AcOH, DIPEA, CH_2Cl_2; (c) NaOMe, MeOH.

We synthesised compounds **20a**-**d** in four steps from D-glucose **16**, but unexpectedly found them to be poorly soluble in water at room temperature. Fluorimetry measurements using 1,6-diphenyl-1,3,5-hexatriene (DPH) as a probe[34] revealed that no aggregates were present in filtered millimolar solutions of these compounds. This was surprising given that very close analogues of compounds **20a**-**d** have had their CMCs measured.[32] In order to increase the solubility and hopefully promote surfactant behaviour, we replaced the glucose head group with maltose to give compounds **25a**-**25d**. Fluorimetry measurements using DPH revealed the formation of micelles at millimolar concentrations, with the CMC inversely proportional to the alkyne chain length (Table 2.4). No CMC could be obtained for **25d**.

Compound	CMC / mM
25a R = C_6H_{13}	18
25b R = C_8H_{17}	6
25c R = $C_{10}H_{21}$	1
25d R = $C_{12}H_{25}$	-

Table 2.4. Critical micelle concentrations of maltose-based surfactants. CMCs measured by fluorimetry using DPH as a probe. See Chapter 5 for experimental details. Values rounded to nearest whole number.

The final step in the synthesis of compounds **25a**-**d** prior to deprotection was the CuAAC coupling of azide **22** to the alkyne. The reaction proceeded poorly in water/*t*-butanol, even with prolonged heating, giving consistently poor yields of around 30% for all substrates. The yield was improved by using alternative anhydrous conditions.[35] Despite the use of rapid stirring, heating, high concentrations, and an effective co-solvent, the reaction did not proceed efficiently in aqueous conditions.

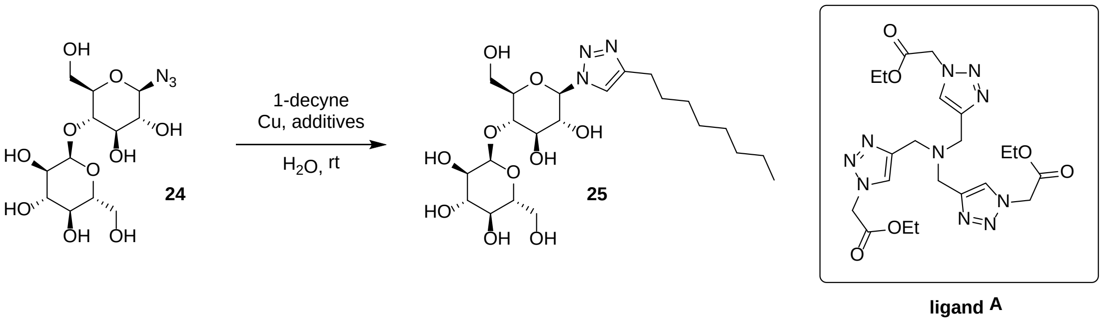

Scheme 2.7. Screen of CuAAC conditions. See Table 2.5 for further details. Ligand A kindly provided by colleagues.

A screen of reaction conditions for the reaction of the deprotected azide **24** with 1-decyne (Scheme 2.7, Table 2.5) revealed that, as reported by Baron *et al.*,[36] the use of phenylenediamine to chelate Cu(I) generated by reduction of $CuSO_4$ in situ by sodium ascorbate gave excellent conversion within several hours. Where Baron *et al.* added *t*-butanol as a cosolvent, we used only water. All other conditions we screened gave poor or no conversion even after several days. These conditions were adapted from the literature, particularly the conditions optimised for bioconjugation reactions by

Hong *et al.*,[30] or were provided by departmental colleagues.[37] Consistent with the literature[36] it appears that these substrates undergo CuAAC in water only sluggishly, presumably owing to the poor solubility of the alkyne. All of these experiments were performed under an inert atmosphere using degassed water.

Reaction conditions	**Result**
$CuSO_4 \cdot 5H_2O$ (1 mol%), sodium ascorbate (20 mol%)	-
$CuSO_4 \cdot 5H_2O$ (1 mol%), sodium ascorbate (20 mol%), ligand A (1 mol%)	-
$CuSO_4 \cdot 5H_2O$ (1 mol%), sodium ascorbate (20 mol%), ligand A (0.5 mol%)	-
CuI (1 mol%), ligand A (1 mol%)	-
CuI (20 mol%), ligand A (20 mol%)	-
CuBr (1 mol%), ligand A (1 mol%)	-
CuBr (20 mol%), ligand A (20 mol%)	-
$CuSO_4 \cdot 5H_2O$ (5 mol%), sodium ascorbate (10 mol%), *o*-phenylenediamine (15 mol%)	Complete within 6 hr

Table 2.5. Screen of CuAAC reaction conditions. Reactions performed in degassed H_2O under Ar using 20 mM **24** and one equivalent of 1-decyne. Reactions were rapidly stirred and monitored by TLC and ESI-MS for 48 hours.

With promising reaction conditions in hand we attempted to quantify the reaction kinetics by ^1H NMR spectroscopy, as before. As seen in Figure 2.9, peaks corresponding to product **25b** appeared at δ = 5.64 and 5.41 ppm. However, these peaks were broad and integrated poorly, and further the peak at 5.41 ppm quickly underwent an upfield shift resulting in complete overlap with an anomeric proton signal from **24**. The triazole peak was invisible under these conditions owing to exchange with D_2O.

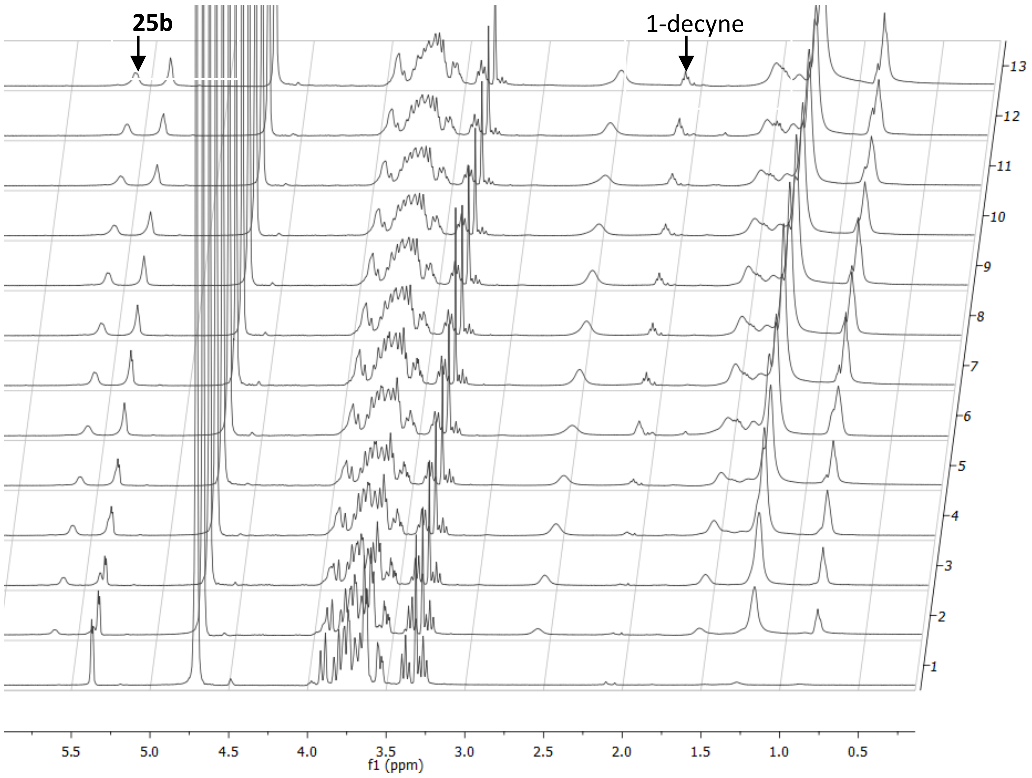

Figure 2.9. Reaction of 24 and 1-decyne. Conditions adapted from Baron *et al.*,[36] see Table 2.5. Azide concentration = 275 mM, 5 eq. 1-decyne. Reaction performed in degassed D_2O (total volume 4 mL) under Ar, initiated by addition of $CuSO_4 \cdot 5H_2O$ in D_2O, and stirred at 800 rpm. Reaction monitored by removing 50 µL and diluting it to 0.6 mL in D_2O for immediate analysis by ^{1}H NMR every 30 min.

Integration of the one isolated peak arising from **25b** at δ = 5.64 ppm using *o*-phenylenediamine (δ = 6.93) as an approximate internal standard revealed two features (Figure 2.10). Firstly, the broad signals being integrated here gave noisy data. Secondly, the reaction rapidly proceeded over the first 90 minutes with no obvious lag period, before slowing considerably. This occurred reproducibly across three experiments. This is most likely attributable to oxidation of the catalyst by air introduced during the sampling procedure, despite the presence of a positive pressure of argon. Indeed, these reactions visibly changed from blue to brown over the first hour of the reaction, and were never seen to reach completion when aliquots were being removed in contrast to when the reaction was left undisturbed and sampled only at its end point.

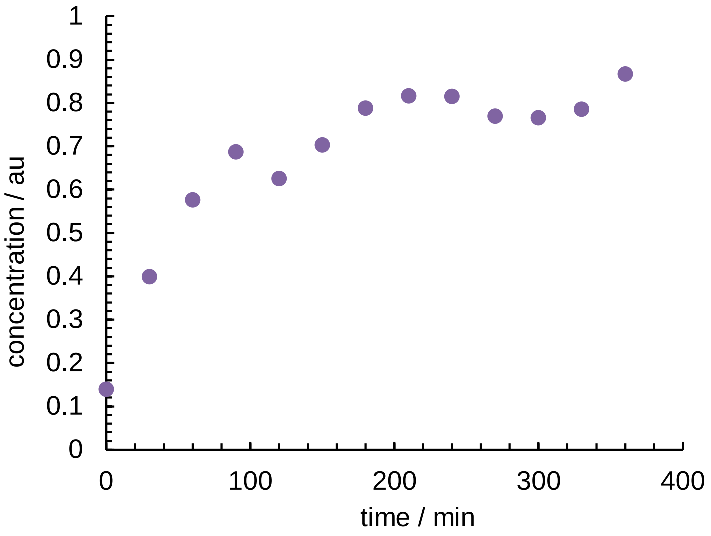

Figure 2.10. Formation of 25b. Product formation monitored by integration of peaks at *d* = 5.64 ppm (anomeric proton of **25b**) and *d* = 6.93 ppm (*o*-phenylenediamine). For conditions see Figure 2.9.

Promisingly, a triplet corresponding to the alkyne proton in 1-decyne emerged at δ = 2.11 ppm, consistent with solubilisation of the alkyne in product micelles. This suggests that physical autocatalysis ought to occur in this reaction and that when an appropriate analytical technique for monitoring this reaction is identified, autocatalytic behaviour will be observed. The most obvious candidate technique is reverse-phase HPLC. The deactivation of the catalyst during aliquot removal must be addressed, initially by increasing the amount of reductant in the system in order to keep the catalyst from oxidising.

Assuming autocatalytic behaviour can be demonstrated as before, DOSY NMR studies should be undertaken to explore the localisation of catalytically-significant species. For example, by recording the diffusion coefficient of the aromatic peaks arising from phenylenediamine, information about the partitioning of the copper catalyst into the micellar interior may be obtained.

2.6. Towards asymmetric physical autocatalysis

Life uses homochiral molecules, and understanding how this situation arose from the racemic prebiotic world is a major challenge in the field. This is generally understood to involve two steps: chiral symmetry breaking followed by asymmetric amplification. Numerous different mechanisms have been proposed for these processes. Most relevant here are absolute asymmetric autocatalysis and phase behaviour models.

Absolute asymmetric catalysis involves the enantioselective autocatalytic amplification of a small enantiomeric excess arising from stochastic imbalances in nominally racemic samples.[38–40] This relies on the combination of enantioselective autocatalysis with a strong non-linear effect, leading to the removal of the minor enantiomer of the product from the system in the form of inactive racemic dimers or higher oligomers.[41] The only known reaction of this kind, the Soai reaction,[15,42,43] is exquisitely sensitive to small ees arising stochastically[44] or from the presence of chiral additives including circularly polarised light[45] and enantiomers distinguished only by isotopic substitution.[46] However, as the Soai reaction consists of the 1,2-addition of dialkylzinc reagents to a limited class of aldehydes under anhydrous, anoxic conditions, it is not considered prebiotically plausible and remains only a proof-of-principle of this fascinating process.

An alternative model for the origin of biological homochirality has been proposed by Blackmond and co-workers.[47] Rather than exploit asymmetric autocatalysis, Blackmond's model relies on the equilibrium phase behaviour of scalemic materials, particularly amino acids (Figure 2.11). This model concerns equilibrium mixtures of scalemic amino acids and a solvent, in which the amino acid is present in excess of its solubility. Under isothermal conditions, three phases will be present: two different solid phases and a solution phase consisting of solvent and amino acid. The point on the phase diagram where these three phases intersect is the *eutectic point*, which is constant and independent of the total enantiomeric excess of the amino acid present in the system.[48]

Eutectic mixtures of this kind can exhibit differences in ee between the solid and solution phases. In the case of compounds that form conglomerate crystals, and hence crystallise into two enantiomeric solid phases, there can be no change in ee: both solid phases are equally soluble, and at equilibrium the enantiomeric excess must therefore be constant in the solid and solution phases.

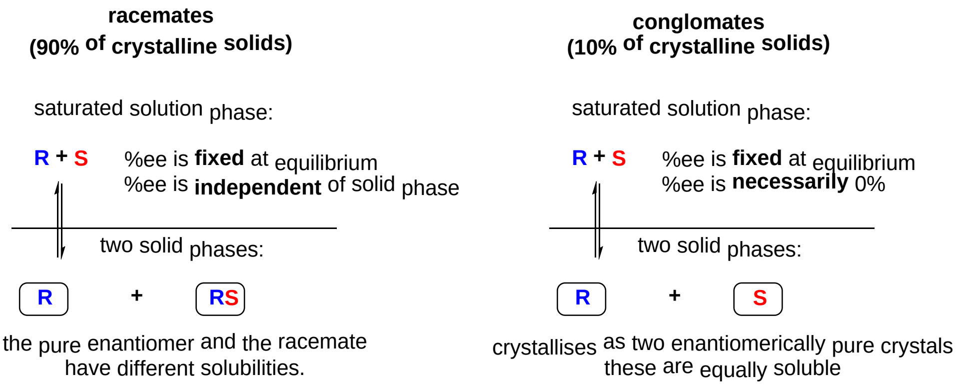

Figure 2.11. Phase behaviour of saturated scalemic compounds. A scalemic sample of a crystalline solid at equilibrium will crystallise into two distinct phases when it is present at a high enough concentration to exceed to the solubility limit of both solid phases. Racemates (left) crystallise into an enantiopure phase consisting of the major enantiomer and a solid phase that is racemic on the unit cell level. Conglomerates (right) form two enantiomeric solid phases with equal solubilities. The two solid phases formed by a racemate are diastereomeric to one another and thus may have differing solubilities, leading to a change in the equilibrium ee of the solution phase relative to that of the overall ee of the combined material.

In the case of compounds that form racemic crystals, however, this is not so. These compounds crystallise into two diastereomeric crystal phases: one phase that is a homochiral crystal of the major enantiomer, and one phase that is, on the unit cell level, a racemic mixture of both enantiomers. These two solid phases have different solubilities, and thus there may be an enrichment or depletion of the enantiomeric excess in the solution phase when compared to the ee as a whole.

Here we describe preliminary experiments exploring asymmetric autocatalytic processes inspired by this model. It is well known that various additives can bias the eutectic composition of amino acid solutions. If a derivative of an amino acid is able to bias the eutectic composition of that amino acid, and that derivative can be generated in situ, we may be able to develop a new prebiotically-relevant asymmetric process.

Our approach was to identify a simple amino acid derivative which meets the following criteria:

a) It can be formed in situ from its amino acid precursor in water;
b) It is amphiphilic and thus potentially capable of physical autocatalysis;
c) Enantiopure samples of the derivative are capable of altering the solution-phase ee of the precursor at the eutectic point.

An ideal result would consist in a molecule which is formed through physical autocatalysis and biases the eutectic solution-phase ee towards the enantiomer of the amino acid precursor corresponding to the product, such that some form of asymmetric autocatalysis with amplification of ee occurs. More realistically, any alteration of the eutectic composition would be a promising start towards this goal.

Alkyl *N*-carbamates formed by the reaction of amino acids and alkyl chloroformates appeared likely to meet the first two criteria. Chloroformates react with amino acids in basic aqueous media to give these products. Under basic conditions the products can be expected to be deprotonated, increasing the likelihood that they will form micelles or other aggregates.

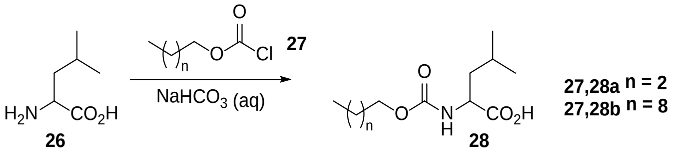

Scheme 2.8. Proposed autocatalytic synthesis of carbamates.

Enantiopure compounds L-**28a** and L-**28b** were synthesised and their aggregation probed by DOSY. At pH 1 these compounds did not aggregate, presumably because the carboxylate groups were protonated and thus not polar enough to impart amphiphilicity to the molecules. At pH 8, compound L-**28a** formed no aggregates at 100 mM concentration. Under these conditions, however, compound L-**28b** did aggregate. This is consistent with the expected behaviour of long- and short-tailed amphiphiles.

With a micelle-forming derivative in hand we explored whether this compound could influence the eutectic composition of its precursor amino acid leucine, **26**. To measure the solution-phase ee of these systems we adopted a protocol described by Husek[49] in which aqueous samples are derivatised using ethyl chloroformate to give volatile products that can be analysed by chiral stationary phase gas chromatography. Applying this procedure to carbamates **28a** and **28b** revealed that the carbamate bonds in these species were stable under the derivatisation conditions, allowing the simultaneous analysis of the ee of both **26** and **28a** in a single measurement. Long-tailed derivatives such as **28b** gave poorly-resolved GC peaks, presumably owing to their lower volatility.

The equilibrium solution ee of **26** was measured as 90% ee by allowing a stirred suspension of 50% ee leucine to equilibrate over 3 days before analysing the filtered solution by enantioselective GC. This is close to the reported literature value of 88%.[48] Unfortunately L-**28b** was found to have no influence on the eutectic solution-phase ee of **26**.

We opted to investigate whether L-**28b** could influence the kinetics of the system rather than the thermodynamic outcome. To achieve this we measured how the ee of product and starting material evolves during the reaction of scalemic samples of **26** with butyl chloroformate. Butyl chloroformate was chosen to simplify analysis. Analysing the effect of **28b** on its own formation would involve back-calculating the ee of newly-formed **28b** after accounting for the presence of pre-formed enantiopure **28b**. Instead, we were able to directly measure the ee of newly-formed **28a** as influenced by **28b**. Further, **28a** was more volatile than **28b** and gave cleaner, more reproducible GC traces.

The reaction of an equilibrated mixture of 50% ee **26** and butyl chloroformate in the presence of one equivalent of L-**28b** was indistinguishable from the corresponding control reaction (Figure 2.12). The solution-phase ee of starting material and product were initially close to the equilibrium value and then rapidly decayed, with **26** reaching 0% ee and **26a** reaching 50% within two hours. No transient amplification or depletion effects in the ee of either species were observed.

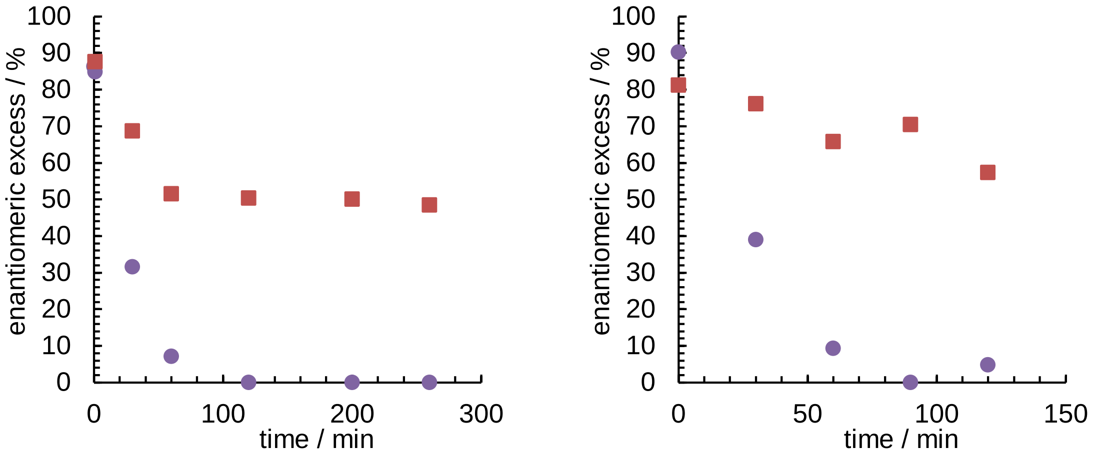

Figure 2.12. Reaction of scalemic leucine with butyl chloroformate. Equilibrated suspensions of 50% ee leucine in 1 M $NaHCO_3$ were stirred rapidly with 1 eq butyl chloroformate in the absence (left) and presence (right) of 1 eq **L-28b**. Analysis of the solution phase was performed by enantioselective GC following derivatisation of filtered aliquots by ethyl chloroformate in ethanol/pyridine. ● %ee of leucine; ■ %ee of **28a**.

The reaction of a non-equilibrated sample of 50% ee **26** made by mixing racemic and enantiopure crystals of **26** together showed rapid equilibration (Figure 2.13), with the transient formation of enantiomerically-enriched **28a** (80% ee) within the first hour. The product ee closely matched that of the solution-phase **26** in this early phase of the reaction. During the second hour of the reaction, the ee of the solution-phase **26** approached zero and the ee of **28a** reached 50% ee, reflecting full consumption of the starting material.

This effect was suppressed considerably if, rather than use a mixture of racemic and enantiopure crystals of **26**, the starting material was prepared by mixing two enantiopure solids. Here, over the first hour there was a slow evolution of a solution-phase ee in both **26** and **28a**. At its peak **26** was enriched to 60% ee, but it was consumed by the reaction before it could reach the equilibrium value of 87%. The product ee was never enantiomerically enriched under these conditions.

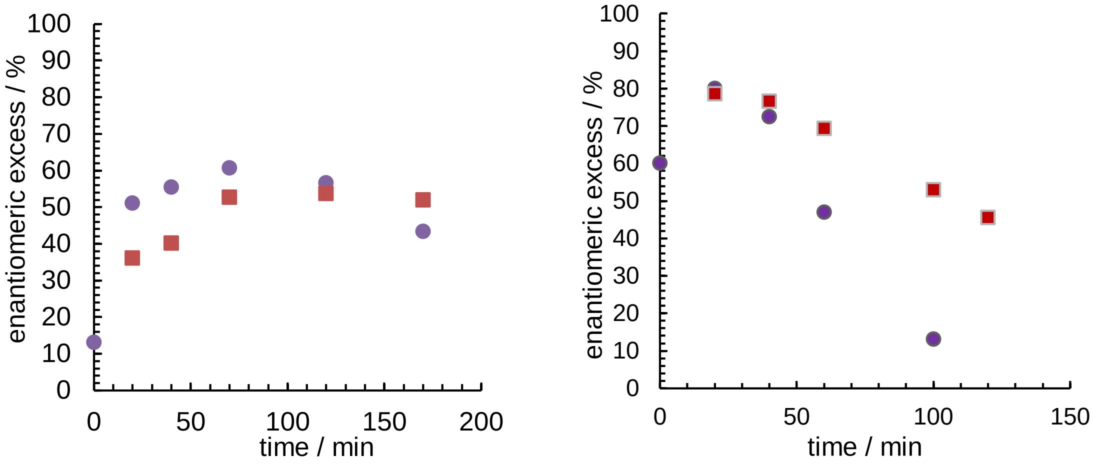

Figure 2.13. Reaction of 'kinetic conglomerates' with butyl chloroformate. Fresh suspensions of 50% ee leucine in 1 M $NaHCO_3$ were stirred rapidly with 1 eq butyl chloroformate. Left: sample prepared by mixing L and D leucine crystals. Right: sample prepared by mixing L and DL leucine crystals. Analysis of the solution phase was performed by enantioselective GC following derivatisation of filtered aliquots by ethyl chloroformate in ethanol/pyridine. ● %ee of leucine; ■ %ee of **28a**.

This is readily explained by reference to the phase behaviour of these species. Under these conditions equilibration of **26** to the eutectic composition is slower and it transiently forms a ‘kinetic conglomerate’.[50] As the two solid phases are enantiomeric they are equally soluble and transiently act like a conglomerate-forming compound. Only as the two phases equilibrate to a racemic and a homochiral solid phase will enantiomeric enrichment in the solution phase be observed. These observations together emphasise the need for these systems to be equilibrated prior to the reaction, and the transient nature of the enantiomerically-enriched product.

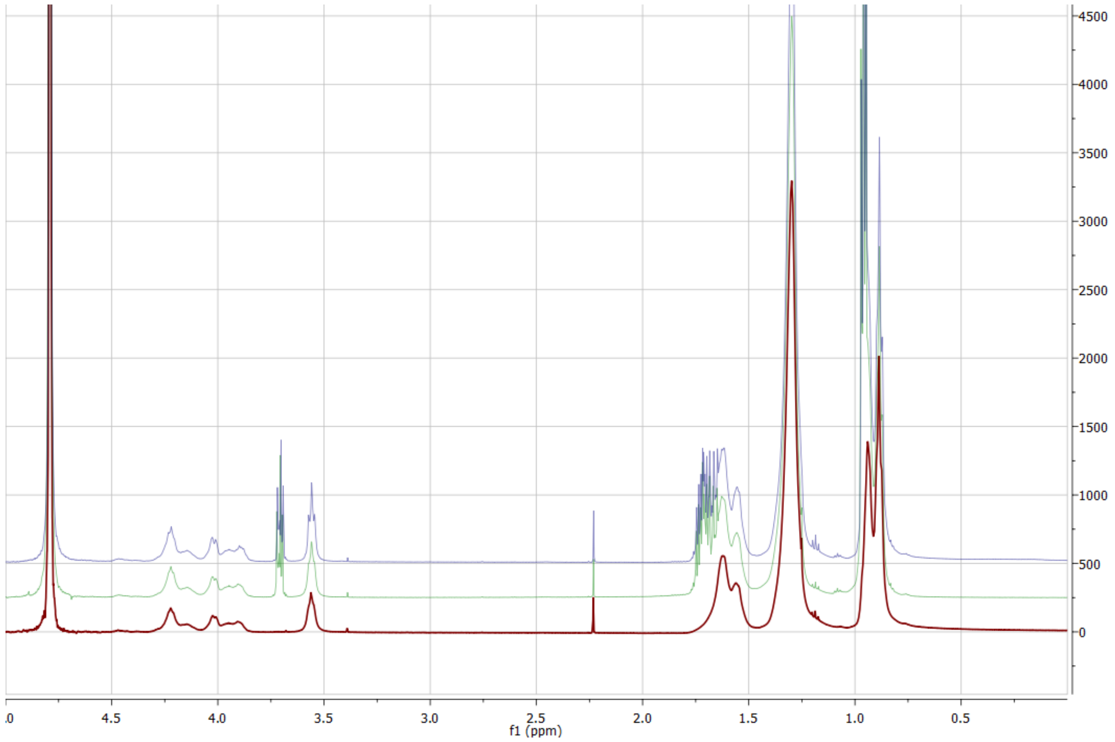

Figure 2.14. Interaction of L-28b with D and L leucine at pH 8. Red: L-**28b** (50 mM) in D_2O. Green: L-**28b** (50 mM) and D-leucine (20 mM). Blue: L-**28b** (50 mM) and L-leucine (20 mM).

Analysis of filtered solutions of **26** and micelles of L-**28b** by ^1H and DOSY NMR revealed no interaction between the derivatives and the amino acids in the solution phase (Figure 2.14, Table 2.6). The presence of **28b** altered neither the chemical shift nor the diffusion coefficient of the amino acids, indicating no intermolecular interactions between the two. Our proposed process would presumably involve favourable interactions between the amino acids and micelles of the product in the solution phase, a situation that is clearly not the case.

Experiment	**D_{Leu} / 10^{-10} m^2s^{-1}**	**D_{28b} / 10^{-10} m^2s^{-1}**
D-Leucine (20 mM)	6.2	-
D-Leucine (20 mM) + L-**28b** (50 mM)	5.5	0.57
L-Leucine (20 mM) + L-**28b** (50 mM)	5.4	0.57

Table 2.6. Diffusion coefficients of leucine and 28b. Experiments performed at pH 8. Full spectra available in the experimental section.

Reasoning that any intermolecular interactions are likely to be more favourable in organic media, we decided to move away from aqueous systems. In organic media surfactants may form reverse micelles which can self-reproduce by the same principle as aqueous micelles.[51,52] With the assistance of a visiting undergraduate student, Alexandra Bogdanova, we screened a wide variety of solvents, bases, and additives, including amino acid carbamates (Table 2.7).

In general, mixtures in apolar organic media gave poor GC traces owing to limited solubility of the amino acids. We adopted a modified derivatisation procedure in which the filtered aliquots were concentrated in vacuo prior to derivatisation with methyl chloroformate. While this procedure improved sensitivity considerably, detection remained unreliable. Here we focused on phenylalanine **29** and its benzyl and decyl *N*-carbamate derivatives **30a** and **30b** because **29** was found to be more soluble in organic media, giving more reliable GC traces than did leucine **26**.

Entry	Solvent	Base	Additive	%ee of 29
1	$CHCl_3$	DIPA	-	87, 84
2	$CHCl_3$	DIPEA	-	86, 74
3	$CHCl_3$	TBAHS	-	-
4	$CHCl_3$/acetone (9:1)	K_2CO_3	-	-
5	$CHCl_3$/acetone (4:1)	K_2CO_3	-	-
6	$CHCl_3$/acetone (1:1)	K_2CO_3	-	-
7	$CHCl_3$/acetone (1:4)	K_2CO_3	-	97
8	Acetone	K_2CO_3	-	85
9	$CHCl_3$/MeOH (19:1)	K_2CO_3	-	-
10	$CHCl_3$/MeOH (9:1)	K_2CO_3	-	-
11	$CHCl_3$/MeOH (4:1)	K_2CO_3	-	-
12	$CHCl_3$/MeOH (19:1)	K_2CO_3	-	-
13	$CHCl_3$/MeOH (19:1)	K_2CO_3	-	-
14	$CHCl_3$/MeOH (19:1)	K_2CO_3	-	-
15	$CHCl_3$/MeOH (99:1)	K_2CO_3	-	81, 40
16	DMF	K_2CO_3	-	72
17	DMSO	K_2CO_3	-	96, 94, 87
18	DMSO	DIPEA	-	92, 85, 87
19	DMSO	DIPA	-	89, 90, 94
20	DMSO	DIPA	L-**30b**	83, 83
21	DMSO	TBAHS	-	91
22	CH_2Cl_2	Et_3N	-	-
23	CH_2Cl_2	DIPEA	-	-
24	CH_2Cl_2	DIPEA	CuI	-
25	CH_2Cl_2	DIPA	-	87
26	CH_2Cl_2	DIPA (85 µL)	-	91
27	CH_2Cl_2	DIPA (850 µL)	-	88
28	CH_2Cl_2	DIPA (850 µL)	L-**30b**	85
29	CH_2Cl_2	DIPA (850 µL)	L-**30a**	-
30	CH_2Cl_2	DIPA (850 µL)	$CuSO_4$	-
31	CH_2Cl_2	DIPA (850 µL)	$MgSO_4$	-
32	CH_2Cl_2	DIPA (850 µL)	CuBr	-

Entry	**Solvent**	**Base**	**Additive**	**%ee of 29**
33	CH_2Cl_2	DIPA (850 µL)	CuI	-
34	CH_2Cl_2	DIPA	NaCl	82, 87
35	CH_2Cl_2	DIPA	NaCl + L-**30a**	89
36	CH_2Cl_2	DIPA	$ZnCl_2$	33, 21, 21
37	CH_2Cl_2	DIPA	$ZnCl_2$ + L-**30a**	46, 89
38	CH_2Cl_2	DIPA	$CuCl_2$	87, 74
39	CH_2Cl_2	DIPA	$CuCl_2$ + L-**30a**	85, 52
40	CH_2Cl_2	DIPA	ZnI_2	62, 52
41	CH_2Cl_2	DIPA	ZnI_2 + L-**30a**	99, 80
42	CH_2Cl_2	DIPA	$MgCl_2\cdot6H_2O$	30
43	CH_2Cl_2	DIPA	$MgCl_2\cdot6H_2O$ + L-**30a**	-
44	CH_2Cl_2	DIPA	$FeCl_3$	-
45	CH_2Cl_2	DIPA	$FeCl_3$ + L-**30a**	54

Table 2.7. Screen of eutectic compositions for phenylalanine. A dash indicates no phenylalanine was detected. Multiple ee values are given where experiments were reproduced.

Some of these additives did appear to influence the eutectic ee. In particular, $ZnCl_2$ and ZnI_2 seemed to reproducibly depress the solution-phase ee of **29** in CH_2Cl_2, and this appeared to be restored by the presence of L-**30a**. While these data are highly preliminary, these conditions offer a promising starting point for this work.

Unfortunately the reaction in chlorinated solvents behaved poorly. Fumes, presumably HCl, evolved upon addition of alkyl or benzyl chloroformates to suspensions of **29** in CH_2Cl_2 or $CHCl_3$, and little to no product was formed. Slow addition of the chloroformate and the use of excess base to neutralise any acid (as in entries 27-33) did not improve this. The poor reactivity is likely the result of the low solubility of the amino acid in organic media, leading to hydrolysis of the chloroformate by residual water in the mixture.

Future work on this project will need to identify suitable conditions for this reaction. With these in hand, the reaction under the conditions in entries 36 and 40 ought to be performed and the evolution of ee over time measured in the presence and absence of L-**30a** and L-**30b**. The use of sub-stoichiometric quantities of the chloroformate may allow the observation of a transient amplification of ee induced by the formation of product in the reaction.

2.7. Towards self-reproducing vesicles

In parallel with efforts to develop self-reproducing micelles we designed a number of substrates intended to yield self-reproducing vesicles. We aimed to develop three-component reactions in which two hydrophobic molecules add to a single hydrophilic molecule to give a two-tailed surfactant. Unfortunately, this work has been hindered by the difficulty of synthesising these compounds.

The substrates we designed can be grouped into three general classes which will be discussed in turn. Firstly, derivatives of *sn*-glycero-3-phosphocholine **31** bearing two identical esters. Secondly, derivatives of 1-palmitoyl-*sn*-glycero-3-phosphocholine **32** bearing a reactive ester at the 2-position. Thirdly, phosphocholine derivatives analogous to those described in section 2.3, in which a single group capable of undergoing double addition is present.

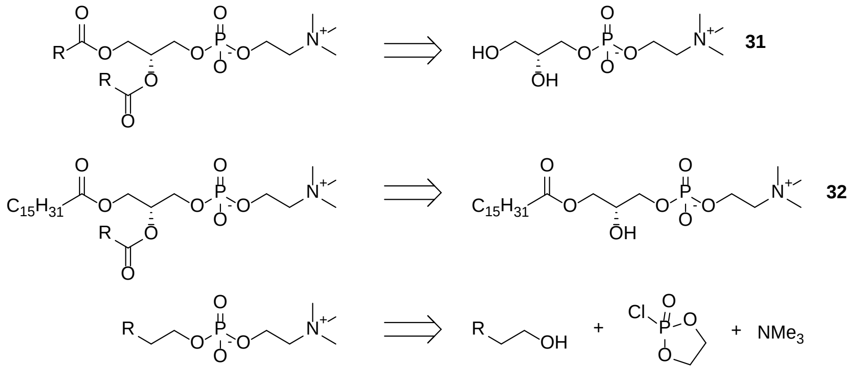

Scheme 2.9. Retrosynthesis of proposed classes of precursors to vesicle-forming compounds.

We focused on synthesising compounds bearing Michael acceptors to be used in thiol-ene reactions. However, we also attempted to synthesise compounds bearing alkynes, to be used in either photochemical thiol-yne reactions or CuAAC reactions.

2.7.1. Homo-diesters

Our initial synthetic approach to these compounds involved direct Steglich esterification of diol **31** with a variety of acids. Here our starting materials were either *rac*-**31**, or the $CdCl_2$ complex of enantiopure **31**. At this stage we were not concerned with stereochemistry, and thus for simplicity this distinction will be neglected in the following discussion.

Diol **31** is poorly soluble in solvents other than water. We examined several methods of circumventing this. Firstly, a mixture of DMSO and CH_2Cl_2 can be used;[53] while this did yield **33**, we found that the work-up procedure inadequately removed the DMSO, which lead to unreliable chromatography procedures.

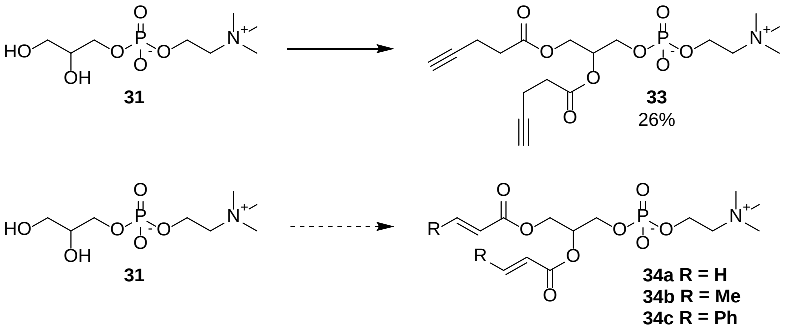

Scheme 2.10. Synthesis of dual Michael acceptors. Conditions are discussed in the text.

Using a complex of **31** and tetraphenylborate in pyridine[54] allowed **33** to be obtained in low yield after two rounds of column chromatography. The best procedure involved using the $CdCl_2$ complex of **31**, which is soluble in $CHCl_3$,[55] and allowed for simpler, more reliable purification of **34** than when DMSO or tetraphenylborate were used. Nonetheless, this was complicated by removal of side-products and unreacted starting material. The use of acid anhydrides[56] offered no consistent improvement. Consequently we were unable to obtain **33** in greater than 90% purity. Given the sensitivity of amphiphiles to additives and contaminants, this was not acceptable for our purposes.

Attempts to synthesise **34a** failed owing to the formation of an unidentified yellow precipitate upon the addition of acryoyl chloride or anhydride to complexes of **31** as before. The use of acrylic acid and a carbodiimide coupling reagent led to slow formation of the yellow precipitate, and again, no product by TLC or NMR. This may indicate polymerisation of the acrylate. The use of more stable crotonoyl and cinnamoyl chlorides gave better results, but as before, **34b** and **34c** could not be adequately purified.

Given the lessons learned from the study of two-component reactions (section 2.3), we opted not to develop this synthetic route further in favour of synthesising the analogous maleimide-containing compound **35**. We anticipated that compounds **34a-c** would require harsh conditions to react, leading to wasteful degradation of the valuable starting material and potentially adverse effects on vesicle formation arising from the high ionic strength of the medium. Further **34b** and **34c** can be expected to be less reactive than **34a** or **1**, exacerbating the problem. Additionally, as compound **33** could not be isolated in pure form we did not study its reaction with alkyl azides.

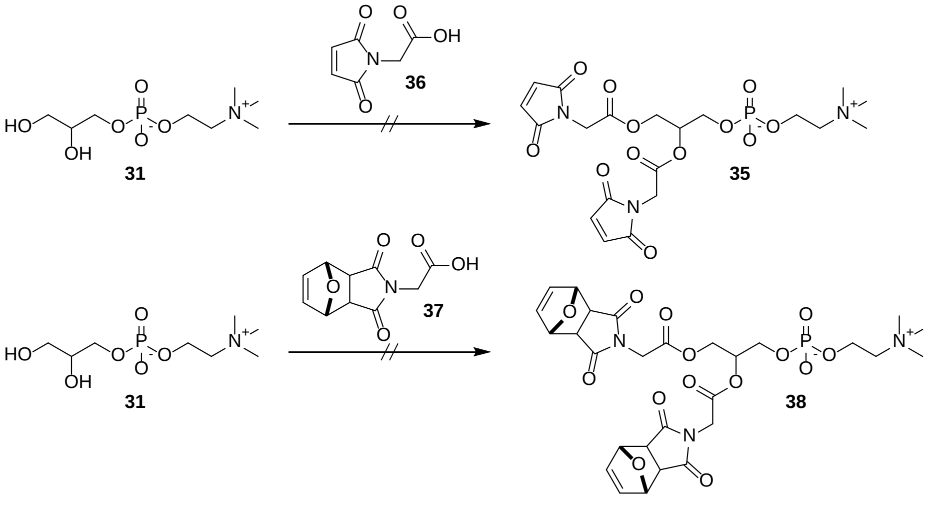

Scheme 2.11. Failed synthetic approach to compound 35.

Initial attempts to synthesise the di-maleimide **35** began by using the same approach, coupling **31** to acids **36** or **37**. Again, solubility and stability problems led to failure. Esterification of the unprotected maleimide **36** invariably led to complete hydrolysis of the maleimide and no product formation, despite efforts to exclude all sources of moisture including freeze-drying all reagents prior to use and including molecular sieves in the reaction. Esterification with protected maleimide **37** failed owing to the insolubility of this compound in chlorinated solvents.

We therefore attempted an alternative retrosynthetic strategy analogous to that used for the synthesis of **9**. Our intended route consisted of protecting a terminal hydroxyl group in glycerol as a TBDMS ether and esterifying both remaining hydroxyl groups with either **36** or **37**, followed by deprotection of the silyl group and addition of the phosphocholine head as before (section 2.4.1). However, as before the instability of **36** towards hydrolysis and the insolubility of **37** limited the success of this approach. Esterification with **36** again led to complete hydrolysis of the maleimide, while reactions with **37** gave unreliable yields. Fortunately, **40** is accessible by defuranylation of **41**, allowing access to both compounds.

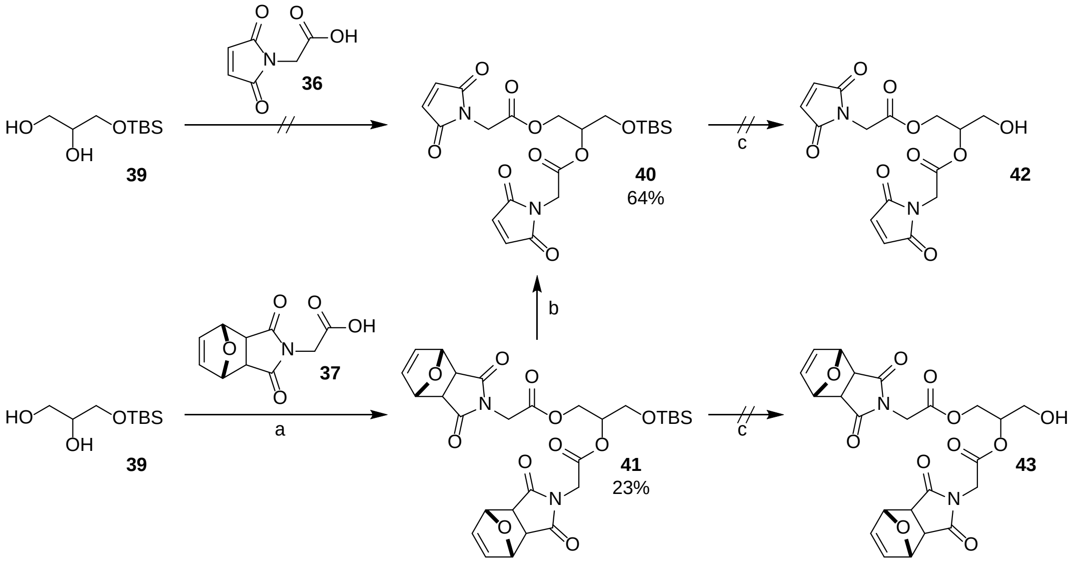

Scheme 2.12. Towards compound 35. (a) EDCI, DMAP, CH_2Cl_2, 0 °C to rt; (b) toluene, reflux; (c) see Table 2.8.

Nonetheless **40** and **41** were obtained in sufficient quantities to attempt to remove the silyl group. All attempts to perform this step (Table 2.8) led to the formation of an unidentified product which was not either **42** or **43**. Despite the difficulties in this synthetic route, it is clearly promising and worth pursuing further.

Reagent	**Conditions**	**Result**
40	TBAF, THF	Hydrolysis of **40**
40	Acetyl chloride, MeOH	Degradation
40	*p*-TsOH, CH_2Cl_2, MeOH	Degradation
41	TBAF, THF	Degradation
41	Acetyl chloride, MeOH	Degradation
41	*p*-TsOH, CH_2Cl_2, MeOH	Degradation

Table 2.8. Desilylation conditions.

2.7.2. Hetero-diesters

We attempted to synthesise compounds in which the 1-position bears a palmitoate ester, and the 2-position a functional ester. This was inspired by work reported by Budin and Devaraj, who reported a micelle-to-vesicle transition driven by the CuAAC reaction of **44** and oleyl azide **45** (Scheme 2.13).[57] These authors did not explicitly consider autocatalytic effects in their system. We attempted to synthesise **44** in order to more directly address this question, and develop an analogous thiol-ene system using compound **47**. We hoped that studying these systems would provide useful insight and experience for the development of three-component reactions.

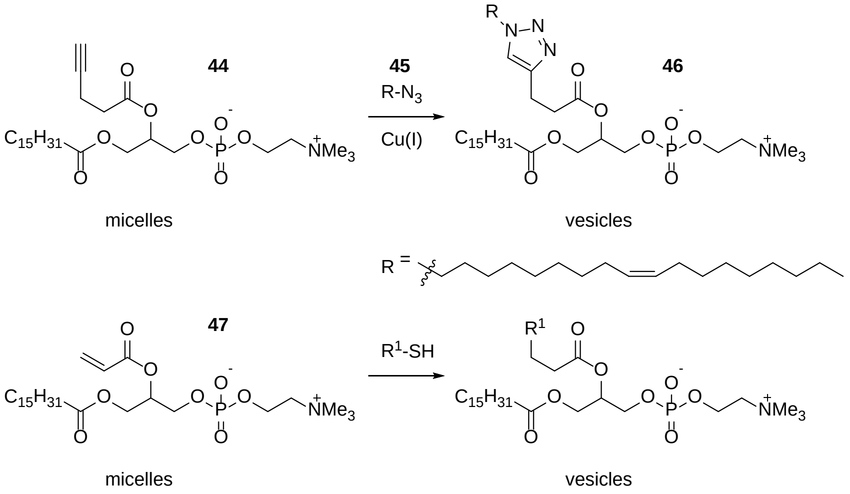

Scheme 2.13. Micelle-to-vesicle transition described by Budin and Devaraj (top) and a proposed thiol-ene analogue (bottom).

While Budin and Devaraj obtained **44** by the direct esterification of commercial **32**, we had to synthesise **32** ourselves owing to its high cost. As before, the large difference in solubility between diol **31** and palmitoic acid posed difficulties in the synthesis. Further, regioselectivity was a significant challenge: monoesters of 1,2-diols can readily migrate intramolecularly, producing the undesired regioisomer.

To bypass these problems we first synthesised **32** regioselectively using conditions developed by Fasoli et al.[58] By ^{1}H NMR we observed none of the undesired 2-palmitoyl regioisomer. Under the conditions used by Budin and Devaraj to synthesise **44** from **32**, we could not adequately separate the product from the residual starting material and the reaction by-products in one round of chromatography. After two rounds of chromatography we obtained only 23% yield of **44** which was contaminated with residual DMAP. We therefore examined an alternative reaction[56] using 4-pentynoic anhydride as an acylating reagent, which gave clean **44** after one round of chromatography.

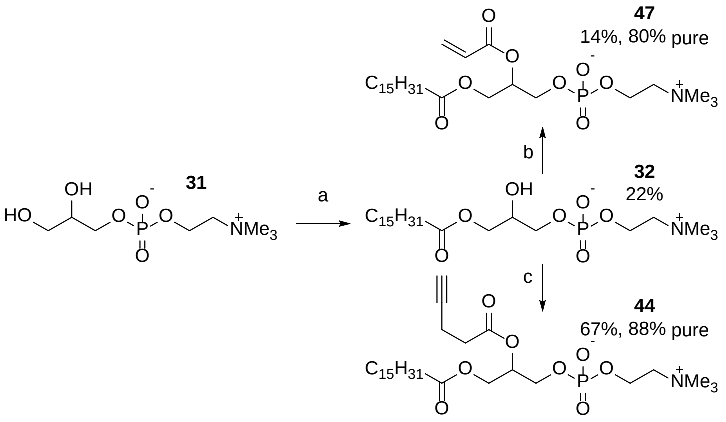

Scheme 2.14. Synthesis of micelle-to-vesicle precursors. (a) i) Dibutyltin oxide, isopropanol, 85°C; ii) palmitoyl chloride, Et_3N, isopropanol; (b) Acryloyl chloride, Et_3N, DMAP, $CHCl_3$; (c) 4-pentynoic anhydride, DMAP, CH_2Cl_2.

We consistently found that formation of **44** was accompanied by 10-15% (by ^1H NMR spectroscopy) of the 1-pentynoyl-2-palmitoyl regioisomer, which would arise from acyl transfer within **32**. This compound coelutes with **44** and was not reported by Budin and Devaraj. The 1-hydroxy-2-palmitoyl isomer was not detected in the spectrum of **32**. Based on the extensive characterisation of ^1H NMR spectra of compounds analogous to **44** by D'Arrigo et al.,[56] we are confident that the major product is the desired regioisomer.

We acylated **32** with acryloyl chloride using a known procedure.[59] As with the attempted synthesis of **35a** (Section 2.6), we found that upon the addition of acryloyl chloride, an insoluble yellow precipitate formed. After two rounds of column chromatography **47** was obtained in 17% yield. As with **45**, the ^1H NMR spectrum suggested the presence of approximately 20% of the regioisomeric ester. The relative success of this reaction compared to the synthesis of **35a** is likely attributable to the higher solubility of **32** than **31**.

Again, by comparison with the data reported by D'Arrigo et al.[56] we are confident that the major product is **47**. However, the two regioisomers could not be separated by column chromatography. Given the difficulties in synthesising and purifying these compounds, this project was not yet able to move forward. If the yield and purity of **47** can be improved to satisfactory levels, however, a thiol-ene micelle-to-vesicle transition analogous to that described by Budin and Devaraj ought to be within reach.

2.7.3. Dual addition substrates

As an alternative to using lipid precursors bearing two functional groups, we designed a substrate capable of undergoing two sequential additions to a single functional group. Alkyne **49** was easily synthesised from pentynoic acid in two steps, giving pure **49** in acceptable yield. This compound is a suitable precursor for sequential photochemical additions of thiols.

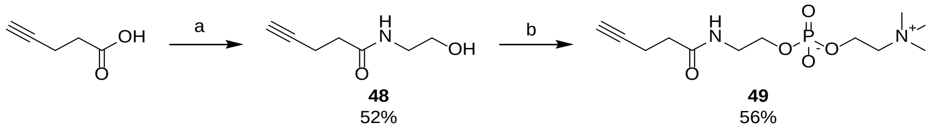

Scheme 2.15. Synthesis of dual addition substrate 49. (a) DCC, NHS, THF, then ethanolamine; (b) i. 2-chloro 1,3,2-dioxaphospholane 2-oxide, Et_3N, THF, 0 °C to rt; ii. trimethylamine, MeCN, heated in sealed vessel, 18 h.

Photochemical thiol-yne or thiol-ene reactions in water have been reported both using radical initiators[60,61] and in their absence.[62] A screen of a variety of photochemical reaction conditions between **49** and various thiols gave no conversion. The use of photoinitiators or a high-powered 254 nm mercury lamp did not lead to addition. In the latter case these intense conditions led to some decomposition of **49** to a more polar product.

Thiol	Additives	Wavelength	Result
Butanethiol (1 eq)	-	350 nm	No conversion.
Butanethiol (10 eq)	-	350 nm	No conversion.
Decanethiol (1 eq)	-	350 nm	No conversion.
Decanethiol (10 eq)	-	350 nm	No conversion.
Butanethiol (10 eq)	SDS (40 mM)	350 nm	No conversion.
Butanethiol (10 eq)	-	254 nm	Decomposition.
Decanethiol (5 eq)	-	254 nm	Decomposition.
Decanethiol (10 eq)	-	254 nm	Decomposition.
Decanethiol (10 eq)	$Ru(bpy)_3(PF_6)_2$ (1 mol%), *p*-toluidine (50 mol%)	Visible light	No conversion.
Decanethiol (20 eq)	$Ru(bpy)_3(PF_6)_2$ (1 mol%), *p*-toluidine (50 mol%)	Visible light	No conversion.
Hexanethiol (4 eq)	$Ru(bpz)_3(PF_6)_2$ (1 mol%), *p*-toluidine (50 mol%)	Visible light	No conversion.
Decanethiol (10 eq)	Michler's ketone (1 mol%)	350 nm	No conversion.
Decanethiol (10 eq)	4-dimethylamino benzophenone (1 mol%)	350 nm	No conversion.

Table 2.9. Screen of thiol-yne reaction conditions. Conditions: **49** (500 mM) in degassed H_2O under rapid stirring. Reactions were monitored for at least 24 hours.

Following completion of this work, Devaraj and co-workers reported the successful photochemical thiol-yne reaction of a very similar compound to **49** using 2,2-dimethoxy-2-phenylacetophenone (DMPA) as a radical initiator under irradiation at 354 nm.[63] This reaction worked well in DMF, but in water was sluggish and lead mostly to oxidation of the thiol. The reaction in water only proceeded when seeded with vesicles of DPPC to solubilise the thiol in the aqueous phase. These observations serve to highlight the challenges associated with the development of physical autocatalytic reactions and perhaps to explain the failure of our screen to identify suitable reaction conditions for this reaction and indeed others, including the CuAAC reactions described earlier (section 2.5).

2.8. Conclusion

The work described here achieved the stated goal of demonstrating self-reproducing micelles driven by irreversible bond-forming reactions. These reactions can proceed under mild conditions compatible with other systems that may be incorporated into protocell models. The use of more complex reactions involving bond formation driven by photochemistry or a secondary catalytic cycle appears to be more challenging and may require the presence of pre-formed micelles or vesicles to proceed. In general, these reactions are highly sensitive to many physical parameters and tend to yield kinetic profiles that are only qualitatively reproducible, making detailed kinetic study challenging.

The novel systems developed here will form the conceptual basis for experimental demonstrations of competition and selection between physical autocatalysts, an almost untouched area of experimental chemistry (see Chapter 4). As such this work contributes significantly to the future study of autocatalysis as a fundamental class of chemical reaction.

2.9. References

1 A. J. Bissette, B. Odell and S. P. Fletcher, *Nat. Commun.*, 2014, **5**, 4607.

2 R. G. Laughlin, *Colloids Surfaces A Physicochem. Eng. Asp.*, 1997, **128**, 27–38.

3 P. A. Bachmann, P. L. Luisi and J. Lang, *Nature*, 1992, **357**, 57–59.

4 R. Nguyen, L. Allouche, E. Buhler and N. Giuseppone, *Angew. Chem. Int. Ed.*, 2009, **48**, 1093–1096.

5 K. Kurihara, M. Tamura, K. Shohda, T. Toyota, K. Suzuki and T. Sugawara, *Nat. Chem.*, 2011, **3**, 775–781.

6 T. F. Zhu and J. W. Szostak, *J. Am. Chem. Soc.*, 2009, **131**, 5705–5713.

7 H. Takahashi, Y. Kageyama, K. Kurihara, K. Takakura, S. Murata and T. Sugawara, *Chem. Commun.*, 2010, **46**, 8791–8793.

8 R. Wick, P. Walde and P. L. Luisi, *J. Am. Chem. Soc.*, 1995, **117**, 1435–1436.

9 P. Walde, R. Wick, M. Fresta, A. Mangone and P. L. Luisi, *J. Am. Chem. Soc.*, 1994, **116**, 11649–11654.

10 D. Segré, D. Ben-Eli, D. W. Deamer and D. Lancet, *Orig. Life Evol. B.*, 2001, **31**, 119–145.

11 D. Segré, D. Lancet, O. Kedem and Y. Pilpel, *Orig. Life Evol. B.*, 1998, **28**, 501–514.

12 C. H. Hoyle and C. N. Bowman, *Angew. Chem. Int. Ed.*, 2010, **49**, 1540–1573.

13 R. Matsuno, K. Takami and K. Ishihara, *Langmuir*, 2010, **26**, 13028–32.

14 T. Buhse, R. Nagarajan, D. Lavabre and J. C. Micheau, *J. Phys. Chem. A*, 1997, **101**, 3910–3917.

15 A. J. Bissette and S. P. Fletcher, *Angew. Chem. Int. Ed.*, 2013, **52**, 12800–12826.

16 D. G. Blackmond, *Angew. Chem. Int. Ed.*, 2009, **48**, 386–390.

17 M. P. Mower and D. G. Blackmond, *J. Am. Chem. Soc.*, 2015.

18 T. D. W. Claridge, *High-Resolution NMR Techniques in Organic Chemistry*, Elsevier Science, 2nd Editio., 2004.

19 T. C. Wong, in *Encyclopedia of Surface and Colloid Science*, ed. P. Somasundaran, CRC Press, 2nd Editio., 2006, pp. 3738–3756.

20 T. Buhse, D. Lavabre, R. Nagarajan and J. C. Micheau, *J. Phys. Chem. A*, 1998, **102**, 10552–10559.

21 P. L. Luisi and F. J. Varela, *Orig. Life Evol. B.*, 1989, **19**, 633–643.

22 P. Stilbs, *J. Colloid Interface Sci.*, 1981, **80**, 608–610.

23 Y. Takaoka, A. Ojida and I. Hamachi, *Angew. Chem. Int. Ed.*, 2013, **52**, 4088–106.

24 S. D. Fontaine, R. Reid, L. Robinson, G. W. Ashley and D. V Santi, *Bioconjug. Chem.*, 2015, **26**, 145–52.

25 W. H. Heath, F. Palmieri, J. R. Adams, B. K. Long, J. Chute, T. W. Holcombe, S. Zieren, M. J. Truitt, J. L. White and C. G. Willson, *Macromolecules*, 2008, **41**, 719–726.

26 B. A. Rosenzweig, N. T. Ross, D. M. Tagore, J. Jayawickramarajah, I. Saraogi and A. D. Hamilton, *J. Am. Chem. Soc.*, 2009, **131**, 5020–5021.

27 R. J. Pearson, E. Kassianidis, A. M. Z. Slawin and D. Philp, *Org. Biomol. Chem.*, 2004, **2**, 3434–3441.

28 S. Matsui and H. Aida, *J. Chem. Soc. Perkin Trans. 2*, 1978, 1277.

29 V. V Rostovtsev, L. G. Green, V. V Fokin and K. B. Sharpless, *Angew. Chem. Int. Ed.*, 2002, **41**, 2596–2599.

30 V. Hong, S. I. Presolski, C. Ma and M. G. Finn, *Angew. Chem. Int. Ed.*, 2009, **48**, 9879–9883.

31 E. Mahon, M. Barboiu and T. Aastrup, *Chem. Commun.*, 2010, **46**, 2441–2443.

32 V. Neto, R. Granet and P. Krausz, *Tetrahedron*, 2010, **66**, 4633–4646.

33 R. A. Akula, D. P. Temelkoff, N. D. Artis and P. Norris, *Heterocycles*, 2004, **63**, 2719–2726.

34 A. Chattopadhyay and E. London, *Anal. Biochem.*, 1984, **139**, 408–412.

35 C. Shao, X. Wang, Q. Zhang, S. Luo, J. Zhao and Y. Hu, *J. Org. Chem.*, 2011, **76**, 6832–6836.
36 A. Baron, Y. Blériot, M. Sollogoub and B. Vauzeilles, *Org. Biomol. Chem.*, 2008, **6**, 1898–1901.
37 A. J. M. Howden, V. Geoghegan, K. Katsch, G. Efstathiou, B. Bhushan, O. Boutureira, B. Thomas, D. C. Trudgian, B. M. Kessler, D. C. Dieterich, B. G. Davis and O. Acuto, *Nat. Methods*, 2013, **10**, 343–6.
38 D. A. Singleton and L. K. Vo, *J. Am. Chem. Soc.*, 2002, **124**, 10010–10011.
39 I. D. Gridnev, J. M. Serafimov, H. Quiney and J. M. Brown, *Org. Biomol. Chem.*, 2003, **1**, 3811–3819.
40 K. Soai, I. Sato, T. Shibata, S. Komiya, M. Hayashi, Y. Matsueda, H. Imamura, T. Hayase, H. Morioka, H. Tabira, J. Yamamoto and Y. Kowata, *Tetrahedron-Asymmetry*, 2003, **14**, 185–188.
41 D. G. Blackmond, C. R. McMillan, S. Ramdeehul, A. Schorm and J. M. Brown, *J. Am. Chem. Soc.*, 2001, **123**, 10103–10104.
42 T. Gehring, M. Busch, M. Schlageter and D. Weingand, *Chirality*, 2010, **22**, E173–E182.
43 K. Soai, T. Shibata, H. Morioka and K. Choji, *Nature*, 1995, **378**, 767–768.
44 K. Soai and T. Kawasaki, *AIP Conf. Proc.*, 2008, **979**, 68–79.
45 T. Shibata, J. Yamamoto, N. Matsumoto, S. Yonekubo, S. Osanai and K. Soai, *J. Am. Chem. Soc.*, 1998, **120**, 12157–12158.
46 T. Kawasaki, Y. Matsumura, T. Tsutsumi, K. Suzuki, M. Ito and K. Soai, *Science*, 2009, **324**, 492–495.
47 M. Klussmann, H. Iwamura, S. P. Mathew, D. H. Wells, U. Pandya, A. Armstrong and D. G. Blackmond, *Nature*, 2006, **441**, 621–3.
48 M. Klussmann, T. Izumi, A. J. P. White, A. Armstrong and D. G. Blackmond, *J. Am. Chem. Soc.*, 2007, **129**, 7657–60.
49 P. Hušek, *J. Chromatogr. A*, 1991, **552**, 289–299.
50 M. Klussmann, S. P. Mathew, H. Iwamura, D. H. Wells, A. Armstrong and D. G. Blackmond, *Angew. Chem. Int. Ed.*, 2006, **45**, 7989–92.
51 P. A. Bachmann, P. L. Luisi and J. Lang, *Chimia (Aarau).*, 1991, **45**, 266–268.
52 P. A. Bachmann, P. Walde, P. L. Luisi and J. Lang, *J. Am. Chem. Soc.*, 1990, **112**, 8201–8203.
53 M. R. Jorgensen, Y. Bhurruth-Alcor, T. Røst, P. Bohov, M. Müller, C. Guisado, K. Kostarelos, E. Dyrøy, R. K. Berge, A. D. Miller and J. Skorve, *J. Med. Chem.*, 2009, **52**, 1172–1179.
54 Z. Huang, M. R. Jaafari and F. C. Szoka Jr., *Angew. Chem. Int. Ed.*, 2009, **48**, 4146–4149.
55 F. M. Menger, M. G. Wood, S. Richardson, Q. Zhou, A. R. Elrington and M. J. Sherrod, *J. Am. Chem. Soc.*, 1988, **110**, 6797–6803.
56 P. D’Arrigo, A. Mele, C. Rossi, D. Tessaro and S. Servi, *J. Am. Oil Chem. Soc.*, 2008, **85**, 1005–1011.
57 I. Budin and N. K. Devaraj, *J. Am. Chem. Soc.*, 2012, **134**, 751–753.
58 E. Fasoli, A. Arnone, A. Caligiuri, P. Paola D’Arrigo, L. de Ferra and S. Servi, *Org. Biomol. Chem.*, 2006, **4**, 2974–2978.
59 I. A. Gorodetskaya, T.-L. Choi and R. H. Grubbs, *J. Am. Chem. Soc.*, 2007, **129**, 12672–12673.
60 E. L. Tyson, M. S. Ament and T. P. Yoon, *J. Org. Chem.*, 2013, **78**, 2046–50.
61 E. L. Tyson, Z. L. Niemeyer and T. P. Yoon, *J. Org. Chem.*, 2014, **79**, 1427–36.
62 A. B. Lowe, *Polymer (Guildf).*, 2014, **55**, 5517–5549.
63 C. Y. Zhou, H. Wu and N. K. Devaraj, *Chem. Sci.*, 2015, **6**, 4365–4372.

Chapter 3

Direct observation of physical autocatalysis by interferometric scattering microscopy

3. Direct observation of physical autocatalysis by iSCAT.

3.1. Overview

This chapter describes the application of ultra-high resolution microscopy to autocatalytic systems. Through the analysis of physical autocatalysis on the single-particle level, the complex dynamics of these reactions are revealed with remarkable sensitivity.

The work in this chapter was undertaken in collaboration with Jaime Ortega-Arroyo (JAO), who provided training and support in the use of the iSCAT instrument and data analysis software. The iSCAT experiments described in sections 3.3.2 and 3.3.4 were carried out in collaboration with JAO. All quantitative analysis was performed by, or using software written by, JAO.

3.2. Introduction

Physical autocatalysis offers a prebiotically-relevant route from simple molecules to large, catalytically-active aggregates. The dynamic behaviours of the products of physical autocatalysis, micelles and vesicles, have been studied for decades. Nonetheless, many important aspects of these systems remain poorly understood, such as the factors controlling the growth and division of vesicles.[1,2]

More comprehensive studies of physical autocatalysis are hindered by technological hurdles. The method of choice varies with the system under investigation: giant vesicles ($R_H > 1$ µm) have been studied using optical and fluorescence microscopy,[3,4] while smaller vesicles ($R_H < 1$ µm, hereafter simply called vesicles) and micelles are typically studied using ensemble methods owing to their small size. Techniques used to study sub-micron systems include NMR,[5] HPLC,[6] FRET,[7] DLS,[8] and ESR.[9,10] Studies of all of the above have been complemented by the use of electron microscopy (EM),[11–15] which has allowed direct analysis of individual vesicles to determine, for example, size distributions and to distinguish between newly-formed and pre-existing vesicles using labels.

This brief survey highlights a major hurdle for the study of sub-micron systems: the lack of direct, single-particle, real-time methods. While the division of individual giant vesicles has been directly observed in real time using optical microscopy,[3] the dynamics of sub-micron micelles and vesicles must be inferred from ensemble data or disruptive EM. The latter remains the most important direct method used to analyse sub-micron vesicles, but is highly disruptive, typically involving the rapid freezing of samples[16] and occasionally the use of labels such as ferritin.[11,12] While EM provides exquisitely detailed images of individual micelles and vesicles, it necessarily precludes any observation of the dynamics of these systems. At best, researchers have been able to capture intermediate states and infer dynamics from there.[14]

More recently, super-resolution techniques exploiting single-molecule fluorescence have become increasingly important. Indeed, these methods were recognised with the Nobel Prize in Chemistry 2014. While super-resolution fluorescence microscopy is widespread in the biological and biomedical sciences,[17] and has been used to study vesicles and other lipid aggregates in that context,[18] to our knowledge they have not yet been applied to physical autocatalysts and related systems. Despite the undoubted importance of these techniques, they are limited in several ways. Most immediately the need for a fluorescence label inherently limits the duration and time resolution of these experiments, as repeated measurement eventually leads to photobleaching and loss of signal.[19] Further, the presence of a fluorescent label may disrupt the dynamics of lipid systems. These features may limit the success of fluorescence-based super-resolution techniques in the study of physical autocatalysis on the nanometre scale.

The ability to directly observe the dynamics of individual micelles and vesicles in real time without the need for labels, which might perturb the system or limit the experimental conditions, would be enormously beneficial. Beyond simply obtaining intuitively appealing videos of vesicle growth and division, this would directly reveal the individual and collective behaviour of autocatalytic systems in unprecedented detail. Studies of this kind would offer a valuable complement to ensemble techniques and EM and provide valuable insight into the behaviour of physical autocatalysts. Developing more comprehensive models of these systems would, in turn, aid the development of novel protocellular systems and improve our understanding of the self-reproduction of prebiotic systems.

Interferometric scattering microscopy (iSCAT) is a powerful technique that allows the imaging of single nanoscopic objects in situ in real time.[20] No complex sample preparation or labelling is required, and scatterers as small as individual proteins in solution can be detected directly.[21,22] By avoiding the need for labels or disruptive sample preparation, iSCAT is able to probe the dynamics of complex systems natively in real time. It has previously been used to study the rearrangement of phospholipid vesicles on a surface into a supported bilayer, validating previous theoretical and indirect experimental work in a compelling and intuitive way.[23]

iSCAT is therefore a highly promising technique for the study of physical autocatalysis on the single-particle level. This chapter describes the first investigations of physical autocatalysis and prebiotic systems by iSCAT.

3.2.1. Principles of iSCAT

The iSCAT experiment relies on the scattering of light by nanoscopic particles in solution or on a surface (Figure 3.1).[20,22] The solution to be analysed is deposited on a glass coverslip placed above a microscope objective, and a light beam is passed through the sample from below. At the glass-water interface 0.5% of this light is reflected back and collected. Where the light passing through the sample encounters a nanoscopic particle some of that light is scattered back towards the source and a portion of this is collected.

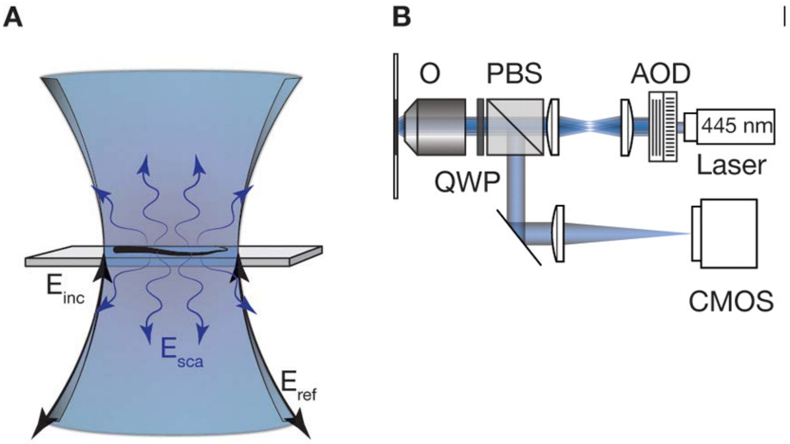

Figure 3.1. The iSCAT experiment. (A) Illustration of the sample region. E_{inc}, incident light field; E_{ref}, reflected light field; E_{sca}, scattered light field. **(B)** Instrument schematic. O, objective; QWP, quarter wave plate; PBS, polarizing beam splitter; AOD, acousto-optic deflector. Reproduced from [21] with permission**.**

By comparing the scattered light with the reference light field provided by reflection from the glass-water interface, the intensity and location of scattering events can be reconstructed. With appropriate processing this provides an intuitive image of particles on or near the surface of the coverslip. The intensity of detected light is determined by equation (3.1):

$$I_{det} = |E_i|^2\{r^2 + |s|^2 - 2r|s|\sin\theta\} \tag{3.1}$$

Where E_i is the incident light field amplitude, r is the reflectivity of the interface, s is the scattering amplitude, and θ is the combination of the scattering phase and the phase of the reflected light field.

The three terms of the equation correspond to contributions from the reflected light field, light scattered by particles, and interference. For small (< 50 nm) particles, $|s|^2$ is negligible and thus the interference term $2r|s|\sin\theta$ dominates. Consequently the signal contrast becomes proportional to $|s|$ (equation 3.2):

$$\frac{I_{particle}}{I_{background}} = 1 - \frac{2r|s|\sin\theta}{r^2} \tag{3.2}$$

Where $I_{particle}$ and $I_{background}$ are the intensities of a scattering particle and the background field, respectively.

This offers a crucial advantage over comparable dark-field techniques which measure the pure scattering of photons by particles, given by $|s|^2$. The scattering amplitude s is proportional to the particle volume and hence to D^3, where D is the particle diameter. As a result of equations 3.1 and 3.2, iSCAT has a lower size dependence (D^3) than pure scattering techniques (D^6), allowing the detection of very small particles or even single molecules.

In short, the iSCAT experiment relies on the collection of all light that is reflected or scattered back towards the source. In the absence of any scattering particles, the detected light is simply a uniform light field. Where particles scatter light, a ‘shadow’ in this field is seen, with a contrast relative to the background that is proportional to the particle volume.

3.2.2. Data processing and interpretation

After processing iSCAT yields images and videos that are for the most part intuitive. A general understanding of how the data are processed significantly aids interpretation, and an overview is provided here. All data in this chapter were processed using software developed in-house by members of the Kukura group and the FIJI distribution of ImageJ (http://fiji.sc/Fiji). The emphasis here is on providing general insight into how data were processed rather than detailed descriptions of the methods used. The figures used here to illustrate each step depict data from section 3.3 consisting simply of micelles binding to the iSCAT coverslip.

As a result of equation (3.1), iSCAT signals are observed as dark (negative contrast) spots on a light background. As particles increase in size the scattering term $|s|^2$ comes to dominate the interference term in equation (3.1), and thus the signals begin to appear as light spots. The particle size required for this inversion of contrast to occur depends on the refractive index of the particles.

Particles of sizes smaller than the diffraction limit all appear as diffraction-limited spots. Thus a 5 nm and 10 nm micelle will both occupy the same number of pixels. The true size of such particles can be distinguished by examining the intensity of the spots, or rather, the contrast between the spots and the background field. This is reflected in the *z*-scale bars below each figure in this chapter. The values on the *z*-scale bar represent the contrast required for a spot to be saturated.

Background noise and artefacts arise from several sources, but these are routinely removed during both data acquisition and subsequent processing. First, undesired reflections within the optical apparatus and inhomogeneities in the illumination field add a constant artefact to the image which entirely overwhelms the signal from small scatters (Figure 3.2A). This is easily subtracted using a median filter,[24] and the result is referred to here as the *flat field image*. The median filter involves recording a series of images while moving the sample laterally across the camera. The time average of these images yields an image consisting of any artefacts that are independent of the sample. Dividing subsequent images by this flat field image thus removes any such artefacts (Figure 3.2 B,C). As can be seen in Figure 3.2 the application of a median filter reduces the contrast by orders of magnitude, allowing the nanoscopic roughness of the glass surface to be imaged. A median filter is applied to all images in this chapter.

Large artefacts may appear as a result of secondary reflections from interfaces above the glass-water interface, most commonly the air-water interface. These reflections create a pattern of parallel bands called fringes that can overwhelm the small signal from the sample particles without appropriate processing. These fringes and other non-static artefacts that are much larger than typical particles of interest can be removed by applying a pseudo-flat field, termed here a *size filter*. This consists of a band pass filter which removes large features while retaining the smaller features of interest. By dividing the raw or flat field image by the size filtered image, images can be obtained in which the principle source of background noise is the shot noise of the light source – that is, the intrinsic variation in the photon flux reaching the detector.

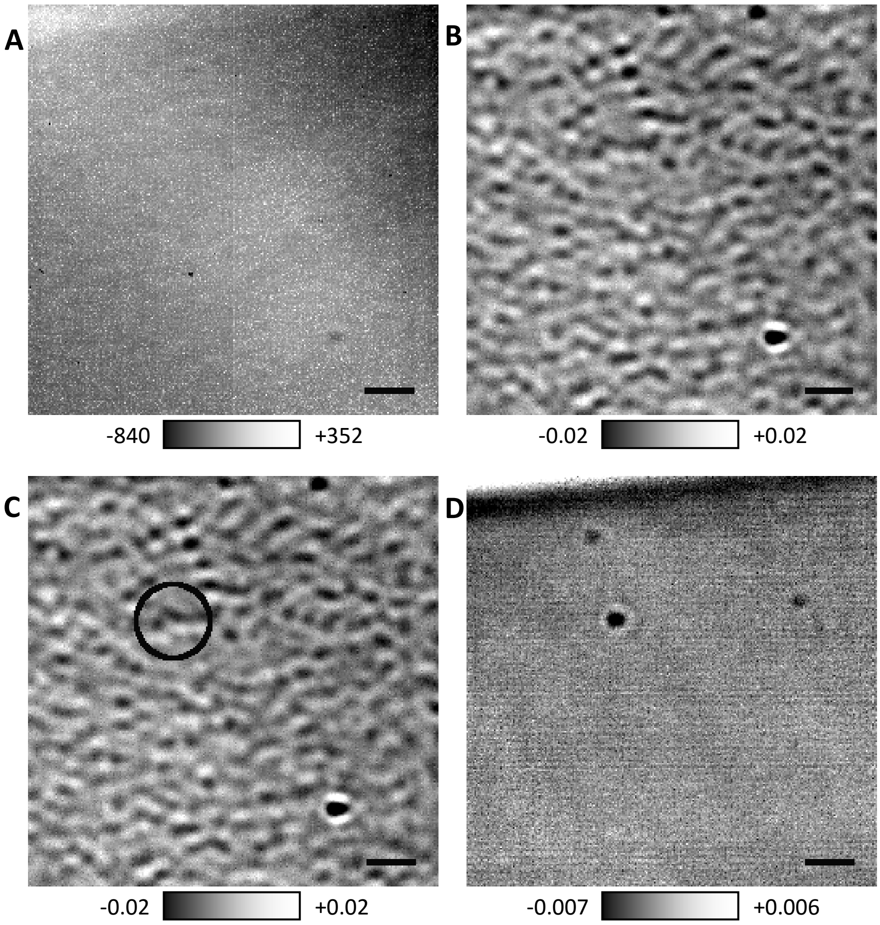

Figure 3.2. Standard data processing methods. (A) Raw image prior to any filtering; **(B)** Image of a blank coverslip following the application of a median filter; **(C)** Image of a bound micelle of **3c** (circled) after the application of a median filter. Image recorded within 3 seconds of the image in panel B; **(D)** Image in panel C following background subtraction, clearly revealing micelles of **3c**. Scale bars = 1 µm.

Imperfections in the glass surface scatter light and thus the raw image typically has numerous apparent particles which appear as a general roughness of the surface. While these imperfections may overwhelm very small scatterers such as micelles, this background is constant in a given location on the coverslip and can therefore be subtracted to give a clean image of the objects of interest. Here this process is simply referred to as *background subtraction*. This generally works when analysing particles that are dynamic, either binding or moving laterally over time: by subtracting the average of a set of frames from each image, the dynamic elements can be isolated from the background (Figure 3.2 D). As can be seen in Figure 3.2, background subtraction removes the remaining sample-independent artefacts and further reduces the contrast to below 1%, allowing the clean visualisation of individual particles. When considering lateral motion, the average of all frames is subtracted; when considering the accumulation of particles over time, the average of 50-200 frames recorded before particles begin to appear can be subtracted.

In a single frame the signal arising from a small scatterer such as a micelle is too small to be reliably detected by the iSCAT instrument used for this work. To overcome this problem the time average of multiple frames is taken. By averaging, or binning, typically 100-150 frames in this way, small particles that bind to the surface can be detected reproducibly. While simple background subtraction isolates newly-landed or mobile particles from the existing surface roughness and other scatterers, often it is of interest to distinguish between particles more finely. In particular, in this work we are interested in quantifying the rate of binding and unbinding to the surface. One way to study this more closely is through *consecutive image subtraction*. This involves subtracting the frame-binned image at time t from the frame-binned image at time $t+n$, where n is the number of frames being binned. This clearly reveals the ongoing binding and unbinding of particles from the surface.

The images that result from the use of these techniques are similar to those acquired using other ultra-high resolution techniques such as single molecule fluorescence. As such, analytical methods developed elsewhere can be readily applied to iSCAT data, and the images themselves are intuitive to interpret. The experiments described here were generally performed by recording a 256 × 256 pixel window, corresponding to approximately 8.4 × 8.4 µm region, at 1000 frames per second.

3.3. Application of iSCAT to an autocatalytic thiol-ene reaction

3.3.1. Design and synthesis

We decided to apply iSCAT to the autocatalytic thiol-ene reactions described in Chapter 2. The substrates described previously form aggregates that were too small to detect using the iSCAT instrument available to us. When solutions of aggregates of **3b** and **15** were analysed by iSCAT no signal was detected, even when averaging hundreds of frames recorded at 1 kHz. By DOSY the micellar radii were estimated to be on the order of 1 to 1.5 nm.

To overcome this problem we designed an analogue of the first-generation thiol-ene substrate **3b** (Scheme 3.1). The principle of this design was simple: the product would ideally form either large micelles ($R_H > 5$ nm) or vesicles, and would aggregate at concentrations around or below 1 mM, so that even very dilute solutions of the compound can be investigated.

The most obvious way to achieve this is to use a thiol with a longer chain. A longer tail can be expected to increase the hydrodynamic radius, but also to raise the melting point of the thiol and possibly the Krafft temperature of the product. Ideally, the thiol ought to be a liquid at room temperature to allow it to be used neat rather than as a solution, and the Krafft temperature of the product ought to be below room temperature to avoid the need to heat samples prior to analysis. Introducing unsaturation into the thiol chain can serve to lower the melting point of the thiol and the Krafft temperature of the product by disrupting crystalline packing of both compounds. Long-chain singly-unsaturated fatty alcohol derivatives meet these criteria; given the ubiquity of oleic acid (*cis*-9-octadecenoic acid) in studies of prebiotic chemistry, we chose to use oleyl mercaptan **2c** as the nucleophile.

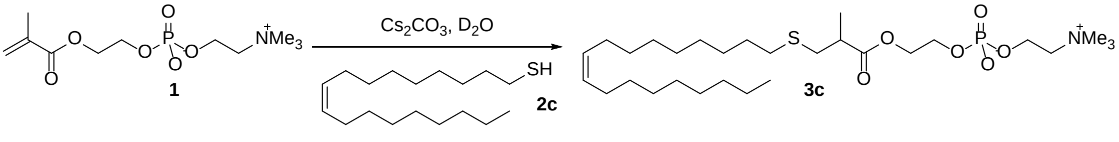

Scheme 3.1. Modified thiol-ene reaction. The reaction is analogous to the first-generation thiol-ene reaction described in Chapter 2 and proceeds under the same reaction conditions.

The phospholipid product **3c** was analysed by DLS at millimolar concentrations and found to form a mixture of micelles and vesicles (see Chapter 5). Surface tension measurements indicated a sharp CMC around 1 mM. These properties were favourable for our iSCAT studies: the compound aggregated at low concentrations, allowing for the analysis of dilute solutions unlikely to saturate the iSCAT coverslip, and formed particles large enough to be detected. Further, the formation of a mixture of micelles and vesicles offered an opportunity to exploit the unique capacity of iSCAT to simultaneously detect and distinguish between individual particles of a range of sizes in real time.

3.3.2. Measurement of reaction kinetics by iSCAT

Analysis of **3c** by iSCAT showed that above 1 mM micelles bound to the coverslip, and out-of-focus particles in the solution above produced a general flickering in the image. By carefully tuning the concentration controlled binding could be achieved, allowing for reliable detection of individual micelles and quantification of the size distribution. Each particle that lands has a different contrast to the background, which is proportional to the size of the particle. Comparing the contrast histogram to the size distribution obtained by DLS revealed a good match between the two, strongly supporting the identity of the observed particles as micelles of **3c** (Figure 3.3). The contrast of these particles was comparable to that obtained previously from proteins of a similar size.[21] Under these conditions the larger vesicles seen in the DLS distribution were not generally observed, presumably because there are far fewer vesicles than there are micelles and thus the probability of one binding under these dilute conditions was low.

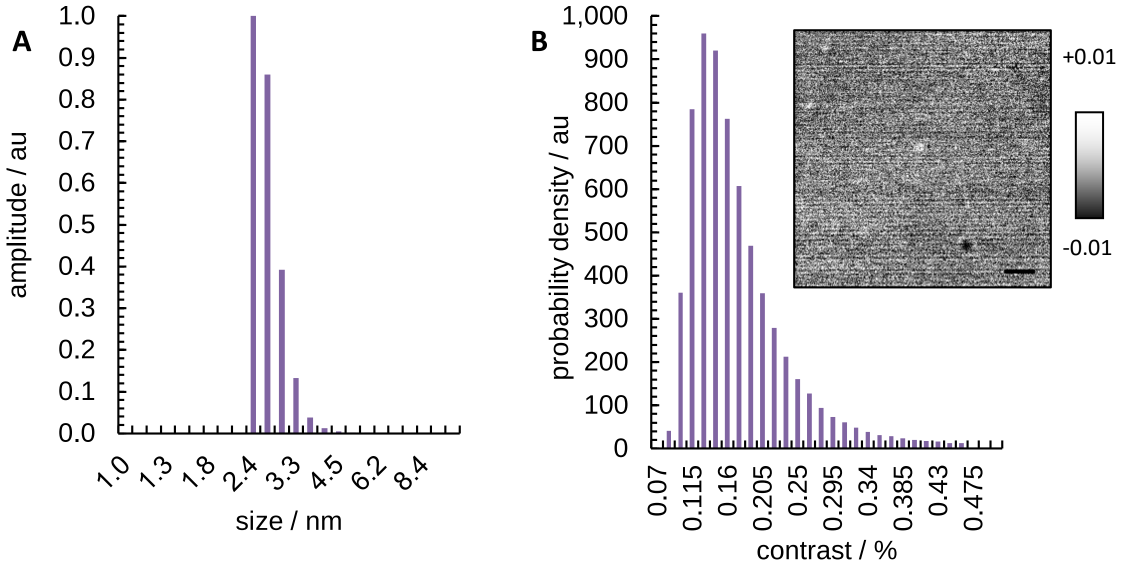

Figure 3.3. Detection of 3c by DLS and iSCAT. (A) DLS number distribution of **3c** (1 mM). Mass and intensity distributions are available in Chapter 5. **(B)** iSCAT contrast distribution of **3c** (1 mM). Inset: Background subtraction image of a micelle of **3c**. The particle has a contrast of -0.14%.

We next attempted to demonstrate autocatalytic behaviour. Under the reaction conditions described in Chapter 2, **1** and **2c** did not react even after several days owing to the effective insolubility of **2c**. Given the much smaller scale and larger surface area to volume ratio on the microscale we attempted to study the reaction by iSCAT regardless, as these physical parameters proved to have a significant influence on rate in our earlier studies.

Negative control experiments revealed few or no particles landing on the iSCAT coverslip when the sample consisted of either water, an aqueous solution of Michael acceptor **1** and Cs_2CO_3, or a biphasic mixture of thiol **2c** and aqueous Cs_2CO_3. These experiments rule out false positives arising from the formation of thiolate-based aggregates or simple etching of the glass surface by the strongly basic conditions of the reaction. Careful washing of the silicone gasket prior to the experiment was crucial to ensuring no false positives were obtained. To further ensure false positives were avoided, at the start of each reaction the coverslip was checked for cleanliness and the mixture of thiol **2c** and aqueous Cs_2CO_3 was allowed to equilibrate for at least 10 minutes prior to the addition of a solution of **1** to initiate the reaction.

Confident that we could detect particles of **3c** and distinguish them from potential false positives we carried out experiments analogous to those described in chapter 2. In the absence of any product we expected to see a lag period in which few or no particles bind to the interface, followed by a period of rapid, ideally exponential, reactivity. In the presence of pre-formed product (at or close to the CMC), we expected to see a reduction or elimination of the lag period.

Several caveats apply here. Firstly, under these conditions the aqueous phase was not stirred and cannot be considered a homogeneous solution. Secondly, even in negative controls consisting solely of milliQ water, occasional apparent binding events were observed. These are unavoidable and should not be mistaken for product formation. Either or both of these effects may lead to intermittent binding during the lag phase.

Finally, it is important to note what is actually being measured here. iSCAT cannot detect monomer concentrations, but rather the binding and unbinding of product micelles to the coverslip. To a first approximation the rate of binding is proportional to the concentration of micelles in the aqueous phase. We therefore took the rate of binding as a measure of product concentration. It is possible that the heterogeneity of the aqueous phase undermines this assumption.

The reaction was simple to perform. All materials were filtered through 0.2 µm pore filters prior to use. A small quantity, typically 4 µL, of water was placed in a well in a silicone gasket on the coverslip. Before any active samples were loaded the coverslip was checked to ensure it was clean and in focus. Neat thiol was then distributed across the top of the aqueous phase and the mixture was allowed to equilibrate for some time to ensure no false positives were generated. The reaction was then initiated by adding an equal volume of double-concentrated solution of **1** and Cs_2CO_3 to the aqueous phase and gently mixing it using a micropipette. The refractive index of the solution changed upon addition of this concentrated solution, requiring the focus to be adjusted. For a given coverslip this was typically a constant value, and so the first experiment was used to find the correct focal plane before acquiring data in subsequent experiments.

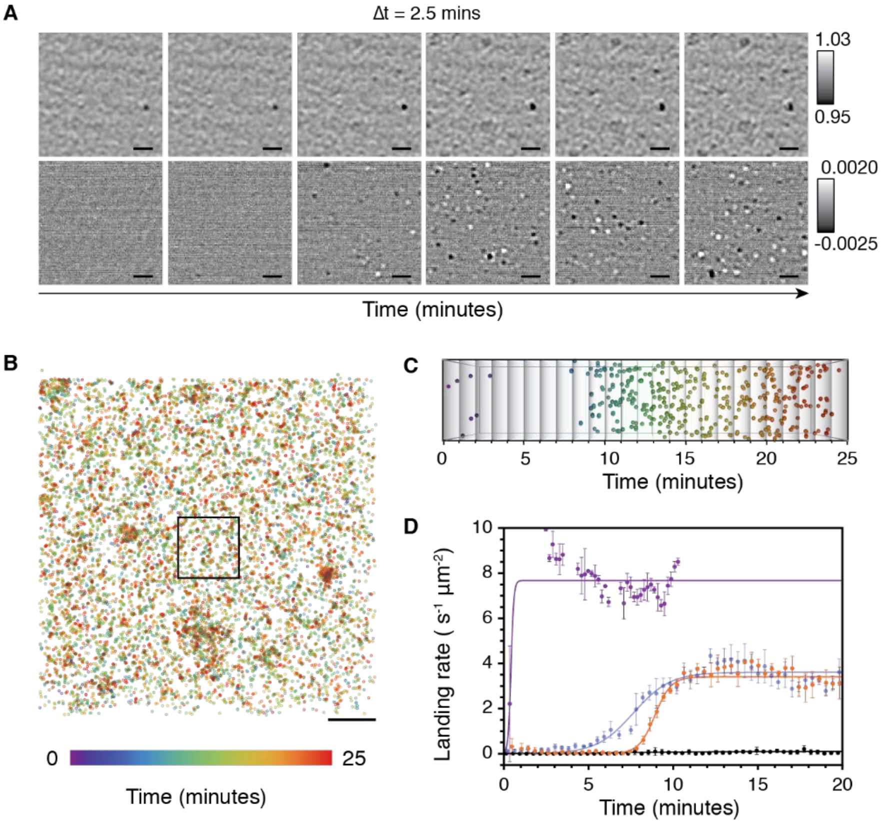

Figure 3.4. Measurement of reaction kinetics by iSCAT. (A) Flat field (top) and consecutive subtraction (bottom) images of the reaction of **1** and **2c** (600 mM **1**, 200 mM Cs_2CO_3, 1.25 eq **2c**; total aqueous volume 8 µL); **(B)** Super-resolution map of the location of each binding event; **(C)** *z*-axis of the super-resolution map in the region indicated by the box in panel B; **(D)** Kinetic profiles of the binding of micelles for two reactions (blue and orange), a reaction seeded with 1 mM **3c** (purple), and a negative control in the absence of **1** (black). Data points with error-bars represent the average and standard deviation of consecutive measurements sampled once every six seconds. Figure kindly provided by Jaime Ortega-Arroyo. An animated version of this figure is available in the electronic appendix. Scale bars = 1 µm.

As seen in Figure 3.4, the predicted behaviour was achieved reproducibly. Allowing **1** and **2c** to react at concentrations similar to those used in our previous ensemble studies reliably gives an exponential kinetic profile (panel D, blue and orange lines). The apparently sigmoidal shape is an artefact of this technique: once the coverslip was saturated with particles, the binding rate levelled off and was equal to the unbinding rate, resembling a Langmuir adsorption isotherm. This does not indicate completion of the reaction, which needed only to reach <1% conversion in order to produce sufficient aggregates to saturate the coverslip. Pleasingly the saturation binding and unbinding rates were equal for the two experiments, and omission of **1** from the aqueous phase gave no reactivity (panel D, black line).

To demonstrate the influence of product on the kinetics we replaced the initial aqueous phase with a dilute solution of **3c** (panel D, purple line). At 1 mM, few or no aggregates were seen to bind to the cover slip, but the presence of aggregates in solution was indicated by a general flickering produced by out-of-focus scatterers. When the reaction was initiated under these conditions no lag period was observed: the coverslip was saturated immediately by particles, with equal binding and unbinding rates.

iSCAT also provided information that would be difficult to obtain through other techniques, such as the change in size distribution with a time resolution of seconds. Figure 3.5 shows the evolution in average particle contrast over time for the two unseeded reactions shown in Figure 3.4. In the early stages of the reaction there were very few particles, giving noisy data arising from the limited sample present. As the reaction proceeds the average contrast converged to around 0.15%, consistent with the qualitative observation that the vast majority of particles landing throughout the reaction are small micelles as expected from the DLS number distribution (Figure 3.3A)

In some experiments we observed a shift in the size distribution, which is inferred from the particle contrast distribution as described above, from small micelles towards particles an order of magnitude larger. This observation was not reproducible, however, and so no interpretation of it is offered here. Nonetheless, the possibility of obtaining time-resolved size distributions in this manner is exciting.

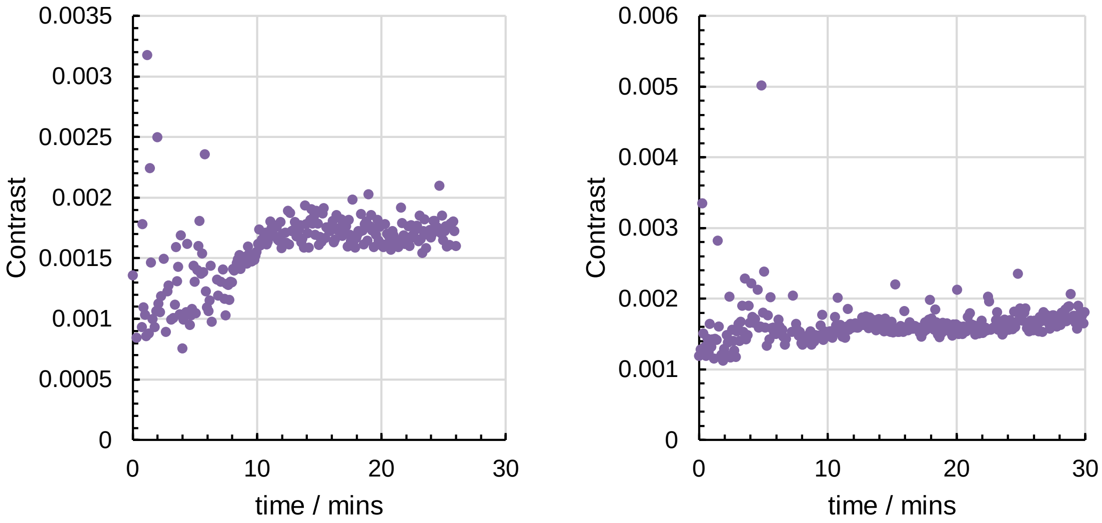

Figure 3.5. Change in size distribution over time. Points correspond to the average particle contrast at each time point.

These experiments demonstrate the feasibility of following autocatalytic reaction kinetics using iSCAT. This includes generating super-resolution maps of the location of each binding and unbinding event, with a resolution on the order of nanometres (Figure 3.4, panels B and C). This was achieved by identifying the centre of mass of each particle during data analysis, allowing super-resolution data to be extracted from diffraction-limited spots. The maps shown here appear somewhat sparse as a result of the limited sampling rate, but clearly demonstrate that physical autocatalysis can now be studied with remarkable sensitivity.

While it was not possible under these conditions to follow the reaction beyond its initial phase, the behaviour observed during this window was consistent with ensemble experiments and provided considerably higher quality data than the NMR experiments reported in Chapter 2. The use of iSCAT to study physical autocatalysis thus has considerable advantages over ensemble experiments, allowing reaction kinetics to be reproducibly quantified in situ with excellent time resolution and providing single-particle level information. Further, when performing the reaction on the microscale we used far fewer equivalents of thiol than we did on the millilitre scale, using only 1.25 equivalents here compared to 10 equivalents in the experiments described in Chapter 2. The altered physical parameters thus allowed an otherwise slow reaction to proceed highly efficiently.

3.3.3. Modelling of reaction kinetics

The kinetic data obtained by iSCAT are of higher quality than those reported in Chapter 2. We therefore decided to use these data to test several mechanistic hypotheses through kinetic modelling. While a number of kinetic models for physical autocatalytic reactions have been described in the literature,[25,26] we initially opted to study simpler models in order to capture the most prominent features of the reaction. The three simplified mechanisms shown in Figure 3.6 were considered in turn.

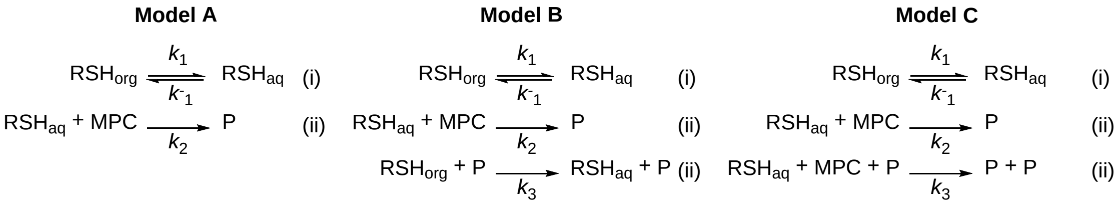

Figure 3.6. Simplified mechanistic models for physical autocatalysis. (A) Non-catalytic system with no product effects; **(B)** Autocatalytic system with simplified stoichiometry; **(C)** Phase-transfer system with simplified stoichiometry.

Unlike other models in the literature, here micelle formation is not explicitly considered, and the catalytic stoichiometry is assumed to be 1:1 for simplicity. This is unlikely to be physically accurate, but provides a simple model of autocatalysis. We initially avoided modelling micelle formation directly as this would involve questionable assumptions about the stoichiometry of micelle formation. Further, the binding rate measured by iSCAT is assumed to be proportional to the total concentration of **3c** in both monomeric and micellar states. A final constraint on the model is the initial concentration of **1**, which was artificially limited in order to model the saturation of the coverslip.

As a result of this final assumption, the rate constants obtained here are abstract and do not refer to real concentrations (i.e. rate constants are reported in min^{-1}). Consequently the absolute values of rate constants here are not meaningful. Rather, the relative values of rate constants are taken as a measure of catalytic efficiency and the goodness of fit as a test of the chemical plausibility of each hypothesis.

The three models described here were developed in order to address two questions: firstly, can simple phase behaviour not involving product molecules account for the behaviour of the system? Secondly, can the data be used to distinguish between a truly autocatalytic mechanism, in which the product catalyses the bond-forming step, and a phase transfer mechanism, in which the product alters the solubility of the thiol in the aqueous phase?

In all three models, the thiol is assumed to be sparingly soluble in the aqueous phase and to equilibrate between the organic and aqueous phases.

Model A considers a null hypothesis in which the product has no effect on the system: the thiol **2c** equilibrates between the organic and aqueous phases and then reacts irreversibly with **1** to give **3c**. Attempts to fit this model to the observed kinetic data failed, giving first-order kinetics and tending to maximise k_1/k_{-1}. When $k_{-1} = 0$ and $k_1 > k_2$, i.e. the thiol dissolves rapidly and then reacts slowly with **1**, a very slight lag phase is seen in simulations before the onset of first-order behaviour (Figure 3.7). Nonetheless, this does not account for the observed kinetic profile.

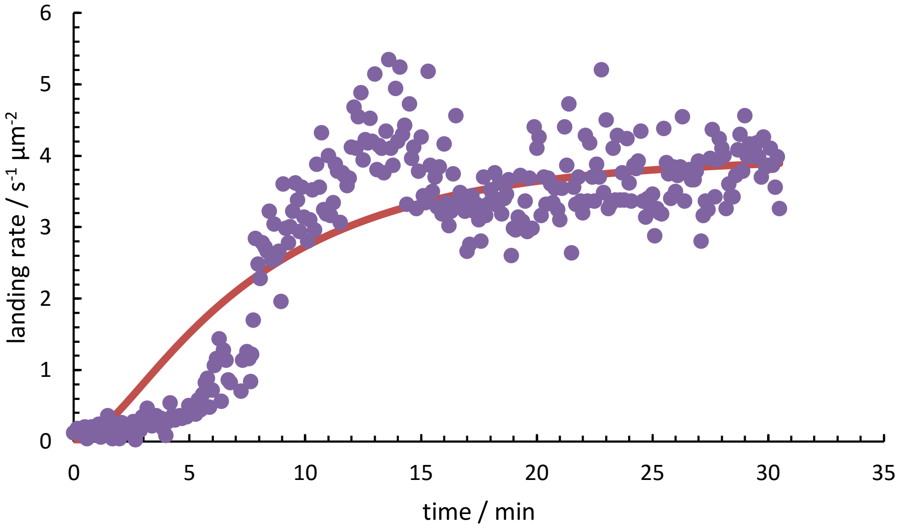

Figure 3.7. Fit to Model A. ● Experimental data points; red line: best fit to model A.

Model B includes an autocatalytic pathway in which **3c** catalyses its own formation from aqueous **2c** and **1**. The equilibrium constant between organic and aqueous thiol is constrained such that $k_1/k_{-1} < 10^{-4}$, i.e. the thiol is poorly soluble in the aqueous phase. This prevents the fitting process from leading to a chemically implausible scenario in which the thiol is freely water-soluble. In this model the autocatalytic efficiency can be considered as the ratio of k_3/k_2, i.e. the ratio of the rate constants for the autocatalytic and noncatalytic pathways.[27]

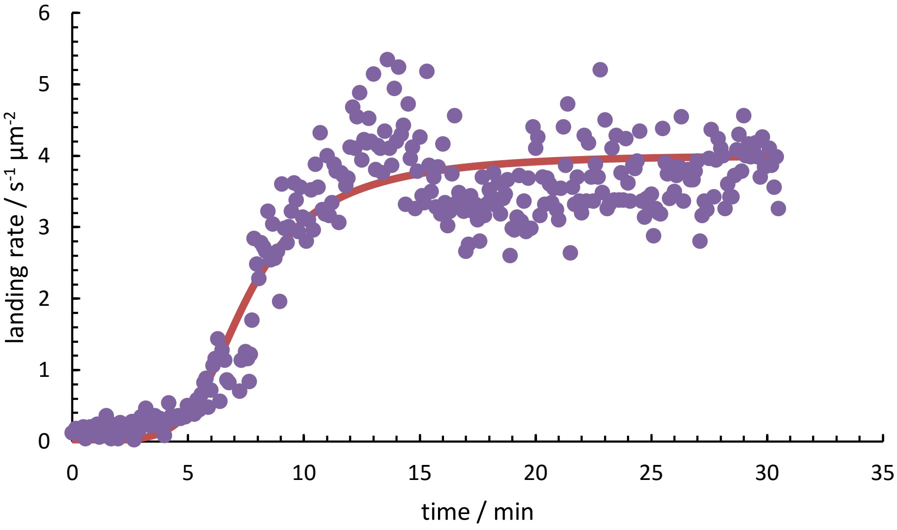

Figure 3.8. Fit to Model B. ● Experimental data points; red line: best fit to model B.

Fitting this model to the experimental data gives close agreement when the rate of thiol dissolution is sufficiently rapid ($k_1 > 0.5$). Below this value the fit between the data and model is qualitatively poor, and the root mean square error (RMSE) rises from ~26 to over 35. Above $k_1 = 0.8$, varying the rate of equilibration reveals a trend in which increasingly rapid equilibration requires lower autocatalytic efficiency to achieve the observed kinetic behaviour (Table 3.1). The rate of equilibration in a real system is presumably influenced by physical parameters including the shape of the reactive interface, the rate of stirring, and the temperature, as well as the solubility of the thiol and the pH of the aqueous phase. This model predicts that the bond-forming reaction is slow compared to the rate of thiol equilibration.

Min k_{-1}	**Max k_1**	**k_{-1}**	**k_1**	**k_1/k_{-1}**	**k_3/k_2**	**k_3**	**k_2**	**RMS**	**STD**
8000	0.8	8144.98	0.80	9.822E-05	1090.655	0.379477	0.000348	26.2309	26.407
10,000	1	11866.3	0.788554	6.64532E-05	1255.628	0.568223	0.000453	26.2337	26.4098
30,000	3	32819.5	1.72068	5.24286E-05	207.5531	0.590009	0.002843	26.1291	26.3045
60,000	6	60608	3.90857	6.44893E-05	85.2196	0.432325	0.005073	26.0736	26.2486
100,000	10	123905	4.19068	3.38217E-05	84.07594	0.822351	0.009781	26.0707	26.2456
500,000	50	591899	49.4155	8.34864E-05	58.0998	0.316433	0.005446	26.0332	26.2079
10^6	100	1013360	98.7239	9.74223E-05	57.24214	0.270579	0.004727	26.0315	26.2062
10^7	1000	10000800	999.81	9.9973E-05	56.45735	0.263146	0.004661	26.0299	26.2046

Table 3.1. Variation of autocatalytic efficiency with rate of thiol equilibration. Units reported in min^{-1}. RMS = Root mean square error. STD = Standard deviation.

Model C, rather than invoking chemical autocatalysis, invokes dissolution of the thiol by the product. Rather than catalyse the reaction of **1** and **2c**, the product provides a low-energy pathway for dissolution of **2c** into the aqueous phase. This is modelled as an irreversible conversion from organic to aqueous thiol, occurring in parallel with the background equilibrium between the two phases.

As before, the background equilibrium constant for the thiol is assumed to be $k_1/k_{-1} < 10^{-4}$. Here, the autocatalytic efficiency is approximated as k_3/k_1. This is equal to the ratio of 'new' and 'old' equilibrium constants, where $K_{new} = k_3/k_{-1}$ and $K_{eq} = k_1/k_{-1}$, with k_1 assumed to be negligible in the modified equilibrium constant as $k_3 >> k_1$.

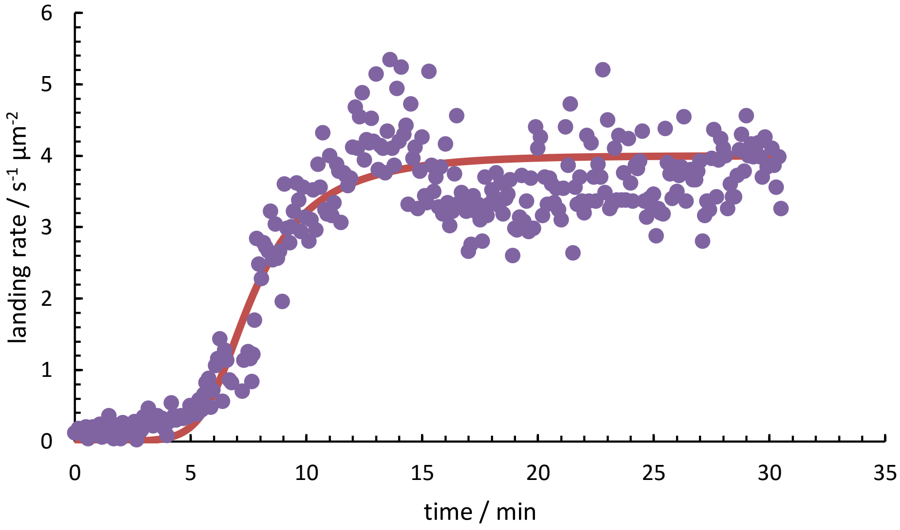

Figure 3.9. Fit to Model C. ● Experimental data points; red line: best fit to model C.

The fit for this model is qualitatively and quantitatively (as measured by RMSE) comparable to that of model B. Notably, it fits the data over a wider range of values for k_1: where model B begins to break down when $k_1 < 0.5$, here the RMSE remains acceptable even when $k_1 = 10^{-6}$. While the absolute values of these rate constants are not meaningful, this flexibility may indicate a broader explanatory power for this model.

As before with increasing k_1, the catalytic efficiency required to account for the observed behaviour decreases (Table 3.2). Notably, the modified equilibrium constant k_3/k_{-1} is always less than 1, indicating that the thiol is not required to be highly soluble in the aqueous phase for the reaction to proceed.

Min k_{-1}	Max k_1	Actual k_{-1}	Actual k_1	k_1/k_{-1}	k_3/k_1	k_3	k_2	RMS	STD
0.01	0.000001	13.3363	0.000001	7.5E-08	186416	0.186416	0.00482	26.4369	26.6143
0.1	0.00001	41.9532	0.00001	2.38E-07	15708.2	0.157082	0.012468	26.4062	26.5835
1	0.0001	54.4352	0.0001	1.84E-06	269.078	0.026908	0.078866	26.1313	26.3067
10	0.001	191.609	0.001	5.22E-06	134.312	0.134312	0.043132	26.064	26.2389
100	0.01	113.87	0.001399	1.23E-05	73.90313	0.103423	0.032127	26.0565	26.2314
1000	0.1	2544.34	0.016578	6.52E-06	73.79568	1.22337	0.057042	26.0551	26.2299
10^4	1	13130.6	0.023234	1.77E-06	59.63054	1.38545	0.252106	26.0346	26.2093
10^5	10	101341	0.098069	9.68E-07	58.19413	5.70704	0.469456	26.0327	26.2074

Table 3.2. Variation of phase transfer efficiency with rate of thiol equilibration. Units reported in min^{-1}. RMS = Root mean square error. STD = Standard deviation.

In both models, when the rate of thiol equilibration is high, the autocatalytic efficiency required to achieve the kinetic behaviour observed by iSCAT is approximately ~50, and the required efficiency is negatively correlated with the rate of thiol equilibration. The rate of thiol equilibration is likely to be strongly influenced by the efficiency of mixing of the two phases, which under the iSCAT conditions is low.

A limitation of these models is the assumption that the thiol is in equilibrium between organic and aqueous phases. While this is likely true for the short, partially soluble thiols used in Chapter 2, thiol **2c** is effectively insoluble in the aqueous phase. To account for this we adapted the phase transfer kinetic model for autocatalytic ester hydrolysis developed by Buhse *et al*.[25]

$$EC_{org} \xrightleftharpoons{k_1/k_{-1}} EC_{int} \qquad \text{(i)}$$

$$OH^- + EC_{org} \xrightarrow{k_2} C + EtOH \qquad \text{(ii)}$$

$$xC \xrightleftharpoons{k_3/k_{-3}} M \qquad \text{(iii)}$$

$$yEC_{int} + M \xrightleftharpoons{k_4/k_{-4}} MEC \qquad \text{(iv)}$$

$$MEC \xrightleftharpoons{k_5/k_{-5}} M + yEC_{aq} \qquad \text{(v)}$$

$$EC_{aq} + OH^- \xrightarrow{k_6} C + EtOH \qquad \text{(vi)}$$

Figure 3.10. Phase transfer model for autocatalytic ester hydrolysis.

The latter model consists of six steps. The hydrophobic ester, ethyl caprylate (EC), equilibrates between the bulk organic phase and an interfacial phase. The latter represents small microphases dispersed through the aqueous medium by rapid stirring, or the accessible interface present in the absence of stirring. The material present in the interfacial phase can react slowly with hydroxide to give the caprylate product (C) and the ethanol byproduct. The caprylate aggregates reversibly into micelles (M) with a defined aggregation number (*x*). In turn, each micelle can bind to *y* molecules of interfacial ester to give a mixed micelle (MEC), which can dissociate reversibly in the bulk aqueous phase to release *y* molecules of the ester. In the aqueous phase, the ester can undergo hydrolysis at a higher rate than it can in the interfacial phase.

This model involves some assumptions which, while necessary for simplicity, reduce its applicability to our system. Micelle formation is assumed to be well-defined, giving a monodisperse population of aggregates of *x* molecules. DLS measurements of **3c** (Figure 3.3) indicate that this compound forms aggregates with a range of sizes, rendering this assumption invalid here. Similarly, the assumption that the stoichiometry of phase transfer is well-defined, with mixed micelles consisting of a 1:*y* ratio of surfactant to thiol may be invalid.

Our adaptation of this model attempted to simplify it in order to draw out the most important features (Figure 3.11). The equilibration between organic and interfacial thiol and subsequent slow reaction to give product are collapsed into a single slow step. Micelle formation is retained, and the aggregation number arbitrarily set to x = 100. The phase transfer step is simplified into a single equilibrium catalysed by micelles, with no mixed micelles explicitly considered in the model. The final reaction in the aqueous phase is retained.

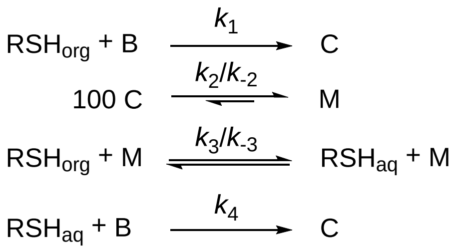

Figure 3.11. Simplified phase-transfer model for autocatalytic thiol-ene reaction.

Fitting this model to the iSCAT data gives the following parameters (Table 3.3):

Parameter	Value	Comment
k_1	1.14×10^{-7}	Slow
k_2	5.57	K_{eq} = 124
k_{-2}	0.045	
k_3	0.0021	$K_{eq} = 2.6 \times 10^{-4}$
k_{-3}	8.13	
k_4	0.48	Fast, $k_4/k_1 = 4.2 \times 10^6$

Table 3.3. Parameters for simplified phase-transfer model.

These rate constants appear chemically reasonable: the background reaction is very slow compared to the micelle-mediated reaction; micelle formation is strongly favoured; and the micelle-mediated transfer of thiol into the aqueous phase is thermodynamically unfavourable, but kinetically significant.

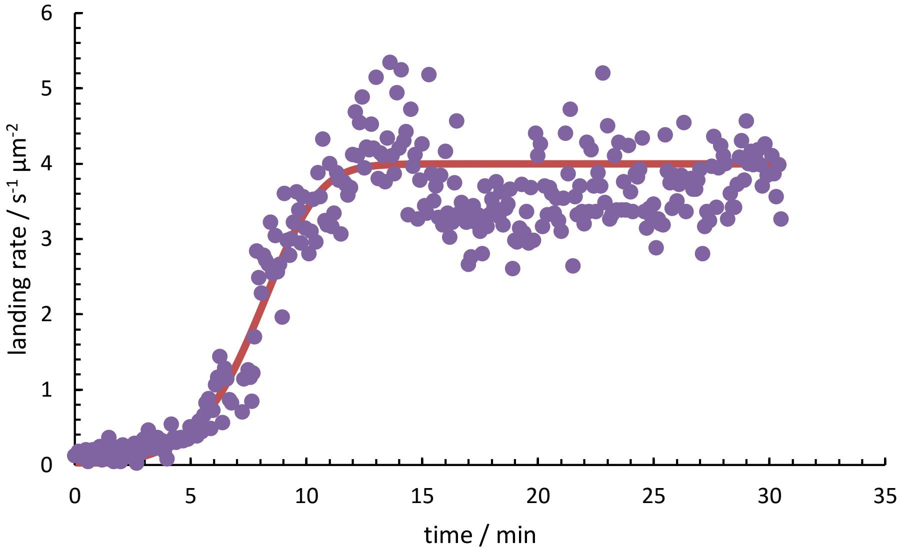

3.12. Fit to model D. ● Experimental data points; red line: best fit to model D.

Simulating the reaction using these parameters reveals that both the aqueous thiol and monomeric **3c** form steady state concentrations, with the concentration of thiol in the aqueous phase rising as micelles form. This agrees with the behaviour observed by NMR in Chapter 2, in which micelle formation coincided with the observation of thiol in the aqueous phase.

While this simple kinetic analysis does not distinguish conclusively between the mechanistic scenarios considered, it does nonetheless support the conclusion that the observed kinetic behaviour does arise from the behaviour of product molecules rather than the kinetics of simple phase behaviour. More generally, this demonstrates that the measurements made by iSCAT can be explained in chemical terms and related back to mechanistic hypotheses. Further systematic experimentation may allow more rigorous characterisation of the kinetic behaviour of these reactions, and the development of a more complete mechanistic picture. The use of iSCAT is advantageous as it allows the critical reactive period in which autocatalysis begins to be monitored closely in situ and with remarkable sensitivity.

3.3.4. Direct observation of reactive interface by iSCAT

During the experiments shown in Figure 3.4 we unexpectedly observed the formation of supported lipid bilayers on the coverslip (Figure 3.13). Once the coverslip was saturated by aggregates during the reaction it appeared as a rough surface of varying refractive indices. At long reaction times, typically around one hour, this roughness slowly transformed back towards a smooth appearance. This could indicate an increase in the unbinding rate and a reversion to bare glass. However, aggregates were then seen to diffuse across these smooth regions, behaviour which was not seen when samples of aqueous **3c** were deposited on a clean glass surface. The diffusion of numerous aggregates across the bilayer surface is clearly visible in Movie 5.3 (see electronic appendix).

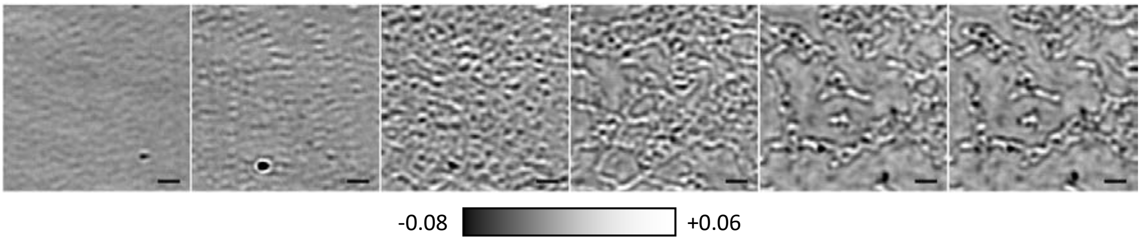

Figure 3.13. Supported bilayer formation. At reaction times of around 1 hr bilayer formation is observed. An animated version of this figure is available in the electronic appendix. Images are the average of 10 frames. Scale bars = 1 µm.

This behaviour is consistent with a previous study by the Kukura group of the formation of supported bilayers by iSCAT.[23] Interestingly, this effect was limited to the illuminated region: after bilayer formation, panning the observation window laterally across the coverslip revealed that the region of bilayer formation was square and limited to the formerly illuminated area. The bilayer rapidly expanded to the newly-illuminated region (Figure 3.14). This suggests that the rearrangement from surface-bound micelles and vesicles to supported bilayers is promoted by the laser, presumably because the high-powered beam required for these high-speed experiments heats the sample slightly.

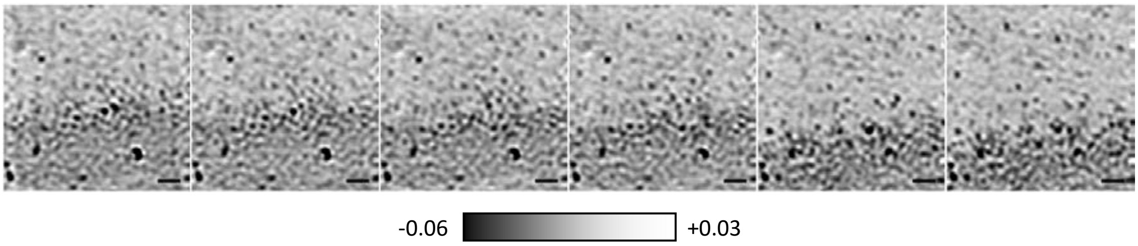

Figure 3.14. Expansion of the supported bilayer. Panning the laser to a previously dark region adjacent to a region of bilayer reveals a saturated surface which is rapidly consumed by the expanding bilayer. Images are of the same sample illustrated in Figure 3.13 and are each the average of 50 frames. An animated version of this figure is available in the electronic appendix. Scale bars = 1 µm.

The observation of bilayer formation prompted us to search for other examples of complex behaviour in this reaction. In particular, we hoped to identify unambiguous examples of the growth and division of aggregates, or the synthesis of new aggregates at the thiol-water interface. In order to directly visualise the interface we created thiol-water interfaces perpendicular to the glass coverslip. We achieved this by first depositing neat thiol **2c** on the coverslip and then displacing it with water. After finding a suitable interface under the microscope, we then initiated the reaction as before by addition of **1** and Cs_2CO_3 to the aqueous phase. Under these conditions we observed a variety of complex processes occurring at the thiol-water interface and in the thiol phase itself.

Note that in these images the thiol phase appears with negative contrast despite its very large size. This is the result of the differing refractive indices of water and the thiol. The amount of reflected light is proportional to the ratio of the refractive indices of the glass and the sample medium, and this ratio is smaller when the bulk liquid is thiol than when it is water. As such the thiol phase appears darker than the aqueous phase.

At the interface between micrometre-scale thiol droplets and the aqueous phase we saw the gradual consumption of the interface by newly formed lipid aggregates (Figure 3.15). Initially aggregates landed on the surface around the droplet much as they did in the experiments described in section 3.3.2. Plotting the number of bound particles per unit area against the distance from the interface revealed a negative correlation (Figure 3.15C). This is consistent with the reaction generating these particles occurring at or near the thiol-water interface of this specific drop, rather than being generated at an interface distant from the surface or in the bulk aqueous phase.

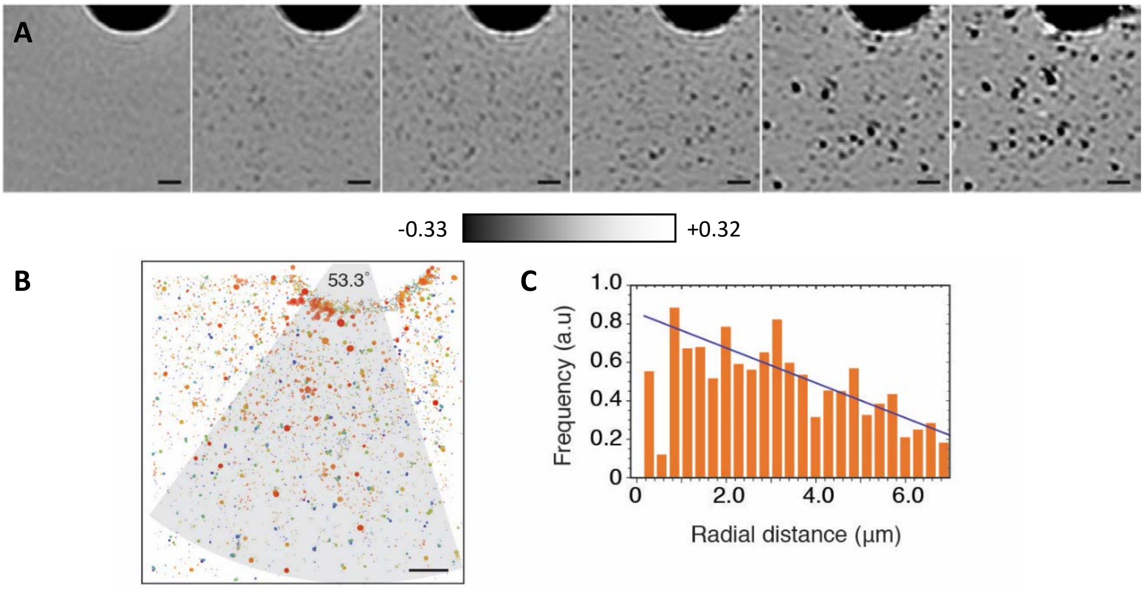

Figure 3.15. Direct visualisation of the reactive interface around a micrometre-scale droplet. (A) Flat-field images reveal the accumulation of particles around a thiol droplet and the breakdown of the thiol-water interface; **(B)** Super-resolution map of binding events; **(C)** Negative correlation of binding

frequency per unit area with radial distance from droplet edge in the shaded area shown in panel B. Solid line represents a fit to a linear function. Panels B and C kindly provided by Jaime Ortega-Arroyo. An animated version of this figure is available in the electronic appendix. Images are the average of 10 frames. Scale bars = 1 µm.

The association of reactivity with the interface became obvious as the reaction progressed. The initially smooth interface began to break down beginning with the formation of small aggregates along it (Figure 3.16A). Following this, connected clusters of aggregates rapidly emerged from sites along the interface. These did not grow in a smooth, continuous manner, but rather in discrete bursts of rapid growth. This process led to the formation of extended structures surrounding the droplet (Figure 3.16B). Background subtraction clearly revealed the formation and expansion of new material during this process, both within the lipid structures and at the growth front (Figure 3.16C), as well as the landing of vesicles outside these extended structures.

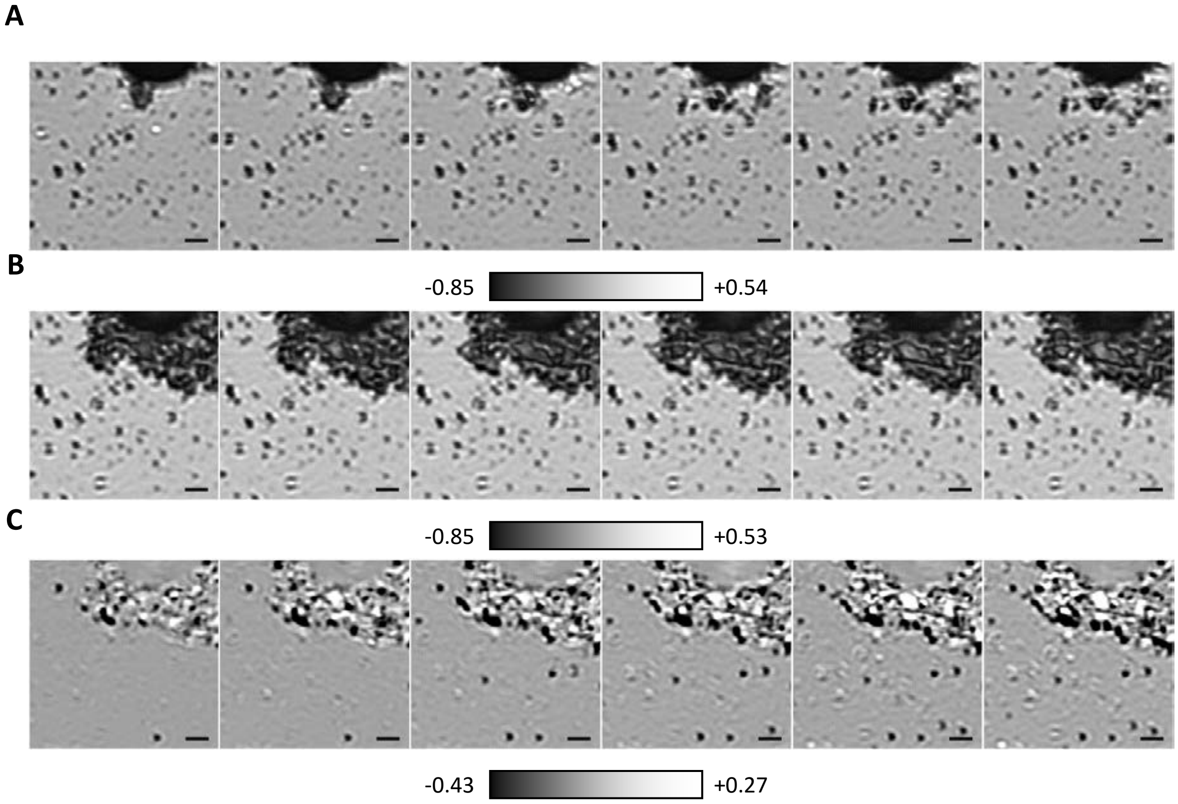

Figure 3.16. Proliferation of aggregates at the reactive interface. **(A)** Flat field images showing rapid breakdown of the thiol-water interface; **(B)** Flat field images showing proliferation of extended structures around the thiol droplet; **(C)** Background subtraction images showing the formation of new

material around the thiol droplet. Animated versions of each panel are available in the electronic appendix. Images are the average of 50 frames. Scale bars = 1 µm.

Eventually the entire droplet was surrounded by an extended network of particles; unlike the bilayers observed before, this effect was not limited to the illuminated area (see Movie 5.7 in the electronic appendix). Panning the observation window revealed that these structures surrounded the entire droplet but did not form away from the droplet, consistent with the proposed biphasic reaction pathway. Throughout this entire sequence of events, the extended lipid structures were highly dynamic, undergoing changes in shape and size and flickering in a manner consistent with reactivity.

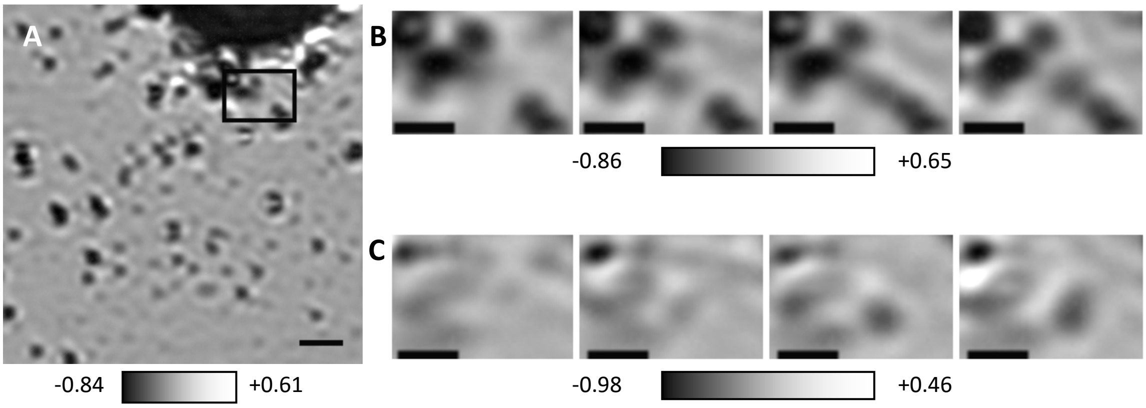

Figure 3.17. Possible division event. (A) Location of zoom in panels B and C. Scale bar = 1 µm; **(B)** Flat field images of possible division event. Δt = 60 ms, scale bars = 0.5 µm; **(C)** Background subtraction images corresponding to those in panel B. Δt = 60 ms, scale bars = 0.5 µm. An animated version of this figure is available in the electronic appendix.

This process clearly involved the growth and proliferation of lipid aggregates, many of which were large and probably consisted of bilayer structures. Isolating an individual, unambiguous division event was not possible, however, as the newly-formed material remained connected to or at least near to the extended network (Figure 3.17A). At best, the formation and growth of new vesicles could be observed, but it is not clear whether these remained attached to the parent vesicle or not (Figure 3.17B and C). Nonetheless, this observation suggests that direct, real-time observation of the division of vesicles and potentially more complex protocells can be achieved using iSCAT.

Observation of a macroscopic thiol-water interface was also possible. Here, the curvature of the interface was small, with the interface extending linearly for many micrometres. Proliferation of vesicles around a static drop was not observed here. Rather, the interface slowly retreated to be replaced by an extended lipid-rich phase (Figure 3.18A). This latter phase was clearly distinct from the bulk aqueous phase; indeed, in this region very little binding was seen in the aqueous phase, while the intermediate phase was seen to be highly active (Figure 3.18B and C).

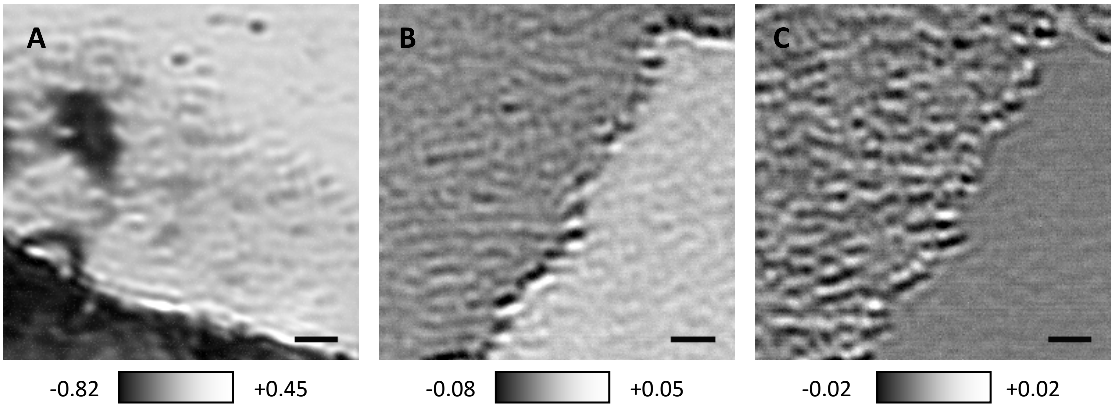

Figure 3.18. Formation of active lipid phase around the reactive interface. (A) Flat field image showing the coexistence of thiol, aqueous, and intermediate phases; **(B)** Flat field image showing the interface between aqueous and intermediate phases; **(C)** Background subtraction image of panel B showing high activity in the intermediate phase and little activity in the aqueous phase. Animated versions of panels B and C are available in the electronic appendix. Images are the average of 10 frames. Scale bars = 1 µm.

Interestingly the retreat of the thiol phase was not a continuous process as might be expected (Figure 3.19). Rather, individual aggregates formed at the interface and merged with the intermediate phase, pushing the thiol phase back in a series of discrete events. Consecutive image subtraction of these data clearly revealed the discrete events (Figure 3.19B): by overlaying the differential series on the flat-field images, the colocalisation of these discrete events with the retreating interface can be seen (Figure 3.19C). It is possible that these discrete events were the formation of individual vesicles at the interface, or simply the physical demixing and retreat of the two phases.[28] In either case we were able to observe this process with remarkable sensitivity.

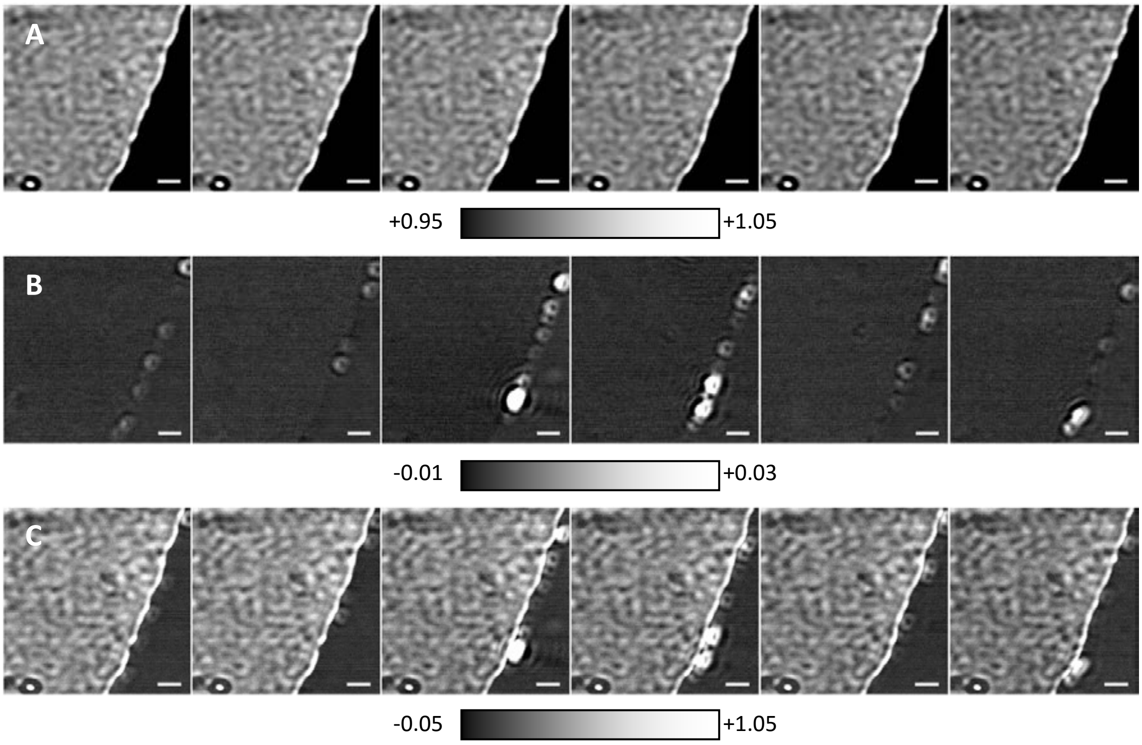

Figure 3.19. Discrete movement of thiol-water interface. The interface between the aqueous (light) and thiol (dark) phases moves towards the right in discrete bursts rather than as a continuous process. **(A)** Flat field images; **(B)** Consecutive subtraction images highlighting individual bursts of activity; **(C)** Composite image of panels A and B highlighting colocalisation of activity and the motion of the interface. Δt = 400 ms, scale bars = 1 µm. An animated version of this figure is available in the electronic appendix.

In addition to these observations at the interface, events in the bulk thiol phase could be observed. This was more difficult than observation of the aqueous phase owing to the higher refractive index of the thiol compared to water, which reduced the amount of reflected light reaching the detector. Most immediately this interfered with the autofocus system, reducing sensitivity and stability. Nonetheless we were able to detect nanoscopic water-in-thiol droplets and microphases (Figure 3.20). Initially these features appeared relatively stable, but under the influence of the laser they were seen to fuse and unbind.

Notable events seen in this experiment include the fusion of nanometre-scale drops with larger, micrometre-scale water phases (Figure 3.20B), and the fusion of nanoscopic water-in-thiol particles, possibly reverse micelles (Figure 3.20C). Micrometre-scale water phases were seen repeatedly and often contained smaller particles, presumably thiol droplets or vesicles. These aqueous phases were not static and flickered rapidly, consistent with the presence and potentially synthesis of micelles in this phase.

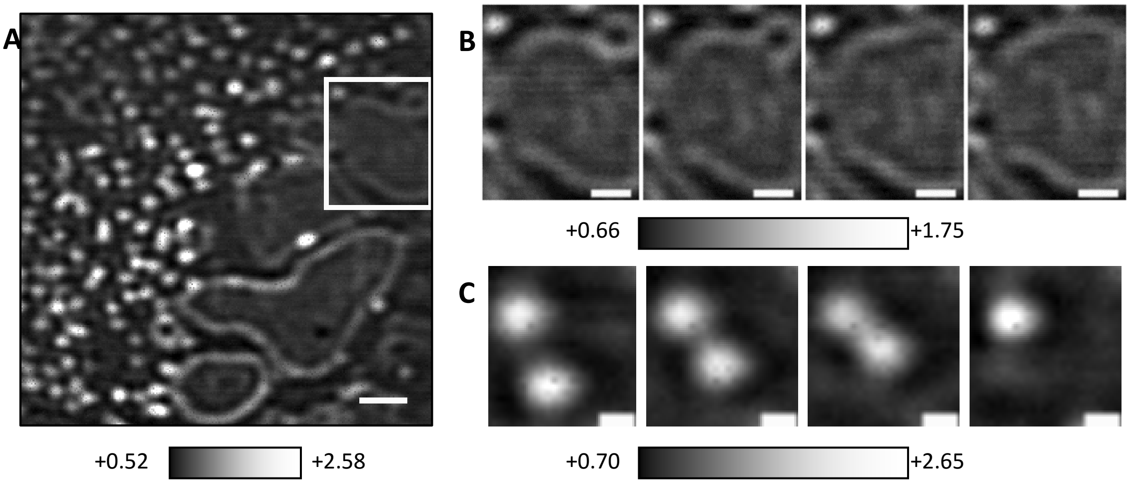

Figure 3.20. Dynamic behaviours of inverted structures. (A) Wide view of thiol phase containing micro- and nanometre scale inverted structures. The box indicates the location of panel B. Scale bar = 1 µm; **(B)** Fusion of small water-in-oil droplet with the surface of a larger droplet. Δt = 100 ms, scale bars = 500 nm; **(C)** Fusion of nanometre-scale water-in-oil droplets. Δt = 18 ms, scale bars = 200 nm. Animated versions of panels B and C are available in the electronic appendix.

The observation of reverse micelles and related structures in the thiol phase was unexpected. This highlights the value of using iSCAT to study systems of this kind. The NMR studies in Chapter 2 deliberately used a large sample volume in order to exclude any bulk thiol from the probe. We simply did not consider any reactivity in the organic phase. Self-reproducing reverse micelles composed of fatty acids are known,[29–31] as is the coexistence of vesicles with inverted structures.[32] This work raises the possibility that self-reproducing reverse micelles may coexist with self-reproducing micelles or vesicles in other reported systems. To our knowledge this has yet to be demonstrated.

All of the observations made at these lateral interfaces were highly dependent on the nature of the interface under investigation. While thiol drops could reliably be generated by this method, the result was effectively random and no control could be exerted over the size or location of the thiol droplets. This was advantageous for exploratory work of this kind, allowing the observation of interfaces of a variety of sizes and shapes, but necessarily led to only qualitative reproducibility.

Future studies of this or related systems would benefit greatly from a more reliable method of generating micrometre-scale thiol-in-water droplets on the surface. As an alternative, assays involving the immobilisation of preformed vesicles or thiol drops in defined locations on an otherwise passivated surface would allow the controlled observation of the dynamics of individual particles.

3.4. Conclusion

The experiments described here demonstrate that it is possible to study physical autocatalysis on the single-particle level in real time and that this approach is likely to prove highly fruitful. Even preliminary experimentation on simple autocatalytic reactions revealed remarkably complex behaviour on the nanometre scale which would be difficult to infer from indirect ensemble methods or static EM images. The temporal and spatial resolution achieved here is comparable or indeed superior to that achievable using super-resolution fluorescence microscopy, and has the advantage that high-speed observation can continue indefinitely without being limited by the photophysics of a fluorescent label. This enabled us to directly observe dynamic processes occurring at long reaction times such as supported bilayer formation and the breakdown of a reactive interface, and the generality of this label-free technique allowed the simultaneous observation of the bulk aqueous and organic phases.

As such, this work sets an important precedent for the future study of physical autocatalysis. The further application of iSCAT to related systems can be expected to offer new insight into the process of vesicle growth and division, the influence of reaction conditions on the dynamics of physical autocatalysis, and ultimately the characterisation of more complex protocells. The application of iSCAT to other systems of prebiotic relevance is ongoing.

3.5. References

1 P. Stano and P. L. Luisi, *Chem. Commun.*, 2010, **46**, 3639–3653.

2 K. Ruiz-Mirazo, C. Briones and A. de la Escosura, *Chem. Rev.*, 2014, **114**, 285–366.

3 K. Kurihara, M. Tamura, K. Shohda, T. Toyota, K. Suzuki and T. Sugawara, *Nat. Chem.*, 2011, **3**, 775–781.

4 T. F. Zhu and J. W. Szostak, *J. Am. Chem. Soc.*, 2009, **131**, 5705–5713.

5 R. Nguyen, L. Allouche, E. Buhler and N. Giuseppone, *Angew. Chem. Int. Ed.*, 2009, **48**, 1093–1096.

6 M. D. Hardy, J. Yang, J. Selimkhanov, C. M. Cole, L. S. Tsimring and N. K. Devaraj, *Proc. Natl. Acad. Sci. U.S.A.*, 2015, **112**, 201506704.

7 I. A. Chen and J. W. Szostak, *Biophys. J.*, 2004, **87**, 988–998.

8 P. L. Luisi, P. S. S. Rasi and F. Mavelli, *Artif. Life*, 2004, **10**, 297–308.

9 B. Dejanović, K. Mirosavljević, V. Noethig-Laslo, S. Pecar, M. Sentjurc and P. Walde, *Chem. Phys. Lipids*, 2008, **156**, 17–25.

10 H. Fukuda, A. Goto, H. Yoshioka, R. Goto, K. Morigaki and P. Walde, *Langmuir*, 2001, **17**, 4223–4231.

11 N. Berclaz, E. Blochliger, M. Muller and P. L. Luisi, *J. Phys. Chem. B*, 2001, **105**, 1065–1071.

12 N. Berclaz, M. Muller, P. Walde and P. L. Luisi, *J. Phys. Chem. B*, 2001, **105**, 1056–1064.

13 P. Walde, R. Wick, M. Fresta, A. Mangone and P. L. Luisi, *J. Am. Chem. Soc.*, 1994, **116**, 11649–11654.

14 P. Stano, E. Wehrli and P. L. Luisi, *J. Phys-Condens. Mat.*, 2006, **18**, S2231.

15 E. Blochliger, M. Blocher, P. Walde and P. L. Luisi, *J. Phys. Chem. B*, 1998, **102**, 10383–10390.

16 J. L. S. Milne, M. J. Borgnia, A. Bartesaghi, E. E. H. Tran, L. A. Earl, D. M. Schauder, J. Lengyel, J. Pierson, A. Patwardhan and S. Subramaniam, *FEBS J.*, 2013, **280**, 28–45.

17 B. O. Leung and K. C. Chou, *Appl. Spectrosc.*, 2011, **65**, 967–980.

18 C. Kuo and R. M. Hochstrasser, *J. Am. Chem. Soc.*, 2011, **133**, 4664–7.

19 L. Schermelleh, R. Heintzmann and H. Leonhardt, *J. Cell Biol.*, 2010, **190**, 165–75.

20 J. Ortega-Arroyo and P. Kukura, *Phys. Chem. Chem. Phys.*, 2012, **14**, 15625–36.

21 J. Ortega Arroyo, J. Andrecka, K. M. Spillane, N. Billington, Y. Takagi, J. R. Sellers and P. Kukura, *Nano Lett.*, 2014, **14**, 2065–70.

22 M. Piliarik and V. Sandoghdar, *Nat. Commun.*, 2014, **5**.

23 J. Andrecka, K. M. Spillane, J. Ortega-Arroyo and P. Kukura, *ACS Nano*, 2013, **7**, 10662–70.

24 N. J. B. McFarlane and C. P. Schofield, *Mach. Vis. Appl.*, 1995, **8**, 187–193.

25 T. Buhse, R. Nagarajan, D. Lavabre and J. C. Micheau, *J. Phys. Chem. A*, 1997, **101**, 3910–3917.

26 P. V Coveney and J. A. D. Wattis, *P. Roy. Soc. Lond. A Mat.*, 1996, **452**, 2079–2102.

27 R. Issac and J. Chmielewski, *J. Am. Chem. Soc.*, 2002, **124**, 6808–6809.

28 A. Deblais, R. Harich, D. Bonn, A. Colin and H. Kellay, *Langmuir*, 2015, **31**, 5971–5981.

29 P. A. Bachmann, P. Walde, P. L. Luisi and J. Lang, *J. Am. Chem. Soc.*, 1991, **113**, 8204–8209.

30 P. A. Bachmann, P. L. Luisi and J. Lang, *Chimia (Aarau).*, 1991, **45**, 266–268.

31 P. A. Bachmann, P. Walde, P. L. Luisi and J. Lang, *J. Am. Chem. Soc.*, 1990, **112**, 8201–8203.

32 K. Edwards, M. Silvander and G. Karlsson, *Langmuir*, 1995, **11**, 2429–2434.

Chapter 4

Conclusions and future work

4. Conclusions and future work.

The aim of this work was to develop and characterise novel examples of physical autocatalysis driven by irreversible bond-forming reactions. This goal was achieved and extended to the single-particle level using iSCAT, revealing previously unknown features of these reactions. The ground has now been laid for more ambitious demonstrations of competition and selection processes between physical autocatalysts and the study of the dynamics of individual micelles and vesicles with unprecedented sensitivity.

4.1. Limitations of experimental work

The primary limitation of the work described in Chapter 2 is the choice to use NMR spectroscopy to characterise the reaction kinetics. NMR spectroscopy provides rich structural information and can simultaneously measure the changing concentrations and chemical environments of the various species present in these systems and complements the DOSY NMR studies we used to probe the mechanism. However it also imposes a limitation on the range of accessible concentrations owing to its low sensitivity, and produced noisy kinetic data. While autocatalytic systems are known to exhibit poorly-reproducible kinetics, particularly with regards to the length of the lag period,[1] the analysis procedure used here introduced further sources of noise, specifically poor integration of signals owing to sample heterogeneity and variations in sample concentration arising from the sampling process. As can be seen in Figure 2.10, even direct sampling of the aqueous layer without dilution led to considerable noise in the kinetic data.

We opted to use NMR spectroscopy for its simplicity and accessibility. In hindsight this was a sub-optimal choice, and an assay based on reverse phase HPLC-MS or other chromatographic techniques may have proven superior. Alternatively, in situ IR analysis using a ReactIR system may have provided high quality data by eliminating errors arising from sampling. In general, the development of in situ analysis methods for the study of biphasic systems would be hugely advantageous for future work in this area.

Obtaining robust kinetic data with low noise would have allowed more thorough kinetic studies. The quantitative comparison of the influence of chain length on reaction rate would have proven particularly valuable and complemented our DOSY NMR studies. As it is, we were left to draw conclusions from the general observation that long-chain thiols react more slowly than do shorter thiols.

Efforts towards the development of three-component reactions were limited primarily by synthetic difficulties. In general the synthesis of complex phospholipid precursors analogous to **35** requires the coupling of components of very different solubilities, and in the case of **35**, the coupling of very poorly-soluble maleimide precursors. Further maleimides are highly unstable at high pH, restricting the range of reaction conditions that can be used for their synthesis and limiting the yield of the final reaction with trimethylamine.

These substrates are nonetheless worth pursuing. Related efforts by other researchers, particularly Devaraj and colleagues,[2] have found that the biphasic synthesis of lipids from immiscible precursors is difficult. For example, the thiol-yne reaction described by Devaraj does not proceed without a surfactant owing to the oxidation of the thiol in the absence of other reaction pathways. This is not a problem under the mild reaction conditions used to drive our second-generation thiol-ene reaction, and as such the successful synthesis of compound **35** can be expected to lead to the successful de novo synthesis of lipids under autocatalytic conditions.

The study of our first-generation reaction by iSCAT was surprising and pleasing in equal measure. Our initial goal was simply to visualise micelles of **3c**. This in itself is an achievement: the optical detection of unlabelled, mobile <5 nm micelles in real time has not to our knowledge been reported before. Measuring the reaction kinetics by iSCAT has advantages and disadvantages compared to NMR. It is limited in that once the coverslip is saturated the kinetics can no longer be monitored, thus restricting measurement to the lag period and the initial moments of the reaction. Further at this point we are unable to distinguish between particles on the basis of composition or lamellarity, being restricted to size alone. In this sense NMR is superior, allowing complete kinetic profiles to be obtained for each reaction component that gives isolated peaks.

However, iSCAT gives much cleaner, less noisy data for the window in which observation is possible. Further, this window is perhaps the most interesting region of a physical autocatalytic reaction, reflecting the gradual accumulation of product through background pathways and the onset of autocatalysis. In this sense iSCAT serves as a powerful technique for the in situ analysis of autocatalytic reaction kinetics. Qualitative examination of Figure 3.4 reveals close agreement with our observations regarding physical autocatalysis: within an individual reaction the data are of high quality, but there is considerable variation between nominally identical experiments. This variation appears in both the duration of the lag period and in the gradient of the reaction period. These differences most likely arise from unavoidable differences in the physical geometry of each reaction and the relative position of the observation region and the reactive interface. As such, iSCAT serves to validate our previous observation that physical autocatalysis is a highly contingent process which relies on a variety of physical parameters.

The work described in Chapter 3 sets an important precedent for future studies of physical autocatalysis. While super-resolution fluorescence microscopy and indeed iSCAT studies of lipid aggregates have been reported previously, to our knowledge this is the first time a super-resolution microscopy technique has been applied to physical autocatalysis. The use of iSCAT rather than a fluorescence-based method has considerable advantages, providing superior temporal resolution and spatial precision, and being limited only by the sensitivity of the imaging camera rather than the behaviour of a fluorescent label. We have revealed remarkably complex phenomena occurring on the nanometre scale during physical autocatalysis, opening up many more questions than have been answered here.

4.2. Recommended future work

4.2.1. Development of successful synthetic and autocatalytic conditions

A number of the systems described in Chapter 2 failed to reach fruition, owing either to difficulties in the synthesis and purification of precursors, or our inability to find suitable reaction conditions. These ought to be revisited.

The CuAAC reactions are highly promising, giving good yields in the presence of phenylenediamine. If a suitable analytical technique can be identified, most likely reverse phase HPLC, the reaction of **24** and linear terminal alkynes ought to be readily characterised and hopefully shown to be autocatalytic. The failure of the reaction shown in Figures 2.9 and 2.10 is likely the result of catalyst deactivation in the presence of oxygen introduced during the sampling process. This may be remedied by increasing the pressure of the inert atmosphere, increasing the quantity of the ascorbate reductant, or by more rigorously degassing the solvent through freeze-pump-thaw cycles.

Analysis of this system by DOSY NMR may offer insight into the location of the reaction site, as indicated by the partitioning of the catalyst between the micelle and bulk solution. If other reaction conditions using ligands of varying polarity can be found, a more systematic exploration of the influence of catalyst hydrophobicity can be attempted. Ultimately this work may allow the fine control of the dominant reaction pathway in a physical autocatalytic system, similar to the use of membrane-bound catalysts by Sugawara and co-workers.

These conditions have not yet been applied to **33** or **44**. In the case of **44** these conditions ought to be easily applied and may be expected to quickly lead to positive results. Before these can be applied to **33**, however, a more reliable purification procedure must be identified. Further study of these systems would benefit from the study of the reactivity of **44** first in order to gain experience in the study of micelle-to-vesicle transitions before attempting the de novo synthesis of lipids through the reaction of **33**.

The synthesis of dimaleimide compound **35** is challenging owing to the poor solubility of its precursors. It can be expected that with further work this synthetic route will succeed, however. If not, alternative retrosyntheses can be identified, or different substrates designed which are more synthetically accessible. With these compounds in hand, autocatalysis can be expected to occur under the same or similar conditions to compound **9**. As with compound **33** fully characterising this system can be expected to be challenging. While the high reactivity of the maleimide moiety should overcome the intrinsically low reactivity of biphasic systems, a problem reported by other researchers,[2] multiple possible reaction pathways exist in these systems.

As noted in Chapter 2, Devaraj and co-workers recently described the thiol-yne reaction of a close analogue of compound **49**.[2] Applying their reaction conditions to compound **49** ought to enable this project to move forward.

4.2.2. Elaboration of substrate scope

The work described in this thesis clearly demonstrates that physical autocatalysis can be driven by irreversible covalent bond-forming reactions. One immediate priority is to extend the scope of compatible reactions. In particular, prebiotically-plausible reactions should be explored.

A disadvantage of the systems studied herein is their lack of prebiotic plausibility. Proposed prebiotic syntheses of phosphocholine lipids have been reported,[3,4] but regardless phospholipids of this kind are not commonly accepted as having existed on the early earth.[5,6] As such, complex phospholipids bearing Michael acceptors similar to **1** and **9** are simply not plausible prebiotic molecules.

The aim of this work was not to develop reactions that may have occurred historically, but rather to model relevant behaviours; as such, the implausibility of the substrates here is not a major flaw. Nonetheless the development of prebiotically plausible self-reproducing micelles would provide enrich the inventory of prebiotic components, extending the set of substrates which could plausibly have formed the membranes of the earliest protocells. These studies would serve to link the model studies described here to historically plausible scenarios, enhancing the value of this work to the research community.

4.2.3. Competition and selection between physical autocatalysts

The reactions established here can now be used to develop more ambitious studies of prebiotic behaviour. Competition and selection experiments analogous to those reported with other classes of autocatalyst[7] may provide insight into fundamental aspects of autocatalysis and prebiotic behaviour. Such experiments would be valuable and the systems described here provide the conceptual basis required for their development. A brief justification for this claim is given here, followed by a proposed starting point for this research. A fuller discussion of this proposal has been published in *Orig. Life Evol. Biospheres*.[8]

As discussed in Chapter 1, the lipid world proposed by Segré *et al.*[9] postulates that the first form of life was a population of auto- and mutually-catalytic lipid aggregates such as micelles or vesicles. If the composition of each aggregate is inherited upon division then compositions that provide an advantage, such as a high autocatalytic efficiency or a tendency to divide, may come to dominate the system. This is claimed to enable some form of evolution in such systems. However, there is little direct experimental evidence that the lipid world and related ideas have merit: that a prebiotic population of micelles and vesicles of variable composition and auto- or cross-catalytic efficiency might have been subject to some form of natural selection, and hence a viable step from the primordial ooze towards the first living organism. Clearly there is room and need for further demonstrations of selection between physical autocatalysts.

While a limited form of competition between autocatalytic hydrolysis reactions has been demonstrated,[10] bond-forming reactions offer the potential of combinatorial synthesis. In hydrolysis reactions, each precursor can give rise to a limited number of surfactants or co-surfactants. For instance, oleate hydrolysis yields oleate and oleic acid, forming self-buffered vesicles,[11] while hydrolysis of octyl octanoate gives octanoate and the octanol co-surfactant necessary for aggregation.[12] The hydrolysis of non-symmetrical anhydrides could yield two different surfactant molecules, but generally to observe the competition of aggregates of n surfactants, one must begin with at least $n/2$ precursors. This limitation is practical rather than fundamental: molecules with multiple hydrolysis sites could yield more than two surfactant products.

The use of bond-forming reactions overcomes this limitation. From n hydrophilic ‘head’ precursors and m hydrophobic ‘tail’ precursors, one would obtain up to $n \times m$ amphiphilic products which could act as competing autocatalysts. Studying the competition between surfactants synthesised under these conditions may provide valuable evidence for the lipid world model. As discussed in section 2.2, using micelles rather than vesicles is advantageous here: micelles typically have lower aggregation numbers than vesicles, potentially increasing the sensitivity of catalytic function to compositional variation.

A starting point for this line of research would be to mix Michael acceptor **1** with an excess of two alkyl thiols, such a hexanethiol **2b** and decanethiol **2a.** The product distribution will be determined by several factors, including the higher solubility and hence reactivity of **2b** compared to **2a**, the lower CMC of product **3a** compared to **3b**, and any selectivity arising from autocatalytic effects. The product distribution can be expected to change over time as autocatalytic pathways come into operation. After determining a set of conditions yielding a reproducible product distribution, the reaction should then be repeated in the presence of varying quantities of each product.

If micelles of either product exert any selectivity towards one or the other thiol, this ought to be reflected in the product distribution. Initially, the final distribution following complete consumption of **1**, the limiting reagent, would be analysed by LC-MS. If the evolution of product distribution over time is reproducible then transient biases in the product distribution towards one or the other product could also be looked for. Even a transient alteration of the product distribution would be an exciting result indicating the potential for selectivity in these systems.

4.2.4. Re-examination of small micellar systems by iSCAT

The work carried out in Chapter 3 was limited by the sensitivity of the camera used for imaging. In order to detect small micelles we had to average hundreds of individual frames, reducing our time resolution by orders of magnitude. The data were recorded at 1 kHz, but as a result of frame binning our time resolution is on the order of hundreds of milliseconds.[13] On this timescale the micelles diffuse a significant distance, blurring the resulting image, lowering the contrast, and thus giving a higher detection threshold than would otherwise be possible.

To address this limitation the Kukura group has purchased a highly sensitive cardiac imaging camera. This is around three orders of magnitude more sensitive than the instrument used here and can record images at 2.5 kHz. Once an iSCAT instrument equipped with this camera is in operation, we ought to be able to robustly detect even very small (R_H ~ 1 nm) micelles without the need to average hundreds of frames.

This will enable us to study the thiol-ene reactions developed in Chapter 2 using iSCAT. In contrast to compound **3c**, compounds **3b** and **15** do not form any vesicles. By limiting the nature of the product aggregates in this way we should be able to better understand the observed behaviour and distinguish between different particle types by iSCAT. Observing the reactive interface generated in these systems may reveal aspects of their behaviour that are hidden in ensemble studies. For instance, at the interface these compounds may form more complex aggregates than micelles.

4.2.5. Characterisation of laser-dependent reactivity

The system examined by iSCAT in Chapter 3 exhibited laser-dependent behaviour: for example, the conversion of micelles of **3c** to a supported bilayer was only observed in illuminated regions. These effects are likely in part the result of the incident power at the sample, approx. 10 kW/cm^2 and may be expected to complicate future high-speed imaging studies.

Characterising these or other illumination-dependent behaviours would aid future work by allowing for this variable to be accounted for, and potentially by informing the design of substrates for future studies. To address this in the case of bilayer formation, we propose to use two illumination sources. Here the primary iSCAT beam will be of a much lower incident power and hence temporal resolution, allowing the wide-field observation of the phase transition from bound particles to supported bilayer. A second, high-powered incident beam will then be applied to a small area within this field. If bilayer formation is indeed induced by the high-powered incident beam, this experiment ought to allow the controlled initiation of this rearrangement.

If this assay can be successfully developed then it may prove to be a general test for laser-induced behaviour, allowing more comprehensive characterization of the factors driving complex behaviour in physical autocatalytic systems.

4.2.6. Development a of robust iSCAT assay

The studies reported in Chapter 3 relied on some serendipity. A critical factor in achieving reliable binding of well-defined particles is the surface chemistry, which must interact favourably with the product aggregates. In addition to the effects of the surface noted in Chapter 3, preliminary experiments with other systems including oleate vesicles revealed variable behaviour depending upon the surfactant structure and surface preparation method.

Further, the behaviours observed in Chapter 3 occur in a complex environment, making the isolation of individual events difficult. While these conditions are well-suited to kinetic studies, more detailed mechanistic questions require more control.

To achieve this a reliable immobilisation protocol for vesicles should be developed. The general technique of passivating a surface towards nonspecific binding and including a low concentration of a biomolecule to enable specific binding is well-developed in single-molecule methodology. A particularly promising approach involves the passivation of the surface using polysorbate, with specific binding mediated by the interaction of streptavidin with biotin.[14] This would allow the immobilisation of a small number of 'seed' vesicles on the surface for detailed study.

By studying the dynamics of growth and potentially division during the addition or autocatalytic synthesis of fresh surfactant we may be able to quantify the kinetics of these processes on the single-particle level with high reproducibility and remarkable sensitivity. This may also aid the study of micelle-to-vesicle transitions starting from immobilised micelles, the matrix effect in vesicle division, and the development of more complex p incorporating model metabolic or genetic systems.

4.3. Conclusion

Chapter 1 noted that between us and an account of the origins of life lie both conceptual and technological barriers. The work described herein attempted to address aspects of each problem in turn.

Conceptually, we are now in a position to attempt thorough experimental studies of competition and selection processes between different physical autocatalysts (see section 4.2.3). Such experiments may inform our understanding of whether physical autocatalysts could ever be considered living systems subject to natural selection.

Technically, we have directly observed the dynamics and self-reproduction of micelles and vesicles for the first time. Using single-particle microscopy revealed the remarkable complexity evident on the nanometre scale in even simple autocatalytic reactions. The further development of this project can be expected to deepen our understanding of physical autocatalysis and the origins of life.

4.4. References

1 M. P. Mower and D. G. Blackmond, *J. Am. Chem. Soc.*, 2015.

2 C. Y. Zhou, H. Wu and N. K. Devaraj, *Chem. Sci.*, 2015, **6**, 4365–4372.

3 M. Rao, J. Eichberg and J. Oró, *J. Mol. Evol.*, 1982, **18**, 196–202.

4 W. R. Hargreaves, S. J. Mulvihill and D. W. Deamer, *Nature*, 1977, **266**, 78–80.

5 P.-A. Monnard and D. W. Deamer, *Anat. Rec.*, 2002, **268**, 196–207.

6 A. Pohorille and D. Deamer, *Res. Microbiol.*, 2009, **160**, 449–56.

7 A. J. Bissette and S. P. Fletcher, *Angew. Chem. Int. Ed.*, 2013, **52**, 12800–12826.

8 A. J. Bissette and S. P. Fletcher, *Orig. Life Evol. Biosph.*, 2015, **45**, 21–30.

9 D. Segré, D. Ben-Eli, D. W. Deamer and D. Lancet, *Orig. Life Evol. B.*, 2001, **31**, 119–145.

10 K. Kurihara, M. Tamura, K. Shohda, T. Toyota, K. Suzuki and T. Sugawara, *Nat. Chem.*, 2011, **3**, 775–781.

11 P. Walde, R. Wick, M. Fresta, A. Mangone and P. L. Luisi, *J. Am. Chem. Soc.*, 1994, **116**, 11649–11654.

12 P. A. Bachmann, P. Walde, P. L. Luisi and J. Lang, *J. Am. Chem. Soc.*, 1990, **112**, 8201–8203.

13 J. Ortega Arroyo, J. Andrecka, K. M. Spillane, N. Billington, Y. Takagi, J. R. Sellers and P. Kukura, *Nano Lett.*, 2014, **14**, 2065–70.

14 B. Hua, K. Y. Han, R. Zhou, H. Kim, X. Shi, S. C. Abeysirigunawardena, A. Jain, D. Singh, V. Aggarwal, S. A. Woodson and T. Ha, *Nat. Methods*, 2014, **11**, 1233–1236.

Chapter 5

Experimental section

5. Experimental Section

5.1. General experimental.

Synthetic intermediates that were isolated in pure form but are not referred to in the results and discussion chapters are not assigned compound numbers. Compound names are non-IUPAC and provided solely for reference; where trivial names were not available, names were generated using ChemBioDraw Ultra 14 software. Some of the data in this chapter have previously been published in *Nat. Commun.*[1]

Procedures using oxygen- and/or moisture-sensitive materials were performed with anhydrous solvents under an atmosphere of anhydrous argon in flame-dried flasks, using standard Schlenk techniques. Analytical TLC was performed on precoated glass-backed plates (Silica Gel 60 F_{254}; Merck), and visualised using aqueous ceric ammonium molybdate (CAM), aqueous basic potassium permanganate, or ninhydrin stains. Flash column chromatography was carried out using Apollo Scientific silica gel 60 (0.040 – 0.063 nm), Merck 60 Å silica gel, VWR (40-63 µm) silica gel and Sigma Aldrich silica gel. Pressure was applied at the column head via a flow of nitrogen with the solvent system used in parentheses.

Unless stated otherwise, commercially available reagents were purchased from Sigma-Aldrich, Fisher Scientific, Apollo Scientific, Alfa Aesar or TCI UK and were used without purification. Petroleum ether refers to light petroleum boiling in the range 40-60 °C. Deuterated solvents were purchased from Sigma-Aldrich.

Dry $CHCl_3$, THF, CH_2Cl_2, Et_2O, toluene, benzene, hexane, pentane, DMF, and acetonitrile were collected fresh from an mBraun SPS-800 solvent purification system having been passed through anhydrous alumina columns. Dry methanol and DMSO were purchased from Sigma-Aldrich with a Sure/Seal. All other dry solvents were dried over 3 Å molecular sieves and stored under argon. All other solvents were used as purchased from Sigma-Aldrich, Rathburn, or Fisher Scientific.

Cooling of reaction mixtures to 0 °C was achieved using an ice-water bath. Cooling to –10 °C was achieved using a salt-ice bath. Cooling to –78 °C was achieved using a dry ice-acetone bath. Other temperatures were obtained by using a Julabo FT902 immersion cooler or the heating plate of the stirrer.

All NMR spectra were recorded at rt. NMR spectra were recorded using Bruker DPX-200 (200 MHz), DPX-250 (250 MHz), DRX-500 (500 MHz) or AVC-500 (500 MHz) spectrometers. ^{13}C and ^{31}P NMR spectra were recorded using Bruker AVC-500 (500/125 MHz) and DRX-500 (500/200 MHz) spectrometers respectively. Chemical shifts are reported in ppm from the residual solvent peak. Chemical shifts (δ) are given in ppm and coupling constants (*J*) are quoted in hertz (Hz). Resonances are described as s (singlet), d (doublet), t (triplet), q (quartet), and m (multiplet).

DOSY NMR measurements were performed using a Bruker AVII-500 equipped with a TFI probehead at 298 K using the 2D sequence for diffusion measurement using double stimulated echo for convection compensation and longitudinal eddy current delay, using bipolar gradient pulses for diffusion, and using three spoil gradients (Bruker terminology: dstebpgp35) pulse sequence.[2,3] The samples were thoroughly mixed using a Vortex Genie 2 mixer (Scientific Industries), and were then clarified using a hand centrifuge (Hettich, model 1011), and then measured. Samples containing saturated thiol consequently had a small layer of neat thiol above the D_2O layer; sufficient D_2O was used to ensure that the thiol layer was not detectible by the

NMR probe. Experiments were performed in two stages: initially 1D edited DOSY experiments were used to optimise the diffusion period Δ for each compound. The 2D dstebpgp35 sequence was then used, based on the optimised Δ from the previous procedure and with δ = 4 ms, with gradient amplitude ranging from 2% to 85% with 16 points in between. Data were analysed using the T1T2 module in TOPSPIN 3.2, and plots were generated using the eddosy module.

High-resolution mass spectra were recorded using a Bruker MicroTOF spectrometer by the internal service at the University of Oxford. Low-resolution mass spectra were recorded using a Walters LCT premier XE.

Infrared measurements (thin film) were carried out using a Bruker Tensor 27 FTIR with internal calibration in the range 4000-600 cm^{-1}.

Optical rotations were recorded using a Perkin-Elmer 241 polarimeter at 25 °C in a 10 cm cell in the stated solvent. $[\alpha]_D$ values are given in 10^{-1} deg·cm^2 g^{-1}, with concentration c given as g/100 mL.

Melting points of recrystallised compounds were measured on a Reichert melting point stage and are uncorrected. Recrystallisation solvents are reported in parentheses.

Fluorimetry was performed using a Varian Cary Eclipse Fluorescence Spectrophotometer (Varian, Oxford, UK) with Cary Eclipse software. The slit width for both excitation and emission was set at 5 nm.

Chiral GC measurements were conducted on a HP6890 (H_2 as vector gas) or HP6850 (H_2 as vector gas) GC using a Chirasil-L-Val column (Agilent). Samples were injected through a split inlet at 250 °C and detected by flame ionisation at 300 °C. Temperature programs are described as follows: initial temperature (°C) - initial time (min) - temperature gradient (°C/min) - final temperature (°C) – holding time.

pD measurements of samples in D_2O were made using a Jenway 3510 pH meter calibrated using standard reference samples in H_2O. pD values were estimated from the observed pH* values according to Krężel and Bal.[4]

DLS measurements were recorded using a Viscotek 802 DLS instrument and analysed with OmniSize software. All samples were prepared in ultrapure Milli-Q water and filtered through 0.2 µm PTFE filters before measuring. Reported data are the result of 10 × 10 second measurements.

5.1.1. Distillation of trimethylamine

Pure trimethylamine was obtained by distillation from a 45% w/w solution in H_2O. Gaseous trimethylamine was liberated from the solution by addition of KOH pellets at rt with the rate of evolution controlled by adjusting the rate of stirring. The gas was passed over KOH pellets and then $CaCl_2$ pellets, and condensed in a flame-dried trap at -78 °C. The pure liquid was transferred to reactions using a chilled syringe under argon. Trimethylamine was generally used within 3 h of being distilled; when overnight storage was required, the liquid was stored at -78 °C under a positive pressure of dry argon.

5.2. Synthesis of reaction components.

Oleyl mercaptan 2c

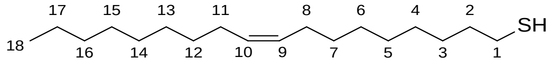

To a stirred solution of oleyl alcohol (85%, 1.0 mL, 2.7 mmol) and Et_3N (0.56 mL, 4.0 mmol, 1.5 eq) in CH_2Cl_2 (15 mL) was added mesyl chloride (0.23 mL, 3.0 mmol, 1.1 eq) dropwise at 0 °C. The reaction was stirred until the alcohol was fully consumed (TLC control, 1:4 Et_2O/hexane) and then diluted with H_2O (10 mL). The layers were separated and the organic layer was washed sequentially with aqueous HCl (1 M, 10 mL), $NaHCO_3$ (saturated, 10 mL) and brine (10 mL). The organic layer was dried ($MgSO_4$) and concentrated in vacuo to give the crude mesylate (1.1 g), which was used without further purification.

The crude mesylate (1.1 g) and thiourea (250 mg, 3.3 mmol, 1.05 eq) were refluxed in EtOH (2 mL) for 5h. Aqueous NaOH (2.5 M, 2 mL) was added and the solution refluxed for a further 2 h. The solution was allowed to cool to rt and acidified with HCl (2 M), and then extracted twice with Et_2O (15 mL). The combined organic layers were washed with brine (30 mL), dried ($MgSO_4$) and concentrated in vacuo. The crude product was purified by flash column chromatography (hexane; SiO_2) to give pure oleyl thiol **2c** (200 mg, 0.70 mmol, 26% yield).

^{1}H NMR (400 MHz, $CDCl_3$) δ_H / ppm 5.38 (m, 2 H, $C\underline{H}$-9 and $C\underline{H}$-10), 2.51 (q, J = 7.4 Hz, 2 H, $C\underline{H}_2$-1), 1.98 (m, 4 H, $C\underline{H}_2$-8 and $C\underline{H}_2$-11), 1.59 (q, J = 7.4 Hz, 2 H, $C\underline{H}_2$-2), 1.44 – 1.16 (m, 22 H, $(CH_2)_5$-3-7 and $(CH_2)_6$-12-17), 0.88 (t, J = 6.7 Hz, 3 H, $C\underline{H}_3$-18).

^{13}C NMR (101 MHz, $CDCl_3$) δ_C / ppm 130.1, 129.9, 34.2, 32.8, 32.1, 29.9, 29.9, 29.7, 29.6, 29.5, 29.4, 29.2, 28.5, 27.4, 27.3, 24.8, 22.8, 14.3.

HRMS (EI/FI) *m/z* calcd for $C_{18}H_{36}S$ $[M]^+$: 284.2538, found: 284.2531.

Decyl-*S*-PC 3a

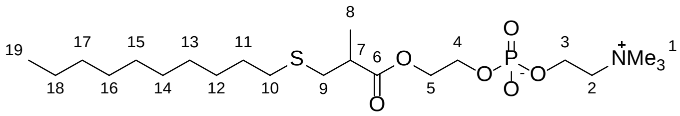

Synthesised according to Matsuno *et al.*[5] A solution of **1** (100 mg, 0.34 mmol) and **2a** (78 µL, 0.37 mmol, 1.1 eq) in EtOH (1 mL) was degassed by bubbling Ar gas through it for 20 min. DIPA (cat.) was added and the reaction was stirred for 18 h. The solvent was removed in vacuo and the residue was washed with hexane. The sample was freeze-dried to give pure **3a** (106 mg, 0.23 mmol, 67%).

^{1}H NMR (400 MHz, CD_3OD) δ_H / ppm 4.35 – 4.20 (m, 4 H, C$\underline{H}_2$-3 and C$\underline{H}_2$-5), 4.07 (dt, *J* = 7.1, 4.9 Hz, 2 H, C$\underline{H}_2$-4), 3.70 – 3.59 (m, 2 H, C$\underline{H}_2$-2), 3.23 (s, 9 H, N(C$\underline{H}_3$)$_3$-1), 2.81 (dd, *J* = 12.6, 7.4 Hz, 1 H, C$\underline{H}_A$CH$_B$-9), 2.71 (m, 1 H, C$\underline{H}$-7), 2.60 (dd, *J* = 12.6, 6.2 Hz, 1 H, CH$_A$C$\underline{H}_B$-9), 2.53 (t, *J* = 7.1 Hz, 2 H, C$\underline{H}_2$-10), 1.57 (m, 2 H, C$\underline{H}_2$-11), 1.44 – 1.26 (m, 14 H, (C$\underline{H}_2$)$_7$-12-18), 1.24 (d, *J* = 6.9 Hz, 3 H, C$\underline{H}_3$-8), 0.90 (t, *J* = 6.8 Hz, 3 H, C$\underline{H}_3$-19).

^{13}C NMR (101 MHz, CD_3OD) δ_C / ppm 175.4, 66.2 – 66.0 (m), 63.8 (d, *J* = 7.9 Hz), 63.3 (d, *J* = 5.5 Hz), 59.0 (d, *J* = 5.3 Hz), 53.5 – 53.1 (m), 40.2, 34.9, 32.0, 31.7, 29.4, 29.3, 29.1, 29.0, 28.5, 22.4, 15.8, 13.1.

^{31}P NMR (200 MHz, CD_3OD) δ_p / ppm 0.80.

MS (ESI) *m/z*: 470.3 $[M+H]^+$.

IR (MeOH, v_{max}/cm^{-1}): 3382, 2925, 2854, 1725, 1652, 1460, 1217, 1082, 967.

Hexyl-*S*-PC 3b

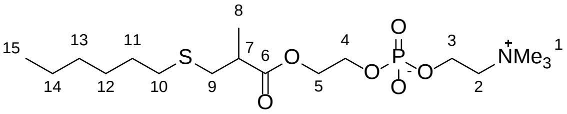

Synthesised according to Matsuno *et al.*[5] A solution of **1** (2.50 g, 8.47 mmol) and **2b** (1.30 mL, 9.15 mmol, 1.08 eq) in EtOH (10 mL) was degassed by bubbling Ar gas through it for 20 min. DIPA (cat.) was added and the reaction was stirred for 18 h. The solvent was removed in vacuo and the residue washed with hexane and then acetone. The sample was freeze-dried to give pure **3b** (2.45 g, 5.92 mmol, 70%).

^{1}H NMR (500 MHz, CD_3OD) δ_H / ppm 4.36 - 4.20 (m, 4 H, $C\underline{H}_2$-3 and $C\underline{H}_2$-5), 4.08 (dt, *J* = 7.0, 4.9 Hz, 2 H, $C\underline{H}_2$-4), 3.69 - 3.60 (m, 2 H, $C\underline{H}_2$-2), 3.24 (s, 9 H $N(C\underline{H}_3)_3$-1), 2.80 (dd, *J* = 13.7, 7.4 Hz, 1 H, $C\underline{H}_AH_B$-9), 2.71 (m, 1 H, $C\underline{H}$-7), 2.60 (dd, *J* = 12.9, 6.3 Hz, 1 H, $CH_AC\underline{H}_B$-9), 2.53 (t, *J* = 7.3 Hz, 2 H, $C\underline{H}_2$-10), 1.56 (quin, *J* = 7.4 Hz, 2 H, $C\underline{H}_2$-11), 1.45 - 1.26 (m, 6 H, $(C\underline{H}_2)_3$-12-13-14), 1.24 (d, *J* = 6.9 Hz, 3 H, $C\underline{H}_3$-8), 0.91 (t, *J* = 7.0 Hz, 3 H, $C\underline{H}_3$-15).

^{13}C NMR (125 MHz, CD_3OD) δ_C / ppm 176.9, 67.5 (dt, *J* = 7.4, 3.1 Hz), 65.3 (d, *J* = 7.9 Hz), 64.7 (d, *J* = 5.5 Hz), 60.5 (d, *J* = 5.0 Hz), 54.8 (t, *J* = 3.8 Hz), 41.6, 36.3, 33.4, 32.6, 30.7, 29.6, 23.7, 17.3, 14.5.

^{31}P NMR (200 MHz, CD_3OD) δ_p / ppm 0.81.

HRMS (ESI) *m/z* calcd for $C_{17}H_{36}NNaO_6PS$ $[M+Na]^+$: 436.1893, found: 436.1892.

Oleyl-*S*-PC 3c

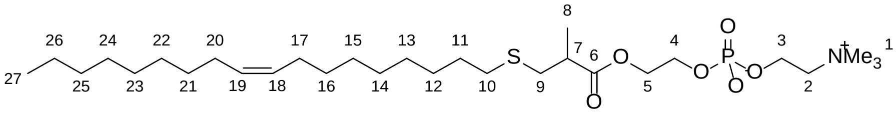

Synthesised according to Matsuno *et al.*[5] A solution of **1** (100 mg, 0.34 mmol) and **2c** (106 mg, 0.37 mmol, 1.1 eq) in EtOH (1 mL) was degassed by bubbling Ar gas through it for 15 min. DIPA (cat.) was added and the reaction was stirred for 18 h. The solvent was removed in vacuo and the residue washed with hexane and then purified by flash column chromatography (65:35:5 $CHCl_3$/MeOH/H_2O; SiO_2). The sample was freeze-dried to give pure **3c** (125 mg, 0.22 mmol, 64%).

^{1}H NMR (500 MHz, CD_3OD) δ_H / ppm 5.49 – 5.40 (m, 2 H, C$\underline{H}$-18 and C$\underline{H}$-19), 4.41 – 4.32 (m, 4 H, C$\underline{H}_2$-3 and C$\underline{H}_2$-5), 4.15 (dt, *J* = 7.0, 4.9 Hz, 2 H, C$\underline{H}_2$-4), 3.75 – 3.70 (m, 2 H, C$\underline{H}_2$-2), 3.31 (s, 9, N(C$\underline{H}_3$)$_3$-1), 2.89 (dd, *J* = 12.9, 7.4 Hz, 1 H, C$\underline{H}_A$H$_B$-9), 2.79 (m, 1 H, C$\underline{H}$-7), 2.68 (dd, *J* = 12.9, 6.4 Hz, 1 H, CH$_A$H$_B$-9), 2.60 (t, *J* = 7.3 Hz, 2 H, C$\underline{H}_2$-10), 2.16 – 2.02 (m, 4 H, C$\underline{H}_2$-17 and C$\underline{H}_2$-20), 1.64 (quin, *J* = 7.3 Hz, 2 H, C$\underline{H}_2$-11), 1.51 – 1.35 (m, 22 H, (C$\underline{H}_2$)$_{11}$-12-16 and 21-26), 1.32 (d, *J* = 6.9 Hz, 3 H, C$\underline{H}_3$-8), 0.98 (t, *J* = 6.8 Hz, 3 H, C$\underline{H}_3$-27).

^{13}C NMR (126 MHz, CD_3OD) δ_C / ppm 176.7, 131.5, 131.5, 67.4 (dt, *J* = 6.7, 3.0 Hz), 65.2 (d, *J* = 7.8 Hz), 64.7 (d, *J* = 5.4 Hz), 60.4 (d, *J* = 5.0 Hz), 55.0 – 54.4 (m), 41.6, 36.3, 33.6, 33.4, 33.1, 33.1, 30.8, 30.8, 30.6, 30.6, 30.5, 30.5, 30.4, 30.2, 30.1, 29.9, 29.9, 28.1, 23.8, 17.2, 14.5.

^{31}P NMR (202 MHz, CD_3OD) δ_p / ppm 0.83.

HRMS (ESI) *m/z* calcd for $C_{29}H_{59}NO_6PS$ [M+H]$^+$: 580.37952, found: 580.37900.

4,10-Dioxatricyclo[5.2.1.0^{2,6}]-dec-8-ene-3,5-dione 6

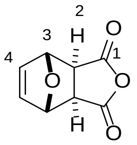

Synthesised according to Heath *et al.*[6] To a solution of maleic anhydride (4 g, 40.8 mmol) in benzene (20 mL) was added furan (3 mL, 41.3 mmol, 1.01 eq). The reaction was stirred for 18 h and the resultant precipitate filtered and washed with cold Et_2O to give pure **6** as an amorphous white solid (4.0 g, 24.1 mmol, 59%). None of the corresponding *endo* product was observed by ^{1}H NMR.

^{1}H NMR (400 MHz, DMSO-d_6) δ_H / ppm 6.58 (s, 2 H, C<u>H</u>-4), 5.34 (s, 2 H, C<u>H</u>-3), 3.31 (s, 2 H, C<u>H</u>-2).

^{13}C NMR (101 MHz, DMSO-d_6) δ_C / ppm 172.0, 137.3, 82.1, 49.6.

MS (ESI) *m/z*: 167.1 $[M+H]^+$.

4-(2-Hydroxyethyl)-10-oxa-4-azatricyclo[5.2.1.0^{2,6}]-dec-8-ene-3,5-dione 7

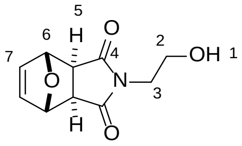

Synthesised according to Heath *et al.*[6] To a stirred suspension of **6** (3.75 g, 22.6 mmol) in dry MeOH (10 mL) was added ethanolamine (1.37 mL, 22.6 mmol, 1.0 eq). The solid dissolved upon addition and the solution was heated for 24 h at reflux. The reaction was allowed to cool to rt and then cooled at -20 °C for 18 h. The resultant crystals were collected by filtration to give pure **7** (2.77 g, 13.2 mmol, 59%).

^{1}H NMR (400 MHz, DMSO-d_6) δ_H / ppm 6.55 (s, 2 H, C<u>H</u>-7), 5.12 (s, 2 H, C<u>H</u>-6), 4.79 (t, *J* = 5.8 Hz, 1 H, CH_2O<u>H</u>), 3.50 – 3.37 (m, 4 H, C<u>H</u>$_2$-2 and C<u>H</u>$_2$-3), 2.92 (s, 2 H, C<u>H</u>-5).

^{13}C NMR (101 MHz, DMSO-d_6) δ_C / ppm 177.0, 136.9, 80.7, 57.7, 47.6, 41.1.

MS (ESI) *m/z*: 210.4 $[M+H]^+$.

Mp = 133.8 – 136.1 °C (MeOH).

2-Maleimidoethanol 8

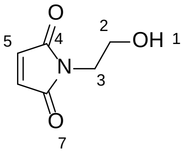

Synthesised according to Heath *et al.*[6] A suspension of **7** (3.75 g) in dry toluene (40 mL) was stirred in a round-bottomed flask equipped with a Vigreux condenser and a drying tube loaded with $CaCl_2$. The suspension was heated at reflux for 7 h to give a clear solution which was then filtered while still hot. The filtrate was allowed to cool to rt and then cooled to 2-8 °C overnight. The resultant white crystals were collected by filtration to give pure **8** (1.75 g, 12.4 mmol, 69%).

^{1}H NMR (400 MHz, DMSO-d_6) δ_H / ppm 7.01 (s, 2 H, C<u>H</u>-5), 4.79 (m, 1 H, CH_2O<u>H</u>), 3.46 (m, 4 H, C<u>H</u>$_2$-2 and C<u>H</u>$_2$-3).

^{13}C NMR (101 MHz, DMSO-d_6) δ_C / ppm 171.1, 134.5, 75.0, 57.9.

MS (ESI) *m/z* 164.1 $[M+Na]^+$.

Mp = 69.6 – 71.4 °C (toluene).

Maleimidophosphorylcholine 9

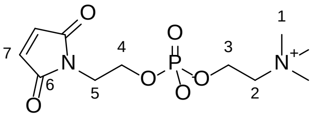

A solution of **8** (4.30 g, 30.5 mmol) and Et_3N (6.4 mL, 45.7 mmol, 1.5 eq) in dry THF (200 mL) was cooled to 0 °C and 2-chloro-1,3,2-dioxaphospholane 2-oxide (3.2 mL, 33.5 mmol, 1.1 eq) was added dropwise. The reaction was allowed to warm to rt and to react until complete consumption of starting material (TLC control, EtOAc). The reaction mixture was filtered through SiO_2 (eluting with EtOAc) and concentrated to a solid white residue. The crude solid was added under Ar to a 100 mL pressure tube containing a stirrer bar and dry MeCN (80 mL) was added. The tube was cooled to –20 °C and freshly distilled NMe_3 (2 mL, excess), stored at –78 °C, was added. The tube was quickly sealed and then heated to 80 °C overnight. Upon cooling to rt the MeCN was decanted and a red precipitate, crude **4**, was purified by flash column chromatography (7:3 MeCN/H_2O; SiO_2) to give pure **9** (2.8 g, 9.1 mmol, 30%).

^1H NMR (700 MHz, CD_3OD) δ_H / ppm 6.83 (s, 2 H, C$\underline{H}$-7), 4.24 (m, 2 H, C$\underline{H}_2$-3), 4.01 (dt, *J* = 6.2, 5.6 Hz, 2 H, C$\underline{H}_2$-4), 3.74 (t, *J* = 5.7 Hz, 2 H, C$\underline{H}_5$-5), 3.63 (m, 2 H, C$\underline{H}_2$-2), 3.22 (s, 9 H, N(C$\underline{H}_3$)$_3$-1).

^{13}C NMR (176 MHz, CD_3OD) δ_C / ppm 172.6, 135.3 (m), 67.6 (m), 63.6 (d, *J* = 5.1 Hz), 60.6 (d, *J* = 5.1 Hz), 54.8 (m), 39.5 (d, *J* = 7.9 Hz).

^{31}P NMR (202 MHz, CD_3OD) δ_p / ppm 0.94.

HRMS (ESI) *m/z* calcd for $C_{11}H_{19}N_2NaO_6P$ $[M+Na]^+$: 329.0873, found: 329.0868.

IR (MeOH, ν_{max}/cm^{-1}): 3378, 1702, 1480, 1438, 1410, 1230, 1067.

Octyl-*S*-SPC 15

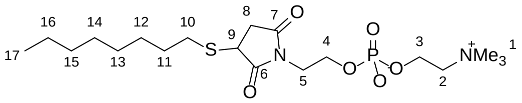

A stirred solution of **9** (500 mg, 1.6 mmol) and octanethiol **14** (0.32 mL, 1.8 mmol, 1.1 eq) in EtOH (10 mL) was degassed by gently bubbling Ar gas through it for 15 min. DIPA (cat.) was added and the reaction was stirred at rt until complete consumption of **9** (TLC control, 7:3 MeCN/H_2O, approx. 4 h). The solvent was evaporated and the residue washed with hexane (3 × 10 mL) and then freeze-dried to give pure **6** (701 mg, 95.9%).

^{1}H NMR (700 MHz, D_2O) δ_H / ppm 4.25 (br. m, 2 H, C$\underline{H}_2$-3), 4.03 (dd, *J* = 9.0, 4.1 Hz, 1 H, C$\underline{H}$-9), 4.00 (q, *J* = 5.7 Hz, 2 H, C$\underline{H}_2$-4), 3.77 (m, 2 H, C$\underline{H}_2$-5), 3.63 (m, 2 H, C$\underline{H}_2$-2), 3.31 (dd, *J* = 18.9, 8.9 Hz, 1 H, C$\underline{H}_A$$H_B$-8), 3.19 (s, 9 H, N(C$\underline{H}_3$)$_3$-1), 2.72 (m, 3 H, CH$_A$$\underline{H}_B$-8 and C$\underline{H}_2$-10), 1.59 (quin, *J* = 7.4 Hz, 2 H, C$\underline{H}_2$-11), 1.36 (m, 2 H, C$\underline{H}_2$-12), 1.32 - 1.18 (m, 8 H, (C$\underline{H}_2$)$_4$-13-16), 0.83 (t, *J* = 6.88 Hz, 3 H, C$\underline{H}_3$-17).

^{13}C NMR (176 MHz, D_2O) δ_C / ppm 179.7, 178.3, 66.0 (m), 61.9 (d, *J* = 5.1 Hz), 59.5 (d, *J* = 5.1 Hz), 54.0 (t, *J* = 4.1 Hz), 40.1, 39.6 (d, *J* = 7.6 Hz), 36.2, 31.1, 30.6, 28.4, 28.3, 28.2, 27.8, 22.0, 13.4.

^{31}P NMR (202 MHz, D_2O) δ_p / ppm 0.88.

HRMS (ESI) *m/z* calcd for $C_{19}H_{37}N_2NaO_6PS$ [M+Na]$^+$: 475.2002, found: 475.2011.

Tetra-*O*-acetyl-1-deoxy-1-azido-β-D-glucopyranose 17

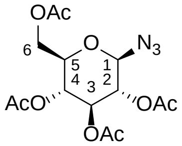

Azide **17** was synthesised according to Mahon *et al.*[7] via peracetylation of D-glucose, conversion to the 1-bromo derivative, and displacement with sodium azide as follows.

I_2 chips (500 mg, 2.0 mmol, 0.04 eq) were added in one portion to a stirred suspension of D-glucose (10.0 g, 55.7 mmol) in Ac_2O (50 mL) at rt. Upon dissolution of the solid after (approx. 1 h) and concurrent disappearance of glucose (TLC control, 2:1 petroleum ether/EtOAc), the reaction mixture was diluted with CH_2Cl_2 (50 mL) and poured into a separating funnel containing 1 M aqueous $Na_2S_2O_4$ (50 mL) and ice. Upon shaking, the intense colour faded. The aqueous layer was extracted with CH_2Cl_2 (2 × 20 mL) and the combined organic layers were washed with saturated aqueous $NaHCO_3$ (3 × 20 mL), dried (Na_2SO_4) and concentrated in vacuo to yield the peracetylated product (23 g, quantitative yield, α:β ~ 6:1) as an amorphous white solid. Analytical samples were further purified by filtration through silica (eluting with 1:1 EtOAc/petroleum ether). The anomeric ratio was determined by ^{1}H NMR and the proton spectrum was assigned as a 1:0.15 α:β mixture with reference to the literature.[8]

^{1}H NMR (400 MHz, $CDCl_3$) δ_H / ppm 6.33 (d, *J* = 3.6 Hz, 1 H, C$\underline{\text{H}}$-1$_{\alpha}$), 5.72 (d, *J* = 8.3 Hz, 0.15 H, C$\underline{\text{H}}$-1$_{\beta}$), 5.46 (t, *J* = 9.6 Hz, 1 H, C$\underline{\text{H}}$-3$_{\alpha}$), 5.25 (t, *J* = 9.4 Hz, 0.15 H, C$\underline{\text{H}}$-3$_{\beta}$), 5.19 - 5.06 (m, 2.3 H, C$\underline{\text{H}}$-2$_{\alpha}$, C$\underline{\text{H}}$-2$_{\beta}$, C$\underline{\text{H}}$-4$_{\alpha}$, C$\underline{\text{H}}$-4$_{\beta}$), 4.33 - 4.22 (m, 1.15 H, C$\underline{\text{H}}_{\text{A}}H_{\text{B}}-6_{\alpha}$ and C$\underline{\text{H}}_{\text{A}}H_{\text{B}}-6_{\beta}$), 4.16 - 4.06 (m, 2.15 H, CH-5$_{\alpha}$ and CH$_{\text{A}}\underline{\text{H}}_{\text{B}}-6_{\alpha}$ and CH$_{\text{A}}\underline{\text{H}}_{\text{B}}-6_{\beta}$), 3.84 (dt, *J*

= 10.0, 2.2 Hz, 0.15 H, C$\underline{H}$-5$_\beta$), 2.23 (s, 3 H, C$\underline{H}_3$CO$_\alpha$), 2.12 (s, 0.45 H, C$\underline{H}_3$CO$_\beta$), 2.10 (s, 3.45 H, C$\underline{H}_3$CO$_\alpha$ and C$\underline{H}_3$CO$_\beta$), 2.06 - 2.00 (m, 12 H, 4 × C$\underline{H}_3$CO$_\alpha$).

^{13}C NMR (100 MHz, CDCl$_3$) δ_C / ppm 170.6, 170.2, 169.6, 169.4, 168.7, 89.0, 69.8 (2 C), 69.1, 67.8, 61.4, 20.8, 20.7, 20.6, 20.5, 20.4.

MS (ESI) *m/z*: 413.1 [M+Na]$^+$.

IR (CHCl$_3$, ν_{max}/cm^{-1}): 1749, 1369, 1151, 1015.

$[\alpha]^{20}_D$ =+68.7 (*c* = 0.89, CHCl$_3$).

The crude product (20.0 g, 51.2 mmol) was dissolved in AcOH (80 mL). HBr (40 mL, 33% solution in AcOH) was added slowly (over 5 min) at 0°C and the reaction stirred at rt until complete (TLC control, 3:1 petroleum ether/EtOAc, approx. 3 h). The reaction mixture was diluted with CH$_2$Cl$_2$ (100 mL). The layers were separated, and the organic layer was washed with H$_2$O (2 × 100 mL) and then saturated aqueous NaHCO$_3$ (3 × 100 mL). The organic layer was dried (Na$_2$SO$_4$) and concentrated in vacuo to give a brown oil (17.6 g).

The crude bromide was dissolved in CHCl$_3$ (90 mL) and saturated aqueous NaHCO$_3$ (90 mL) was added. Tetrabutylammonium iodide (15.8 g, 42.8 mmol, 1.0 eq) was added, followed by NaN$_3$ (slow addition, 5 min, 13.9 g, 213.8 mmol, 5 eq) and the reaction was stirred at rt for 18 h. The layers were partitioned and the organic layer washed with H$_2$O (80 mL), saturated aqueous NaHCO$_3$ (80 mL) and brine (80 mL). The organic layer was dried (Na$_2$SO$_4$) and concentrated in vacuo to give a brown solid (19.2 g). The crude product was recrystallised from a minimum of hot MeOH to give **2** (8.23 g, 22.1 mmol, 43% over two steps) as a white crystalline solid.

^{1}H NMR (400 MHz, CDCl$_3$) δ_H / ppm 5.23 (t, *J* = 9.6 Hz, 1 H, C$\underline{H}$-3), 5.11 (t, *J* = 10.2 Hz, 1 H, C$\underline{H}$-4), 4.96 (t, *J* = 9.6 Hz, 1 H, C$\underline{H}$-2), 4.66 (d, *J* = 8.9 Hz, 1 H, C$\underline{H}$-1), 4.28 (dd, *J* = 13.0 Hz, 2.1 Hz, 1 H, C$\underline{H}_A$H$_B$-6), 4.18 (dd, *J* = 12.3, 2.1 Hz, 1 H, CH$_A\underline{H}_B$), 3.80 (m, 1 H, C$\underline{H}$-5), 2.08 (s, 3 H, C$\underline{H}_3$CO), 2.04 (s, 3 H, C$\underline{H}_3$CO), 2.02 (s, 3 H, C$\underline{H}_3$CO), 2.00 (s, 3 H, C$\underline{H}_3$CO).

^{13}C NMR (100 MHz, CDCl$_3$) δ_C / ppm 170.6, 170.1, 169.3, 169.2, 87.9, 74.0, 72.6, 70.6, 67.9, 61.6, 20.7, 20.6, 20.5, 20.4.

MS (ESI) *m/z* 769.21 (60, $[M_2 + Na]^+$), 369.09 (100, $[M + Na]^+$).

IR (CHCl$_3$, ν_{max}/cm^{-1}): 2957, 2117, 1745, 1213, 1036.

$[\alpha]^{20}_D$ = –13.4 (*c* = 0.99, CHCl$_3$), lit.[9] –19.0 (*c* = 1.0, CHCl$_3$).

Mp = 123.4-125.0 °C (MeOH), lit.[9] 126 °C (MeOH).

1-(Tetra-*O*-acetyl-1-deoxy-β-D-glucopyranosyl)-4-hexyl triazole 18a

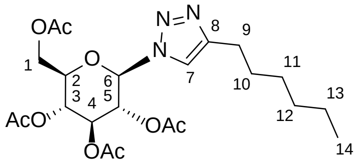

Synthesised according to Shao *et al.*[10] To a stirred suspension of CuI (15 mg, 0.08 mmol, 0.02 eq) in CH$_2$Cl$_2$ (25 mL) was added **17** (1.50 g, 4.0 mmol), DIPEA (28 µL, 0.16 mmol, 0.04 eq), AcOH (9.2 µL, 0.16 mmol, 0.04 eq) and 1-decyne (2.1 mL, 11.8 mmol, 1.1 eq). The resultant blue solution was stirred for 18 h, and then diluted with CH$_2$Cl$_2$ (25 mL). Silica gel (15 g) was added and the solvent was removed in vacuo, and then applied to the top of a pre-loaded silica gel column. The column was eluted (7:3 Et$_2$O/petroleum ether and then Et$_2$O) to give **18a** (734 mg, 1.5 mmol, 38%) as an amorphous off-white solid.

^{1}H NMR (400 MHz, CDCl$_3$) δ_H / ppm 7.50 (s, 1 H, C$\underline{H}$-7), 5.85 (d, *J* = 8.8 Hz, 1 H, C$\underline{H}$-6), 5.42 (m, 2 H, C$\underline{H}$-4, C$\underline{H}$-5), 5.24 (t, *J* = 9.5 Hz, 1 H, C$\underline{H}$-3), 4.31 (dd, *J* = 12.6, 5.0 Hz, 1 H, C$\underline{H}_A$H$_B$-1), 4.14 (dd, *J* = 12.6, 1.64 Hz, 1 H, CH$_A\underline{H}_B$), 4.04 - 3.96 (m, 1 H, C$\underline{H}$-2), 2.71 (t, *J* = 7.7 Hz, 2 H, C$\underline{H}_2$-9), 2.09 (s, 3 H, C$\underline{H}_3$CO), 2.07 (s, 3 H, C$\underline{H}_3$CO), 2.03 (s, 3 H, C$\underline{H}_3$CO), 1.87 (s, 3 H, C$\underline{H}_3$CO), 1.72 - 1.61 (m, 2 H, C$\underline{H}_2$-10), 1.39 - 1.24 (m, 6 H, (C$\underline{H}_2$)$_3$-11,12,13), 0.93 - 0.84 (m, 3 H, C$\underline{H}_3$-14).

^{13}C NMR (100 MHz, CDCl$_3$) δ_C / ppm 170.5, 169.9, 169.4, 168.9, 149.2, 118.7, 85.6, 75.0, 72.7, 70.1, 67.7, 61.6, 31.5, 29.1, 28.7, 25.6, 22.5, 20.7, 20.5, 20.5, 20.1, 14.0.

HRMS (ESI) *m/z* calcd for $C_{22}H_{33}N_3NaO_9$ [M+Na]$^+$: 506.2109, found: 506.2101.

IR (CHCl$_3$, ν_{max}/cm^{-1}): 2932, 2859, 1754, 1223.

$[\alpha]^{20}_D = -16.5$ (*c* = 0.92, CHCl$_3$).

1-(Tetra-*O*-acetyl-1-deoxy-β-D-glucopyranosyl)-4-octyl triazole 18b

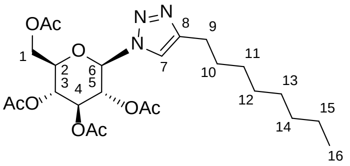

Synthesised according to Shao *et al.*[10] To a stirred suspension of CuI (40.8 mg, 0.21 mmol, 0.02 eq) in CH$_2$Cl$_2$ (40 mL) was added **17** (4.0 g, 10.7 mmol), DIPEA (75 µL, 0.43 mmol, 0.04 eq), AcOH (25 µL, 0.43 mmol, 0.04 eq) and 1-decyne (2.1 mL, 11.8 mmol, 1.1 eq). The resultant blue solution was stirred for 36 h, then diluted with CH$_2$Cl$_2$ (40 mL). Silica gel (35 g) was added and the solvent was removed in vacuo, and then applied to the top of a pre-loaded silica gel column. The column was eluted (7:3

Et_2O/petroleum ether and then Et_2O) to give **18b** (4.60 g, 9.0 mmol, 84%) as an amorphous white solid.

^{1}H NMR (400 MHz, $CDCl_3$) δ_H / ppm 7.50 (s, 1 H, C$\underline{H}$-7), 5.85 (d, *J* = 8.9 Hz, 1 H, C$\underline{H}$-6), 5.50 - 5.35 (m, 2 H, C$\underline{H}$-4, C$\underline{H}$-5), 5.23 (t, *J* = 9.5 Hz, 1 H, C$\underline{H}$-3), 4.31 (dd, *J* = 12.6, 5.0 Hz, 1 H, C$\underline{H}_A$H$_B$-1), 4.14 (dd, *J* = 12.6, 1.8 Hz, 1 H, CH$_A\underline{H}_B$-1), 4.03 – 3.93 (m, 1 H, C$\underline{H}$-2), 2.71 (t, *J* = 7.6 Hz, 2 H, C$\underline{H}_2$-9), 2.08 (s, 3 H, C$\underline{H}_3$CO), 2.07 (s, 3 H, C$\underline{H}_3$CO), 2.03 (s, 3 H, C$\underline{H}_3$CO), 1.86 (s, 3 H, C$\underline{H}_3$CO), 1.72 - 1.61 (m, 2 H, C$\underline{H}_2$-10), 1.39-1.20 (m, 10 H, (C$\underline{H}_2$)$_5$-11-15), 0.93 - 0.82 (t, *J* = 6.4 Hz, 3 H, C$\underline{H}_3$-16),

^{13}C NMR (100 MHz, $CDCl_3$) δ_C / ppm 170.5, 169.9, 169.4, 168.9, 149.3, 118.7, 85.6, 75.0, 72.7, 70.1, 67.7, 61.6, 31.8, 29.3, 29.2, 29.1, 25.6, 22.6, 20.7, 20.5, 20.5, 20.1, 14.1.

HRMS (ESI) *m/z* calcd for $C_{24}H_{37}N_3NaO_9$ $[M+Na]^+$: 534.2422, found: 534.2409.

IR ($CHCl_3$, ν_{max}/cm^{-1}): 2926, 2855, 1748, 1223.

$[\alpha]^{20}_D$ = –10.1 (*c* = 1.02, $CHCl_3$).

1-(Tetra-*O*-acetyl-1-deoxy-β-D-glucopyranosyl)-4-decyl triazole 18c

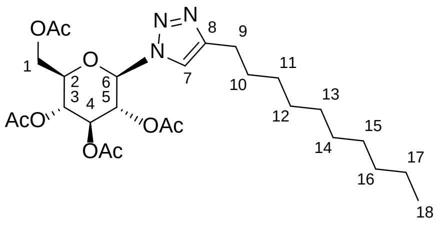

Synthesised according to Shao *et al.*[10] To a stirred suspension of CuI (29.2 mg, 0.15 mmol, 0.02 eq) in CH_2Cl_2 (25 mL) was added **17** (2.86 g, 7.7 mmol), DIPEA (53 µL, 0.31 mmol, 0.04 eq), AcOH (18 µL, 0.31 mmol, 0.04 eq) and 1-dodecyne (1.8 mL, 8.4 mmol, 1.1 eq). The resultant blue solution was stirred for 24 h, then diluted with CH_2Cl_2 (25 mL). Silica gel (25 g) was added and the solvent was removed in vacuo, and then applied to the top of a pre-loaded silica gel column. The column was eluted (7:3 Et_2O/petroleum ether and then Et_2O) to give **18c** (3.50 g, 6.5 mmol, 85%) as an amorphous white solid.

^{1}H NMR (500 MHz, $CDCl_3$) δ_H / ppm 7.50 (s, 1 H, C$\underline{H}$-7), 5.85 (d, *J* = 8.9 Hz, 1 H, C$\underline{H}$-6), 5.42 (quin, *J* = 9.3 Hz, 2 H, C$\underline{H}$-4 and C$\underline{H}$-5), 5.24 (t, *J* = 9.6 Hz, 1 H, C$\underline{H}$-3), 4.31 (dd, *J* = 12.6, 5.0 Hz, 1 H, C$\underline{H}_A H_B$-1), 4.15 (dd, *J* = 12.6, 1.9 Hz, 1 H, C$H_A\underline{H}_B$-1), 4.03 – 3.94 (m, 1 H, C$\underline{H}$-2), 2.76 - 2.66 (m, 2 H, C$\underline{H}_2$-9), 2.09 (s, 3 H, C$\underline{H}_3$CO), 2.07 (s, 3 H, C$\underline{H}_3$CO), 2.03 (s, 3 H, C$\underline{H}_3$CO), 1.87 (s, 3 H, C$\underline{H}_3$CO), 1.75 - 1.60 (m, 2 H, C$\underline{H}_2$-10), 1.39 - 1.18 (m, 14 H, $(C\underline{H}_2)_7$-11-17), 0.88 (t, *J* = 6.9 Hz, 3 H, C$\underline{H}_3$-18).

^{13}C NMR (126 MHz, $CDCl_3$) δ_C / ppm 170.5, 169.9, 169.4, 168.9, 149.3, 118.7, 85.6, 75.1, 72.7, 70.1, 67.8, 61.6, 31.9, 29.6, 29.5, 29.3, 29.3, 29.1, 29.1, 25.6, 22.7, 20.7, 20.5, 20.5, 20.1, 14.1.

HRMS (ESI) *m/z* calcd for $C_{26}H_{41}N_3NaO_9$ $[M+Na]^+$: 562.2735, found: 562.2726.

IR ($CHCl_3$, ν_{max}/cm^{-1}): 2926, 2855, 1750, 1219.

$[\alpha]^{20}_D = -10.8$ (*c* = 0.93, $CHCl_3$).

1-(Tetra-*O*-acetyl-1-deoxy-β-D-glucopyranosyl)-4-dodecyl triazole 18d

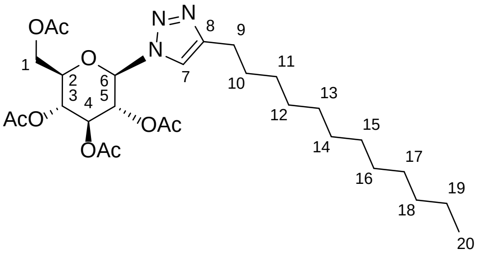

Synthesised according to Shao *et al.*[10] To a stirred suspension of CuI (29.3 mg, 0.15 mmol, 0.02 eq) in CH_2Cl_2 (25 mL) was added **17** (2.87 g, 7.7 mmol), DIPEA (54 µL, 0.31 mmol, 0.04 eq), AcOH (18 µL, 0.31 mmol, 0.04 eq) and 1-tetradecyne (2.1 mL, 8.5 mmol, 1.1 eq). The resultant blue solution was stirred for 26 h, then diluted with CH_2Cl_2 (25 mL). Silica gel (25 g) was added and the solvent was removed in vacuo, and then applied to the top of a pre-loaded silica gel column. The column was eluted (7:3 Et_2O/petroleum ether and then Et_2O) to give **18d** (4.01 g, 7.1 mmol, 92%) as an amorphous white solid.

^{1}H NMR (400 MHz, $CHCl_3$) δ_H / ppm 7.50 (s, 1 H, C$\underline{H}$-7), 5.85 (d, *J* = 9.0 Hz, 1 H, C$\underline{H}$-6), 5.49 - 5.36 (m, 2 H, C$\underline{H}$-4 and C$\underline{H}$-5), 5.24 (t, *J* = 9.7 Hz, 1 H, C$\underline{H}$-3), 4.31 (dd, *J* = 12.4, 5.2 Hz, 1 H, C$\underline{H}_A H_B$-1), 4.14 (dd, *J* = 12.6, 2.1 Hz, 1 H, C$H_A \underline{H}_B$-1), 4.03 – 3.96 (m, 1 H, C$\underline{H}$-2), 2.71 (t, *J* = 7.7 Hz, 2 H, C$\underline{H}_2$-9), 2.09 (s, 3 H, C$\underline{H}_3$CO), 2.07 (s, 3 H, C$\underline{H}_3$CO), 2.03 (s, 3 H, C$\underline{H}_3$CO), 1.87 (s, 3 H, C$\underline{H}_3$CO), 1.72 - 1.60 (m, 2 H, C$\underline{H}_2$-10), 1.38 - 1.20 (m, 18 H, (C$\underline{H}_2$)$_9$-11-19), 0.92 - 0.83 (t, *J* = 6.7 Hz, 3 H, C$\underline{H}_3$-20).

^{13}C NMR (126 MHz, $CDCl_3$) δ_C / ppm 170.5, 169.9, 169.4, 168.9, 149.3, 118.7, 85.6, 75.0, 72.7, 70.1, 67.7, 61.6, 31.9, 29.6, 29.6, 29.5, 29.3, 29.1 (2 C), 25.6, 22.7, 20.7, 20.5, 20.5, 20.1, 14.1.

HRMS (ESI) *m/z* calcd for $C_{28}H_{45}N_3NaO_9$ $[M+Na]^+$: 590.3048, found: 590.3042.

IR ($CHCl_3$, ν_{max}/cm^{-1}): 2921, 2852, 1748, 1224.

$[\alpha]^{20}_D$ = –8.5 (*c* = 1.04, $CHCl_3$).

1-Deoxy-1-azido-β-D-glucopyranose 19

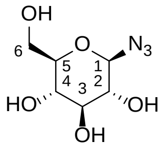

To a stirred suspension of **17** (1.0 g, 2.7 mmol) in MeOH (20 mL) was added a trace of sodium methoxide. Upon dissolution of the solid and concurrent disappearance of **2** (TLC control, approx. 10 min), the solution was neutralised using Amberlyst 15 resin (H^+ form). The resin was filtered off and washed with MeOH (10 mL), and the filtrate was concentrated in vacuo. The residue was freeze-dried to give **19** (340 mg, 1.7 mmol, 62%) as a tacky, hygroscopic white powder.

^{1}H NMR (400 MHz, D_2O) δ_H / ppm 4.66 (d, *J* = 8.7 Hz, 1 H, C$\underline{H}$=1), 3.84 (dd, *J* = 12.4, 2.1 Hz, 1 H, C$\underline{H}_A$$H_B$-6), 3.66 (dd, *J* = 12.4, 5.5 Hz, 1 H, C$H_A$$\underline{H}_B$-6), 3.49 - 3.40 (m, 2 H, C$\underline{H}$-3 and C$\underline{H}$-5), 3.33 (t, *J* = 9.6 Hz, 1 H, C$\underline{H}$-4), 3.18 (t, *J* = 9.0 Hz, 1 H, C$\underline{H}$-2).

^{13}C NMR (100 MHz, D_2O) δ_C / ppm 90.4, 77.9, 75.9, 73.0, 69.5, 60.8.

MS (ESI) *m/z*: 228.2 $[M+Na]^+$.

IR (solid, ν_{max}/cm^{-1}): 3164 (broad), 2119, 1561, 1401.

$[\alpha]^{20}_D$ = – 28.7 (*c* = 1.0, H_2O), lit.[11] – 32 (*c* = 1.0, H_2O).

1-(1-Deoxy-β-D-glucopyranosyl)-4-hexyl triazole 20a

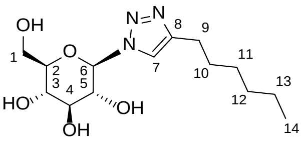

To a stirred suspension of **18a** (228 mg, 0.47 mmol) in MeOH was added a trace of sodium methoxide. Upon dissolution of the solid and concurrent disappearance of **18a** (TLC control, approx. 10 min), the solution was neutralised using Amberlyst 15 resin (H^+ form). The resin was filtered off and washed with MeOH (10 mL), and the filtrate was concentrated in vacuo. The residue was freeze-dried to give **20a** (130 mg, 0.41 mmol, 87%) as a tacky, hygroscopic white powder.

^{1}H NMR (400 MHz, CD_3OD) δ_H / ppm 7.95 (s, 1 H, C$\underline{H}$-7), 5.57 (d, *J* = 9.2 Hz, 1 H, C$\underline{H}$-6), 3.97 - 3.82 (m, 2 H, C$\underline{H}$-5 and C$\underline{H}_A H_B$-1), 3.72 (dd, *J* = 12.4, 5.1 Hz, 1 H, $CH_A\underline{H}_B$-1), 3.65 - 3.55 (m, 2 H, C$\underline{H}$-2 and C$\underline{H}$-4), 3.54 - 3.46 (m, 1 H, C$\underline{H}$-3), 2.71 (t, *J* = 7.6 Hz, 2 H, C$\underline{H}_2$-9), 1.77 - 1.58 (m, 2 H, C$\underline{H}_2$-10), 1.35 (m, 6 H, (C$\underline{H}_2$)$_3$-11,12,13), 0.91 (m, 3 H, C$\underline{H}_3$-14).

^{13}C NMR (100 MHz, CD_3OD) δ_C / ppm 149.3, 122.5, 89.6, 81.1, 78.6, 74.0, 71.0, 62.5, 32.8, 30.6, 30.1, 26.4, 23.7, 14.6.

HRMS (ESI) *m/z* calcd for $C_{14}H_{25}N_3NaO_5$ $[M+Na]^+$: 338.1686, found: 338.1677.

IR (MEOH, ν_{max}/cm^{-1}): 3344 (broad), 2927, 2858, 1459.

$[\alpha]^{20}_D$ = – 2.1 (*c* = 0.61, MeOH).

1-(1-Deoxy-β-D-glucopyranosyl)-4-octyl triazole 20b

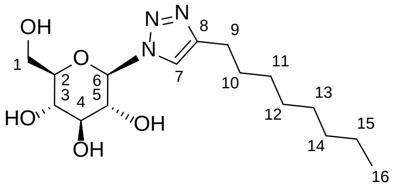

To a stirred suspension of **18b** (551 mg, 1.1 mmol) in MeOH was added a trace of sodium methoxide. Upon dissolution of the solid and concurrent disappearance of **18b** (TLC control, approx. 10 min), the solution was neutralised using Amberlyst 15 resin (H^+ form). The resin was filtered off and washed with MeOH (10 mL), and the filtrate was concentrated in vacuo. The residue was freeze-dried to give **20b** (248 mg, 0.72 mmol, 67%) as a tacky, hygroscopic white powder.

^{1}H NMR (400 MHz, CD_3OD) δ_H / ppm 7.95 (s, 1 H, C$\underline{H}$-7), 5.60 (d, *J* = 9.1 Hz, 1 H, C$\underline{H}$-6), 4.00 – 3.83 (m, 2 H, C$\underline{H}$-5 and C$\underline{H}_A$$H_B$-1), 3.73 (dd, *J* = 12.1, 5.1 Hz, 1 H, C$H_A$$\underline{H}_B$-1), 3.67 - 3.50 (m, 3 H, C$\underline{H}$-2 and C$\underline{H}$-3 and C$\underline{H}$-4), 2.79 - 2.60 (m, 2 H, C$\underline{H}_2$-9), 1.68 (d, *J* = 6.1 Hz, 2 H, C$\underline{H}_2$-10), 1.33 (m, 8 H, (C$\underline{H}_2$)$_4$-11-15), 1.02 – 0.82 (m, 3 H, C$\underline{H}_3$-16).

^{13}C NMR (100 MHz, CD_3OD) δ_C / ppm 148.3, 121.5, 88.4, 80.0, 77.5, 73.0, 69.9, 61.4, 32.1, 29.6, 29.5, 29.4, 29.4, 25.4, 22.8, 13.6.

HRMS (ESI) *m/z* calcd for $C_{16}H_{29}N_3NaO_5$ $[M+Na]^+$: 366.1999, found: 336.1986.

IR (solid, ν_{max}/cm^{-1}): 3287 (broad), 2924, 2854, 1456.

$[\alpha]^{20}_D$ = – 3.1 (*c* = 0.8, MeOH).

1-(1-Deoxy-β-D-glucopyranosyl)-4-decyl triazole 20c

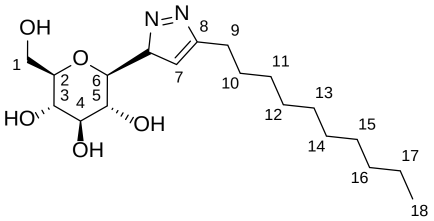

To a stirred suspension of **18c** (400 mg, 0.78 mmol) in MeOH was added a trace of sodium methoxide. Upon dissolution of the solid and concurrent disappearance of **18c** (TLC control, approx. 10 min), the solution was neutralised using Amberlyst 15 resin (H^+ form). The resin was filtered off and washed with MeOH (10 mL), and the filtrate was concentrated in vacuo. The residue was freeze-dried to give **20c** (261 mg, 0.76 mmol, 97%) as a tacky, hygroscopic white powder.

^{1}H NMR (400 MHz, CD_3OD) δ_H / ppm 7.94 (s, 1 H, C$\underline{H}$-7), 5.56 (d, *J* = 9.1 Hz, 1 H, C$\underline{H}$-6), 3.94 - 3.83 (m, 2 H, C$\underline{H}$-5 and C$\underline{H}_A$H$_B$-1), 3.76 - 3.65 (m, 1 H, CH$_A\underline{H}_B$-1), 3.61 - 3.54 (m, 2 H, C$\underline{H}$-2 and C$\underline{H}$-4), 3.54 - 3.45 (m, 1 H, C$\underline{H}$-3), 2.70 (t, *J* = 7.6 Hz, 2 H, C$\underline{H}_2$-9), 1.76 - 1.61 (m, 2 H, C$\underline{H}_2$-10), 1.45 - 1.24 (m, 14 H, (C$\underline{H}_2$)$_7$)-11-17), 0.96 - 0.84 (m, 3 H, C$\underline{H}_3$-18).

^{13}C NMR (100 MHz, CD_3OD) δ_C / ppm 148.2, 121.4, 88.5, 80.1, 77.5, 73.0, 69.9, 61.4, 32.1, 29.8, 29.7, 29.6, 29.5, 29.5, 29.3, 25.3, 22.7, 13.5.

HRMS (ESI) *m/z* calcd for $C_{18}H_{33}N_3NaO_5$ $[M+Na]^+$: 394.2312, found: 394.2305.

IR (MeOH, ν_{max}/cm^{-1}): 3321 (broad), 2922, 2859, 1460.

$[\alpha]^{20}_D$ = – 2.0 (*c* = 0.9, MeOH).

1-(1-Deoxy-β-D-glucopyranosyl)-4-dodecyl triazole 20d

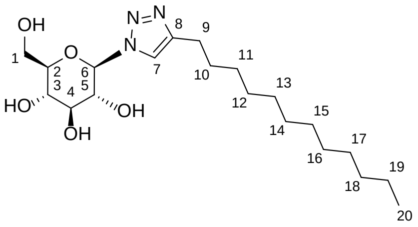

To a stirred suspension of **18d** (340 mg, 0.66 mmol) in MeOH was added a trace of sodium methoxide. Upon dissolution of the solid and concurrent disappearance of **18d** (TLC control, approx. 10 min), the solution was neutralised using Amberlyst 15 resin (H^+ form). The resin was filtered off and washed with MeOH (10 mL), and the filtrate was concentrated in vacuo. The residue was freeze-dried to give **20d** (218 mg, 0.63 mmol, 96%) as a tacky, hygroscopic white powder.

^{1}H NMR (400 MHz, CD_3OD) δ_H / ppm 7.94 (s, 1 H, C$\underline{H}$-7), 5.55 (d, *J* = 9.1 Hz, 1 H, C$\underline{H}$-6), 3.92 - 3.83 (m, 2 H, C$\underline{H}$-5 and C$\underline{H}_A$H$_B$-1), 3.74 - 3.67 (m, 1 H, CH$_A\underline{H}_B$-1), 3.60 - 3.44 (m, 3 H, C$\underline{H}$-2 and C$\underline{H}$-3 and C$\underline{H}$-4), 2.71 (t, *J* = 7.7 Hz, 2 H, C$\underline{H}_2$-9), 1.73 - 1.61 (m, 2 H, C$\underline{H}_2$-10), 1.42 - 1.22 (m, 18 H, (C$\underline{H}_2$)$_9$-11-19), 0.94 - 0.86 (m, 3 H, C$\underline{H}_3$-20).

^{13}C NMR (100 MHz, CD_3OD) δ_C / ppm 148.2, 121.4, 88.5, 80.1, 77.5, 73.0, 69.9, 61.4, 32.1, 29.8, 29.8, 29.7, 29.6, 29.5, 29.4, 29.3, 25.3, 22.7, 13.4.

HRMS (ESI) *m/z* calcd for $C_{20}H_{37}N_3NaO_5$ $[M+Na]^+$: 422.2625, found: 422.2619.

IR (MEOH, ν_{max}/cm^{-1}): 3340 (broad), 2925, 2852, 1463.

$[\alpha]^{20}_D = -1.9$ (*c* = 0.7, MeOH).

Hepta-*O*-acetyl-1-deoxy-1-azido-β-D-maltopyranose 22

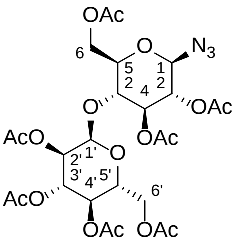

Azide **22** was synthesised according to Mahon *et al.*[7] via peracetylation of D-maltose, conversion to the 1-bromo derivative, and displacement with sodium azide as follows.

Freshly-ground D-maltose monohydrate (10.6 g, 29.4 mmol) was added to a stirred suspension of I_2 (500 mg, 2.0 mmol, 0.07 eq) in Ac_2O (50 mL) at rt. Upon dissolution of the solid after (approx. 1 h) and concurrent disappearance of maltose (TLC control, 1:1 petroleum ether/EtOAc), the reaction mixture was diluted with CH_2Cl_2 (50 mL) and poured into a separating funnel containing 1 M aqueous $Na_2S_2O_4$ (50 mL) and ice. Upon shaking, the intense colour faded. The layers were separated and the organic layer was washed with saturated aqueous $NaHCO_3$ (3 × 50 mL). The organic layer was dried (Na_2SO_4) and concentrated in vacuo to a yellow syrup.

The crude peracetate was dissolved in dry CH_2Cl_2 (120 mL) and HBr (40 mL, 33% solution in AcOH) was added slowly (over 5 min) at 0 °C. The reaction was allowed to warm to rt and stirred until complete (TLC control, 1:1 petroleum ether/EtOAc, approx. 3 h). The reaction was washed with H_2O (60 mL) and then saturated aqueous $NaHCO_3$ (3 × 60 mL). The organic layer was dried (Na_2SO_4) and concentrated in vacuo to a pale oil.

The crude bromide was dissolved in CH_2Cl_2 (120 mL) and saturated aqueous $NaHCO_3$ (90 mL) was added. Tetrabutylammonium iodide (10.9 g, 29.4 mmol) was added, followed by NaN_3 (slow addition, 5 min, 9.5 g, 147 mmol, 5.0 eq) and the reaction was stirred at rt for 6 h. The layers were separated and the organic layer was washed with H_2O (60 mL), saturated aqueous $NaHCO_3$ (60 mL), and brine (60 mL). The organic layer was dried (Na_2SO_4) and concentrated in vacuo to give a brown solid. The crude product was recrystallised from a minimum of hot MeOH to give **22** (11.1 g, 16.8 mmol, 57% over three steps) as a white crystalline solid.

^{1}H NMR (400 MHz, $CDCl_3$) δ_H / ppm 5.42 (d, *J* = 3.9 Hz, 1 H, C$\underline{H}$-1'), 5.36 (t, *J* = 10.0 Hz, 1 H, C$\underline{H}$-3'), 5.27 (t, *J* = 9.0 Hz, 1 H, C$\underline{H}$-3), 5.06 (t, *J* = 9.9 Hz, 1 H, C$\underline{H}$-4'), 4.87 (dd, *J* = 10.6, 4.0 Hz, 1 H, C$\underline{H}$-2'), 4.77 (t, 1 H, *J* = 8.9 Hz, C$\underline{H}$-2), 4.70 (d, *J* = 8.7 Hz, 1 H, C$\underline{H}$-1), 4.52 (dd, *J* = 12.2, 2.2 Hz, 1 H, C$\underline{H}_A$H$_B$-6), 4.29 - 4.21 (m, 2 H, CH$_A\underline{H}_B$-6 and C$\underline{H}_A$H$_B$-6'), 4.09 – 3.99 (m, 2 H, C$\underline{H}$-4 and CH$_A\underline{H}_B$-6'), 3.99 – 3.93 (m, 1 H, C$\underline{H}$-5'), 3.77 (ddd, *J* = 9.7, 4.5, 2.6 Hz, 1 H, C$\underline{H}$-5), 2.17 (s, 3 H, C$\underline{H}_3$CO), 2.11 (s, 3 H, C$\underline{H}_3$CO), 2.06 (s, 3 H, C$\underline{H}_3$CO), 2.05 (s, 3 H, C$\underline{H}_3$CO), 2.03 (s, 3 H, C$\underline{H}_3$CO), 2.02 (s, 3 H, C$\underline{H}_3$CO), 2.01 (s, 3 H, C$\underline{H}_3$CO).

^{13}C NMR (126 MHz, $CDCl_3$) δ_C / ppm 170.5 (2 C), 170.4, 170.1, 169.9, 169.5, 169.4, 95.7, 87.4, 75.0, 74.2, 72.3, 71.4, 69.9, 69.2, 68.6, 67.9, 62.5, 61.4, 20.8, 20.8, 20.7, 20.6, 20.6 (2 C), 20.5.

MS (ESI) *m/z* 684.3 [M + Na]$^+$.

IR ($CHCl_3$, ν_{max}/cm^{-1}): 2120, 1748, 1227, 1036.

$[\alpha]^{20}_D$ = +46.8 (*c* = 1.13, $CHCl_3$), lit.[12] +52.4 (*c* = 1.0, $CHCl_3$).

Mp = 89.0 – 92.4 °C (MeOH), lit.[12] 90 – 91 °C (MeOH).

1-(Hepta-*O*-acetyl-1-deoxy-β-D-maltopyranosyl)-4-hexyl triazole 23a

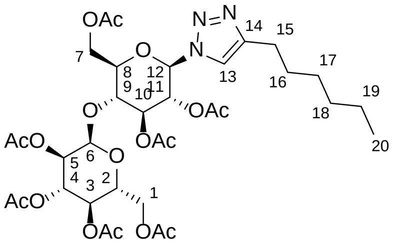

Synthesised according to Mahon *et al.*[7] To a stirred solution of **22** (1.50 g, 2.3 mmol) and 1-octyne (0.67 mL, 4.5 mmol, 2.0 eq) in *t*-butanol (10 mL) was added a solution of $CuSO_4 \cdot 5H_2O$ (110 mg, 0.45 mmol, 0.2 eq) and ascorbic acid (160 mg, 0.91 mmol, 0.4 eq) in H_2O (10 mL). The reaction was stirred at rt for 72 h and then washed with CH_2Cl_2 (3 × 50 mL). The combined organic layers were washed with H_2O (100 mL) and then dried (Na_2SO_4) and concentrated in vacuo. The crude product was purified by flash column chromatography (2:3 EtOAc/petroleum ether; SiO_2) to give **23a** (400 mg, 0.52 mmol, 23%) as an amorphous off-white solid.

^{1}H NMR (400 MHz, $CDCl_3$) δ_H / ppm 7.42 (s, 1 H, C$\underline{H}$-13), 5.86 (d, *J* = 9.4 Hz, 1 H, C$\underline{H}$-12), 5.49 - 5.42 (m, 2 H, C$\underline{H}$-6 and C$\underline{H}$-10), 5.35 (dt, *J* = 19.3, 9.6 Hz, 2 H, C$\underline{H}$-4 and C$\underline{H}$-11), 5.08 (t, *J* = 9.9 Hz, 1 H, C$\underline{H}$-3), 4.88 (dd, *J* = 10.6, 4.0 Hz, 1 H, C$\underline{H}$-5), 4.48 (dd, *J* = 12.4, 2.12 Hz, 1 H, C$\underline{H}_A$$H_B$-7), 4.30 - 4.21 (m, 2 H, C$\underline{H}_A$$H_B$-1 and C$H_A$$\underline{H}_B$-7), 4.19 - 4.11 (m, 1 H, C$\underline{H}$-9), 4.07 (dd, *J* = 12.4, 2.0 Hz, 1 H, C$H_A$$\underline{H}_B$-1), 4.02 – 3.93 (m, 2 H, C$\underline{H}$-2 and C$\underline{H}$-8), 2.70 (t, *J* = 7.7 Hz, 2 H, C$\underline{H}_2$-15), 2.13 (s, 3 H, C$\underline{H}_3$CO), 2.11 (s, 3 H, C$\underline{H}_3$CO), 2.07 (s, 3 H, C$\underline{H}_3$CO), 2.04 (s, 3 H, C$\underline{H}_3$CO), 2.03 (s, 3 H, C$\underline{H}_3$CO), 2.01 (s, 3 H, C$\underline{H}_3$CO), 1.84 (s, 3 H, C$\underline{H}_3$CO), 1.72 - 1.59 (m, 2 H, C$\underline{H}_2$-16), 1.30 (br. s, 6 H, (C$\underline{H}_2$)$_3$-17,18,19), 0.87 (t, *J* = 6.6 Hz, 3 H, C$\underline{H}_3$-20).

^{13}C NMR (100 MHz, $CDCl_3$) δ_C / ppm 170.6, 170.5, 170.3, 169.9, 169.4, 169.2, 149.1, 118.7, 95.9, 85.1, 75.2, 72.4, 70.8, 70.0, 69.2, 68.7, 67.9, 62.5, 61.4, 31.5, 29.0, 28.7, 22.5, 25.5, 20.8, 20.8, 20.7, 20.6, 20.1, 14.0.

HRMS (ESI) *m/z* calcd for $C_{34}H_{49}N_3NaO_{17}$ [M+Na}$^+$: 794.2954, found: 794.2952.

IR ($CHCl_3$, ν_{max}/cm^{-1}): 2932, 2859, 1748, 1224, 1037.

$[\alpha]^{20}_D$ =+47.1 (*c* = 0.97, $CHCl_3$).

1-(Hepta-*O*-acetyl-1-deoxy-β-D-maltopyranosyl)-4-octyl triazole 23b

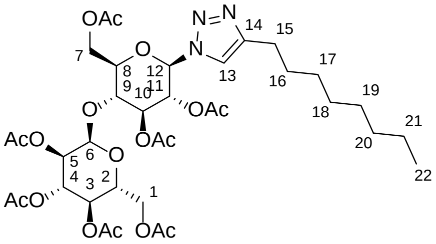

Synthesised according to Mahon *et al.*[7] To a stirred solution of **22** (2.0 g, 3.0 mmol) and 1-decyne (0.60 mL, 3.3 mmol, 1.1 eq) in *t*-butanol (40 mL) was added a solution of $CuSO_4 \cdot 5H_2O$ (150 mg, 0.62 mmol, 0.21 eq) and ascorbic acid (212 mg, 1.2 mmol, 0.4 eq) in H_2O (60 mL). The reaction was stirred at rt for 36 h and then washed with CH_2Cl_2 (3 × 50 mL). The combined organic layers were washed with H_2O (3 × 50 mL) and then dried (Na_2SO_4) and concentrated in vacuo to give pure **23b** (1.7 g, 2.1 mmol, 70%) as an amorphous white solid.

^1H NMR (400 MHz, $CDCl_3$) δ_H / ppm 7.43 (s, 1 H, C$\underline{H}$-13), 5.86 (d, *J* = 9.3 Hz, 1 H, C$\underline{H}$-12), 5.50 - 5.42 (m, 2 H, C$\underline{H}$-6 and C$\underline{H}$-13), 5.40 (dt, *J* = 19.1, 9.6 Hz, 2 H, C$\underline{H}$-4 and C$\underline{H}$-11), 5.08 (t, *J* = 9.9 Hz, 1 H, C$\underline{H}$-3), 4.92 - 4.84 (m, 1 H, C$\underline{H}$-5), 4.48 (dd, *J* = 12.3, 2.08 Hz, 1 H, C$\underline{H}_A$H$_B$-7), 4.30 - 4.22 (m, 2 H, C$\underline{H}_A$CH$_B$-1 and CH$_A\underline{H}_B$-7), 4.19 - 4.11 (m, 1 H, C$\underline{H}$-9), 4.07

(dd, *J* = 12.5, 2.1 Hz, 1 H, CH$_A$C$\underline{\text{H}}_B$-1), 4.01 – 3.94 (m, 2 H, C$\underline{\text{H}}$-2 and C$\underline{\text{H}}$-8), 2.70 (t, *J* = 7.4 Hz, 2 H, C$\underline{\text{H}}_2$-15), 2.13 (s, 3 H, C$\underline{\text{H}}_3$CO), 2.11 (s, 3 H, C$\underline{\text{H}}_3$CO), 2.07 (s, 3 H, C$\underline{\text{H}}_3$CO), 2.04 (s, 3 H, C$\underline{\text{H}}_3$CO), 2.03 (s, 3 H, C$\underline{\text{H}}_3$CO), 2.02 (s, 3 H, C$\underline{\text{H}}_3$CO), 1.84 (s, 3 H, C$\underline{\text{H}}_3$CO), 1.70 – 1.60 (m, 2 H, C$\underline{\text{H}}_2$-16), 1.38 – 1.20 (br. s, 10 H, (C$\underline{\text{H}}_2$)$_5$-17-21), 0.87 (t, *J* = 6.8 Hz, 3 H, C$\underline{\text{H}}_3$-22).

^{13}C NMR (100 MHz, CDCl$_3$) δ_C / ppm 170.6, 170.5, 170.3, 169.9, 169.4, 169.2, 149.0, 118.7, 95.9, 85.1, 75.2, 72.4, 70.8, 70.0, 69.2, 68.7, 67.9, 62.5, 61.4, 31.8, 29.3, 29.2, 29.1, 25.6, 22.6, 20.8, 20.8, 20.7, 20.6, 20.1, 14.1,

HRMS (ESI) *m/z* calcd for $C_{36}H_{53}N_3NaO_{17}$ [M+Na}$^+$: 822.3267, found: 822.3267.

IR (CHCl$_3$, v_{max}/cm^{-1}): 2929, 2857, 1750, 1227, 1038.

$[\alpha]^{20}_D$ = +51.9 (*c* = 0.76, CHCl$_3$).

1-(Hepta-*O*-acetyl-1-deoxy-β-D-maltopyranosyl)-4-decyl triazole 23c

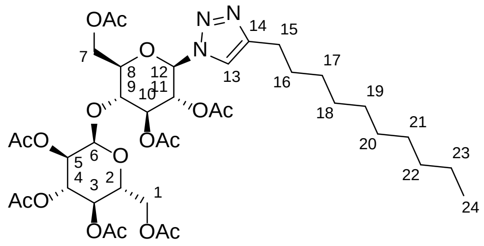

Synthesised according to Mahon *et al.*[7] To a stirred solution of **22** (1.5 g, 2.3 mmol) and 1-dodecyne (0.97 mL, 4.5 mmol, 2.0 eq) in *t*-butanol (10 mL) was added a solution of $CuSO_4 \cdot 5H_2O$ (110 mg, 0.45 mmol, 0.2 eq) and ascorbic acid (160 mg, 0.91 mmol, 0.4 eq) in H_2O (10 mL). The reaction was stirred at rt for 75 h and then washed with CH_2Cl_2 (3 × 50 mL). The combined organic layers were washed with H_2O (100 mL) and then dried (Na_2SO_4) and concentrated in vacuo. The crude product was purified by flash column chromatography (1:3 acetone/petroleum ether; SiO_2) to give **23c** (186 mg, 0.22 mmol, 10%) as an amorphous white solid.

^{1}H NMR (400 MHz, $CDCl_3$) δ_H / ppm 7.42 (s, 1 H, C$\underline{H}$-13), 5.86 (d, *J* = 9.3 Hz, 1 H, C$\underline{H}$-12), 5.49 - 5.42 (m, 2 H, C$\underline{H}$-6 and C$\underline{H}$-10), 5.35 (m, 2 H, C$\underline{H}$-4 and C$\underline{H}$-11), 5.07 (t, *J* = 9.9 Hz, 1 H, C$\underline{H}$-3), 4.88 (dd, *J* = 10.6, 4.0 Hz, 1 H, C$\underline{H}$-5), 4.48 (dd, *J* = 12.4, 2.1 Hz, 1 H, C$\underline{H}_A H_B$-7), 4.30 - 4.21 (m, 2 H, C$\underline{H}_A H_B$-1 and C$H_A \underline{H}_B$-7), 4.14 (t, *J* = 9.2 Hz, 1 H, C$\underline{H}$-9), 4.07 (dd, *J* = 12.4, 2.02 Hz, 1 H, C$H_A \underline{H}_B$-1), 4.01 – 3.93 (m, 2 H, C$\underline{H}$-2 and C$\underline{H}$-8), 2.69 (t, *J* = 7.7 Hz, 2 H, C$\underline{H}_2$-15), 2.13 (s, 3 H, C$\underline{H}_3$CO), 2.11 (s, 3 H, C$\underline{H}_3$CO), 2.06 (s, 3 H, C$\underline{H}_3$CO), 2.03 (s, 3 H, C$\underline{H}_3$CO), 2.02 (s, 3 H, C$\underline{H}_3$CO), 2.01 (s, 3 H, C$\underline{H}_3$CO), 1.84 (s, 3 H, C$\underline{H}_3$CO), 1.70 - 1.58 (m, 2 H, C$\underline{H}_2$-16), 1.39 - 1.17 (br. s, 14 H, (C$\underline{H}_2$)$_7$-17-23), 0.87 (t, *J* = 6.8 Hz, 3 H, C$\underline{H}_3$-24).

^{13}C NMR (100 MHz, $CDCl_3$) δ_C / ppm 170.6, 170.5, 170.3, 169.9, 169.4, 169.2, 149.1, 118.7, 95.9, 85.1, 75.2, 72.5, 70.8, 70.0, 69.2, 68.7, 67.9, 62.5, 61.4, 31.9, 29.6, 29.5, 29.3, 29.3, 29.1, 29.1, 25.6, 22.7, 20.8, 20.8, 20.7, 20.6, 20.2, 14.1.

HRMS (ESI) *m/z* calcd for $C_{38}H_{57}N_3NaO_{17}$ $[M+Na]^+$: 850.3580, found: 850.3584.

IR ($CHCl_3$, ν_{max}/cm^{-1}): 2927, 2856, 1748, 1224, 1036.

$[\alpha]^{20}_D$ = +45.2 (*c* = 0.99, $CHCl_3$).

1-(Hepta-*O*-acetyl-1-deoxy-β-D-maltopyranosyl)-4-dodecyl triazole 23d

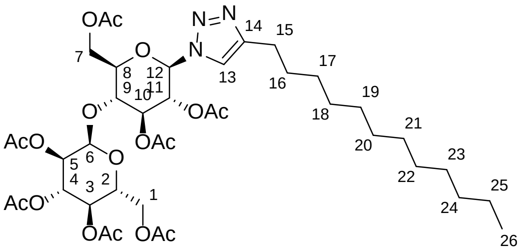

Synthesised according to Mahon *et al.*[7] To a stirred solution of **22** (1.5 g, 2.3 mmol) and 1-tetradecyne (1.1 mL, 4.5 mmol, 1.97 eq) in *t*-butanol (10 mL) was added a solution of $CuSO_4 \cdot 5H_2O$ (110 mg, 0.45 mmol, 0.2 eq) and ascorbic acid (160 mg, 0.91 mmol, 0.4 eq) in H_2O (10 mL). The reaction was stirred at rt for 72 h and then washed with CH_2Cl_2 (3 × 50 mL). The combined organic layers were washed with H_2O (100 mL) and then dried (Na_2SO_4) and concentrated in vacuo. The crude product was purified by flash column chromatography (3:7 acetone/petroleum ether; SiO_2) to give **23d** (355 mg, 0.41 mmol, 18%) as an amorphous white solid.

^{1}H NMR (500 MHz, $CDCl_3$) δ_H / ppm 7.42 (s, 1 H, C$\underline{H}$-13), 5.86 (d, *J* = 9.4 Hz, 1 H, C$\underline{H}$-12), 5.49 - 5.43 (m, 2 H, C$\underline{H}$-6 and C$\underline{H}$-10), 5.38 (t, *J* = 10.0 Hz, 1 H, C$\underline{H}$-4), 5.33 (t, *J* = 9.6 Hz, 1 H, C$\underline{H}$-11), 5.08 (t, *J* = 9.9 Hz, 1 H, C$\underline{H}$-3), 4.89 (dd, *J* = 10.4, 4.4 Hz, 1 H, C$\underline{H}$-5), 4.48 (dd, *J* = 12.4, 2.4 Hz, 1 H, C$\underline{H}_A$H$_B$-7), 4.26 (m, 2 H, C$\underline{H}_A$H$_B$-1 and CH$_A\underline{H}_B$-7), 4.14 (t, *J* = 9.2 Hz, 1 H, C$\underline{H}$-9), 4.08 (dd, *J* = 12.5, 2.21 Hz, 1 H, CH$_A\underline{H}_B$-1), 4.01 – 3.93 (m, 2 H, C$\underline{H}$-2 and C$\underline{H}$-8), 2.73 - 2.65 (m, 2 H, C$\underline{H}_2$-15), 2.13 (s, 3 H, C$\underline{H}_3$CO), 2.11 (s, 3 H, C$\underline{H}_3$CO), 2.07 (s, 3 H, C$\underline{H}_3$CO), 2.04 (s, 3 H, C$\underline{H}_3$CO), 2.03 (s, 3 H, C$\underline{H}_3$CO), 2.02 (s, 3 H, C$\underline{H}_3$CO), 1.84 (s, 3 H, C$\underline{H}_3$CO), 1.71 - 1.60 (m, 2 H, C$\underline{H}_2$-16), 1.39 - 1.17 (m, 18 H, (C$\underline{H}_2$)$_9$-17-25), 0.88 (t, *J* = 7.0 Hz, 3 H).

^{13}C NMR (126 MHz, CDCl$_3$) δ_C / ppm 170.6, 170.5, 170.3, 169.9, 169.9, 169.4, 169.2, 149.1, 118.7, 95.9, 85.1, 75.3, 75.2, 72.5, 70.8, 70.0, 69.2, 68.7, 67.9, 62.5, 61.4, 31.9**,** 29.6, 29.6, 29.6, 29.5, 29.3, 29.1, 29.1, 25.6, 22.7, 20.8, 20.8, 20.7, 20.6, 20.6, 20.1, 14.1.

HRMS (ESI) *m/z* calcd for $C_{40}H_{61}N_3NaO_{17}$ [M+Na]$^+$: 878.3893, found: 878.3870.

IR (CHCl$_3$, ν_{max}/cm^{-1}): 2925, 2856, 1748, 1225, 1037.

$[\alpha]^{20}_D$ = +40.4 (*c* = 0.98, CHCl$_3$).

1-Deoxy-1-azido-β-D-maltopyranose 24

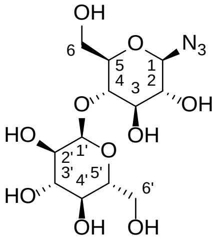

To a stirred suspension of **22** (2.0 g, 3.0 mmol) in MeOH (40 mL) was added a trace of sodium methoxide. Upon dissolution of the solid and concurrent disappearance of **22** (TLC control, approx. 10 min), the solution was neutralised using Amberlyst 15 resin (H$^+$ form). The resin was filtered off and washed with MeOH (10 mL), and the filtrate was concentrated in vacuo. The residue was freeze-dried to give **24** (840 mg, 2.3 mmol, 76%) as a tacky, hygroscopic white powder.

^{1}H NMR (400 MHz, D$_2$O) δ_H / ppm 5.32 (m, 1 H, C$\underline{H}$-1'), 4.67 (d, *J* = 8.6 Hz, 1 H, C$\underline{H}$-1), 3.92 - 3.42 (m, 9 H, C$\underline{H}$-3, C$\underline{H}$-3', C$\underline{H}$-4, C$\underline{H}$-5, C$\underline{H}$-5', C$\underline{H}_2$-6, C$\underline{H}_2$-6'), 3.33 (t, *J* = 8.9 Hz, 1 H, C$\underline{H}$-2'), 3.26 (t, *J* = 9.6 Hz, 1 H, C$\underline{H}$-4'), 3.21 (t, *J* = 9.0 Hz, 1 H, C$\underline{H}$-2).

^{13}C NMR (100 MHz, D_2O) δ_C / ppm 99.8, 90.2, 77.2, 77.0, 76.8, 73.1, 73.0, 73.0, 71.9, 69.5.

MS (ESI) *m/z*: 390.1 $[M+Na]^+$.

IR (solid, v_{max}/cm^{-1}): 3224 (broad), 2121, 1230, 1031.

$[\alpha]^{20}_D = -28.7$ (*c* = 1.0, H_2O).

1-(1-Deoxy-β-D-maltopyranosyl)-4-hexyl triazole 25a

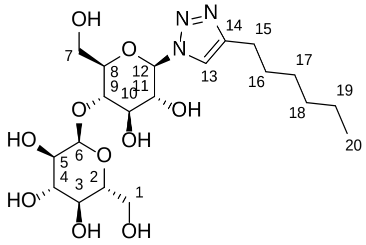

To a stirred suspension of **23a** (360 mg, 0.47 mmol) in MeOH (10 mL) was added a trace of sodium methoxide. Upon dissolution of the solid and concurrent disappearance of **23a** (TLC control, approx. 10 min), the solution was neutralised using Amberlyst 15 resin (H^+ form). The resin was filtered off and washed with MeOH (10 mL), and the filtrate was concentrated in vacuo. The residue was freeze-dried to give **25a** (76 mg, 0.16 mmol, 34%) as a tacky, hygroscopic white powder.

^1H NMR (400 MHz, CD_3OD) δ_H / ppm 7.95 (s, 1 H, C$\underline{H}$-13), 5.59 (d, *J* = 9.0 Hz, 1 H, C$\underline{H}$-12), 5.25 (d, *J* = 2.6 Hz, 1 H, C$\underline{H}$-6), 3.95 (d, *J* = 9.5 Hz, 1 H, C$\underline{H}$-11), 3.91 - 3.80 (m, 4 H, C$\underline{H}_A H_B$-1 and C$\underline{H}_2$-7 and C$\underline{H}$-10), 3.79 - 3.59 (m, 5 H, C$H_A\underline{H}_B$-1 and C$\underline{H}$-3 and C$\underline{H}$-4 and C$\underline{H}$-8 and C$\underline{H}$-9), 3.48 (dd, *J* = 9.4, 2.8 Hz, 1 H, C$\underline{H}$-5), 3.29 (t, *J* = 9.4 Hz, 1 H, C$\underline{H}$-2), 2.71 (t, *J* = 7.4 Hz, 2 H, C$\underline{H}_2$-15), 1.73 - 1.62 (m, 2 H, C$\underline{H}_2$-16), 1.46 - 1.25 (m, 6 H, (C$\underline{H}_2$)$_3$-17-18-19), 0.91 (m, 3 H, C$\underline{H}_3$-20).

^{13}C NMR (100 MHz, CD_3OD) δ_C / ppm 149.4, 122.5, 103.1, 89.4, 80.4, 79.7, 78.4, 75.2, 75.0, 74.3, 73.7, 71.6, 62.8, 62.0, 32.9, 30.6, 30.1, 26.4, 23.8, 14.6.

HRMS (ESI) *m/z* calcd for $C_{20}H_{35}N_3NaO_{10}$ $[M+Na]^+$: 500.2215, found: 500.2212.

IR (MeOH, ν_{max}/cm^{-1}): 3347 (broad), 2927, 2855, 1455, 1303.

$[\alpha]^{20}_D = +50.4$ (*c* = 2.1, MeOH).

1-(1-Deoxy-β-D-maltopyranosyl)-4-octyl triazole 25b

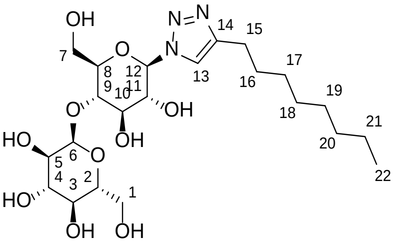

To a stirred suspension of **23b** (150 mg, 0.19 mmol) in MeOH (2 mL) was added a trace of sodium methoxide. Upon dissolution of the solid and concurrent disappearance of **23b** (TLC control, approx. 10 min), the solution was neutralised using Amberlyst 15 resin (H^+ form). The resin was filtered off and washed with MeOH (10 mL), and the filtrate was concentrated in vacuo. The residue was freeze-dried to give **25b** (20 mg, 0.04 mmol, 21%) as a tacky, hygroscopic white powder.

^{1}H NMR (400 MHz, CD_3OD) δ_H / ppm 7.95 (s, 1 H, C$\underline{H}$-13), 5.59 (d, *J* = 9.1 Hz, 1 H, C$\underline{H}$-12), 5.24 (d, *J* = 3.5 Hz, 1 H, C$\underline{H}$-6), 3.95 (t, *J* = 8.8 Hz, 1 H, C$\underline{H}$-11), 3.90 - 3.79 (m, 4 H, C$\underline{H}_A H_B$-1 and C$\underline{H}_2$-7 and C$\underline{H}$-10), 3.79 - 3.60 (m, 5 H, C$H_A\underline{H}_B$-1 and C$\underline{H}$-3 and C$\underline{H}$-4 and C$\underline{H}$-8 and C$\underline{H}$-9), 3.48 (dd, *J* = 9.7, 3.6 Hz, 1 H, C$\underline{H}$-5), 3.29 (t, *J* = 9.2 Hz, 1 H, C$\underline{H}$-2), 2.70 (t, *J* = 7.6 Hz, 2 H, C$\underline{H}_2$-15), 1.73 - 1.62 (m, 2 H, C$\underline{H}_2$-16), 1.32 (d, *J* = 18.8 Hz, 10 H, (C$\underline{H}_2)_5$-17-21), 0.90 (t, *J* = 6.7 Hz, 3 H, C$\underline{H}_3$).

^{13}C NMR (100 MHz, CD_3OD) δ_C / ppm 148.3, 121.4, 101.9, 88.3, 79.3, 78.6, 77.3, 74.1, 73.9, 73.2, 72.5, 70.5, 61.7, 60.8, 32.0, 29.5, 29.5, 29.4, 29.3, 25.3, 22.7, 13.4.

HRMS (ESI) *m/z* calcd for $C_{22}H_{40}N_3NaO_{10}$ $[M+Na]^+$: 506.2708, found: 506.2715.

IR (MeOH, *v*$_{max}$/cm^{-1}): 3348 (broad), 2925, 2856, 1458, 1306.

$[\alpha]^{20}_D$ = + 50.6 (*c* = 1.1, MeOH).

1-(1-Deoxy-β-D-maltopyranosyl)-4-decyl triazole 25c

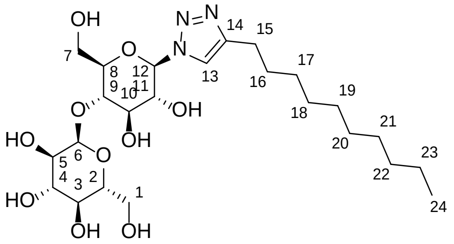

To a stirred suspension of **23c** (186 mg, 0.22 mmol) in MeOH (10 mL) was added a trace of sodium methoxide. Upon dissolution of the solid and concurrent disappearance of **23c** (TLC control, approx. 10 min), the solution was neutralised using Amberlyst 15 resin (H^+ form). The resin was filtered off and washed with MeOH (10 mL), and the filtrate was concentrated in vacuo. The residue was freeze-dried to give **25c** (100 mg, 0.19 mmol, 83%) as a tacky, hygroscopic white powder.

^1H NMR (400 MHz, CD_3OD) δ_H / ppm 7.95 (s, 1 H, C$\underline{H}$-13), 5.59 (d, *J* = 9.2 Hz, 1 H, C$\underline{H}$-12), 5.24 (d, *J* = 3.5 Hz, 1 H, C$\underline{H}$-6), 3.94 (t, *J* = 9.1 Hz, 1 H, C$\underline{H}$-11), 3.90 - 3.79 (m, 4 H, C$\underline{H}_A$H$_B$-1 and C$\underline{H}_2$-7 and C$\underline{H}$-10), 3.79 - 3.61 (m, 5 H, CH$_A\underline{H}_B$-1 and C$\underline{H}$-3 and C$\underline{H}$-4 and C$\underline{H}$-8 and C$\underline{H}$-9), 3.48 (dd, *J* = 10.0, 3.3 Hz, 1 H, C$\underline{H}$-5), 3.29 (t, *J* = 9.4 Hz, 1 H, C$\underline{H}$-2), 2.70 (t, *J* = 7.5 Hz, 2 H, C$\underline{H}_2$-15), 1.67 (m, 2 H, C$\underline{H}_2$-16), 1.45 - 1.21 (br. m, 14 H, (C$\underline{H}_2$)$_7$-17-23), 0.94 - 0.86 (m, 3 H, C$\underline{H}_3$-24).

^{13}C NMR (100 MHz, CD_3OD) δ_C / ppm 149.4, 122.5, 103.1, 89.5, 80.4, 79.7, 78.4, 75.2, 75.0, 74.3, 73.7, 71.6, 62.9, 62.0, 33.2, 30.9, 30.8, 30.7, 30.6, 30.6, 30.4, 26.4, 23.9, 14.6.

HRMS (ESI) *m/z* calcd for $C_{24}H_{43}N_3NaO_{10}$ $[M+Na]^+$: 556.2841, found: 556.2859.

IR (MeOH, ν_{max}/cm^{-1}): 3358 (broad), 2929, 2853, 1453, 1300.

$[\alpha]^{20}_D$ = + 57.3 (*c* = 1.2, MeOH).

1-(1-Deoxy-β-D-maltopyranosyl)-4-dodecyl triazole 25d

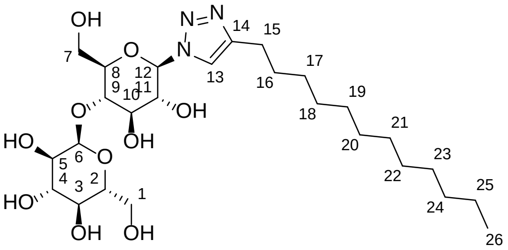

To a stirred suspension of **9d** (355 mg, 0.41 mmol) in MeOH was added a trace of sodium methoxide. Upon dissolution of the solid and concurrent disappearance of **9d** (TLC control, approx. 10 min), the solution was neutralised using Amberlyst 15 resin (H^+ form). The resin was filtered off and washed with MeOH (10 mL), and the filtrate was concentrated in vacuo. The residue was freeze-dried to give **11d** (144 mg, 0.26 mmol, 62%) as a tacky, hygroscopic white powder.

^{1}H NMR (500 MHz, CD_3OD) δ_H / ppm 7.95 (s, 1 H, C$\underline{H}$-13), 5.59 (d, *J* = 9.1 Hz, 1 H, C$\underline{H}$-12), 5.25 (d, *J* = 3.8 Hz, 1 H, C$\underline{H}$-6), 3.95 (t, *J* = 8.9 Hz, 1 H, C$\underline{H}$-11), 3.92 - 3.81 (m, 4 H, C$\underline{H}_A$H$_B$-1 and C$\underline{H}_2$-7 and C$\underline{H}$-10), 3.76 (t, *J* = 9.2 Hz, 1 H, C$\underline{H}$-9), 3.73 - 3.61 (m, 4 H, CH$_A\underline{H}_B$-1 and C$\underline{H}$-3 and C$\underline{H}$-4 and C$\underline{H}$-8), 3.48 (dd, *J* = 9.7, 3.8 Hz, 1 H, C$\underline{H}$-5), 3.29 (t, *J* =

9.6 Hz, 1 H, C<u>H</u>-2), 2.71 (t, *J* = 7.6 Hz, 2 H, C$\underline{H}_2$-15), 1.72 - 1.63 (m, 2 H, C$\underline{H}_2$-16), 1.43 - 1.21 (br. m, 18 H, (C$\underline{H}_2$)$_9$-17-25), 0.90 (t, *J* = 7.3 Hz, 3 H, C$\underline{H}_3$-26).

^{13}C NMR (126 MHz, CD_3OD) δ_C / ppm 149.4, 122.5, 103.1, 89.5, 80.4, 79.7, 78.4, 75.2, 75.0, 74.3, 73.7, 71.6, 62.9, 62.0, 33.2, 30.9, 30.9, 30.9, 30.8, 30.7, 30.6, 30.6, 30.4, 26.4, 23.9, 14.6.

HRMS (ESI) *m/z* calcd for $C_{26}H_{47}N_3NaO_{10}$ $[M+Na]^+$: 584.3154, found: 584.3164.

IR (MeOH, ν_{max}/cm^{-1}): 3352 (broad), 2924, 2851, 1460, 1303.

$[\alpha]^{20}_D$ = + 51.3 (*c* = 1.1, MeOH).

***N*-Carboxybutyl-L-leucine 28a**

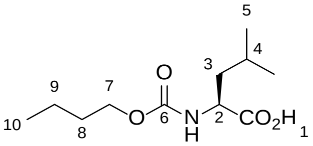

To a rapidly-stirred suspension of L-leucine (100 mg, 0.76 mmol) in saturated aqueous $NaHCO_3$ (1 mL) and acetone (1 mL) was added butyl chloroformate (100 µL, 0.77 mmol, 1.02 eq) at rt. Upon consumption of leucine (TLC control, EtOAc, approx. 2 h) the reaction was diluted with H_2O (5 mL) and washed with Et_2O (5 mL). The aqueous layer was acidified to pH 2 with aqueous HCl (2 M) and extracted with EtOAc (3 × 10 mL). The combined organic layers were dried (Na_2SO_4) and concentrated in vacuo to give pure **28a** (110 mg, 0.48 mmol, 62%) as an oil.

Characterisation data are provided for the L-enantiomer. The racemate was synthesised via an identical procedure starting from the racemic amino acid.

^{1}H NMR (400 MHz, DMSO-d_6) δ_H / ppm 12.46 (s, 1 H, CO$_2$H), 7.35 (d, *J* = 8.2 Hz, 1 H, NH), 3.93 (t, *J* = 6.7 Hz, 3 H, CH-2 and CH$_2$-7), 1.73 – 1.57 (m, 1 H, CH-4), 1.57 – 1.38 (m, 4 H, CH$_2$-3 and CH-4 and CH$_2$-8), 1.38 – 1.25 (m, 2 H, CH$_2$-9), 0.96 – 0.75 (m, 9 H, C(CH$_3$)$_2$-5 and CH$_3$-10).

^{13}C NMR (101 MHz, DMSO-d_6) δ_C / ppm 175.0 156.9, 64.0, 52.6, 40.1, 31.2, 24.8, 23.3, 21.6, 19.0, 14.1.

HRMS (ESI) *m/z* calcd for $C_{11}H_{20}O_4N$ [M-H]$^-$: 230.13987, found: 230.13978.

IR (DMSO, ν_{max}/cm^{-1}): 3442, 3271, 2934, 2855, 2249, 2124, 1709, 1665, 1545, 1370, 1267, 1226.

***N*-Carboxydecyl-L-leucine 28b**

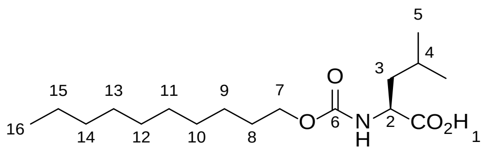

To a rapidly-stirred suspension of L-leucine (100 mg, 0.76 mmol) in saturated aqueous NaHCO$_3$ (1 mL) and acetone (1 mL) was added decyl chloroformate (180 µL, 0.78 mmol, 1.02 eq) at rt. Upon consumption of leucine (TLC control, EtOAc, approx. 4 h) the reaction was diluted with H$_2$O (5 mL) and washed with Et$_2$O (5 mL). The aqueous layer was acidified to pH 2 with aqueous HCl (2 M) and extracted with EtOAc (3 × 10 mL). The combined organic layers were dried (Na$_2$SO$_4$) and concentrated in vacuo to give pure **28b** (175 mg, 0.56 mmol, 73%) as an oil.

Characterisation data are provided for the L-enantiomer. The racemate was synthesised via an identical procedure starting from the racemic amino acid.

^{1}H NMR (400 MHz, DMSO-d_6) δ_H / ppm 12.42 (s, 1 H, CO$_2$H), 7.35 (d, *J* = 8.2 Hz, 1 H, NH), 3.98 – 3.86 (m, 3 H, CH-2 and CH$_2$-7), 1.71 – 1.58 (m, 1 H, CH-4), 1.57 – 1.47 (m, 2 H, CH$_2$-3), 1.47 – 1.34 (m, 2 H, CH$_2$-8), 1.24 (s, 14 H, (CH$_2$)$_7$-9-15), 0.91 – 0.79 (m, 9 H, CH$_3$-16 and C(CH$_3$)$_2$-5).

^{13}C NMR (101 MHz, DMSO-d_6) δ_C / ppm 175.0, 156.8, 64.3, 61.2, 52.5, 40.1, 33.0, 29.6, 29.5, 29.4, 29.2, 29.2, 24.8, 23.4, 22.6, 21.6, 14.4.

HRMS (ESI) *m/z* calcd for $C_{17}H_{32}O_4N$ [M-H]$^-$: 314.23368, found: 314.23392.

IR (DMSO, ν_{max}/cm^{-1}): 3440, 3272, 2926, 2855, 2250, 2124, 1710, 1666, 1622, 1538, 1370, 1263, 1226.

N-Carboxybenzyl-L-phenylalanine 30a

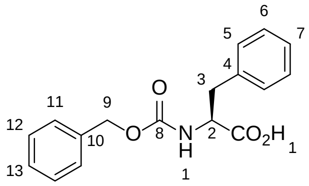

To a rapidly-stirred suspension of L-phenylalanine (100 mg, 0.61 mmol) in saturated aqueous NaHCO$_3$ (1 mL) and acetone (1 mL) was added benzyl chloroformate (100 µL, 0.70 mmol, 1.16 eq) at rt. Upon consumption of phenylalanine (TLC control, EtOAc, approx. 3 h) the reaction was diluted with H$_2$O (5 mL) and washed with Et$_2$O (5 mL). The aqueous layer was acidified to pH 2 with aqueous HCl (2 M) and extracted with EtOAc (3 × 10 mL). The combined organic layers were dried (Na$_2$SO$_4$) and concentrated in vacuo to give pure **30a** (114 mg, 0.38 mmol, 63%) as an oil that solidified upon being refrigerated.

Characterisation data are provided for the L-enantiomer. The racemate was synthesised via an identical procedure starting from the racemic amino acid.

^{1}H NMR (400 MHz, DMSO-d_6) δ_H / ppm 12.72 (s, 1 H, CO$_2$H), 7.65 (d, *J* = 8.4 Hz, 1 H, NH), 7.40 – 7.16 (m, 10 H, CH-4,5,6,7,10,11,12,13), 4.96 (d, *J* = 2.4 Hz, 2 H, CH$_2$-9), 4.18 (ddd, *J* = 10.5, 8.4, 4.4 Hz, 1 H, CH-2), 3.06 (dd, *J* = 13.8, 4.4 Hz, 1 H, CH$_A$H$_B$-3), 2.83 (dd, *J* = 13.8, 10.6 Hz, 1 H, CH$_A$H$_B$-3).

^{13}C NMR (101 MHz, DMSO-d_6) δ_C / ppm 173.8, 156.5, 138.4, 137.5, 129.6, 128.8, 128.6, 128.5, 128.2, 128.0, 65.7, 56.0, 40.0, 36.9.

MS (ESI) *m/z*: 298.1 [M-H]$^-$.

IR (DMSO, ν_{max}/cm^{-1}): 3443, 3261, 2950, 2250, 2125, 1710, 1666, 1589, 1458, 1395, 1376, 1335, 1275, 1228.

N-Carboxydecyl-L-phenylalanine 30b

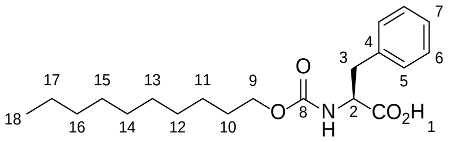

To a rapidly-stirred suspension of L-phenylalanine (100 mg, 0.61 mmol) in saturated aqueous NaHCO$_3$ (1 mL) and acetone (1 mL) was added decyl chloroformate (150 µL, 0.65 mmol, 1.07 eq) at rt. Upon consumption of phenylalanine (TLC control, EtOAc, approx. 4 h) the reaction was diluted with H$_2$O (5 mL) and washed with Et$_2$O (5 mL). The aqueous layer was acidified to pH 2 with aqueous HCl (2 M) and extracted with EtOAc (3 × 10 mL). The combined organic layers were dried (Na$_2$SO$_4$) and concentrated in vacuo to give pure **30b** (179 mg, 0.51 mmol, 85%) as an oil.

Characterisation data are provided for the L-enantiomer. The racemate was synthesised via an identical procedure starting from the racemic amino acid.

^{1}H NMR (400 MHz, DMSO-d_6) δ_H / ppm 12.68 (s, 1 H, $CO_2\underline{H}$), 7.41 (d, J = 8.4 Hz, 1 H, $N\underline{H}$), 7.31 – 7.10 (m, 5 H, $C\underline{H}$-4,5,6,7), 4.14 (ddd, J = 10.6, 8.4, 4.4 Hz, 1 H, $C\underline{H}$-2), 3.92 – 3.79 (m, 2 H, $C\underline{H}_2$-9), 3.05 (dd, J = 14.0, 4.5 Hz, 1 H, $C\underline{H}_AH_B$-3), 2.83 (dd, J = 13.8, 10.5 Hz, 1 H, $CH_A\underline{H}_B$-3), 1.43 (m, 4 H, $C\underline{H}_2$-10 and $C\underline{H}_2$-11), 1.23 (d, J = 3.3 Hz, 12 H, $(C\underline{H}_2)_6$-12-17), 0.85 (t, J = 6.7 Hz, 3 H, $C\underline{H}_3$-18).

^{13}C NMR (101 MHz, DMSO-d_6) δ_C / ppm 173.9, 156.7, 138.5, 129.5, 128.6, 126.8, 64.3, 55.9, 36.9, 33.0, 31.8, 29.6, 29.4, 29.2, 26.0, 25.8, 22.6, 14.4.

HRMS (ESI) *m/z* calcd for $C_{20}H_{30}O_4N$ $[M-H]^-$: 348.21803, found: 384.21831.

IR (DMSO, ν_{max}/cm^{-1}): 3440, 3274, 2927, 2856, 2251, 2125, 1712, 1673, 1539, 1456, 1375, 1245.

1-Palmitoyl-*sn*-glycero-3-phosphocholine 32

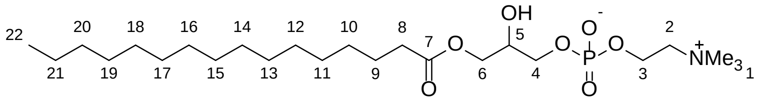

Synthesised according to Fasoli *et al.*[13] A suspension of commercial *sn*-glycero-3-phosphocholine **31** (1.0 g, 3.9 mmol) and dibutyltin oxide (1.07 g, 4.3 mmol, 1.1 eq) in isopropyl alcohol (40 mL) was heated to reflux for 1 h. The suspension was cooled to rt and triethylamine (1.1 mL, 7.8 mmol, 2.0 eq) and palmitoyl chloride (2.4 mL, 7.8 mmol, 2.0 eq) were added. The reaction was stirred at rt for 30 min and then H_2O (40 mL) and heptane (40 mL) were added. The layers were separated and the aqueous-alcohol layer was washed with heptane (3 × 30 mL). The aqueous-alcohol layer was concentrated in vacuo and the residual water was azeotroped with toluene. The residue was dissolved in EtOH (10 mL) and precipitated by addition of acetone (40 mL) at -10 °C to give **32** (0.43 g, 0.87 mmol, 22%) as a white powder.

^{1}H NMR (500 MHz, CDCl$_3$) δ_H / ppm 4.38 - 4.25 (m, 2 H, C$\underline{H}_2$-3), 4.13 – 4.03 (m, 2 H, C$\underline{H}_2$-6), 3.98 – 3.90 (m, 2 H, C$\underline{H}$-5 and C$\underline{H}_A$H$_B$-4), 3.88 - 3.73 (m, 3 H, CH$_A\underline{H}_B$-4 and C$\underline{H}_2$-2), 3.35 (s, 9 H, N(C$\underline{H}_3$)$_3$-1), 2.30 (t, *J* = 7.7 Hz, 2 H, C$\underline{H}_2$-8), 1.62 – 1.52 (m, 2 H, C$\underline{H}_2$-9), 1.34 – 1.20 (s, 24 H, (C$\underline{H}_2$)$_{12}$-10-21), 0.89 (t, *J* = 7.2 Hz, 3 H, C$\underline{H}_3$-22).

^{13}C NMR (126 MHz, CDCl$_3$) δ_C / ppm 173.8, 68.8 (d, *J* = 5.0 Hz), 67.1, 66.1, 65.2, 59.4, 54.2 (3 C), 34.2, 31.9 (3 C), 29.7 (3 C), 29.6, 29.4 (2 C), 29.4, 29.3, 24.9, 22.7, 14.1.

^{31}P NMR (162 MHz, CDCl$_3$) δ_P / ppm -0.98.

MS (ESI) *m/z*: 496.4 [M+H]$^+$.

IR (CHCl$_3$, ν_{max}/cm^{-1}): 3363 (broad), 2923, 2853, 1730, 1216, 1084, 1054, 756.

1,2-Di-(4-pentynoyl)-*sn*-glycero-3-phosphocholine 33

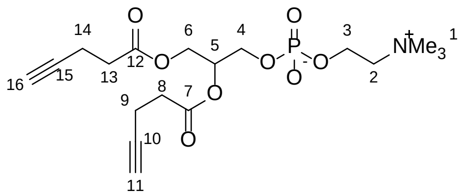

Synthesised according to Menger *et al.*[14] To a solution of *sn*-glycero-3-phosphocholine-CdCl$_2$ **31** (200 mg, 0.45 mmol), DMAP (110 mg, 0.91 mmol, 2.0 eq), and 4-pentynoic acid (178 mg, 1.8 mmol, 4.0 eq) in CHCl$_3$ was added DCC (0.27 mL, 1.8 mmol, 4.0 eq). The flask was covered in tinfoil and stirred for 4 days at rt. The solvent was removed in vacuo and the residue added directly to the top of a pre-loaded silica gel column and eluted (65:25:4 and then 2:3:1 $CHCl_3$/MeOH/H_2O) to give **33** (50 mg, 0.12 mmol, 26%) as a white powder.

^{1}H NMR (500 MHz, $CDCl_3$) δ_H / ppm 5.24 (m, 1 H, C$\underline{H}$-5), 4.42 (dd, *J* = 12.0, 2.6 Hz, 1 H, C$\underline{H}_A H_B$-6), 4.28 (m, 2 H, C$\underline{H}_2$-3), 4.21 (dd, *J* = 12.0, 7.1 Hz, 1 H, CH$_A\underline{H}_B$-6), 3.96 (m, 2 H, C$\underline{H}_2$-4), 3.81 (m, 2 H, C$\underline{H}_2$-2), 3.36 (s, 9 H, N(C$\underline{H}_3$)$_3$-1), 2.61 - 2.44 (m, 8 H, C$\underline{H}_2$-7 and C$\underline{H}_2$-8 and C$\underline{H}_2$-13 and C$\underline{H}_2$-14), 2.18 (t, *J* = 2.5 Hz, 1 H, C$\underline{H}$-16), 2.11 (t, *J* = 2.6 Hz, 1 H, C$\underline{H}$-11).

^{13}C NMR (126 MHz, $CDCl_3$) δ_C / ppm 171.6, 171.4, 82.5, 82.5, 71.0 (d, *J* = 6.9 Hz), 69.8, 69.6, 66.2 (d, *J* = 5.7 Hz), 63.3 (d, *J* = 4.1 Hz), 63.1, 59.3 (d, *J* = 4.1 Hz), 54.3, 33.3, 33.1, 14.3, 14.3.

^{31}P NMR (162 MHz, $CDCl_3$) δ_P / ppm –0.60.

HRMS (ESI) *m/z* calcd for $C_{18}H_{28}NNaO_8P$ $[M+Na]^+$: 440.1445, found: 440.1435.

2-Maleimidoacetic acid 36

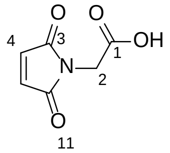

Synthesised according to Sinclair *et al.*[15] Maleic anhydride (19.6 g, 200 mmol) and glycine (15.0 g, 200 mmol, 1.0 eq) were stirred in AcOH (200 mL) at rt for 18 h and then heated at reflux until a clear solution was obtained (approx. 8 h). The reaction was allowed to cool to rt and then the solvent was removed in vacuo. The crude product was purified by flash column chromatography (1:19 AcOH/CH_2Cl_2; SiO_2) to give pure **36** (12.9 g, 83.2 mmol, 42%).

^{1}H NMR (400 MHz, DMSO-d_6) δ_H / ppm 13.18 (s, 1 H, CO$_2$H), 7.13 (s, 2 H, CH-4), 4.14 (s, 2 H, CH$_2$-2).

^{13}C NMR (101 MHz, DMSO-d_6) δ_C / ppm 170.4, 168.9, 135.0, 38.5.

MS (ESI) *m/z*: 154.0 [M-H]$^-$

4-(Carboxymethyl)-10-oxa-4-azatricyclo[5.2.1.0^{2,6}]-dec-8-ene-3,5-dione 37

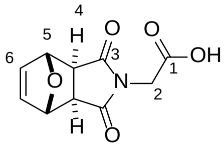

A stirred suspension of **6** (1.0 g, 6.02 mmol) and glycine (452 mg, 6.02 mmol, 1.0 eq) in saturated aqueous NaHCO$_3$ (10 mL) was heated to 60 °C under a reflux condenser. The reaction was monitored by ESI-MS (negative mode) until complete conversion to **37** was indicated and no peaks corresponding to the intermediate di-carboxylate species were present. The reaction was cooled to rt and acidified to pH 2 using aqueous HCl (2 M). The aqueous layer was extracted with EtOAc (3 × 20 mL) and the combined organic layers were dried (Na$_2$SO$_4$) and concentrated in vacuo to give pure **37** (740 mg, 3.32 mmol, 55%) as an amorphous solid.

1H NMR (400 MHz, DMSO-d_6) δ_H / ppm 6.56 (s, 2 H, CH-6), 5.16 (s, 2 H, CH-5), 4.06 (s, 2 H, CH$_2$-2), 3.04 (s, 2 H, CH-4).

^{13}C NMR (101 MHz, DMSO-d_6) δ_C / ppm 175.7, 168.1, 137.2, 80.7, 47.6, 39.4.

MS (ESI) *m/z*: 222.1 [M-H]$^-$.

1-(*t*-Butyldimethylsilanyloxy)propane-1,2-diol 39

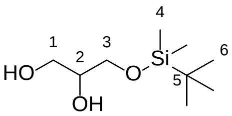

Synthesised following Paterson *et al.*[16] To a solution of glycerol (9 mL, 96 mmol) and imidazole (1.3 g, 19 mmol, 0.2 eq) in CH_2Cl_2 (25 mL) and DMF (8 mL) was added TBDMSCl (1.0 g, 6.6 mmol, 0.07 eq) in CH_2Cl_2 (5 mL) at -10 °C dropwise. The reaction was stirred at rt for 1 h and then diluted with H_2O (25 mL) and CH_2Cl_2 (10 mL). The layers were separated and the aqueous layer was extracted with CH_2Cl_2 (3 × 10 mL). The combined organic layers were washed with H_2O (3 × 10 mL) and brine (10 mL), dried ($MgSO_4$) and concentrated in vacuo. The residue was purified by flash column chromatography (9:11 EtOAc/petroleum ether; SiO_2) to give **39** (688 mg, 3.33 mmol, 17%) as a colourless oil.

^{1}H NMR (400 MHz, $CDCl_3$) δ_H / ppm 3.83 – 3.56 (m, 5 H, $C\underline{H}_2$-1 and $C\underline{H}$-2 and $C\underline{H}_2$-3), 0.90 (s, 9 H, $C(C\underline{H}_3)_3$-6), 0.08 (s, 6 H, $Si(C\underline{H}_3)_2$-4).

^{13}C NMR (101 MHz, $CDCl_3$) δ_C / ppm 70.8, 66.0, 65.3, 24.7, 18.5, -5.4.

MS (ESI) *m/z*: 226.1 $[M+Na]^+$.

3-((*tert*-Butyldimethylsilyl)oxy)propane-1,2-diyl bis(2-(2,5-dioxo-2,5-dihydro-1*H*-pyrrol-1-yl)acetate) 40

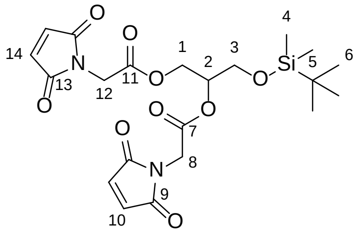

A suspension of **41** (70 mg, 0.11 mmol) in toluene (2 mL) was heated at reflux under a Vigreux condenser and a drying tube loaded with $CaCl_2$. After 28 h the solution was hot filtered and the filtrate was allowed to cool to rt. The solvent was removed in vacuo and the residue was purified by flash column chromatography (2:98 acetone/$CHCl_3$; SiO_2) give pure **40** (35 mg, 0.073 mmol, 64%) as a colourless oil.

^{1}H NMR (400 MHz, $CDCl_3$) δ_H / ppm 6.80 (s, 4 H, C$\underline{H}$-10 and C$\underline{H}$-14), 5.12 (dq, *J* = 7.9, 5.4, 3.9 Hz, 1 H, C$\underline{H}$-2), 4.48 – 4.20 (m, 6 H, C$\underline{H}_2$-1 and C$\underline{H}_2$-8 and C$\underline{H}_2$-12), 3.73 (qd, *J* = 10.9, 5.2 Hz, 2 H, C$\underline{H}_2$-3), 0.89 (s, 9 H, C(C$\underline{H}_3$)$_3$-6), 0.07 (s, 6 H, Si(C$\underline{H}_3$)$_2$-4).

^{13}C NMR (101 MHz, $CDCl_3$) δ_C / ppm 175.7, 175.7, 175.0, 165.5, 165.0, 133.9, 133.9, 133.90, 73.0, 63.7, 60.0, 47.7, 47.7, 38.4, 38.4, 25.7, 18.0, -5.5, -5.5.

MS (ESI) *m/z*: 503.1 $[M+Na]^+$.

3-((*t*-Butyldimethylsilyl)oxy)propane-1,2-diyl bis(2-(1,3-dioxo-1,3,3a,4,7,7a-hexahydro-2*H*-4,7-epoxyisoindol-2-yl)acetate) 41

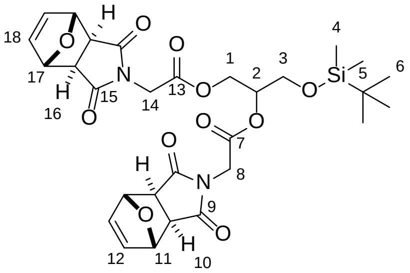

To a solution of **40** (100 mg, 0.48 mmol) and **37** (432 mg, 1.9 mmol, 4 eq) in CH_2Cl_2 (3 mL) at 0 °C was added EDCI·HCl (223 mg, 1.2 mmol, 2.4 eq) and DMAP (47 mg, 0.39 mmol, 0.8 eq) in CH_2Cl_2 (3 mL) dropwise. The reaction was stirred for 2 h until complete conversion of **40** a single major product was observed (TCL control, EtOAc/petroleum ether, 1:1). The reaction was diluted with EtOAc (15 mL) and the organic layer was washed sequentially with 1 M HCl (15 mL), H_2O (15 mL), sat. $NaHCO_3$ (15 mL) and brine (15 mL). The organic layer was dried (Na_2SO_4) and the solvent was removed in vacuo. The residue was purified by flash column chromatography (2:3 EtOAc/petroleum either; SiO_2) to give **41** as a colourless oil (70 mg, 0.11 mmol, 23%).

^{1}H NMR (400 MHz, $CDCl_3$) δ_H / ppm 6.51 (s, 4 H, C$\underline{H}$-12 and C$\underline{H}$-18), 5.28 (s, 4 H, C$\underline{H}$-11 and C$\underline{H}$-17), 5.13 – 5.02 (m, 1 H, C$\underline{H}$-2), 4.40 – 4.24 (m, 6 H, C$\underline{H}_2$-1 and C$\underline{H}_2$-8 and C$\underline{H}_2$-14), 3.76-3.62 (m, 2 H, C$\underline{H}_2$-3), 2.94 (s, 4 H, C$\underline{H}$-10 and C$\underline{H}$-16), 0.85 (s, 9 H, C(C$\underline{H}_3$)$_3$-6), 0.03 (s, 6 H, Si(C$\underline{H}_3$)$_2$-4).

^{13}C NMR (101 MHz, $CDCl_3$) δ_C / ppm 175.3, 175.2, 175.1, 166.4, 166.1, 136.6, 136.6, 136.6, 80.9, 80.9, 73.1, 63.8, 61.0, 47.7, 47.7, 39.7, 39.6, 25.8, 18.2, -5.5, -5.5.

MS (ESI) *m/z*: 639.1 [M+Na]$^+$.

1-Palmitoyl-2-(4-pentynoyl)-*sn*-glycero-3-phosphocholine 44

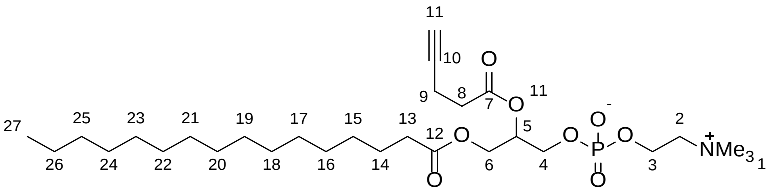

Synthesised according to Pugh *et al.*[17] To a solution of **32** (50 mg, 0.1 mmol) and DMAP (37 mg, 0.3 mmol, 3.0 eq) in CH_2Cl_2 was added **4-pentynoic anhydride** (54 mg, 0.3 mmol, 3.0 eq). The reaction was stirred at rt for 24 h and then concentrated in vacuo. The residue was taken into CH_2Cl_2 and stirred for 1 h with Dowex 50 × 8 cation exchange resin (H^+ form). The resin was filtered off and washed with CH_2Cl_2 and the filtrate was concentrated in vacuo. The residue was taken into $CHCl_3$/MeOH (2:1, 15 mL) and washed once with saturated aqueous $NaHCO_3$ (4 mL). The organic layer was dried (Na_2SO_4) and concentrated in vacuo. The crude product was purified by flash column chromatography (65:35:5 $CHCl_3$/MeOH/33% NH_3; SiO_2) to give a 8:1 mixture (39 mg, 68 µmol, 67%) of **44** and its 1-(4-pentynoyl)-2-palmitoyl regioisomer as a white powder.

^{1}H NMR (500 MHz, $CDCl_3$) δ_H / ppm 5.29 - 5.21 (m, 1 H, C$\underline{H}$-2), 4.37 (dd, *J* = 12.1, 2.8 Hz, 1 H, CH$_A\underline{H}_B$-6), 4.32 (m, 2 H, C$\underline{H}_2$-3), 4.15 (dd, *J* = 11.9, 6.5 Hz, 1 H, CH$_A\underline{H}_B$-6), 3.98 (t, *J* = 5.9 Hz, 2 H, C$\underline{H}_2$-4), 3.82 (m, 2 H, C$\underline{H}_2$-2), 3.37 (s, 9 H, N(C$\underline{H}_3$)$_3$-1), 2.57 (t, *J* = 6.7 Hz, 2 H, C$\underline{H}_2$-8), 2.52 - 2.45 (m, 2 H, C$\underline{H}_2$-9), 2.29 (t, *J* = 7.7 Hz, 2 H, C$\underline{H}_2$-13), 2.12 (t, *J* = 2.5 Hz, 1 H, C$\underline{H}$-11), 1.58 (m, 2 H, C$\underline{H}_2$-14), 1.35 - 1.19 (m, 24 H, (C$\underline{H}_2$)$_{12}$-15-26), 0.88 (t, *J* = 6.9 Hz, 3 H, C$\underline{H}_3$-27).

^{13}C NMR (126 MHz, $CDCl_3$) δ_C / ppm 173.6, 171.3, 82.5, 71.2 (d, *J* = 6.91 Hz), 69.6, 66.3 (d, *J* = 5.48 Hz), 62.7, 63.6 (d, *J* = 4.29 Hz), 59.4 (d, *J* = 3.58 Hz), 54.4, 34.1, 33.3, 31.9, 29.7, 29.7, 29.7, 29.5, 29.4, 29.3, 29.2, 24.9, 22.7, 14.3, 14.1.

^{31}P NMR (162 MHz, $CDCl_3$) δ_P / ppm – 0.82.

HRMS (ESI) *m/z* calcd for $C_{29}H_{54}NNaO_8P$: 598.3479, found: 598.3491.

IR ($CHCl_3$, ν_{max}/cm^{-1}): 3393, 2924, 2754, 2505, 2071, 1729, 1233.

Oleyl azide 45

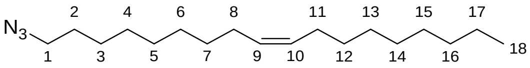

Synthesised via the corresponding bromide according to Basabe *et al.*[18] and Budin and Devaraj.[19]

To a solution of oleyl alcohol (1.79 g, 5.7 mmol, 85% w/w) in CH_2Cl_2 at 0 °C was added CBr_4 (2.07 g, 6.2 mmol, 1.1 eq) and PPh_3 (2.19 g, 8.4 mmol, 1.5 eq) in portions over 2 min. Upon completion (TLC control, 1:5 Et_2O / hexane, approx. 10 min), hexane (50 mL) was added, causing precipitation, and the suspension was filtered through Celite. The filtrate was concentrated and the residue was taken up into 50 mL of hexane. The precipitation procedure was repeated three times, and the crude product was then purified by flash column chromatography (hexane; SiO_2) to yield oleyl bromide (1.51 g, 4.6 mmol, 80%) as a colourless oil.

^1H NMR (400 MHz, $CDCl_3$) δ_H / ppm 5.44 - 5.29 (m, 2 H, C$\underline{H}$-9 and C$\underline{H}$-10), 3.42 (t, *J* = 6.9 Hz, 2 H, C$\underline{H}_2$-1), 2.09 – 1.93 (m, 4 H, C$\underline{H}_2$-8 and C$\underline{H}_2$-11), 1.86 (quin, *J* = 7.2 Hz, 2 H, C$\underline{H}_2$-2), 1.48 - 1.20 (m, 22 H (C$\underline{H}_2$)$_5$-3-7 and (C$\underline{H}_2$)$_6$-12-17), 0.89 (t, *J* = 6.8 Hz, 3 H, C$\underline{H}_3$-18).

^{13}C NMR (100 MHz, $CDCl_3$) δ_C / ppm 130.0, 129.8, 34.0, 32.8, 31.9, 29.8, 29.7, 29.5, 29.3 (3 C), 29.2, 28.8, 28.2, 27.2 (2 C), 22.7, 14.1.

HRMS (EI/FI+) *m/z* calcd for $C_{18}H_{35}Br$ $[M]^+$: 330.1922 and 332.1903, found: 330.1930 and 332.1925.

IR ($CHCl_3$, ν_{max}/cm^{-1}): 2923, 2853, 1464, 1252, 734.

To a solution of **30** (450 mg, 1.4 mmol) in DMF (1 mL) was added NaN_3 (300 mg, 4.6 mmol, 3.4 eq). The reaction was stirred at 85 °C until complete (TLC control, hexane, approx. 6 h) and then the reaction was cooled to rt and H_2O (50 mL) was added. The mixture was extracted with CH_2Cl_2 (3 × 50 mL) and the combined organic layers were dried (Na_2SO_4) and concentrated in vacuo. The crude product was purified by flash column chromatography (hexane; SiO_2) to give **13** (156 mg, 0.53 mmol, 39%) as a colourless oil.

^{1}H NMR (400 MHz, $CDCl_3$) δ_H / ppm 5.43 - 5.28 (m, 2 H, C$\underline{H}$-9 and C$\underline{H}$-10), 3.26 (t, *J* = 7.0 Hz, 2 H, C$\underline{H}_2$-1), 2.08 – 1.93 (m, 4 H, C$\underline{H}_2$-8 and C$\underline{H}_2$-11), 1.61 (quin, *J* = 7.1 Hz, 2 H, C$\underline{H}_2$-2), 1.42 – 1.23 (m, 22 H, (C$\underline{H}_2$)$_5$-3-7 and (C$\underline{H}_2$)$_6$-12-17), 0.89 (t, *J* = 6.4 Hz, 3 H, C$\underline{H}_3$-18).

^{13}C NMR (100 MHz, $CDCl_3$) δ_C / ppm 130.0, 129.8, 51.5, 31.9, 29.8, 29.7, 29.5, 29.4, 29.3, 29.2, 29.1, 28.8, 27.2, 27.2, 26.7, 22.7, 14.1.

IR ($CHCl_3$, ν_{max}/cm^{-1}): 2925, 2856, 2095, 1465, 1261, 734.

1-Palmitoyl-2-acryloyl-*sn*-glycero-3-phosphocholine 47

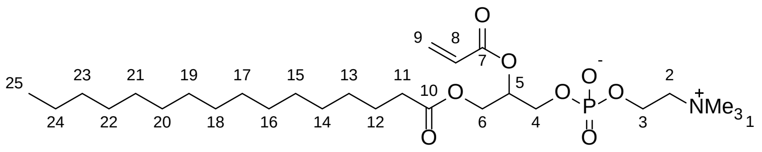

To a solution of **32** (110 mg, 0.22 mmol) and triethylamine (77 µL, 0.55 mmol, 2.5 eq) in $CHCl_3$ (1 mL) was added DMAP (0.5 mg, 4 µmol, 0.02 eq) and acryloyl chloride (27 µL, 0.33 mmol, 1.5 eq) at O °C. The reaction was stirred at rt for 36 h and then concentrated in vacuo. The crude product was purified directly by flash column chromatography (65:35:5 $CHCl_3$/MeOH/33% NH_3; SiO_2). The lipid fraction was collected and further purified by flash column chromatography (65:25:4 $CHCl_3$/MeOH/H_2O; SiO_2) to give a 4:1 mixture (17 mg, 0.03 mmol, 14%) of **47** and its 1-acyloyl-2-palmitoyl regioisomer as a white powder.

^{1}H NMR (500 MHz, $CDCl_3$) δ_H / ppm 6.42 (d, *J* = 17.0 Hz, 1 H, $C\underline{H}_{cis}\underline{H}_{trans}$-9), 6.14 (dd, *J* = 17.0, 10.6 Hz, 1 H, C$\underline{H}$-8), 5.89 (d, *J* = 10.6 Hz, 1 H, $C\underline{H}_{cis}H_{trans}$-9), 5.39 - 5.19 (m, 1 H, C$\underline{H}$-5), 4.41 - 4.16 (m, 4 H, $C\underline{H}_2$-6 and $C\underline{H}_2$-3), 3.99 (m, 2 H, $C\underline{H}_2$-4), 3.74 (m, 2 H, $C\underline{H}_2$-2), 3.31 (s, 9 H, $N(C\underline{H}_3)_3$-1), 2.29 (dt, *J* = 15.2, 7.6 Hz, 2 H, $C\underline{H}_2$-11), 1.68 - 1.49 (m, 2 H, $C\underline{H}_2$-12), 1.40 - 1.12 (m, 24 H, $(C\underline{H}_2)_{12}$-13-24), 0.88 (t, *J* = 6.9 Hz, 3 H, $C\underline{H}_3$-25).

^{13}C NMR (126 MHz, $CDCl_3$) δ_C / ppm 173.6, 165.6, 131.9, 128.1, 71.1 (d, *J* = 7.2 Hz), 66.2, 63.7, 62.8, 59.4, 59.4 (d, *J* = 2.2 Hz), 54.3 (3 C), 34.1, 31.9, 29.7, 29.7 (2 C), 29.7, 29.6, 29.4, 29.3, 29.2, 29.2, 24.9, 22.7, 14.1,

^{31}P NMR (202 MHz, $CDCl_3$) δ_P / ppm 0.38.

HRMS (ESI) *m/z* calcd for $C_{27}H_{53}NO_8P$ $[M+H]^+$: 550.3503, found: 550.3506.

IR ($CHCl_3$, ν_{max}/cm^{-1}): 3315, 2922, 2853, 1738, 1231.

_N_-(2-Hydroxyethyl)pent-4-ynamide 48

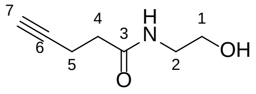

To a solution of 4-pentynoic acid (390 mg, 4.0 mmol) and *N*-hydroxysuccinimide (460 mg, 4.0 mmol, 1.0 eq) in THF (20 mL) was added DCC (907 mg, 4.4 mmol, 1.1 eq) at 0 °C. The reaction was stirred at 0 °C for 10 min before being allowed to warm to rt and react until the starting materials were completely consumed (TLC control, 2:3 petroleum ether/EtOAc, approx. 7 h). The reaction was filtered and concentrated in vacuo before being redissolved in THF (20 mL). Ethanolamine (240 µL, 4.0 mmol, 1.0 eq) was added at 0 °C and the reaction was allowed to warm to rt and react for 18 h. The solvent was removed in vacuo and the residue was purified by flash column chromatography ($CHCl_3$ then 10:1 $CHCl_3$/MeOH; SiO_2) to give pure **48** (290 mg, 2.1 mmol, 52%) as a white solid.

^{1}H NMR (400 MHz, $CDCl_3$) δ_H / ppm 6.35 (s, 1 H, N$\underline{H}$), 3.72 (t, *J* = 4.9 Hz, 2 H, C$\underline{H}_2$-1), 3.43 (q, *J* = 5.5 Hz, 2 H, C$\underline{H}_2$-2), 2.58 – 2.38 (m, 4 H, C$\underline{H}_2$-4 and C$\underline{H}_2$-5), 2.01 (t, *J* = 2.6 Hz, 1 H, C$\underline{H}$-7).

^{13}C NMR (101 MHz, $CDCl_3$) δ_P / ppm 172.4, 83.0, 69.6, 62.2, 42.5, 35.5, 15.0.

MS (ESI) *m/z*: 142.1 $[M+H]^+$, 164.1 $[M+Na]^+$.

N-(2-Hydroxyethyl)pent-4-ynamidoethylphosphocholine 49

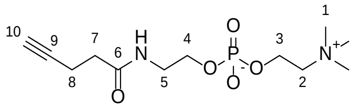

A solution of **48** (1.47 g, 10.4 mmol) and Et_3N (2.2 mL, 15.6 mmol, 1.5 eq) in dry THF (120 mL) was cooled to 0 °C and 2-chloro-1,3,2-dioxaphospholane 2-oxide (1.05 mL, 11.5 mmol, 1.1 eq) was added dropwise. The reaction was allowed to warm to rt and to react until complete consumption of starting material (TLC control, 2:3 petroleum ether/EtOAc). The reaction mixture was filtered through SiO_2 (eluting with acetone) and concentrated to a solid white residue. The crude solid was added under Ar to a 100 mL pressure tube containing a stirrer bar and dry MeCN (40 mL) was added. The tube was cooled to –20 °C and freshly distilled NMe_3 (2 mL, excess), stored at –78 °C, was added. The tube was quickly sealed and then heated to 80 °C overnight. Upon cooling to rt the MeCN was decanted and the crude product was purified by flash column chromatography (1:19 to 3:7 H_2O/MeCN; SiO_2) to give pure **9** (1.8 g, 5.9 mmol, 56%).

^{1}H NMR (400 MHz, CD_3OD) δ_H / ppm 8.18 (s, 1 H, N$\underline{H}$), 4.35 – 4.19 (m, 2 H, C$\underline{H}_2$-3), 3.99 – 3.80 (m, 2 H, C$\underline{H}_2$-4), 3.71 – 3.57 (m, 2 H, C$\underline{H}_2$-5), 3.42 (dd, J = 8.3, 4.4 Hz, 2 H, C$\underline{H}_2$-2), 3.23 (s, 9 H, N(C$\underline{H}_3$)$_3$-1), 2.53 – 2.35 (m, 4 H, C$\underline{H}_2$-7 and C$\underline{H}_2$-8), 2.28 (t, J = 2.4 Hz, 1 H, C$\underline{H}$-10).

^{13}C NMR (101 MHz, CD_3OD) δ_C / ppm 174.0, 83.4, 66.6, 64.4, 63.6, 60.7, 54.9, 41.0, 33.5, 17.9.

^{31}P NMR (162 MHz, CD_3OD) δ_P / ppm -0.18.

HRMS (ESI) *m/z* calcd for $C_{12}H_{23}N_2NaO_5P$ $[M+H]^+$: 329.0873, found: 329.0868.

Pentynoic anhydride

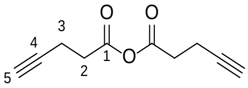

To a solution of 4-pentynoic acid (1.50 g, 15.3 mmol) and oxalyl chloride (2.0 mL, 23.3 mmol, 1.5 eq) in CH_2Cl_2 (20 mL) was added a drop of DMF at 0 °C. The reaction was stirred until the bubbling stopped, at which point it was allowed to warm to rt and stirred for a further 30 min. The solution was concentrated in vacuo and the formation of the acid chloride confirmed by FTIR spectroscopy (1722 cm^{-1}). The crude acid chloride was dissolved in a minimum of THF and added dropwise at 0 °C to a solution of 4-pentynoic acid (1.37 g, 14.0 mmol, 0.9 eq) and triethylamine (2.0 mL, 14.3 mmol, 0.9 eq) in THF (25 mL). The reaction was stirred for 18 h and then filtered and concentrated in vacuo. The residue was dissolved in CH_2Cl_2 (15 mL) and washed with aqueous $NaHCO_3$ (2 × 25 mL, 0.1 M) and brine (25 mL). The organic layer was dried (Na_2SO_4) and concentrated in vacuo to give pentynoic anhydride (1.98 g, 11.1 mmol, 72%) as a brown oil. The anhydride was used without further purification.

^{1}H NMR (400 MHz, $CDCl_3$) δ_H / ppm 2.74 (t, *J* = 7.2 Hz, 4 H, C$\underline{H}_2$-2), 2.56 (td, *J* = 7.2, 2.6 Hz, 4 H, C$\underline{H}_2$-3), 2.03 (t, *J* = 2.6 Hz, 2 H, C$\underline{H}$-5).

^{13}C NMR (100 MHz, $CDCl_3$) δ_C / ppm 167.2, 81.4, 69.7, 34.4, 13.8.

MS (ESI) *m/z* 201.1 $[M+Na]^+$.

IR ($CHCl_3$, ν_{max}/cm^{-1}): 3291, 1820, 1794, 996, 646.

5.3. Supplementary data for Chapter 2.

5.3.1. Autocatalytic synthesis of 3b.

A stock solution of **1** (680 mM), Cs_2CO_3 (200 mM), MeCN (100 mM, 0.15 eq), and optionally **3b** (134 mM, 0.2 eq, >5 × CMC) in D_2O was prepared and allowed to stand for 5 min. It was then divided into 2 mL portions in cylindrical 20 × 70 mm vials with octagonal 15 × 5 mm magnetic stirrer bars. 1-Hexanethiol **2b** (1.9 mL, 13.6 mmol, 10 eq) was added to each vial by ejection from a syringe down the side of the vial so as not to disturb the aqueous layer. The biphasic mixture was stirred at 150 rpm as determined by the digital readout of an *IKA Basic* stirrer/hotplate. Aliquots (0.05 mL) were withdrawn from the aqueous layer and quenched by dilution with 0.6 mL D_2O, and analysed by ^1H NMR spectroscopy on a 250 MHz or 200 MHz machine. Peaks were integrated relative to MeCN (2.06 ppm).

5.3.2. ^1H NMR spectra of first-generation reaction components in D_2O.

Compounds **1** and **2b** were purchased from Sigma Aldrich and used without further purification. The spectrum of **2b** is omitted as it consists of broad, poorly-resolved peaks because of its poor water solubility.

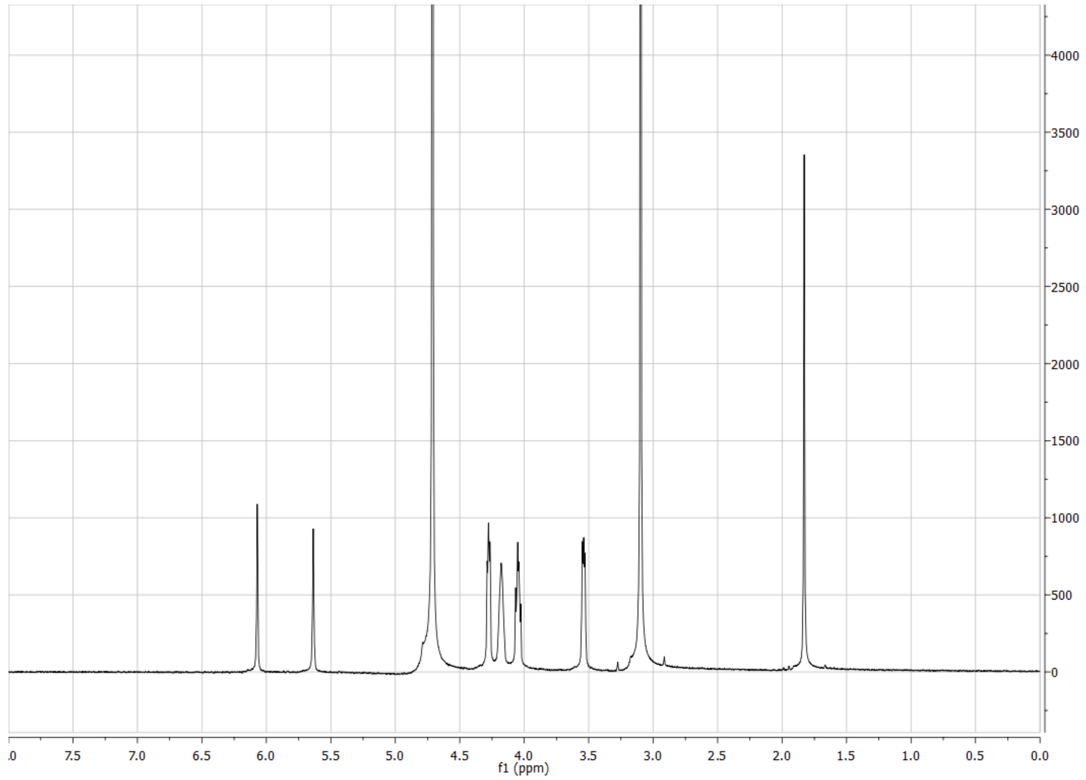

Figure 5.1. ^{1}H NMR spectrum of alkene 1 in D_2O.

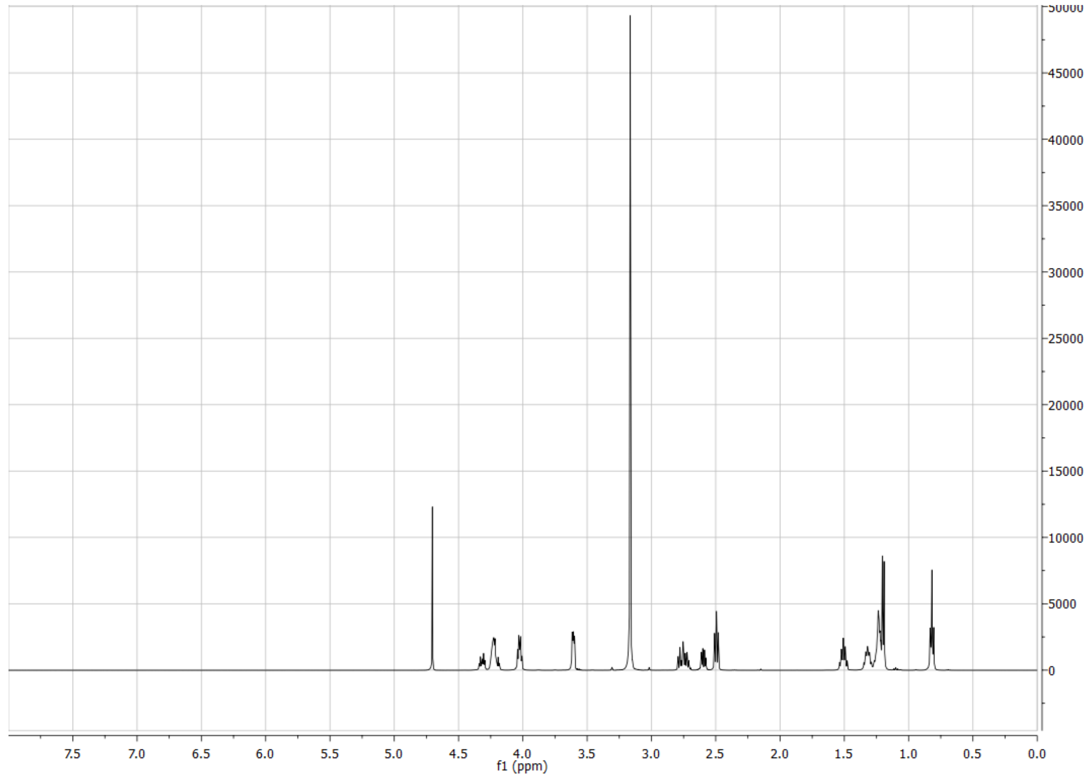

Figure 5.2. ^{1}H NMR spectrum of lipid 3b in D_2O.

5.3.3. Representative ^{1}H NMR data of the autocatalytic synthesis of 3b.

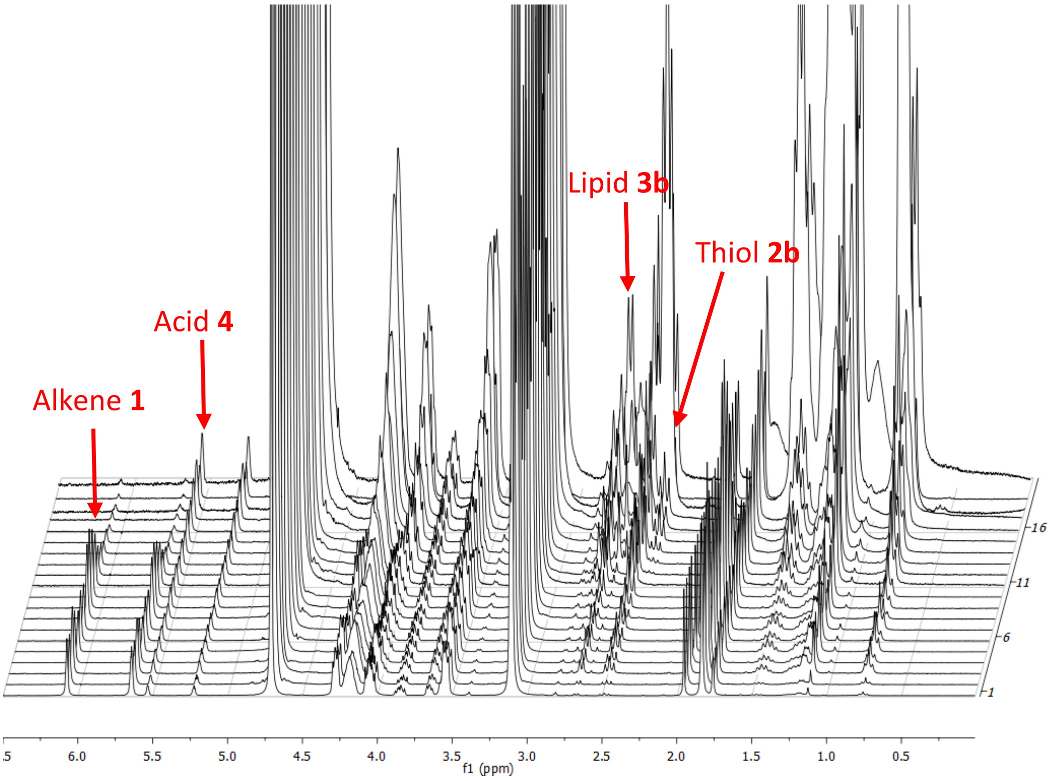

Figure 5.3. Stack plot of one control reaction of 1 with 2b.

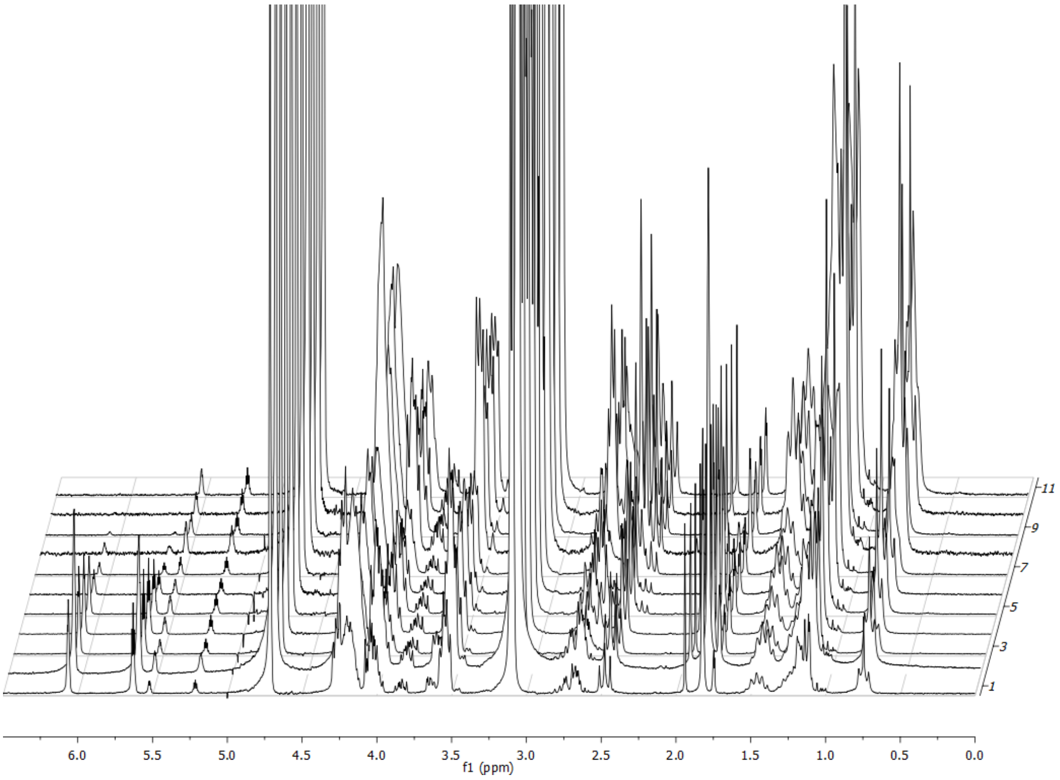

Figure 5.4. Stack plot of one reaction between 1 and 2b seeded with +20 mol% 3b from t = 0.

5.3.4. Complete DOSY data demonstrating association of 2b and 3b.

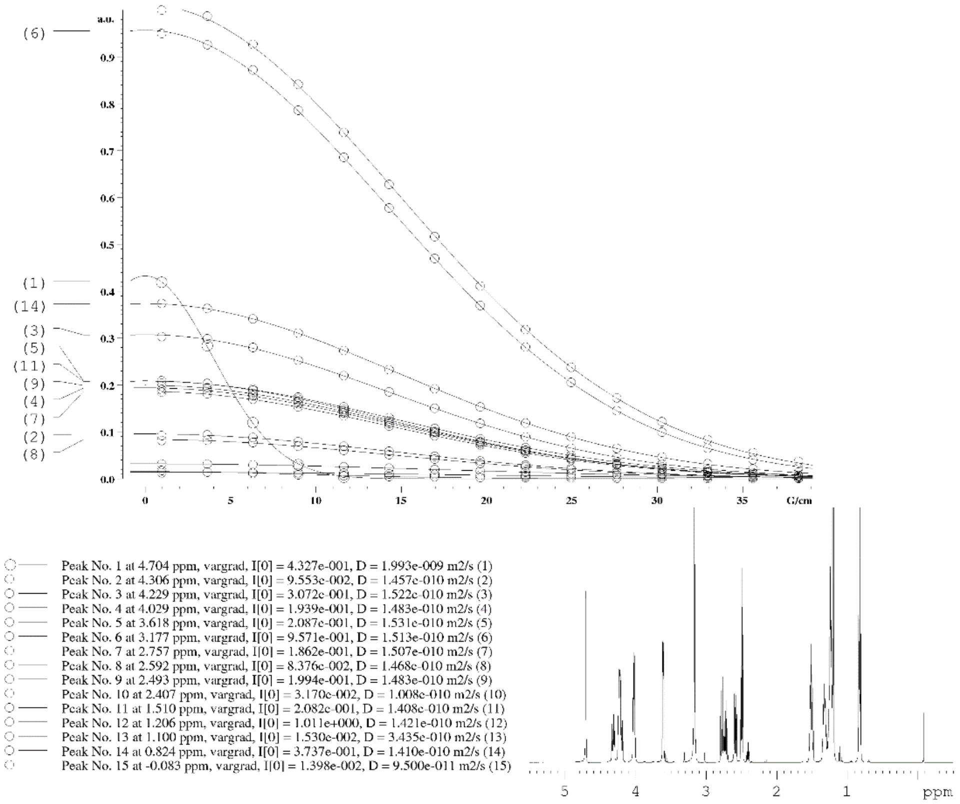

```
Peak No. 1 at 4.704 ppm, vargrad, I[0] = 4.327e-001, D = 1.993e-009 m2/s (1)
Peak No. 2 at 4.306 ppm, vargrad, I[0] = 9.553e-002, D = 1.457e-010 m2/s (2)
Peak No. 3 at 4.229 ppm, vargrad, I[0] = 3.072e-001, D = 1.522e-010 m2/s (3)
Peak No. 4 at 4.029 ppm, vargrad, I[0] = 1.939e-001, D = 1.483e-010 m2/s (4)
Peak No. 5 at 3.618 ppm, vargrad, I[0] = 2.087e-001, D = 1.531e-010 m2/s (5)
Peak No. 6 at 3.177 ppm, vargrad, I[0] = 9.571e-001, D = 1.513e-010 m2/s (6)
Peak No. 7 at 2.757 ppm, vargrad, I[0] = 1.862e-001, D = 1.507e-010 m2/s (7)
Peak No. 8 at 2.592 ppm, vargrad, I[0] = 8.376e-002, D = 1.468e-010 m2/s (8)
Peak No. 9 at 2.493 ppm, vargrad, I[0] = 1.994e-001, D = 1.483e-010 m2/s (9)
Peak No. 10 at 2.407 ppm, vargrad, I[0] = 3.170e-002, D = 1.008e-010 m2/s (10)
Peak No. 11 at 1.510 ppm, vargrad, I[0] = 2.082e-001, D = 1.408e-010 m2/s (11)
Peak No. 12 at 1.206 ppm, vargrad, I[0] = 1.011e+000, D = 1.421e-010 m2/s (12)
Peak No. 13 at 1.100 ppm, vargrad, I[0] = 1.530e-002, D = 3.435e-010 m2/s (13)
Peak No. 14 at 0.824 ppm, vargrad, I[0] = 3.737e-001, D = 1.410e-010 m2/s (14)
Peak No. 15 at -0.083 ppm, vargrad, I[0] = 1.398e-002, D = 9.500e-011 m2/s (15)
```

Figure 5.5. Uptake of hexanethiol 2b into micelles of 3b. Attenuation profile of integrated peaks with increasing gradient amplitude and associated D values for each peak. Hexanethiol (δ = 2.41 ppm, peak no. 10) and TMS (δ = -0.08 ppm, peak no. 15) are clearly seen to move more slowly than the lipid. These data are from the same experiment as Figure 2.5 (right).

5.3.5. Autocatalytic synthesis of 15.

A stock solution of **9** (100 mM), MeCN (100 mM), and optionally **15** (20 mM or 70 mM) in buffered (21 mM Tris, pD 7.85) D_2O was prepared. It was then divided into 3 mL portions in cylindrical 20 × 70 mm vials with octagonal 15 × 5 mm magnetic stirrer bars. 1-Octanethiol **14** (0.53 mL, 10 eq) was added to each vial by ejection from a syringe down the side of the vial so as not to disturb the aqueous layer. The biphasic mixture was stirred at 150 rpm as determined by the digital readout of an *IKA Basic* stirrer/hotplate. Aliquots (0.05 mL) were withdrawn from the aqueous layer and quenched by dilution with 0.6 mL D_2O, and analysed by ^{1}H NMR spectroscopy on a 400 MHz machine. Peaks were integrated relative to MeCN (δ = 2.06 ppm).

5.3.6. ^{1}H NMR spectra of second-generation reaction components in D_2O.

See section 0 for full characterisation of **9** and **16**. Compound **14** was purchased from Sigma Aldrich and used without further purification. The spectrum of **14** is omitted as it consists of broad, poorly-resolved peaks because of its poor water solubility.

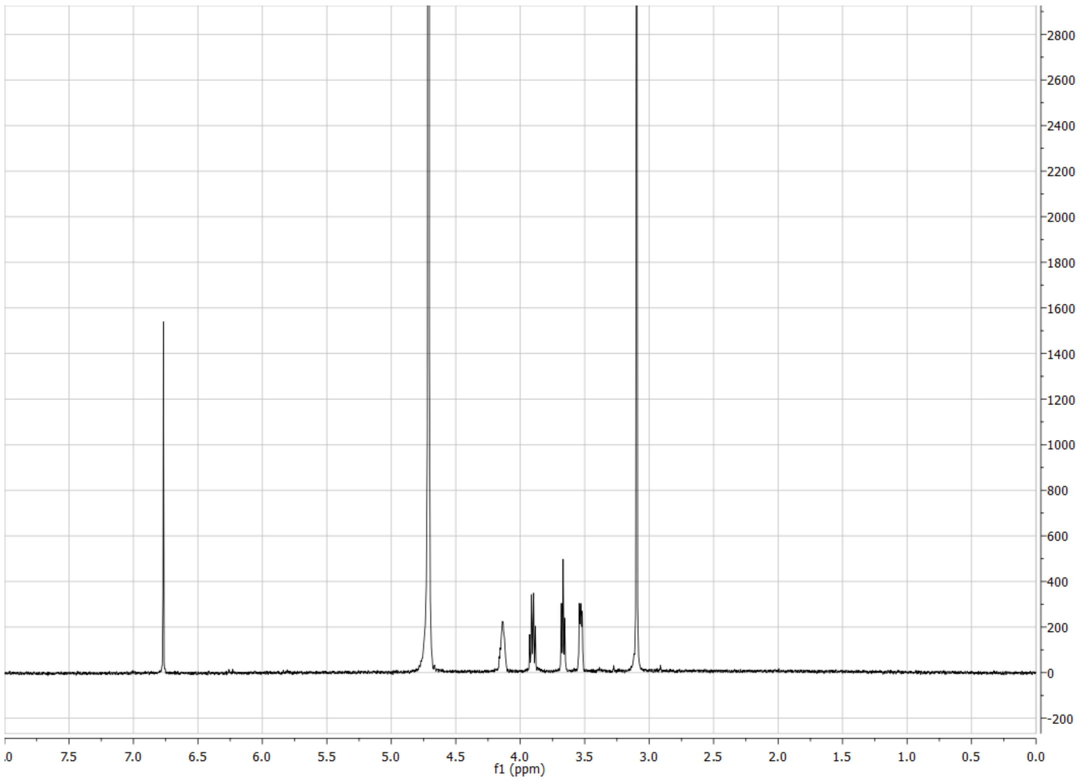

Figure 5.6. ^{1}H NMR spectrum of maleimide 9 in D_2O.

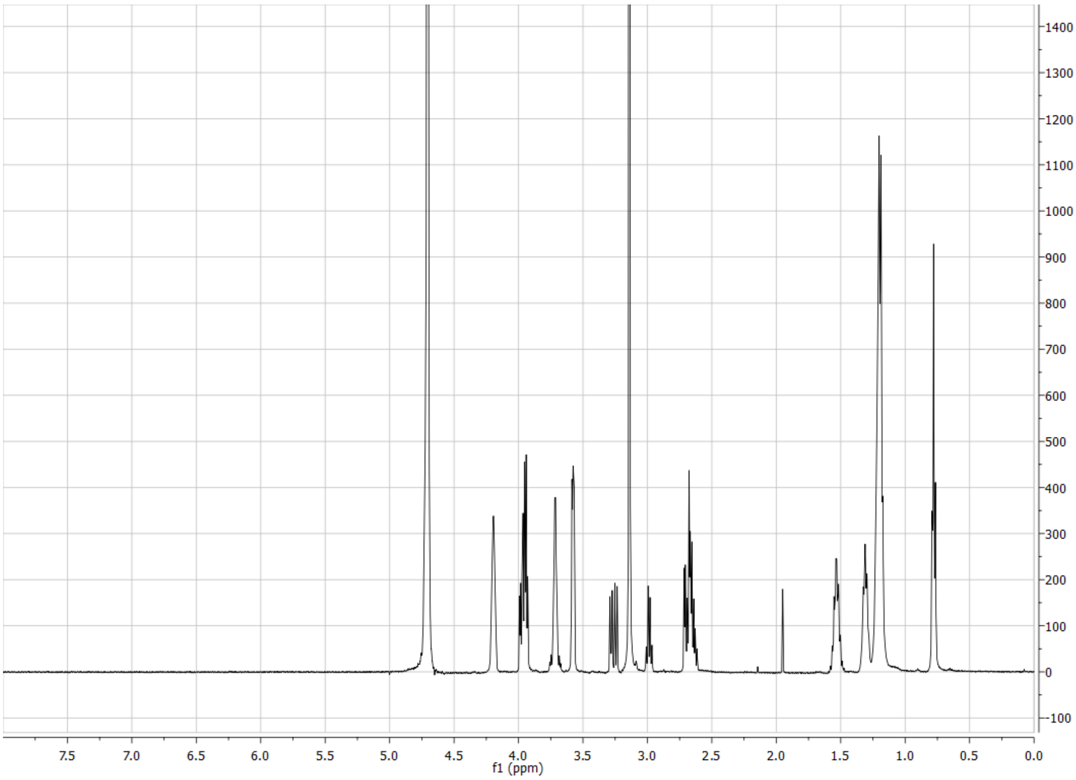

Figure 5.7. ^{1}H NMR spectrum of lipid 15 in D_2O.

5.3.7. Representative ^{1}H NMR data of the autocatalytic synthesis of 15.

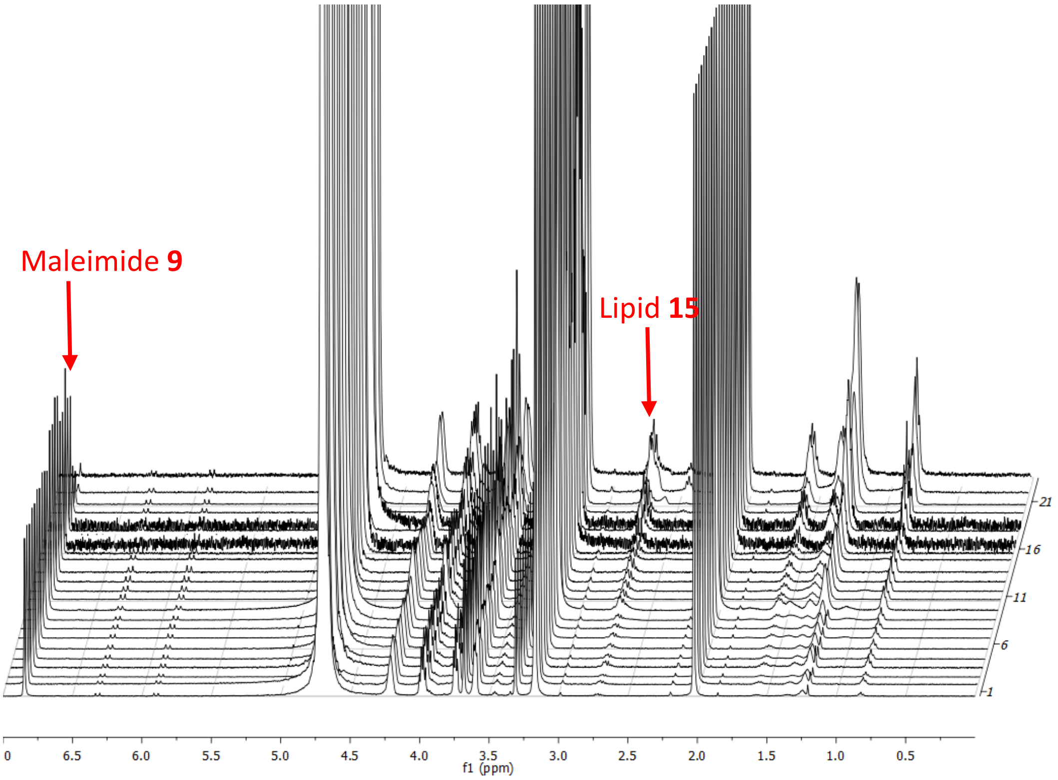

Figure 5.8. Stack plot of one control reaction of 9 with 14.

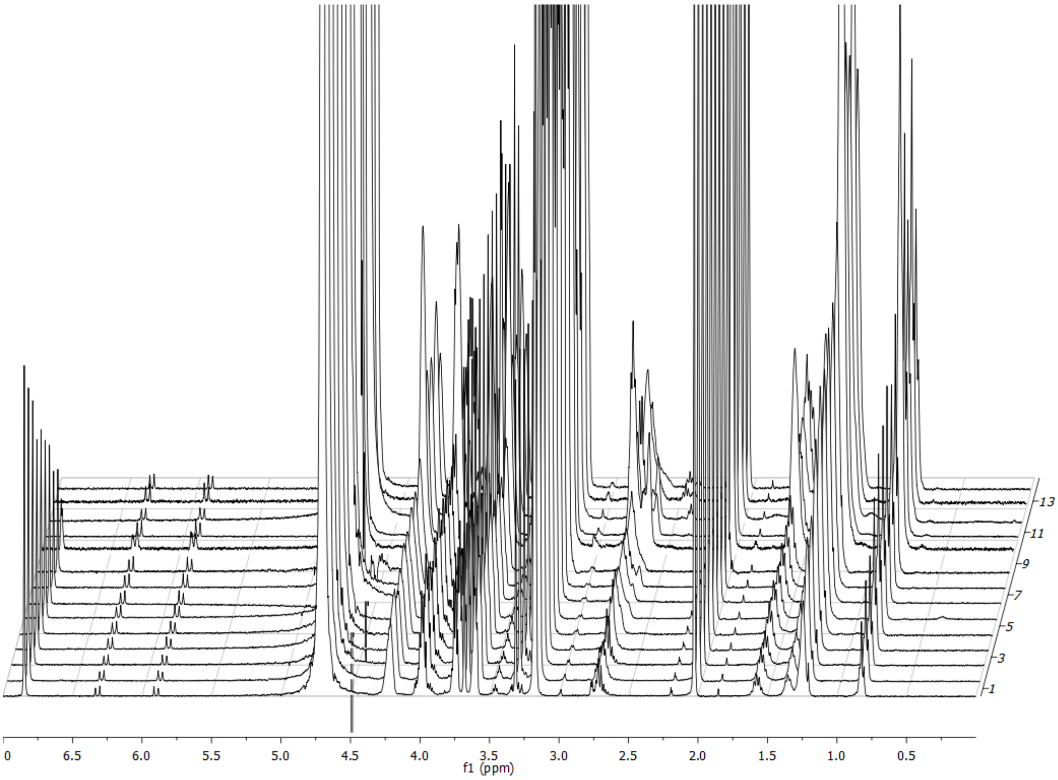

Figure 5.9. Stack plot of one reaction of 9 and 14 seeded with +20 mol% 15 from t = 0.

5.3.8. Complete DOSY data demonstrating association of 14 and 15.

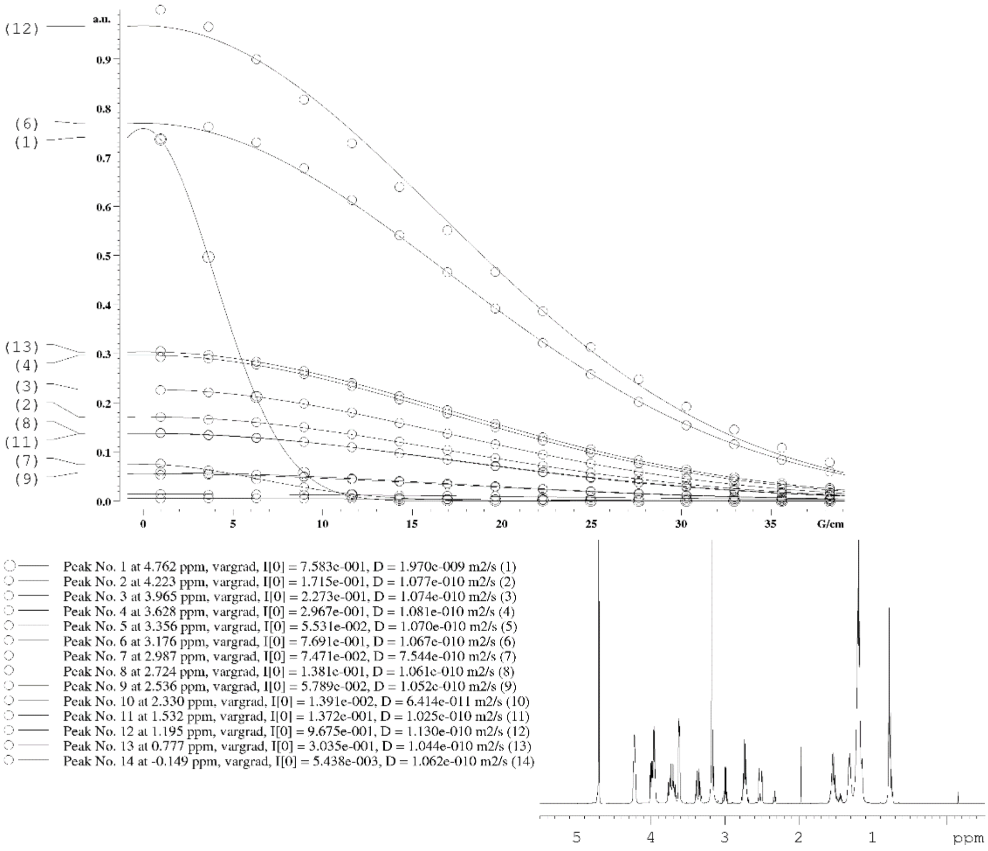

```
Peak No. 1 at 4.762 ppm, vargrad, I[0] = 7.583e-001, D = 1.970e-009 m2/s (1)
Peak No. 2 at 4.223 ppm, vargrad, I[0] = 1.715e-001, D = 1.077e-010 m2/s (2)
Peak No. 3 at 3.965 ppm, vargrad, I[0] = 2.273e-001, D = 1.074e-010 m2/s (3)
Peak No. 4 at 3.628 ppm, vargrad, I[0] = 2.967e-001, D = 1.081e-010 m2/s (4)
Peak No. 5 at 3.356 ppm, vargrad, I[0] = 5.531e-002, D = 1.070e-010 m2/s (5)
Peak No. 6 at 3.176 ppm, vargrad, I[0] = 7.691e-001, D = 1.067e-010 m2/s (6)
Peak No. 7 at 2.987 ppm, vargrad, I[0] = 7.471e-002, D = 7.544e-010 m2/s (7)
Peak No. 8 at 2.724 ppm, vargrad, I[0] = 1.381e-001, D = 1.061e-010 m2/s (8)
Peak No. 9 at 2.536 ppm, vargrad, I[0] = 5.789e-002, D = 1.052e-010 m2/s (9)
Peak No. 10 at 2.330 ppm, vargrad, I[0] = 1.391e-002, D = 6.414e-011 m2/s (10)
Peak No. 11 at 1.532 ppm, vargrad, I[0] = 1.372e-001, D = 1.025e-010 m2/s (11)
Peak No. 12 at 1.195 ppm, vargrad, I[0] = 9.675e-001, D = 1.130e-010 m2/s (12)
Peak No. 13 at 0.777 ppm, vargrad, I[0] = 3.035e-001, D = 1.044e-010 m2/s (13)
Peak No. 14 at -0.149 ppm, vargrad, I[0] = 5.438e-003, D = 1.062e-010 m2/s (14)
```

Figure 5.10. Uptake of octanethiol 14 into micelles of 15. Attenuation profile of integrated peaks with increasing gradient amplitude and associated D values for each peak. Octanethiol 14 (δ = 2.33 ppm) and TMS (δ = -0.15 ppm) are clearly seen to move more slowly than the lipid 15. These data are from the same experiment as Figure 2.8 (right).

5.3.9. 2D DOSY spectra referenced in Table 2.3.

Titles for these plots correspond to row entries in Table 2.3. DOSY NMR spectra of isolated components not shown.

Row A-C: Not shown.

Row D: refer to Figure 2.8 (left).

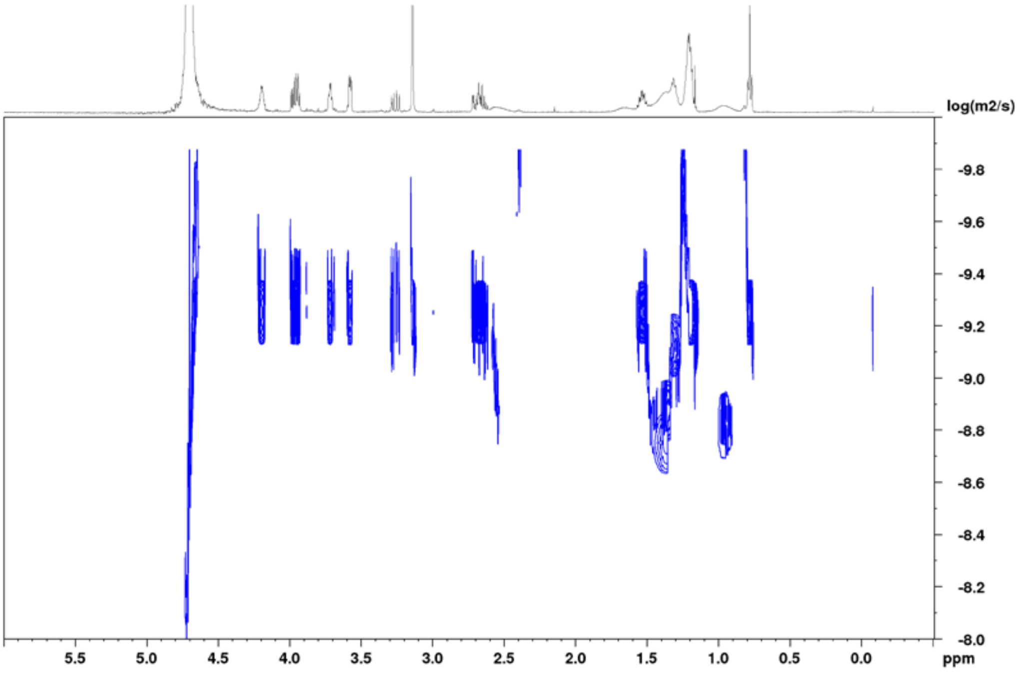

Figure 5.11. Row E: 14 (saturated) + **15** (5 mM) + TMS (saturated).

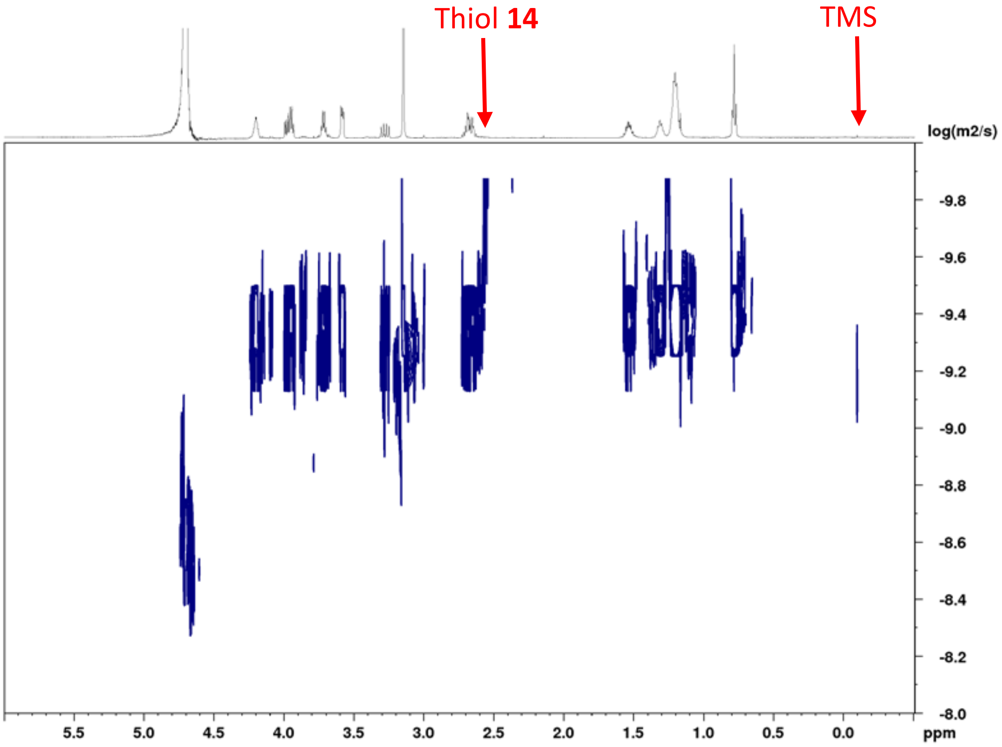

Figure 5.12. Row F: 14 (saturated) + **15** (10 mM) + TMS (saturated).

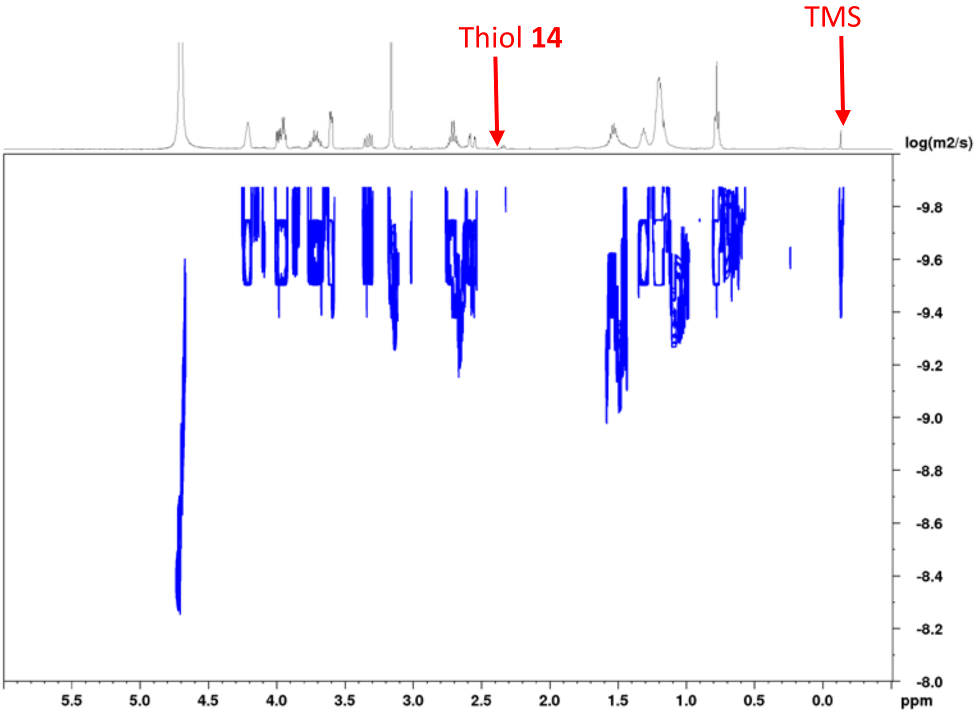

Figure 5.13. Row G: 14 (saturated) + **15** (20 mM) + TMS (saturated).

Row H: refer to Figure 2.8 (right).

Row I: Not shown.

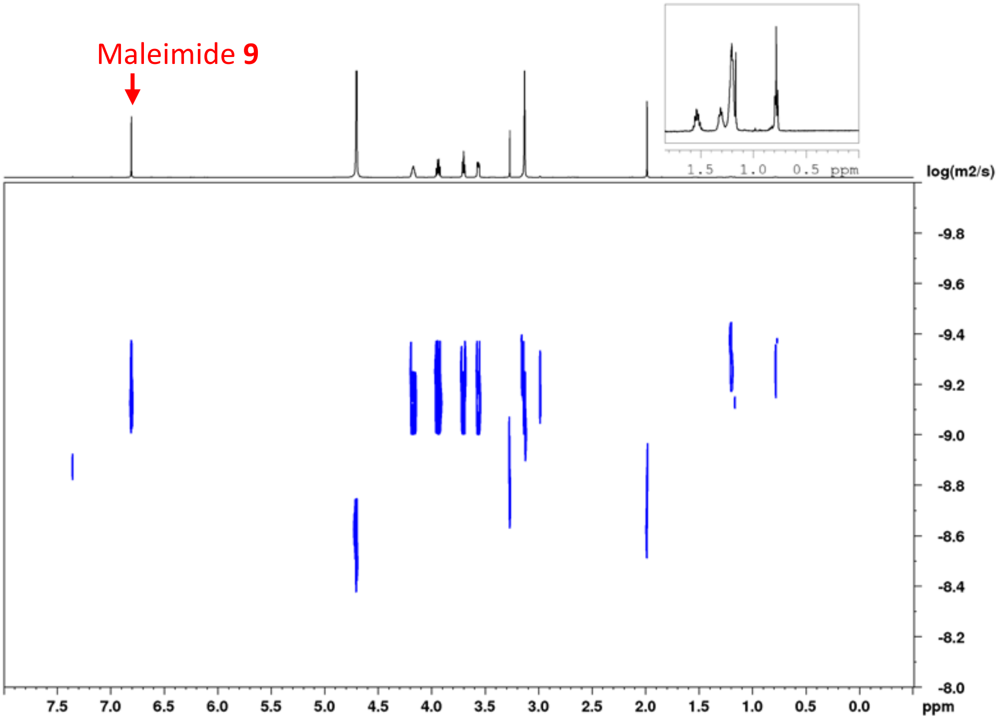

Figure 5.14. Row J: 9 (100 mM) + 15 (**3** mM); control experiment. Inset: zoomed-in region between 2.0-0 ppm for clarity.

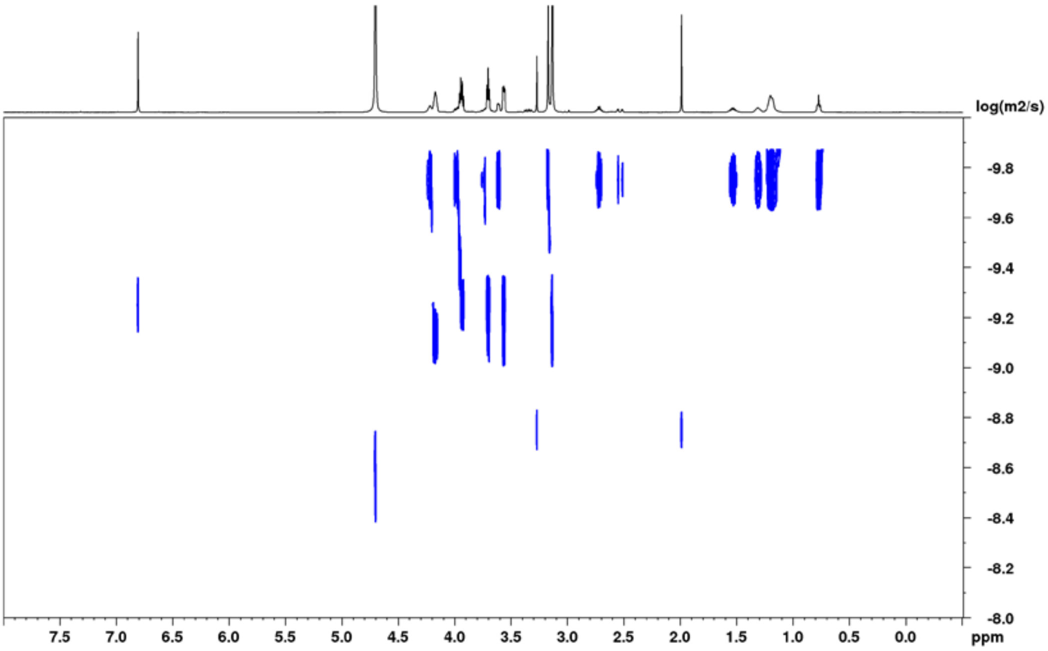

Figure 5.15. Row K: 9 (100 mM) + **15** (50 mM); micelles present; no binding of **9** to **15** observed.

5.3.10. Fluorimetric determination of critical micelle concentrations

The CMCs of compounds **25a-d** were determined by fluorimetry using 1,6-diphenyl-1,3,5-hexatriene (DPH) as a hydrophobic probe following Chattopadhyay and London.[20] Briefly, a solution of DPH in THF (1 µL, 10 mM) was added to a series of solutions (total volume 2 mL in milli-Q water) containing varying concentrations of the compound of interest. The solutions were stored in the dark at rt for 30 min. Samples were allowed to rest in the dark within the fluorimeter for 30 s prior to measurement.

5.3.11. GC derivatisation procedures

The ees of amino acids and their derivatives were analysed as chloroformate derivatives by chiral stationary phase gas chromatography as detailed in the general experimental (section 5.1).

Aqueous samples were derivatised using a procedure adapted from Abe *et al.*[21] A 50 µL aliquot was withdrawn and filtered using a 0.2 µm PTFE syringe filter. The filtrate was diluted in H_2O/EtOH/pyridine (60:32:8, 1 mL) and then ethyl chloroformate (50 µL) was added. The solution was shaken gently until the evolution of gas and heat finished. Chloroform (1 mL) was added and the sample was mixed by shaking. The layers were allowed to separate and the organic layer was removed, dried with Na_2SO_4, and filtered through a 0.2 µm PTFE syringe filter into an HPLC vial. Samples were analysed immediately or stored at 2-8 °C until analysis.

Samples in organic solvents were derivatised using a procedure adapted from Chen *et al.*[22] A 50 µL aliquot was withdrawn and filtered using a 0.2 µm PTFE syringe filter. The filtrate was concentrated in vacuo and redissolved 8 M NH_4OH/MeOH (1:1, 1 mL).

Pyridine (0.1 mL) and then methyl chloroformate (0.1 mL) were added and the solution was shaken gently until the evolution of gas and heat finished. Aqueous $NaHCO_3$ (0.5 mL, saturated) and chloroform (0.5 mL) were added and the layers were mixed by shaking. The layers were allowed to separate and the organic layer was removed, dried with Na_2SO_4, and filtered through a 0.2 µm PTFE syringe filter into an HPLC vial. Samples were analysed immediately or stored at 2-8 °C until analysis.

5.3.12. GC traces of asymmetric reaction components

GC Method A: 100 – 2 – 5 – 200 – 10.

GC Method B: 100 – 5 – 2 – 200 – 20.

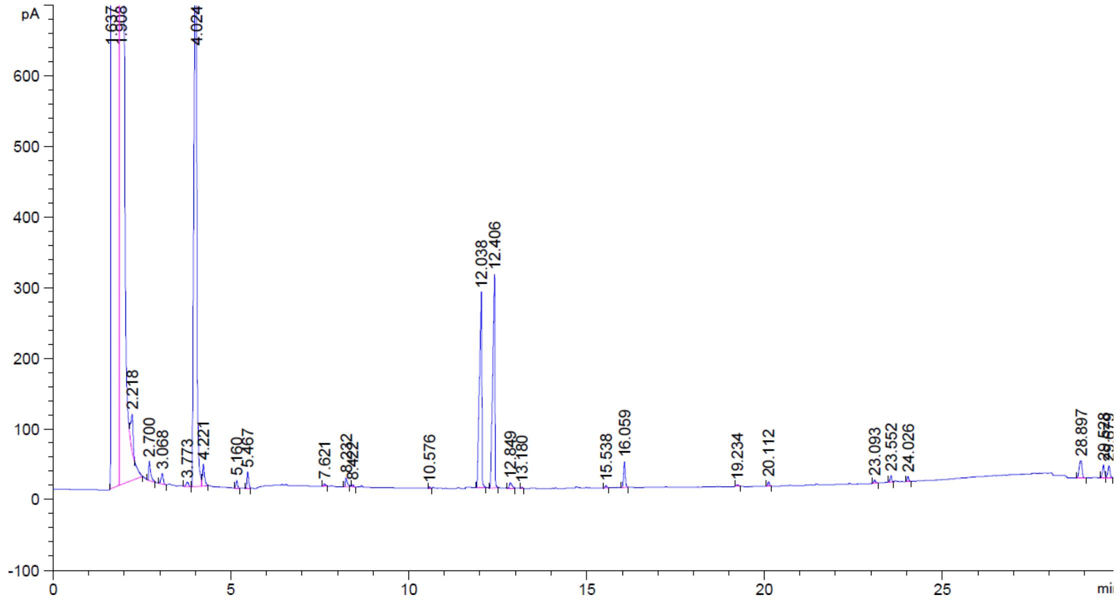

Figure 5.16. GC trace of DL-26 (DL-leucine). Method A.

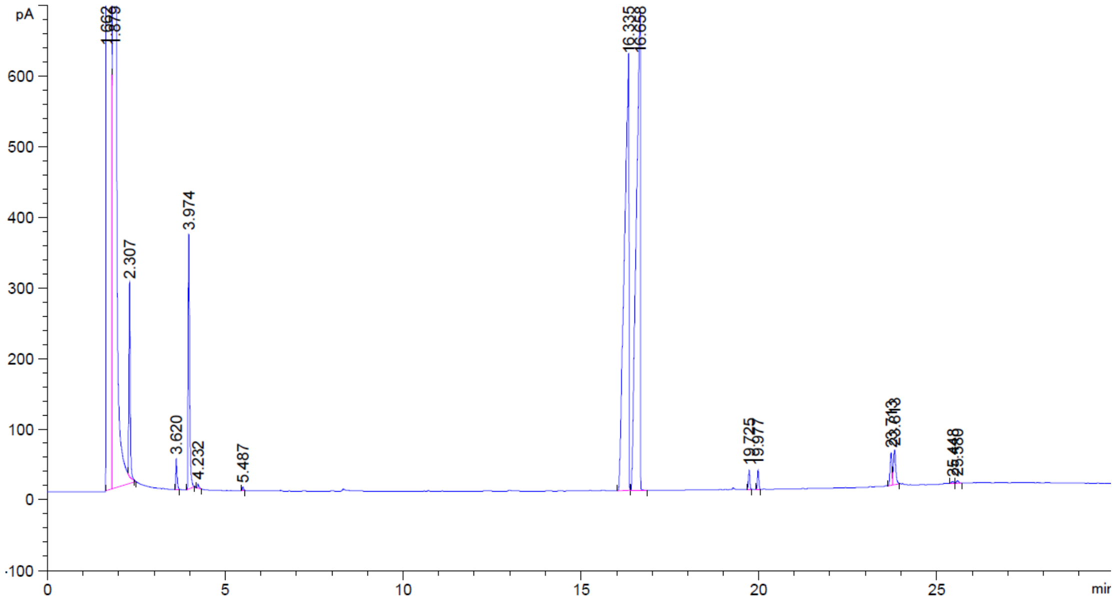

Figure 5.17. GC trace of DL-28a (*N*-(butyloxy)carbonyl-DL-leucine). Method A.

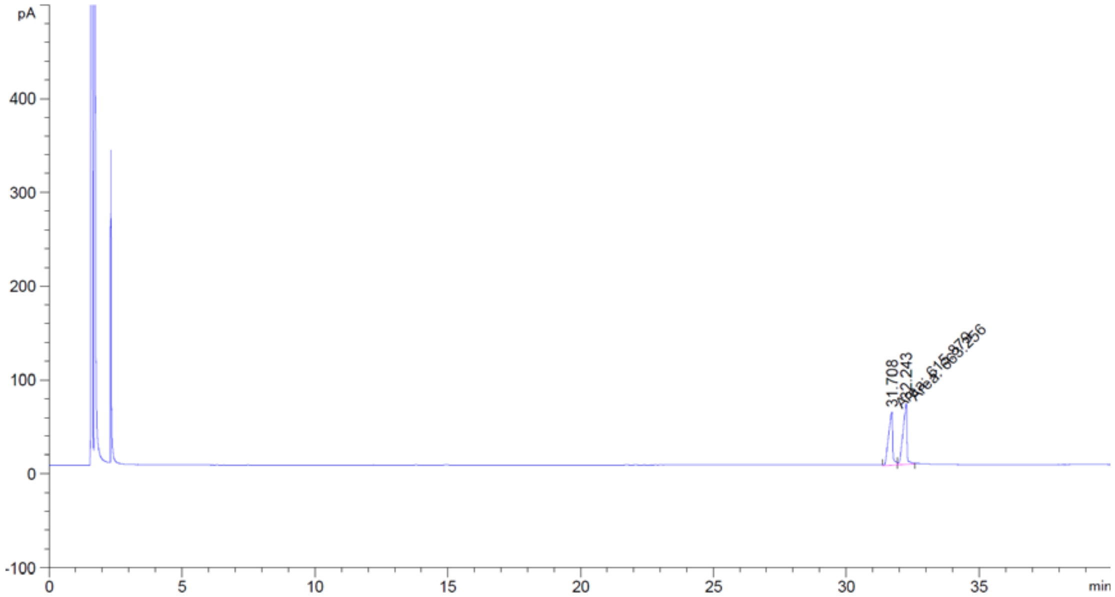

Figure 5.18. GC trace of DL-29 (DL-phenylalanine). Method B.

5.3.13. ^{1}H and DOSY NMR data referenced in Table 2.5.

Samples were prepared in D_2O and titrated to pD 8 using 2 M NaOD. All spectra are referenced relative to the HDO peak at $\delta = 4.79$ ppm.

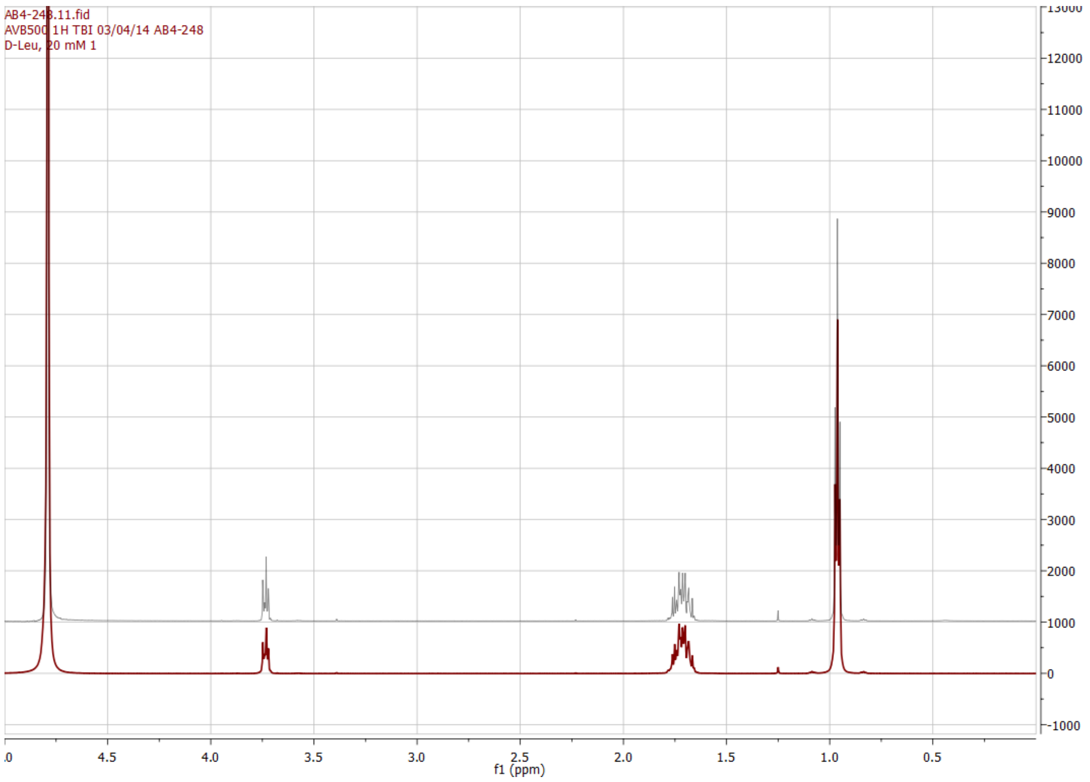

Figure 5.19. ^{1}H NMR spectra of L- and D-leucine (20 mM in D_2O, pH 8).

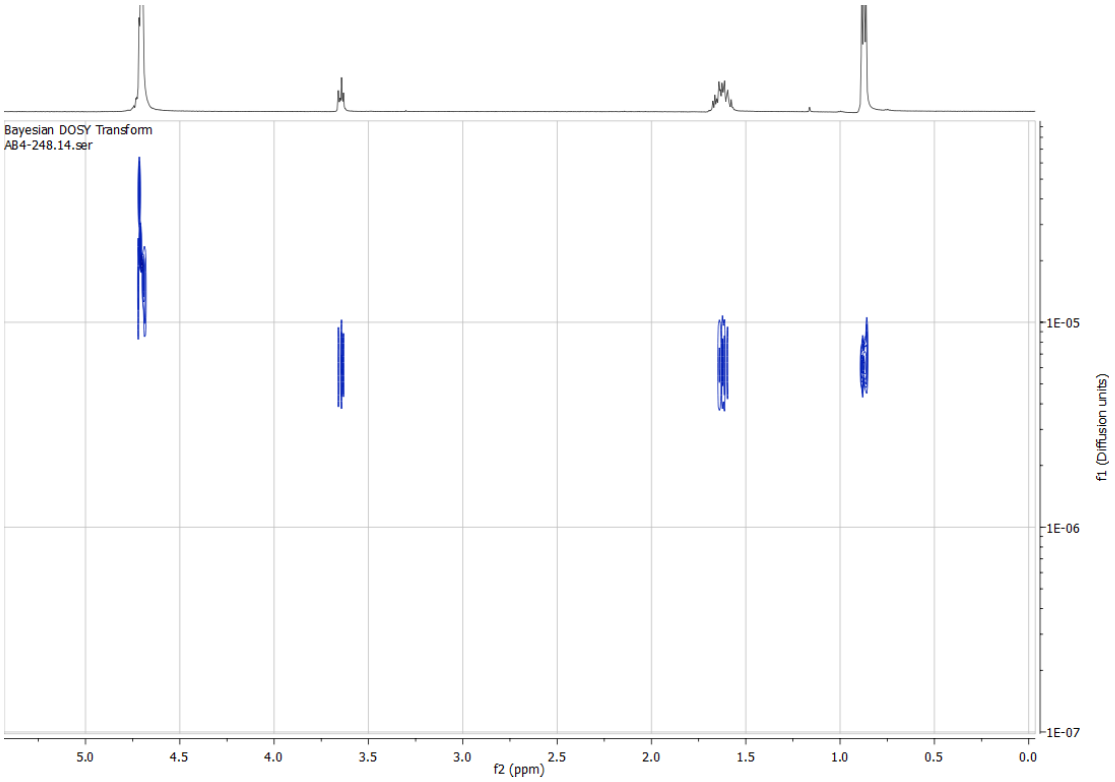

Figure 5.20. DOSY NMR spectrum of D-leucine (20 mM) in D_2O.

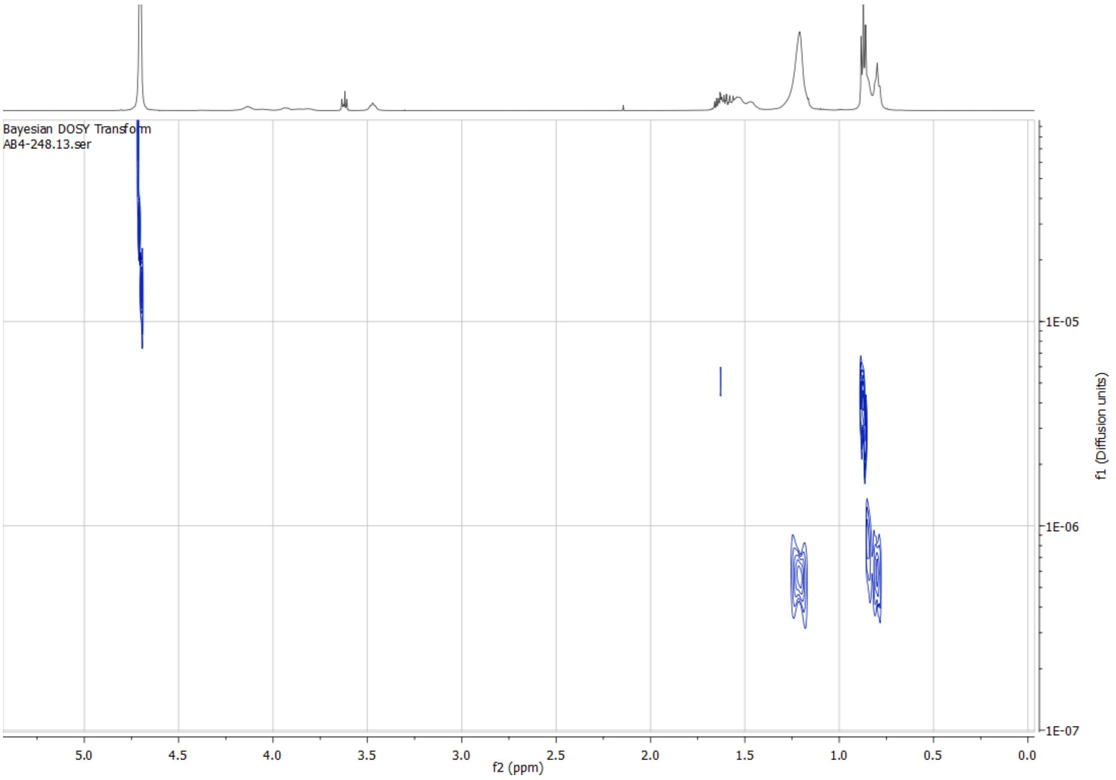

Figure 5.21. DOSY NMR spectrum of D-leucine (20 mM) and L-28b (50 mM) in D_2O.

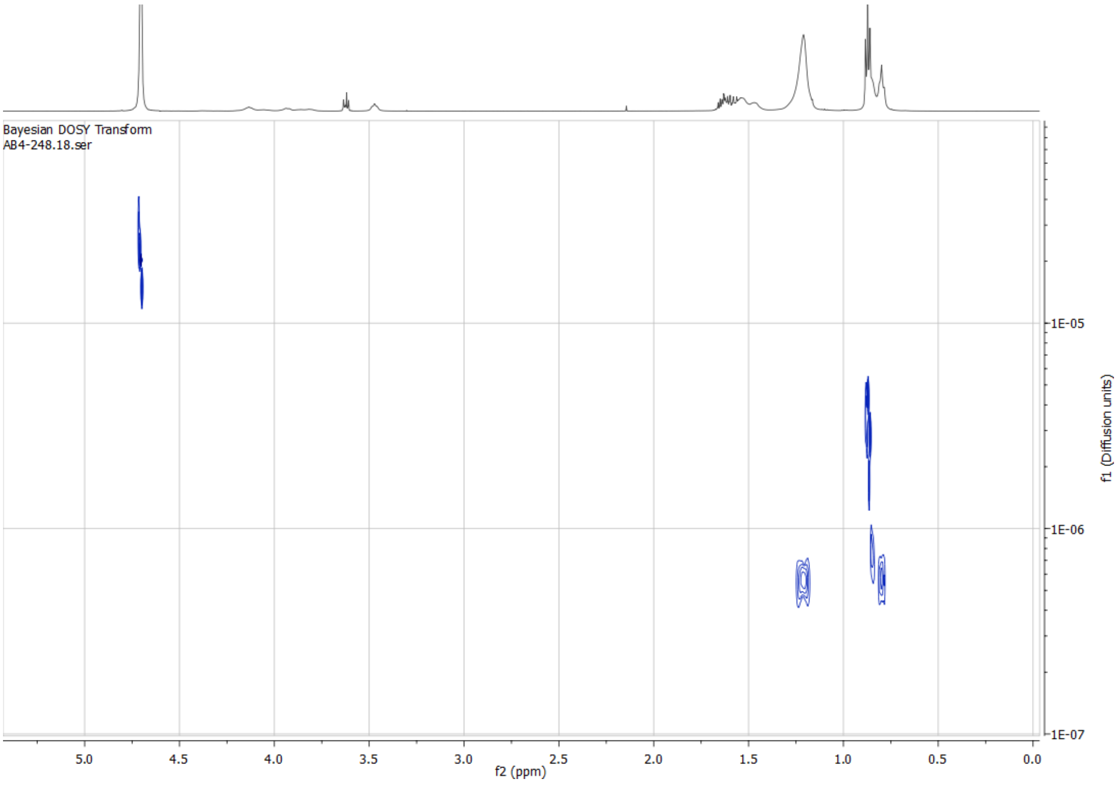

Figure 5.22. DOSY NMR spectrum of L-leucine (20 mM) and L-28b (50 mM) in D_2O.

5.4. Supplementary data for Chapter 3.

5.4.1. DLS size distributions for compound 1c.

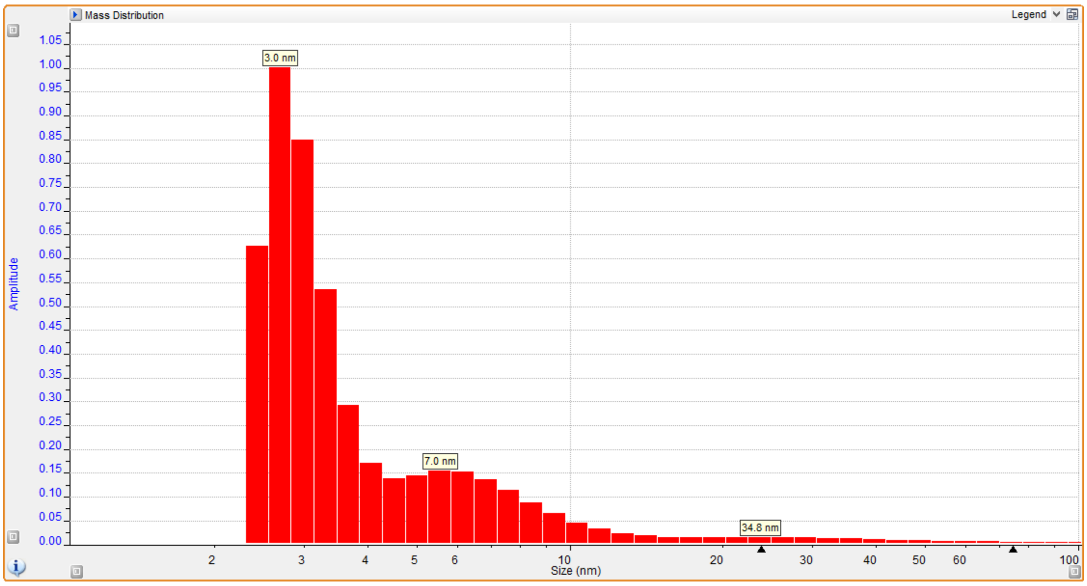

Figure 5.23. Mass distribution of 3c at 1 mM in H_2O.

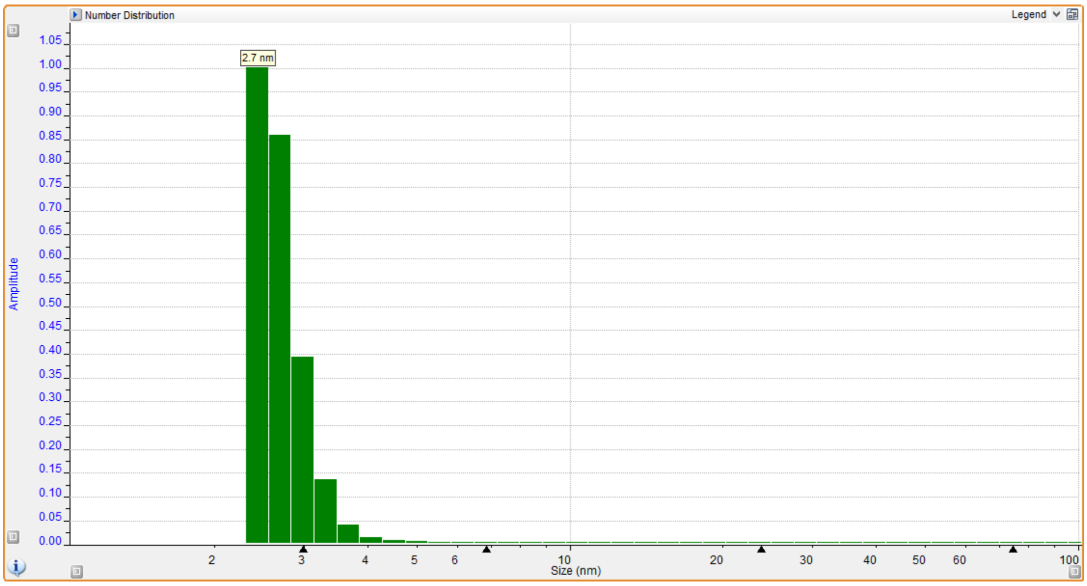

Figure 5.24. Number distribution of 3c at 1 mM in H_2O.

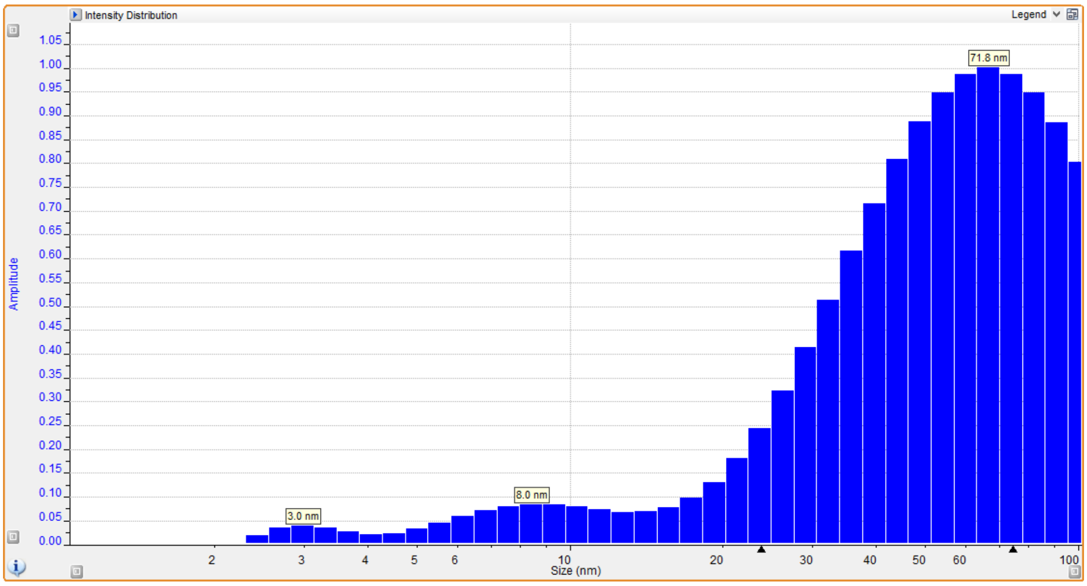

Figure 5.25. Intensity distribution of 3c at 1 mM in H_2O.

5.4.2. iSCAT experimental setup.

The iSCAT experimental setup is not described in complete detail here but is similar to that described by Ortega-Arroyo *et al.*[23] The incident light originates from a 445 nm diode laser, with an approximate incident power of 10 kW/cm^2 on the sample. Frames are recorded at 1 kHz with an exposure time of 0.56 ms using a CMOS camera (Photonfocus MV-D1024-160-CL-8). Unless noted otherwise, images were recorded at 333× magnification (31.8 nm/px), corresponding to an 8.1 × 8.1 µm^2 window.

Focus in the *z*-axis is maintained using an autofocus system relying on the total internal reflection (TIRF) of a 660 nm beam.[24] Movement in the *z* axis results in a corresponding movement in the *xy* plane of a totally internally reflected beam, which is detected and used as the basis for automated correction of the *z* position. This system can maintain the *z* position to within 5 nm consistently.

5.4.3. Sample preparation and experimental conditions.

All samples and reagents were purified before use, prepared using ultrapure Milli-Q water, and filtered through 0.2 µm PTFE filters prior to analysis by iSCAT.

Borosilicate glass coverslips (no. 1.5, 24 × 50 mm, VWR) were cleaned by sequential rinsing with distilled water, ethanol, and distilled water, and then sonicated for 10 min whilst standing in fresh HCl (approx. 0.4 M). The slips were washed with Milli-Q water and dried under a stream of dry nitrogen.

Silicone wells were prepared by washing sequentially with Milli-Q water and EtOH then drying under a stream of dry nitrogen. Unless noted otherwise, studies in section 3.3 used 3 mm diameter, 1 mm depth wells.

All coverslips and wells were prepared on the same day as analysis using fresh components.

A typical reaction between **1** and **2c** was performed as follows. Milli-Q water (4 µL) was deposited into a silicone well and the glass surface inspected to ensure satisfactory cleanliness. Thiol **1** (2 µL, 1.25 eq relative to **2**) was gently deposited atop the aqueous layer and the system was allowed to equilibrate for several minutes. A solution of MPC **2** (1.2 M) and Cs_2CO_3 (400 mM) was injected into the aqueous layer and mixed gently using a micropipette. One second of data, equivalent to 1000 frames, of data were then recorded every 6 seconds.

Negative controls were performed by omitting MPC **2** from the second aqueous solution. Seeded experiments were performed by replacing the initial aqueous solution with a 1 mM solution of **3**.

Direct examination of the thiol-water interface was achieved by first depositing thiol **1** (2 µL) on the glass surface and then displacing it by injection of milli-Q water (4 µL). The reaction site of interest was located and then a solution of MPC **2** (1.2 M) and Cs_2CO_3 (400 mM) was injected into the aqueous layer. Data were recorded manually, typically capturing 5000-10000 frames (5-10 seconds) at a time.

5.4.4. Data analysis methods.

Data were processed and analysed using National Instruments LabVIEW 2011 and the FIJI distribution of imageJ. A median filter was applied to all images as described by Andrecka *et al.*[25] in order to correct for inhomogeneity in the illumination field and systematic noise in the instrument. The median filter consists of a flat field image acquired by recording the temporal average of a series of images recorded while panning the observation region laterally. Background subtraction was achieved by averaging at least 10 frames lacking any signals arising from the sample and dividing subsequent frames by this image. Consecutive image subtraction was achieved by subtracting sets of images temporally offset by time Δt.

All quantitative data analysis was performed using software written by Jaime Ortega-Arroyo. Particle localisation and tracking were performed as described by Spillane *et al.*[26] and Jaqaman *et al.*[27] respectively in order to quantify the reaction kinetics and generate super-resolution binding and unbinding maps.

5.4.5. Kinetic modelling method

Kinetic modelling was performed using COPASI software (http://copasi.org). Parameter estimation was performed on all rate constants. For models A-C, the minimum and maximum values of k_1 and k_{-1} were limited such that $k_{-1}/k_1 > 10{,}000$ in order to exclude scenarios in which the thiol is readily water-soluble. Models were optimised using the evolutionary programming method with 500 generations of a population of size 50.

Initial concentrations of reagents were set to account for the saturation of the coverslip and the reaction stoichiometry, such that [**1**] = 4, [$\mathbf{2c}_{\mathrm{org}}$] = 5, [$\mathbf{2c}_{\mathrm{aq}}$] = 0, and [**3c**] = 0.

5.4.6. Description of supplementary videos.

The iSCAT figures present in Chapter 3 are static images and montages of video data. These are included as an electronic appendix in .gif format along with a copy of this text. While these are viewable with many programs including common browsers, the FIJI distribution of imageJ allows for fine control of the frame rate, easy magnification of small images, and adjustment of the contrast scale. The use of this or a similar program to examine these videos in detail is strongly recommended. FIJI is freely available at http://fiji.sc/Fiji at the time of writing (July 2015).

Unless noted otherwise, scale bars = 1 µm, raw data were recorded at 1 kHz with 333× magnification (32.8 nm/pixel), and the field of view corresponds to 8.1 × 8.1 µm. Video frame rates are given in fps and compared to the real-time rate in Hz. All videos loop continuously.

Movie 5.1. Monitoring the reaction of **1** and **2c** in situ with iSCAT. Supplementary to Figure 3.4. Top: flat-field corrected and differential imaging of the product of the reaction. Each differential image represents the average of 150 frames.

Bottom: landing rate profile with a solid dot indicating the current value at any given time in the movie. Right: cumulative super-resolution map of the centre of mass of the bound product. Figure kindly provided by Jaime Ortega-Arroyo.

Movie 5.2. Supported bilayer formation. Supplementary to Figure 3.6. Each frame is the average of 10 images. Movie is a montage of approx. 1 hr of observation and runs at 10 fps. Contrast scale: -0.08 to +0.06.

Movie 5.3. Advance of supported bilayer. Supplementary to Figure 3.7. Each frame is the average of 50 images. Playback speed: 20 fps. Actual speed: 20 Hz. Contrast scale: -0.06 to +0.03.

Movie 5.4. Direct observation of the reactive interface. Supplementary to Figure 3.8. Each frame is the average of 10 images. Movie is a montage of approx. 25 min and runs at 5 fps. Contrast scale: -0.33 to +0.32.

Movie 5.5. Proliferation of aggregates around the reactive interface. Supplementary to Figure 3.9A. Each frame is the average of 50 images. Playback speed: 20 fps. Actual speed: 20 Hz. Contrast scale: -0.85 to +0.54.

Movie 5.6. Further proliferation around the reactive interface. Supplementary to Figure 3.9B and C. Left: flat field image. Right: background subtraction image highlighting the formation of new material. Each frame is the average of 50 images. Playback speed: 20 fps. Actual speed: 20 Hz. Contrast scale: -0.85 to +0.53.

Movie 5.7. Complete enclosure of reactive interface by aggregates. This image is of the same droplet as in Movies 5.4-5.6 with the imaging region panned laterally to include the entire drop. Each frame is the average of 100 images. Playback speed: 10 fps. Actual speed: 10 Hz. Contrast scale: -0.79 to +1.96.

Movie 5.8. Proposed division event. Supplementary to Figure 3.10. The division event can be seen in context in Movie 5.5. Left: flat field image; right: background subtraction image. Frames are not time-averaged. Playback speed: 500 fps. Actual speed: 1 kHz. Scale bar = 500 nm. Contrast scales: left -0.86 +0.48; right -0.70, +0.42.

Movie 5.9. Formation of intermediate phase. Supplementary to Figure 3.11. Each frame is the average of 10 images. Playback speed: 50 fps. Actual speed: 100 Hz. Contrast scale: -0.08 to +0.05

Movie 5.10. Background subtraction image of intermediate phase, corresponds to Movie 5.9. Each frame is the average of 10 images. Playback speed: 50 fps. Actual speed: 100 Hz. Contrast scale: -0.02 to +0.02

Movie 5.11. Discrete movement of thiol-water interface. Supplementary to Figure 3.12. Left: flat field image; centre: consecutive subtraction image; right: composite image. Each frame is the average of 50 images. Playback speed: 20 fps. Actual speed: 40 Hz. Contrast scale: left +0.95 to +1.05, centre -0.01 to +0.03, right -0.05 to +1.05.

Movie 5.12. Fusion of inverted droplets. Supplementary to Figure 3.13B. Frames are not time-averaged. Playback speed: 500 fps. Actual speed: 1 kHz. Scale bar = 500 nm. Contrast scale: +0.66 to +1.75.

Movie 5.13. Fusion of inverted droplets. Supplementary to Figure 3.13B. Same data as Movie 5.12 played at a slower rate. Frames are not time-averaged. Playback speed: 20 fps. Actual speed: 1 kHz. Scale bar = 500 nm. Contrast scale: +0.66 to +1.75.

Movie 5.14. Fusion of small inverted droplets. Supplementary to Figure 3.13C. Frames are not time averaged. Playback speed: 20 fps. Actual speed: 1 kHz. Scale bar = 200 nm. Contrast scale: +0.70 to +2.46.

5.5. References

1 A. J. Bissette, B. Odell and S. P. Fletcher, *Nat. Commun.*, 2014, **5**, 4607.

2 A. Jerschow and N. Müller, *J. Magn. Reson. Ser. A*, 1996, **123**, 222–225.

3 A. Jerschow and N. Müller, *J. Magn. Reson.*, 1997, **125**, 372–375.

4 A. Krężel and W. Bal, *J. Inorg. Biochem.*, 2004, **98**, 161–166.

5 R. Matsuno, K. Takami and K. Ishihara, *Langmuir*, 2010, **26**, 13028–32.

6 W. H. Heath, F. Palmieri, J. R. Adams, B. K. Long, J. Chute, T. W. Holcombe, S. Zieren, M. J. Truitt, J. L. White and C. G. Willson, *Macromolecules*, 2008, **41**, 719–726.

7 E. Mahon, M. Barboiu and T. Aastrup, *Chem. Commun.*, 2010, **46**, 2441–2443.

8 P. Tiwari and A. K. Misra, *J. Org. Chem.*, 2006, **71**, 2911–2913.

9 V. Neto, R. Granet and P. Krausz, *Tetrahedron*, 2010, **66**, 4633–4646.

10 C. Shao, X. Wang, Q. Zhang, S. Luo, J. Zhao and Y. Hu, *J. Org. Chem.*, 2011, **76**, 6832–6836.

11 D. Lim, M. A. Brimble, R. Kowalczyk, A. J. A. Watson and A. J. Fairbanks, *Angew. Chem. Int. Ed. Engl.*, 2014, **53**, 11907–11.

12 D. Dunstan and L. Hough, *Carbohydr. Res.*, 1972, **23**, 17–21.

13 E. Fasoli, A. Arnone, A. Caligiuri, P. Paola D'Arrigo, L. de Ferra and S. Servi, *Org. Biomol. Chem.*, 2006, **4**, 2974–2978.

14 F. M. Menger, M. G. Wood, S. Richardson, Q. Zhou, A. R. Elrington and M. J. Sherrod, *J. Am. Chem. Soc.*, 1988, **110**, 6797–6803.

15 A. J. Sinclair, V. del Amo and D. Philp, *Org. Biomol. Chem.*, 2009, **7**, 3308–18.

16 I. Paterson, O. Delgado, G. J. Florence, I. Lyothier, M. O'Brien, J. P. Scott and N. Sereinig, *J. Org. Chem.*, 2005, **70**, 150–60.

17 C. Pugh, B. Raveendra, A. Singh, R. Samuel and G. Garcia, *Synlett*, 2010, **13**, 1947–1950.

18 P. Basabe, M. de Román, I. S. Marcos, D. Diez, A. Blanco, O. Bodero, F. Mollinedo, B. G. Sierra and J. G. Urones, *Eur. J. Med. Chem.*, 2010, **45**, 4258–69.

19 I. Budin and N. K. Devaraj, *J. Am. Chem. Soc.*, 2012, **134**, 751–753.

20 A. Chattopadhyay and E. London, *Anal. Biochem.*, 1984, **139**, 408–412.

21 I. Abe, T. Nishiyama and T. Nakahara, *Anal. Sci.*, 1994, **10**, 501–504.

22 W.-P. Chen, X.-Y. Yang, A. D. Hegeman, W. M. Gray and J. D. Cohen, *J. Chromatogr. B*, 2010, **878**, 2199–208.

23 J. Ortega Arroyo, J. Andrecka, K. M. Spillane, N. Billington, Y. Takagi, J. R. Sellers and P. Kukura, *Nano Lett.*, 2014, **14**, 2065–70.

24 K. Bellve, C. Standley, L. Lifshitz and K. Fogarty, *Biophys. J.*, 2014, **106**, 606a.

25 J. Andrecka, J. Ortega Arroyo, Y. Takagi, G. de Wit, A. Fineberg, L. MacKinnon, G. Young, J. R. Sellers and P. Kukura, *Elife*, 2015, **4**, e05413.

26 K. M. Spillane, J. Ortega-Arroyo, G. de Wit, C. Eggeling, H. Ewers, M. I. Wallace and P. Kukura, *Nano Lett.*, 2014, **14**, 5390–7.

27 K. Jaqaman, D. Loerke, M. Mettlen, H. Kuwata, S. Grinstein, S. L. Schmid and G. Danuser, *Nat. Methods*, 2008, **5**, 695–702.